OCS Study
MMS 2004-036

Coastal Marine Institute

Observational and Predictive Study of Inner Shelf Currents over the Louisiana-Texas Shelf

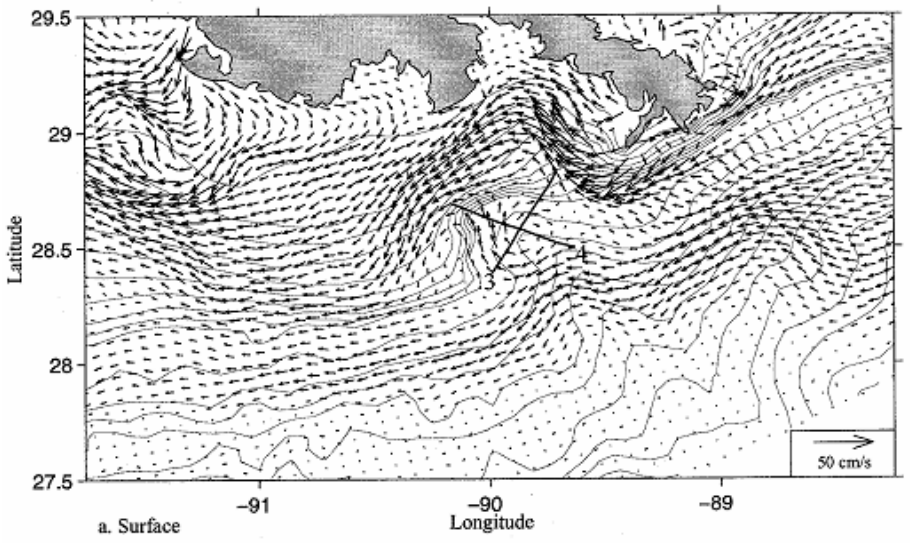

a. Surface

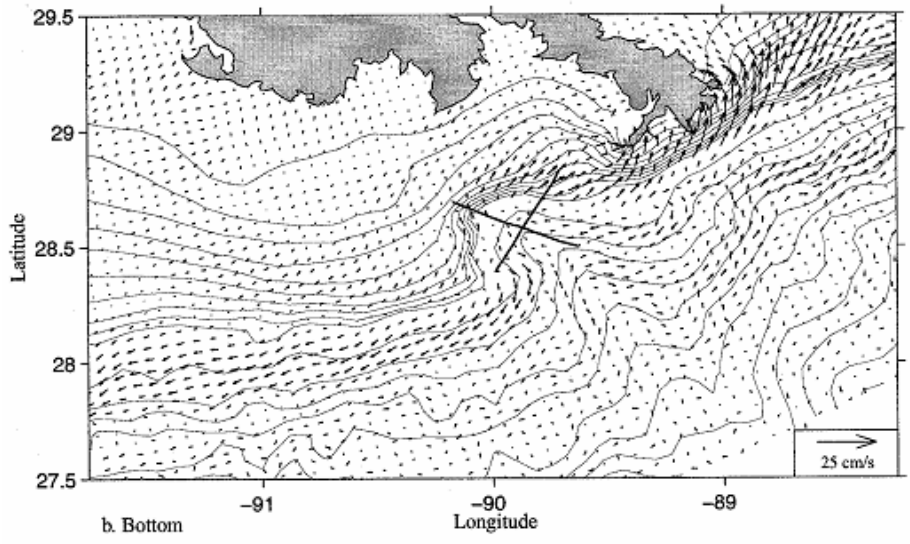

b. Bottom

U.S. Department of the Interior
Minerals Management Service
Gulf of Mexico OCS Region

Cooperative Agreement
Coastal Marine Institute
Louisiana State University

OCS Study
MMS 2004-036

Coastal Marine Institute

Observational and Predictive Study of Inner Shelf Currents over the Louisiana-Texas Shelf

Authors

Lawrence J. Rouse, Jr.
William J. Wiseman, Jr.
Leslie C. Bender
Norman L. Guinasso, Jr.
F. J. Kelly
David A. Brooks
Yao-Tsi Lo
J. She
and
A. Valle-Levinson

December 2004

Prepared under MMS Contract
14-35-0001-30660-19943
by
Coastal Marine Institute
Louisiana State University
Baton Rouge, Louisiana 70803

Published by

U.S. Department of the Interior
Minerals Management Service
Gulf of Mexico OCS Region

Cooperative Agreement
Coastal Marine Institute
Louisiana State University

AUTHORS AND THEIR AFFILIATIONS

Lawrence J. Rouse, Jr.
William J. Wiseman, Jr.
Department of Oceanography and Coastal Sciences
and Coastal Studies Institute
Louisiana State University
Baton Rouge, Louisiana

Leslie C. Bender
Norman L. Guinasso, Jr.
Geochemical and Environmental Research Group
Texas A&M University
College Station, Texas

F. J. Kelly
Conrad Blucher Institute for Surveying and Science
Texas A&M University – Corpus Christi
Corpus Christi, Texas

David A. Brooks
Yao-Tsi Lo
Department of Oceanography
Texas A&M University
College Station, Texas

J. She
Danish Meteorological Institute
Copenhagen, DK-2100 Denmark

A. Valle-Levinson
Center for Coastal Physical Oceanography
Old Dominion University
Norfolk, Virginia

DISCLAIMER

This report was prepared under contract between the Minerals Management Service (MMS) and Louisiana State University. This report has been technically reviewed by the MMS, and it has been approved for publication. Approval does not signify that the contents necessarily reflect the views and policies of the MMS, nor does mention of trade names or commercial products constitute endorsement or recommendation for use. It is, however, exempt from review and compliance with the MMS editorial standards.

REPORT AVAILABILITY

Extra copies of this report may be obtained from the Public Information Office (Mail Stop 5034) at the following address:

U.S. Department of the Interior
Minerals Management Service
Gulf of Mexico OCS Region
Public Information Office (MS 5034)
1201 Elmwood Park Boulevard
New Orleans, Louisiana 70123-2394

Telephone: (504) 736-2519 or
1-800-200-GULF

CITATION

Suggested citation:

Rouse, L.J., W.J. Wiseman, Jr., L.C. Bender, N.L. Guinasso, Jr., F.J. Kelly, D.A. Brooks, Y-T. Lo, J. She, and A. Valle-Levinson. 2004. Observational and predictive study of inner shelf currents over the Louisiana-Texas shelf. U.S. Dept. of the Interior, Minerals Management Service, Gulf of Mexico OCS Region, New Orleans, LA. OCS Study MMS 2004-036. 207 pp.

ABOUT THE COVER

Plan view of model derived near surface and near bottom velocity fields in the region between the Mississippi River Delta and the Atchafalaya Bay 90 days into the model run.

TABLE OF CONTENTS

TABLE OF CONTENTS
(continued)

TABLE OF CONTENTS
(continued)

LIST OF FIGURES

LIST OF FIGURES
(continued)

LIST OF FIGURES
(continued)

LIST OF FIGURES
(continued)

LIST OF FIGURES
(continued)

LIST OF FIGURES
(continued)

LIST OF FIGURES
(continued)

LIST OF FIGURES
(continued)

LIST OF FIGURES
(continued)

LIST OF FIGURES
(continued)

LIST OF FIGURES
(continued)

LIST OF TABLES

Page

Chapter 1

1.0 INTRODUCTION

Upon exiting the Mississippi and Atchafalaya River Deltas, the relatively fresh river waters flow westward along the coast to form the Louisiana Coastal Current (Wiseman and Kelly, 1994). The waters of this current system move downcoast (in the sense of phase propagation of Kelvin waves) most of the year and are readily identifiable along the Mexican coast of the Gulf of Mexico during the late fall, winter, and early spring. The flow is highly responsive to wind forcing, the most important synoptic wind pattern being cold air outbreaks (Huh et al., 1984), which occur on time scales of 3 to 10 days during the winter season (DiMego et al., 1976; Fernandez-Partagas and Mooers, 1975). Driven by such events, the current may reverse direction for a brief period of time and flow upcoast. During summer, when winds are weaker, the coastal waters of Louisiana are highly stratified and the surface flow may be incoherent with the near-bottom currents on sub-tidal time scales. Along the south Texas coast, the winds become upwelling favorable in late spring and the mean flow reverses direction and moves upcoast. For periods of a month or longer the direction of the mean current over the western Louisiana inner shelf may be eastward (Cochrane and Kelly, 1986).

An understanding of the currents within this coastal system is important to a number of environmentally important processes. Not the least of these is oil spills, since any spill in nearshore waters is immediately transported by the waters of this current system and any spill in Outer Continental Shelf waters must transit this current system before impacting the highly productive marshes and estuaries of coastal Louisiana and Texas. Much of this country's imported oil is lightered from super tankers offshore Louisiana and Texas. Offshore production contributes an important but significantly smaller amount than lightering. The volume of oil lightered last year from Southwest pass to Corpus Christi was about 275 million barrels; equivalent to almost 200 EXXON VALDEZ loads (Larry Smith, Calero Refining; personal communication). The volume continues to increase.

LATEX, the Louisiana-Texas Shelf Physical Oceanography Program funded by the MMS, has produced fascinating science about the economically important shelf region west of the Mississippi Delta. The analysis and synthesis effort now in progress will both answer many questions and generate new ones. One way to build on the LATEX results is to implement a core field program that provides real-time observations accessible to all. New investigations can then efficiently pursue the ideas and questions generated by recent studies about ocean processes. In some cases the data from the core program will suffice; in others, small temporary additions to the cores program would augment the standard observations. The results would allow us to understand the dynamics of near-surface coastal flow on scales not measured by LATEX.

Shortly after the end of the field portion of LATEX, the Texas General Land Office (TGLO) directed Texas A&M University to implement a program that provides real-time surface currents and water temperature at selected locations along the Texas coast. The Texas Automated Buoy System (TABS) is now in operation (Chaplin and Kelly, 1995), feeding the TGLO's oil spill trajectory model with the input necessary for rapid effective response (Martin et al., 1997). TABS is a long term operational system. While the primary purpose of TABS is to provide the

TGLO with information critical to early oil spill response operations, it also has tremendous research potential, particularly if the number of sites and the spatial extent are increased. TABS data are obviously useful to a myriad of other studies and applications ranging from vessel operations and fishing to transport of larvae and the distribution of sea-turtle strandings.

We added buoys to the TABS system and extended it into the shelf region off Louisiana with the following objectives:

> To provide the scientific community with a core observational program upon which numerous individual research projects can be built.
>
> To produce a framework for the assimilation of real-time observations of currents, wind and sea level into a "nowcast" of Louisiana-Texas circulation. This work would use the time-space correlation results derived from LATEX.
>
> To investigate the applicability of simple shelf-wave propagation models, such as those valid on the west Florida shelf, for the Louisiana-Texas shelf.
>
> To extend a long-term database that will advance our understanding of physical processes responsible for inner shelf circulation in the LATEX region.

Strategic and tactical oil spill response planning require knowledge of the expected inner shelf current field. Historical information on the coastal current field and its relationship to the climatology of regional wind forcing are important information used in risk analysis and to determine the optimal placement of clean up resources, e.g. booms and skimmers. Near-real time data on near surface flows and simple models of the wind-driven response of the coastal waters, which can assimilate real data to update nowcasts and short period forecasts of the flow field, will assist in the tactical deployment of resources, both human and material, during a spill response.

1.1 METHODOLOGY

TGLO and Texas A&M University operate multiple offshore TABS buoys (Figure 1.1). TABS buoys take a five-minute average of current velocity, direction and water temperature two meters below the surface every thirty minutes. A shore-based computer automatically acquires the data via cellular phone four or more times per day, performs QA/QC functions, and adds the observations to the TABS data base, which is publicly accessible through an interactive World Wide Web page: http://gergu3.tamu.edu/Tglo (Lee et al., 1996).

The TABS buoy is a modified spar design constructed of closed-cell, cross-linked, polyethylene foam with a polyurethane fabric-reinforced skin. It has an internal radar reflector, and a central, stainless steel, water tight tube that houses the current meter and communications subsystems. A Marsh-McBirney electro-magnetic 2-axis current sensor extends from the bottom of the buoy. Two solar panels provide power through rechargeable batteries to the communications subsystem and a marine lantern. The current meter has an independent battery pack. Reliable

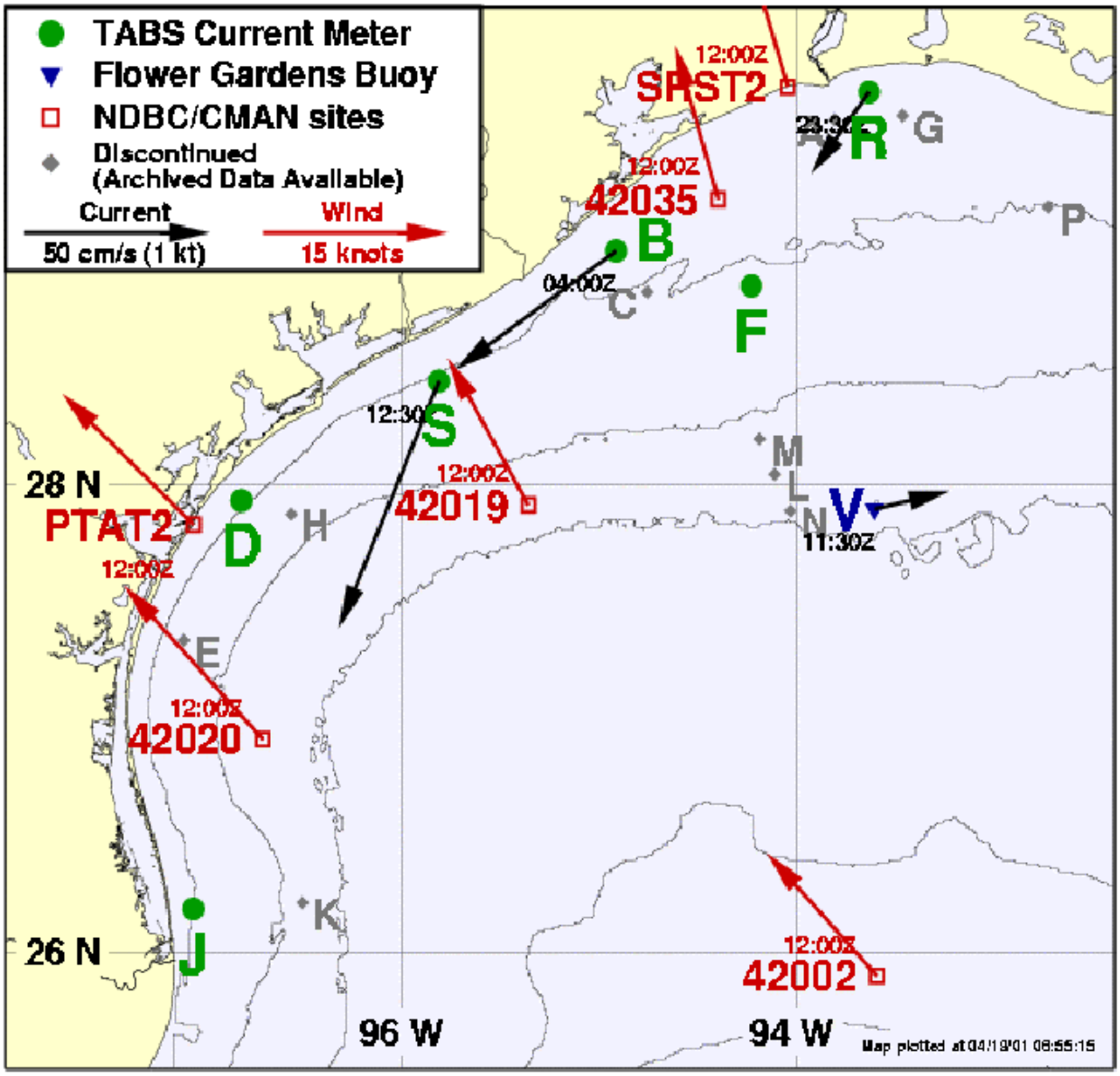

Figure 1.1 Map showing the location of Buoy P, in Louisiana waters, as well as the other TABS Buoy sites and real-time current vectors. The figure is taken from the TABS Website: resolute.gerg.tamu.edu/tglo. The map also shows NOAA Data Buoy Center (NDBC) real-time meteorological sites and wind vectors.

two-way communication is accomplished with the MNP-10 data communication protocol (Chaplin and Kelly, 1995).

To access the TABS data via the website, the user selects a station via an active map showing buoy, meteorological and sea level stations. The user may view the latest available data or select archived data from the TABS database. The data are available in graphic or numeric form (or both) and can be captured by the user. Interesting early results included observation of an impulse response in the coastal jet following the passage of a strong storm in April 1995, the currents (Figure 1.2) off Galveston during tropical storm Dean (which passed directly over two buoys in August 1995), inertial oscillations during the summer months and reversals in the coastal current during the Buffalo Marine oil spill (Figure 1.3).

A new buoy, designated P, was deployed over the inner shelf offshore western Louisiana. The buoy was serviced numerous times and, while data coverage as not continuous, large volumes of quality controlled data were collected, thus demonstrating the feasibility of operating TABS buoys offshore western Louisiana with existing resources and communications networks. The data collected from this buoy and from the R/V Gyre during the initial deployment cruise are described in the next chapter. Plots of the remaining data are presented as appendices. Initial results of a numerical model of the Texas-Louisiana shelf are also briefly discussed in the chapter.

Historical data sets collected by the TABS array prior to this effort were carefully analyzed to determine their statistical relationship to one another, to coastal winds, and to coastal water levels. This analysis isolates scales at which purely statistical nowcasts of the near surface currents might be reliable and isolates dynamical balances in the inner shelf water which should be pursued in further modeling efforts.

Among other results, a geopotential high over the inner shelf near 93.5º W, a hypothesized, transient, seasonal response to wind and riverine forcing, is used to explain observed flow patterns. The signals of longshore propagating flows, consistent with coastally-trapped wave theory, are identified in the data. Cross-shore flows, consistent with upwelling theory are also clearly present in the data.

1.2 RELEVANCE

This project addressed two framework areas: (1) modeling of environmental processes and systems and (2) new information about the structure/function of affected systems via application of descriptive and experimental means.

Current structure is an important determinant of many environmental processes including oil spill motion and the movement of living marine resources. While models are being developed for the entire Gulf of Mexico, they presently cannot be run in response to real time scenarios nor do they fully resolve the inner shelf circulation. Therefore, it is important to develop simple

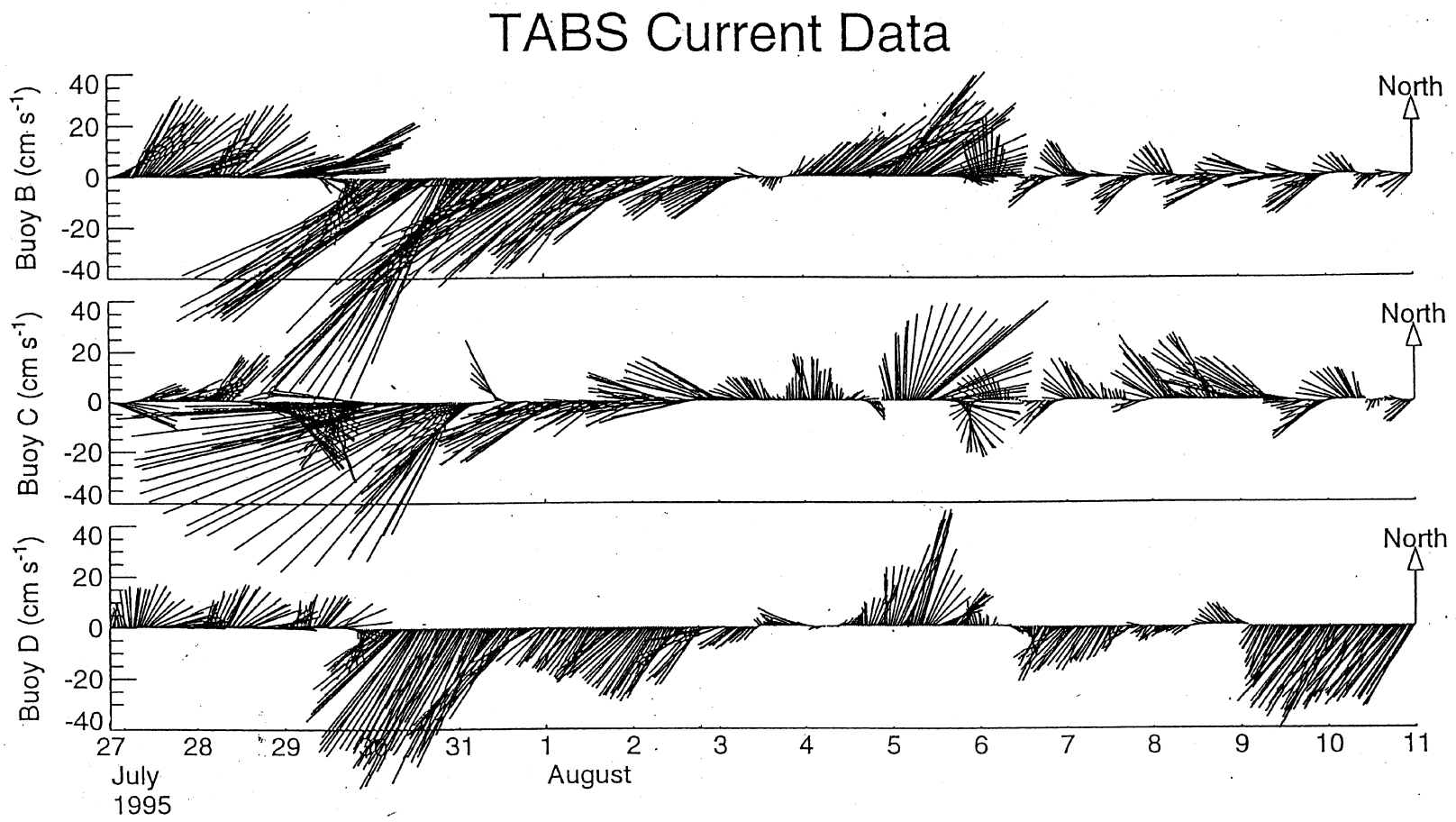

Figure 1.2 Currents measured by the TABS buoy array during Tropical Storm Dean. The buoy locations are shown in Figure 1.1.

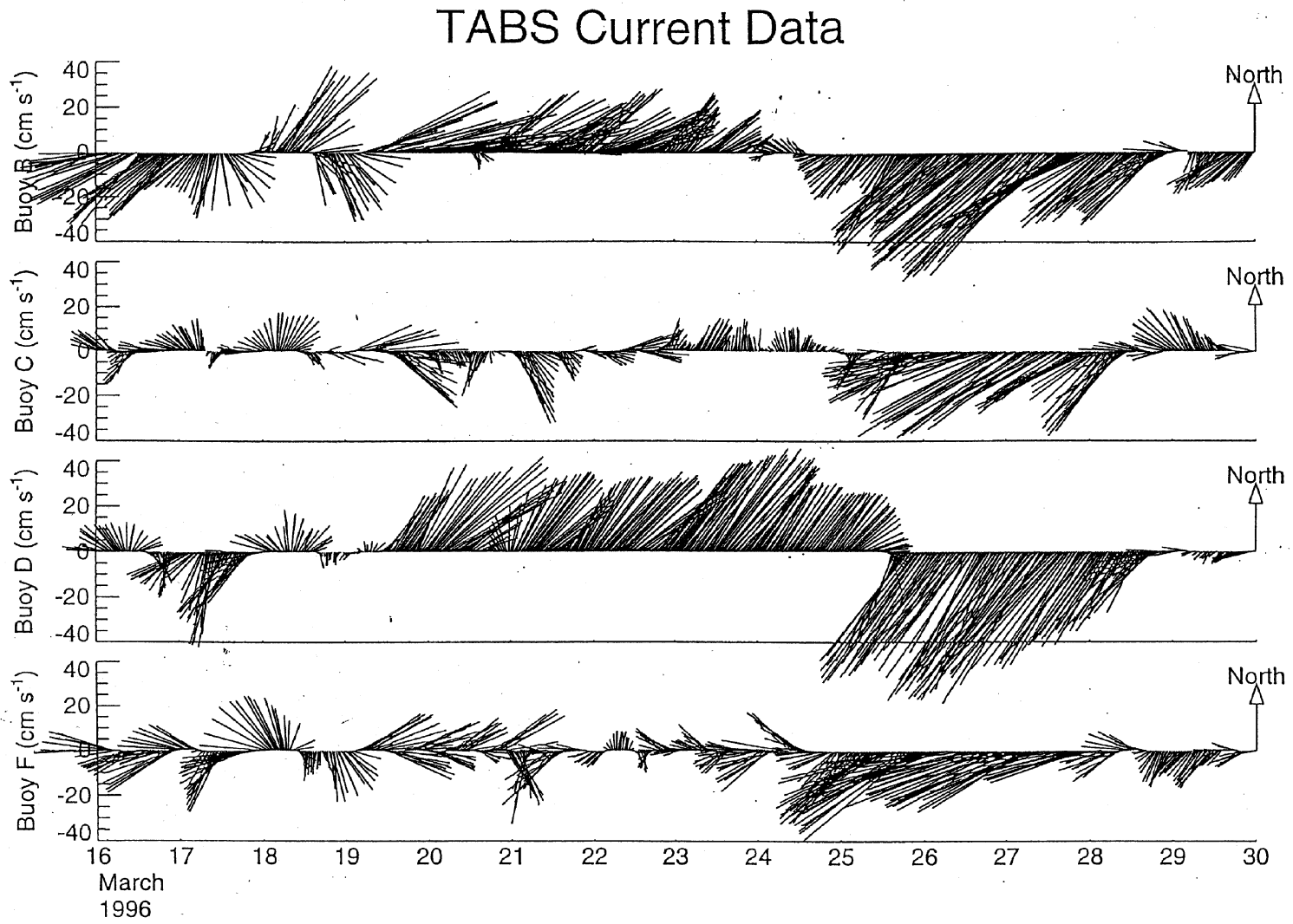

Figure 1.3 Currents measured by the TABS buoy array following the Buffalo Marine oil spill. The buoy locations are shown in Figure 1.1.

techniques, based on dynamical principles where possible, to 'nowcast' or predict such current structures. These predictors/'nowcastors' must be initialized with real-time data. The TABS array project provides a system for delivering such real-time data. It provides synoptic data that will allow understanding of the dynamics of coastal near surface flows on scales not measured by LATEX.

1.3 SUMMARY

A coastal current of low-salinity waters originating from the Mississippi and Atchafalaya Deltas dominates the Louisiana-Texas inner shelf. Relatively swift wind-driven flows in excess of a knot (0.5 m/s) are not uncommon within this system. These waters respond quickly and intensively to local and far-field wind forcing. Knowledge of the flow within these waters is important for both strategic and tactical planning for oil spill response. From a strategic sense, it is important to know the characteristics of the flow in a statistical sense: the maximum expected flows and the expected response to climatological wind variability. This knowledge will assist in the stockpiling of response equipment. From a tactical standpoint, it is important to know in which direction the currents are flowing when a spill occurs:, a simple model of wind-driven currents in conjunction with a forecast of regional winds will allow anticipation of shifts in the transport of spilled materials.

Texas A&M University has deployed an initial array of buoys in Texas coastal waters that measure near-surface currents and water temperature. The buoys of the Texas Automated Buoy System (TABS) report the measured data in near-real time via cellular telephone to a base station. Computers automatically perform quality control procedures and post the observations to a publicly accessible home on the Internet. We extended this array into western Louisiana waters. The data were processed and the meters maintained exactly as the present Texas array is handled. The Texas A&M buoy operated intermittently, but provided a significant volume of data that passed all quality control tests and demonstrated the feasibility of extending the TABS array into Louisiana waters using the present technology and communication networks. Data collected during the deployment cruise, which also surveyed regions of the shelf as far east as the Mississippi Delta, are discussed in the text and plots are presented in the appendices. Finally, initial results of a modeling exercise carried out at Texas A&M demonstrate their ability to model the flows over the LATEX shelf region. Results of this portion of the project are covered in Chapter 2.

Analyses of historical TABS data by scientists at Old Dominion University both add credence to the interpretation of previously collected data from a variety of sources and suggest new patterns. A geopotential high over the inner shelf near 93.5º W, a hypothesized, transient, seasonal response to wind and riverine forcing, is used to explain observed flow patterns. The signals of longshore propagating flows, consistent with coastally trapped wave theory, are identified in the data. Cross-shore flows, consistent with upwelling theory are also clearly present in the data. Results of this portion of the project are covered in Chapter 3.

Chapter 2

2.0 INTRODUCTION

This chapter describes the work conducted by Texas A&M University (TAMU). This includes deployment and operation of a TABS buoy in the offshore waters of western Louisiana (Chapter 2.1), coastal oceanographic observations made during the cruise that deployed the buoy (Chapter 2.2), and the results of modeling efforts (Chapter 2.3).

2.1 TABS BUOY DEPLOYMENT AND OPERATION

The Geochemical and Environmental Research Group (GERG) at TAMU developed and continues to operate the TABS program for the Texas General Land Office (TGLO). The heart of (the Texas Automated Buoy System TABS) is an array of seven buoys (Figure 1.1) that report ocean current velocities and water temperatures in real time (Chaplin and Kelly 1995, Magnell et al. 1998). The primary mission of TABS is to provide critical data for spill response (Martin et al. 1997). The TGLO also recognizes the value of TABS to the public and scientific community (Kelly et al. 1998). Therefore, TABS automatically posts all observations to a Website (http://resolute.gerg.tamu.edu/tglo) where the data can be freely viewed and downloaded.

The TGLO also encourages collaborative projects that build on the TABS core program. This project is one such example. Another, entitled "Gulf of Mexico Ocean Modeling System" (OMS), was one of the projects of the National Ocean Partnership Program. The Office of Naval Research, with Dynalysis of Princeton, Inc., serving as the lead organization, funded OMS. The project's objective was to produce nowcasts and forecasts of surface and subsurface velocities for the entire Gulf of Mexico and distribute them publicly via an Internet Web site (www.dynalysis.com). Buoys L, M and N in Figure 2.1 were funded by OMS.

Using funds donated by the Marine Industry Group (MIRG), a partnership of oil companies operating in the Gulf of Mexico, GERG purchased hardware needed for a new Model II buoy to deploy in the coastal waters of western Louisiana. The TABS II was developed in cooperation between GERG and Woods Hole Group/Advanced Coastal Environmental Systems (ACES), Inc. Magnell et al. (1998) describe the details of the new design. The four major design enhancements are (1) a new geostationary satellite telephone system, (2) an increased size of the flotation package, (3) an Argos satellite data transmission system that is automatically activated if the primary communications system fails, and (4) an electronic command and control system based on the ACES Remote System Monitor, which includes a powerful microprocessor and multiple analog and digital I/O ports. On January 20, 1998, GERG deployed the first TABS II buoy for several months of test and evaluation next to Buoy B off Galveston. After some refinements, three TABS II buoys were installed during April-May 1998 for the OMS project.

The TABS II buoy for this project was installed at Site P (Figure 1.1) on 22 July 1998 during cruise 98-G-9 from Galveston, Texas, to Biloxi, Mississippi, aboard the TAMU Research Vessel *Gyre*. Hydrographic observations collected during 98-G-9 are described in the Chapter 3. TABS Buoy R was also deployed during this cruise.

Buoy P was recovered on 24 November 1998 during the *R/V Gyre's* return from the Northeastern Gulf of Mexico (NEGOM) cruise N4 funded by US Minerals Management (MMS). Initially, the data recorded by Buoy P were very good. The current velocity sensor on Buoy P was a Marsh-McBirny, Inc. (MMI) electromagnetic 4" diameter model. Prior to deployment, all surfaces of the sensor, except for the four sensing electrodes and the voltage reference electrode, were painted with anti-fouling paint. However, beginning about 7 September 1998, an offset began to creep into the velocity measurements, as evidenced by sporadic spikes and excessively high values in the speed data. The velocity data for the remainder of the deployment are considered bad. Biological fouling is the suspected cause. When recovered, the sensors had large barnacles growing on the electrode tips.

Buoy P was reinstalled three months later on 1 March 1999 as part of a TABS cruise on the *R/V Glorita*, operated by TDI-Brooks International. The buoy operated until it was recovered on 15 August 1999 as part of a *R/V Gyre* cruise. The sensor failed a zero test performed after recovery, which entails placing the unit in still water and recording the sensor's velocity measurements. A non-zero velocity, i.e., failure of the test, infers a velocity offset is present in the data. There are two specific periods in July 1999 when the velocity data is rejected.

A replacement for Buoy P was immediately reinstalled on 15 August 1999 as part of the above TABS cruise on the *R/V Gyre*. The buoy operated until it was recovered for the final time on 19 February 2000. Post-analysis of the data indicated that velocity sensor worked quite well until approximately 20 October 1999, when high speeds and the velocity spikes suggested biological fouling was causing problems. These sporadic spikes continued through 1 December 1999, after which time the spikes apparently ceased and the velocity data for December 1999 appears to be good. During the first five days in January 2000 all the data are missing due to transmission problems. Beginning on 8 January 2000, biological fouling is again suspected to cause spikes in the speed data and the remaining data is highly suspect.

In spite of the loss of data noted above, there were 15,953 half-hourly records of useable velocity data and 21,333 half-hourly records of temperature data. Figure 2.1 shows a summary analysis of the useable velocity data. The page is divided into three parts. The top shows a table of the basic statistics for the flow. The middle shows a scatter plot and the bottom provides a table of the joint frequency of speed and direction. All velocities are in cm s^{-1}. During this entire period, the scalar current speed averaged 19.14 cm s^{-1}. The mean vector flow was 5.57 cm s^{-1} towards the west at 276^{O} True. Only 1% of the time did the current exceed 60 cm s^{-1}. A principal axis ellipse analysis of the velocities shows the rotation angle is aligned along the 288.8 – 108.8^{O} direction. The major axis of the variance ellipse was 18.74 cm s^{-1} and the minor axis was 13.27 cm s^{-1}

Individual time-series plots of all the data collected by Buoy P are shown in Appendix A. A typical example of the data is shown in Figure 2.2. Velocity data that did not pass QC criteria are not plotted and are not used in any analysis presented in this report.

Figure 2.3 shows the probability distribution, by one-degree bins, of the current direction over the entire period of useable velocity data. A predominant peak at 286º true, i.e., westward flow,

TABS Buoy P

START TIME: 07/22/1998 00:00 STOP TIME: 02/19/2000 16:00 UTC

	Num pts.	Mean	Std Dev	Minimum	Maximum
SPEED:	15953	19.14	13.86	0.15	98.43
U COMP:	15953	-5.54	18.25	-98.04	78.37
V COMP:	15953	0.59	13.94	-68.99	72.12

MEAN CURRENT VECTOR: 5.57 cm s^{-1} @ 276.1° True

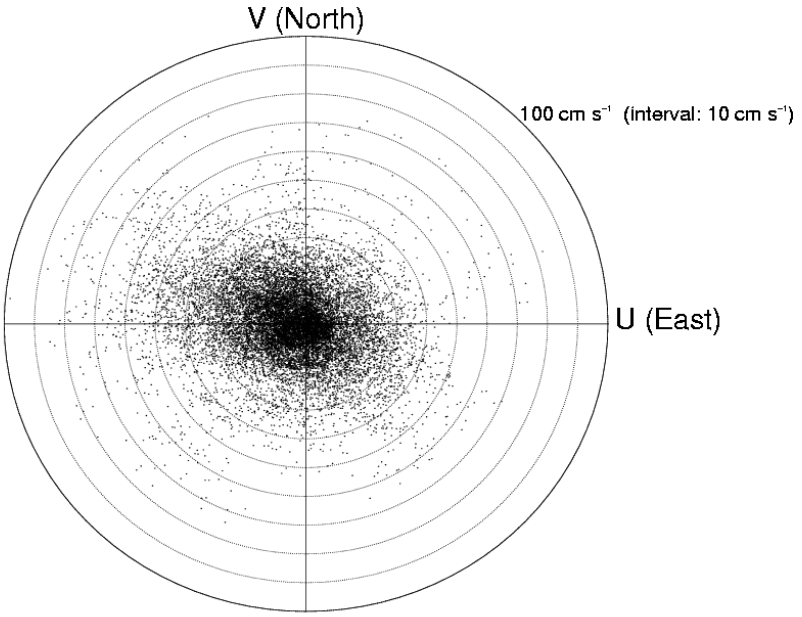

Speed (cm/s)	N	NE	E	SE	S	SW	W	NW	TOTAL
< 5	1.20	1.45	1.38	1.51	1.44	1.33	1.40	1.07	10.78
5 - 10	1.82	1.42	2.10	2.56	2.37	2.89	3.06	2.19	18.40
10 - 15	2.09	1.20	1.46	2.04	2.19	2.68	3.27	3.12	18.05
15 - 20	1.64	1.10	1.57	1.52	1.47	1.99	3.17	2.60	15.06
20 - 25	1.01	0.80	1.30	1.30	0.96	1.17	2.38	2.21	11.13
25 - 30	0.67	0.59	0.90	0.95	0.66	0.68	2.12	1.83	8.41
30 - 35	0.36	0.29	0.62	0.69	0.47	0.50	1.58	1.21	5.73
35 - 40	0.21	0.14	0.39	0.57	0.24	0.26	1.37	0.73	3.91
> 40	0.52	0.21	0.43	0.72	0.23	0.85	3.58	1.99	8.53
TOTAL	9.53	7.20	10.14	11.86	10.04	12.35	21.93	16.95	

Figure 2.1 Summary page for Buoy P current velocity data collected between 22 July 98 and 19 February 2000. Top: basic statistics; middle: scatter plot; bottom: joint frequency distribution.

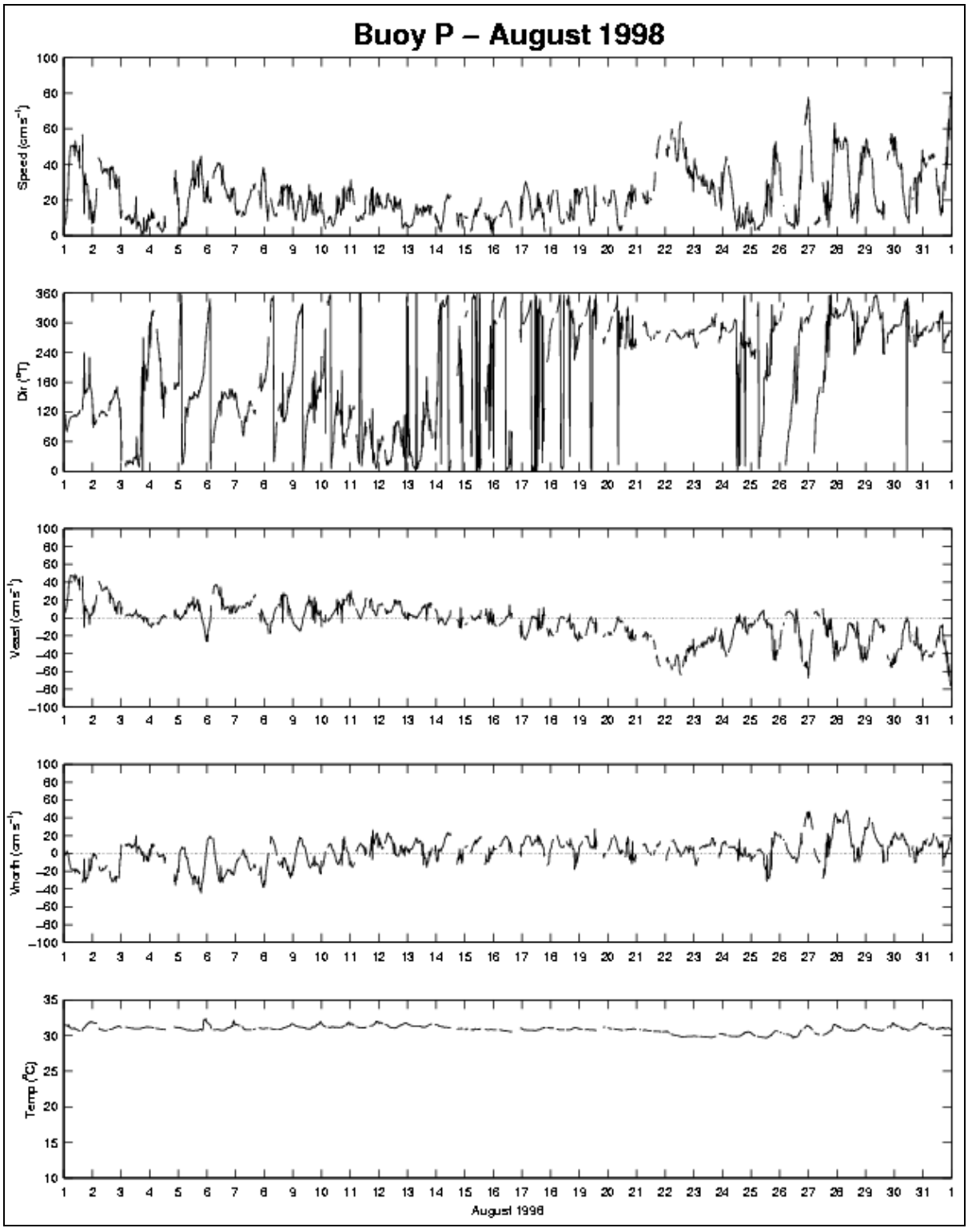

Figure 2.2 Time series plot of current velocity and water temperature from Buoy P during August 1998.

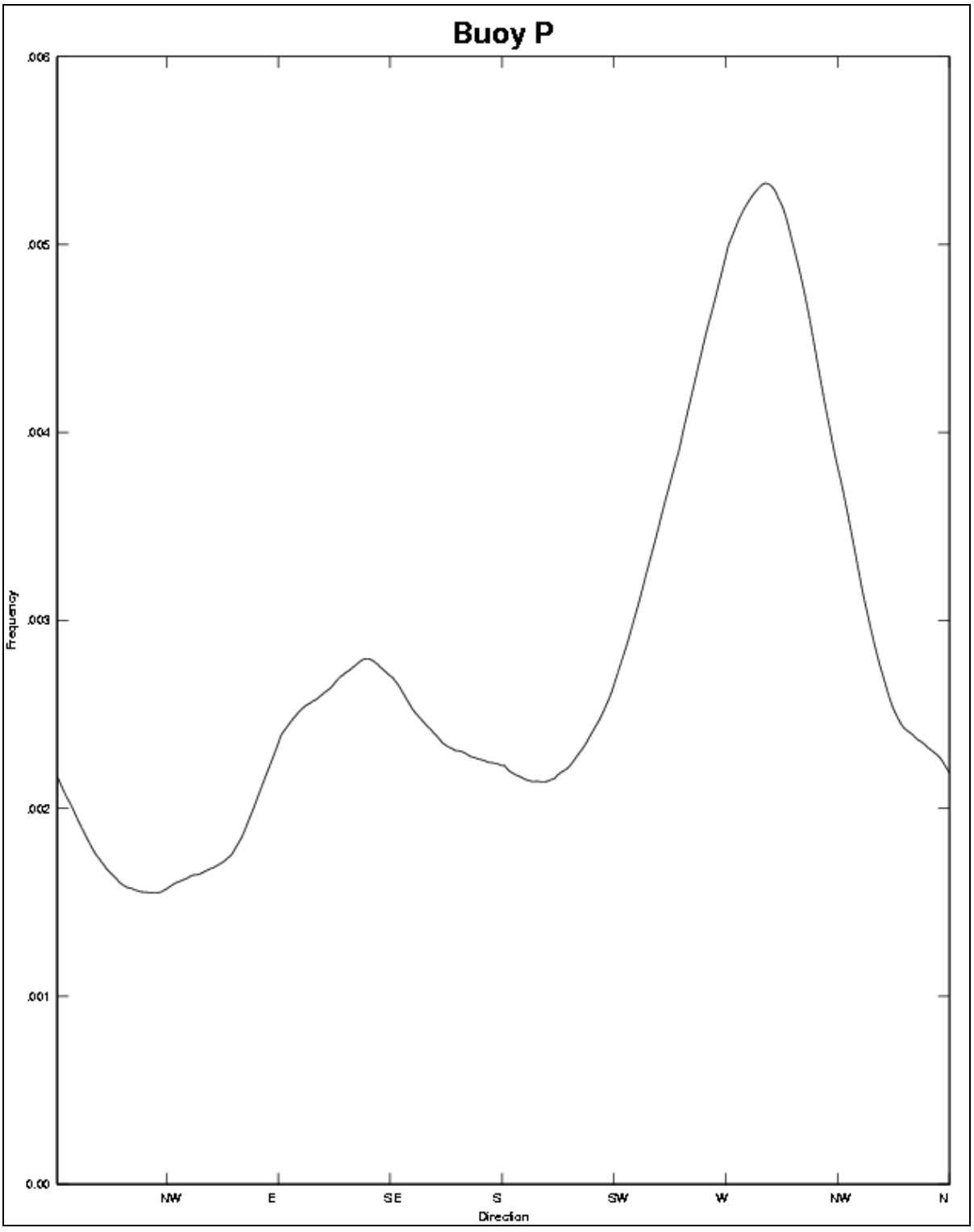

Figure 2.3 Probability distribution function of the current directions collected from July 1998 to 19 February 2000. The prominent direction of 286 degrees, down-shelf flow is clearly seen and the minor peak is nearly 180 degrees in the other direction.

is clearly seen in the record and is supported by the principal axis results noted above. A secondary peak at 126^{O} true is seen as well. This bimodal distribution is a convincing indication of the Louisiana Coastal Current reported by Wiseman and Kelly (1994). While not shown here, other buoys in the TABS program show the same bimodal distribution in the direction.

Finally, Figure 2.4 shows the probability distribution, in 0.1 cm s^{-1} bins, for the current speed. The distribution is remarkable in its notable similarity to a two-parameter gamma distribution.

Figure 2.5 shows the record length temperature distribution, as well as a fitted curve. There were 21,333 data points that passed quality control, the mean temperature was 25.33°C, and the standard deviation was 4.78°C. The minimum temperature of 14.36°C occurred on 12 February 2000 at 1800 GMT and the maximum temperature of 31.01°C occurred on 4 August 1999 at 0130 GMT. The smooth line represents the annual signal plus two harmonics, at 6 months and 4 months, found from a least squares fit of the sinusoidal signals to the data.

2.2 *R/V GYRE* CRUISE

Cruise 98-G-9 left Galveston 2200 CDT 20 July 1998 and returned to Biloxi at 0830 CDT 25 July 1998.

Besides the deployment of Buoy P, the cruise performed a number of other tasks and collected hydrographic data that supplements the database across the Louisiana-Texas shelf.

2.2.1 CTD Measurements

We used the opportunity of cruise 98-G-9 to occupy 55 CTD stations using a Sea-Bird Electronics, Inc. 911+ CTD with rosette sampler. Station locations are depicted in Figure 2.6 and enumerated in Table 2.1. Continuous profiles with pressure were made of temperature, conductivity, downwelling irradiance (with a Photosynthetically Available Radiation (PAR) sensor), transmissivity, fluorometry, and dissolved oxygen. The Sea-Bird SBE-911+ CTD is a research grade CTD system that offers high quality profiles of oceanic temperature, salinity[1], and density at all ocean depths. The SBE-911 uses ultra-stable time-response matched sensors and fast, high-resolution parallel sampling for data acquisition.

In addition to providing precise measurements of temperature and salinity with depth, the TAMU/GERG Sea-Bird CTD system has other sensors integrated into its data acquisition unit. Oxygen is measured with a "Beckman" polarographic type *in situ* oxygen sensor. Downwelling irradiance is measured with a Biospherical Instruments, Inc. Model QSP-200L irradiance profiling sensor. Particle scattering is measured with a Sea Tech light scattering sensor. In addition to the light scattering sensor, the CTD is equipped with a SeaTech, Inc. 25-cm transmissometer. Samples for discrete measurements of suspended particulate concentration and

[1] Salinity as currently defined by the Practical Salinity Scale, has no units. Values are given simply as a number, e.g., 35.00).

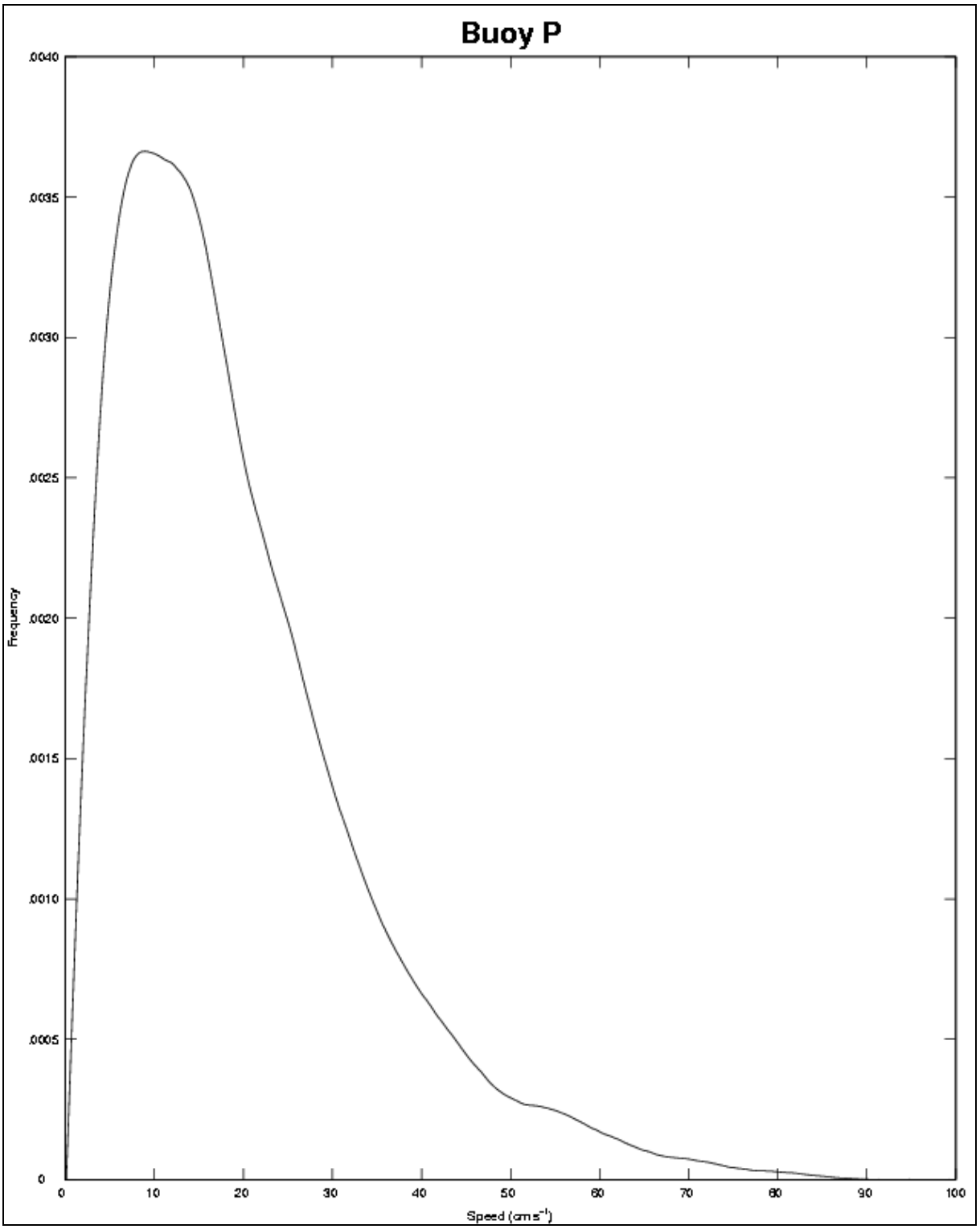

Figure 2.4 Probability distribution function of the current speed data collected from July 1998 to 19 February 2000. While the average speed is 19.14 cm s^{-1}, the median speed is 9.0 cm s^{-1}.

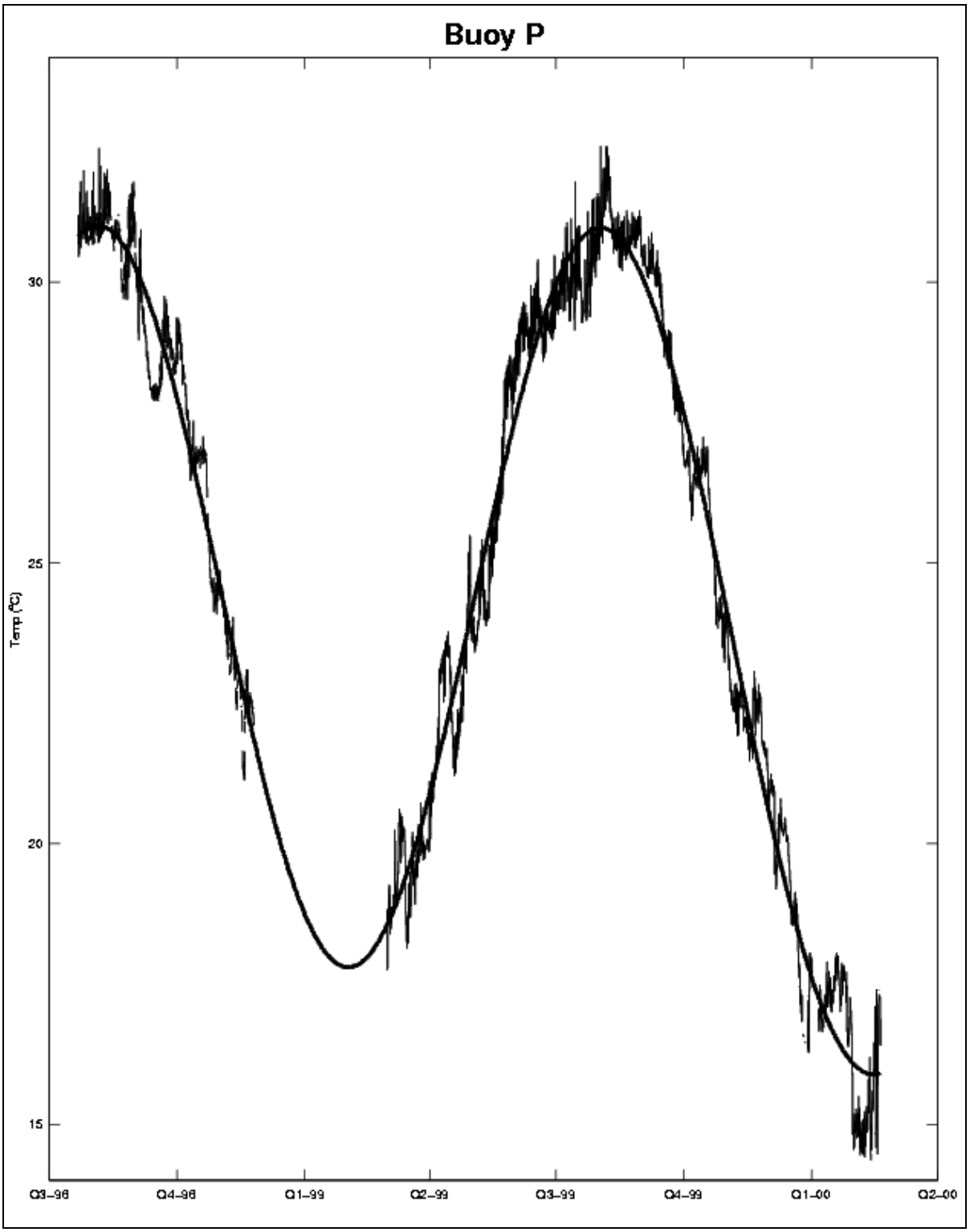

Figure 2.5 Time series plot of Buoy P water temperature collected from July 1998 to 19 February 2000. The smooth line is a linear-fit to a yearly sinusoidal signal plus two harmonics, 6-months and 4-months.

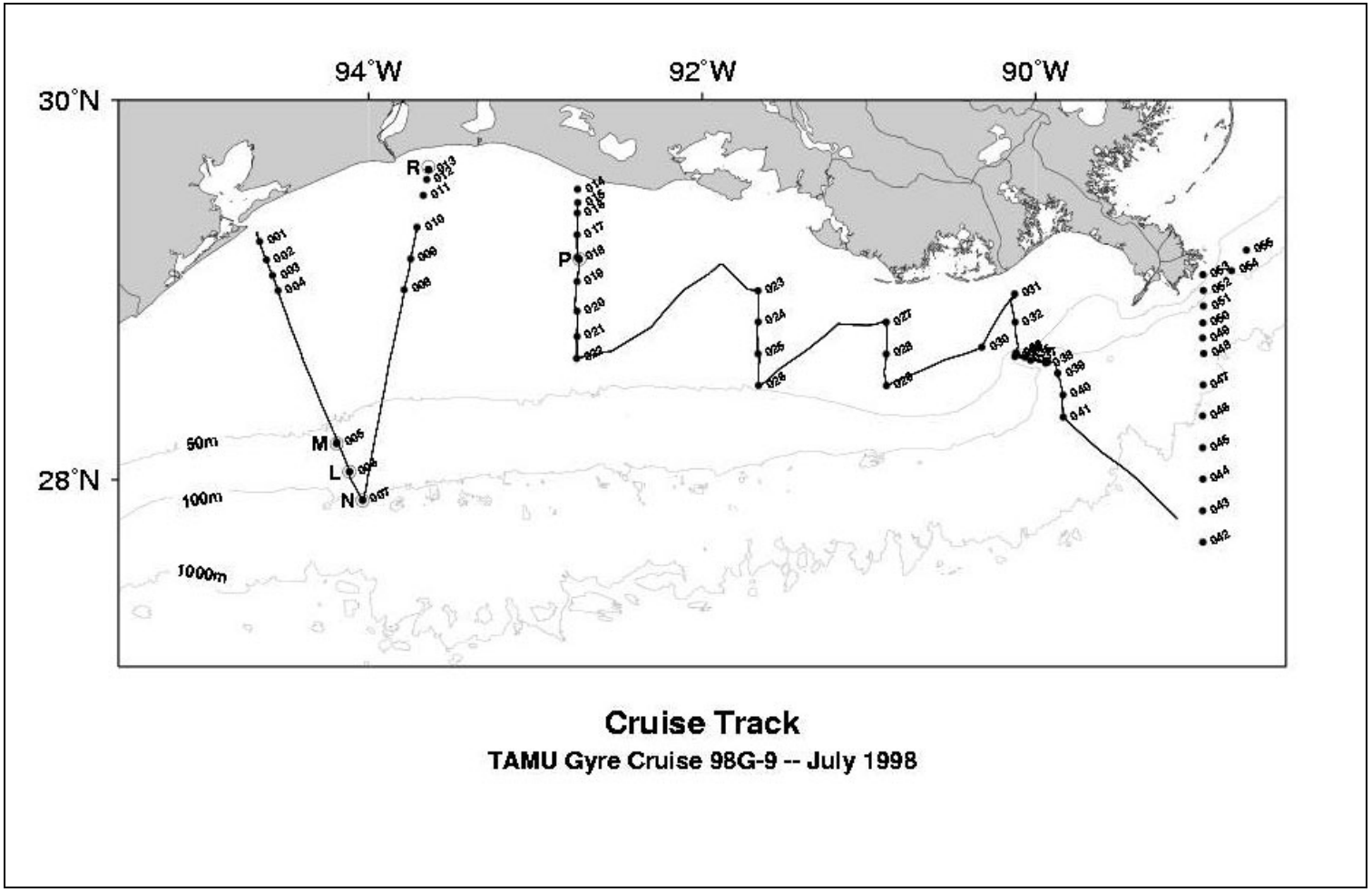

Figure 2.6 Cruise track of *R/V Gyre* cruise 98-G-9. The connected line indicates where ADCP data was collected. The dots indicate station numbers where CTD profiles were collected. Buoy locations are designated by letters.

Table 2.1

List of CTD Station Identifiers and Location

Station	Longitude W	Latitude N
001	94.60383	29.25800
002	94.56400	29.16233
003	94.52683	29.08017
004	94.49400	29.00117
005	94.14150	28.19833
006	94.06417	28.04100
007	93.98567	27.89100
008	93.73733	29.00450
009	93.69850	29.16750
010	93.66050	29.33383
011	93.62300	29.50133
012	93.60250	29.58450
013	93.59133	29.63600
014	92.69767	29.53317
015	92.69717	29.46317
016	92.70017	29.40733
017	92.70050	29.29417
018	92.69633	29.17500
019	92.70100	29.04817
020	92.70050	28.89167
021	92.70033	28.75850
022	92.70367	28.64250
023	91.61617	29.00017
024	91.61500	28.83517
025	91.61583	28.66767
026	91.61267	28.49967
027	90.84717	28.83367
028	90.84733	28.66633
029	90.84633	28.49883
030	90.27383	28.70200
031	90.07733	28.98283
032	90.07483	28.83400
033	90.07033	28.66800
034	90.06783	28.67100
035	90.01617	28.64967
036	90.07550	28.65350
037	89.98133	28.63283
038	89.89133	28.61850
039	89.81917	28.56350
040	89.78683	28.44900
041	89.78583	28.33167
042	88.94867	27.66683
043	88.94950	27.83400
044	88.94917	28.00233
045	88.95033	28.16883
046	88.94967	28.33800
047	88.94783	28.50267
048	88.94450	28.66883
049	88.95000	28.75000
050	88.94867	28.82967
051	88.94517	28.91817
052	88.94533	29.00100
053	88.94900	29.08467
054	88.77700	29.10483
056	88.68733	29.21367

dissolved oxygen were drawn from the 10-liter PVC Niskin bottles mounted on the General Oceanics Rosette sampler, which is part of the CTD profiling system.

There were a total of seven across-shelf transects made during *R/V Gyre* cruise 98G9 (Figure 2.6 and Table 2.1). In the figures that follow Transect 1 refers to stations 001 through 007. Transect 2 refers to stations 007 through 013. Transect 3 refers to stations 014 through 022. Transect 4 refers to stations 023 through 026. Transect 5 refers to stations 027 through 029. Transect 6 refers to stations 031 through 041. Transect 7 refers to stations 042 through 053, but is divided into two parts, 7A – stations 042 through 049, and 7B – stations 049 through 053.

2.2.2 Temperature Salinity (TS) Plots

Figure 2.7. shows the temperature salinity relationship for all 55 CTD stations collected during the cruise. Figures 2.8 shows the TS relationship for transect 3 where Buoy P is moored. The TS relationships for the other transects, as well as the deepest stations on each transect, are shown in Appendix B. Evidence of a Loop Current intrusion is seen in the salinities exceeding 36.5. The most prominent feature in the deep water is the salinity minimum that represents the core of the Antarctic Intermediate Water (AAIW), which enters the Gulf of Mexico at water depths of 700 800 m. This is most clearly seen on transect 7A.

2.2.3 Sections – Contour Plots

2.2.3.1 Temperature

Contours of temperature along transect 3 are shown in Figure 2.9 contoured temperature plots for other transects are in Appendix B. CTD station locations are identified across the top of the figure, as well as the position of each data point. The data quality is high. A strong thermocline at about the 30-m depth is evident. Maximum temperature in excess of 31º C is seen along this transect while the minimum temperature of 5º C is seen only for the deepest stations (see Appendix B) and not at all along transect 3.

2.2.3.2 Salinity

Contours of salinity along transect 3 are shown in Figures 2.10. Contoured salinity plots for other transects are in Appendix B. CTD station locations are identified across the top of the figure, as well as the position of each data point. The data quality is, again, high. There is a suggestion of coastal upwelling in the data. The following points can be noted in the plots of Appendix B. The evidence of a Loop Current intrusion is seen at stations 042 through 045 where the salinity exceeds 36.5. A very strong halocline between 5- and 10-m depth is seen in transects 5 and 6. The maximum surface salinity is seen on transect 1. The minimum surface salinity is seen on transect 5.

2.2.3.3 Density

Contours of computed potential density anomaly along transect 3 are shown in Figure 2.11. Potential density anomaly distributions for other transects are contoured in Appendix B. CTD

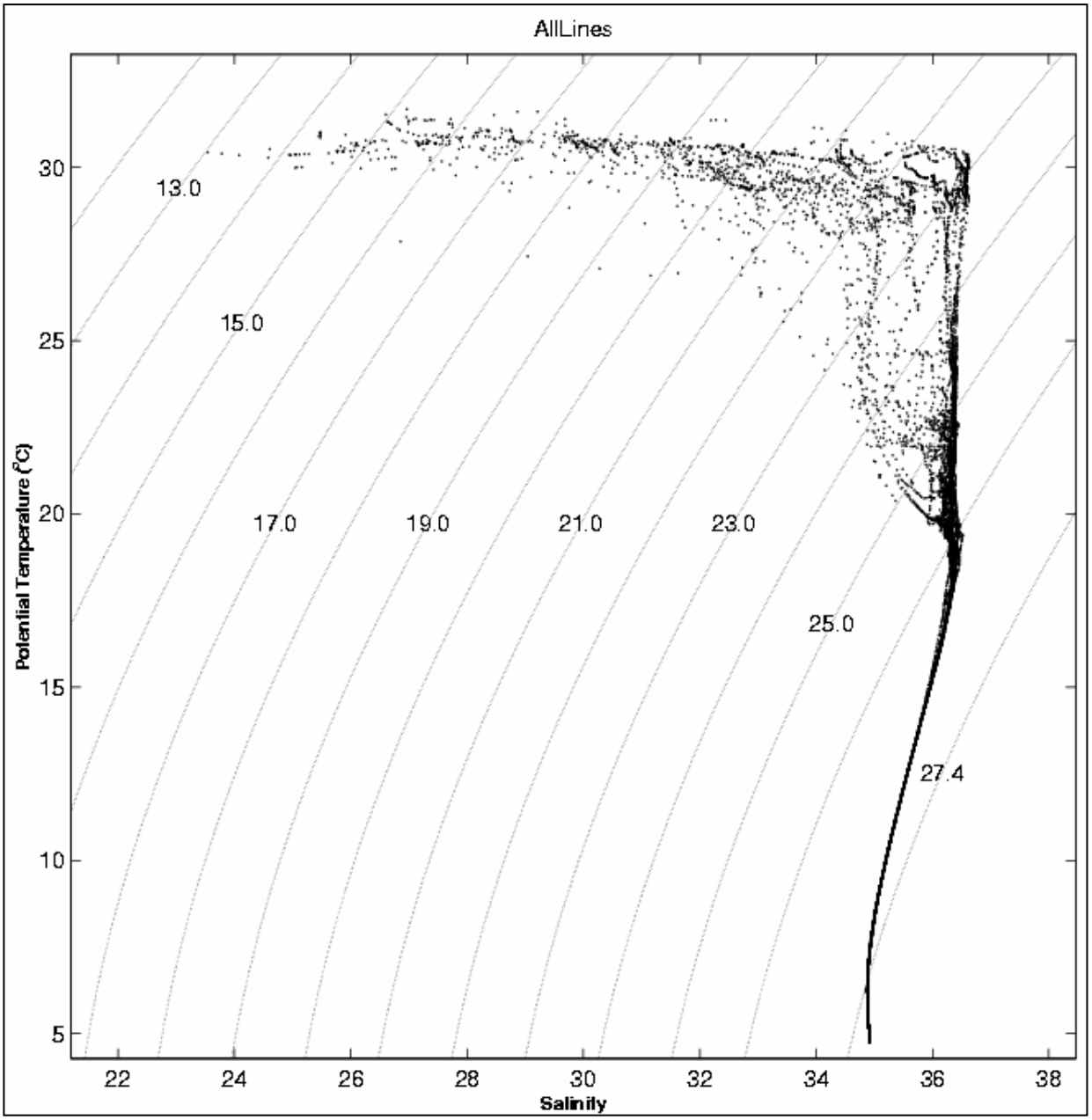

Figure 2.7 Temperature Salinity relationship for all CTD stations sampled during *R/V Gyre* cruise 98-G-9.

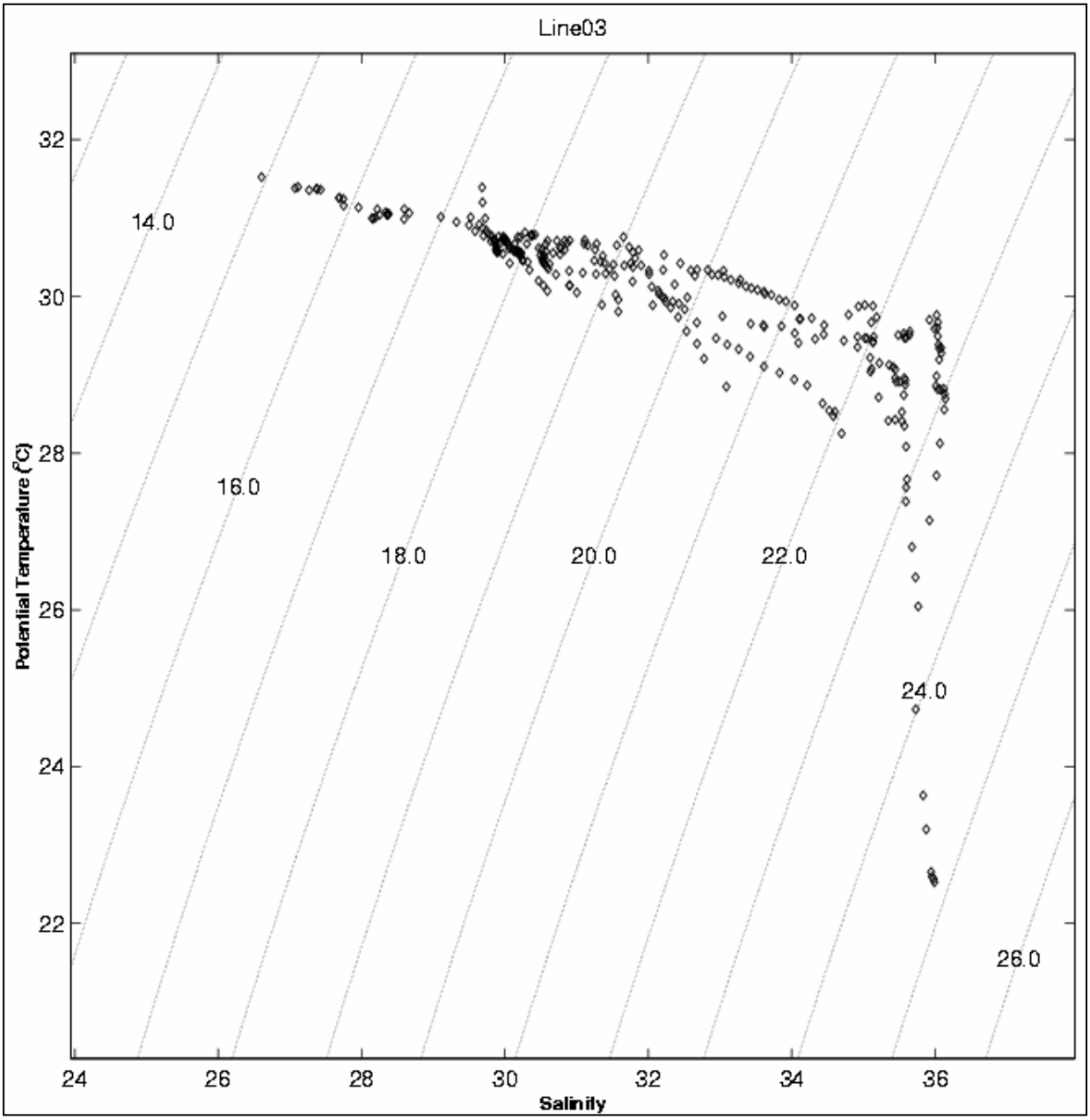

Figure 2.8 Temperature Salinity relationship for CTD stations along Transect 3 (Figure 2.6, Stations 14 – 22) sampled during *R/V Gyre* cruise 98-G-9.

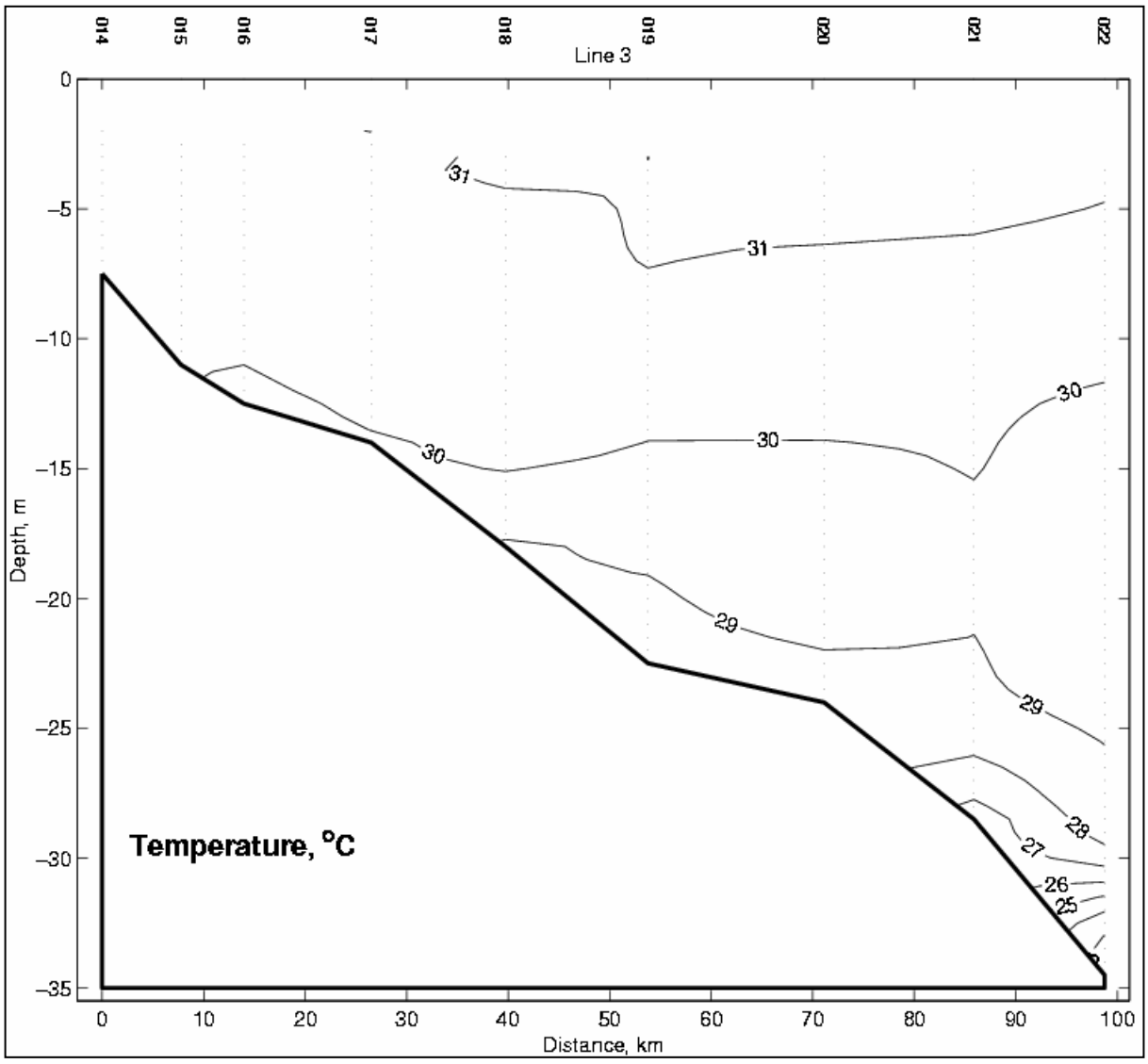

Figure 2.9 Vertical profile of temperature for Transect 3 (Figure 2.6, Stations 14 – 22). The contour interval is 1°C.

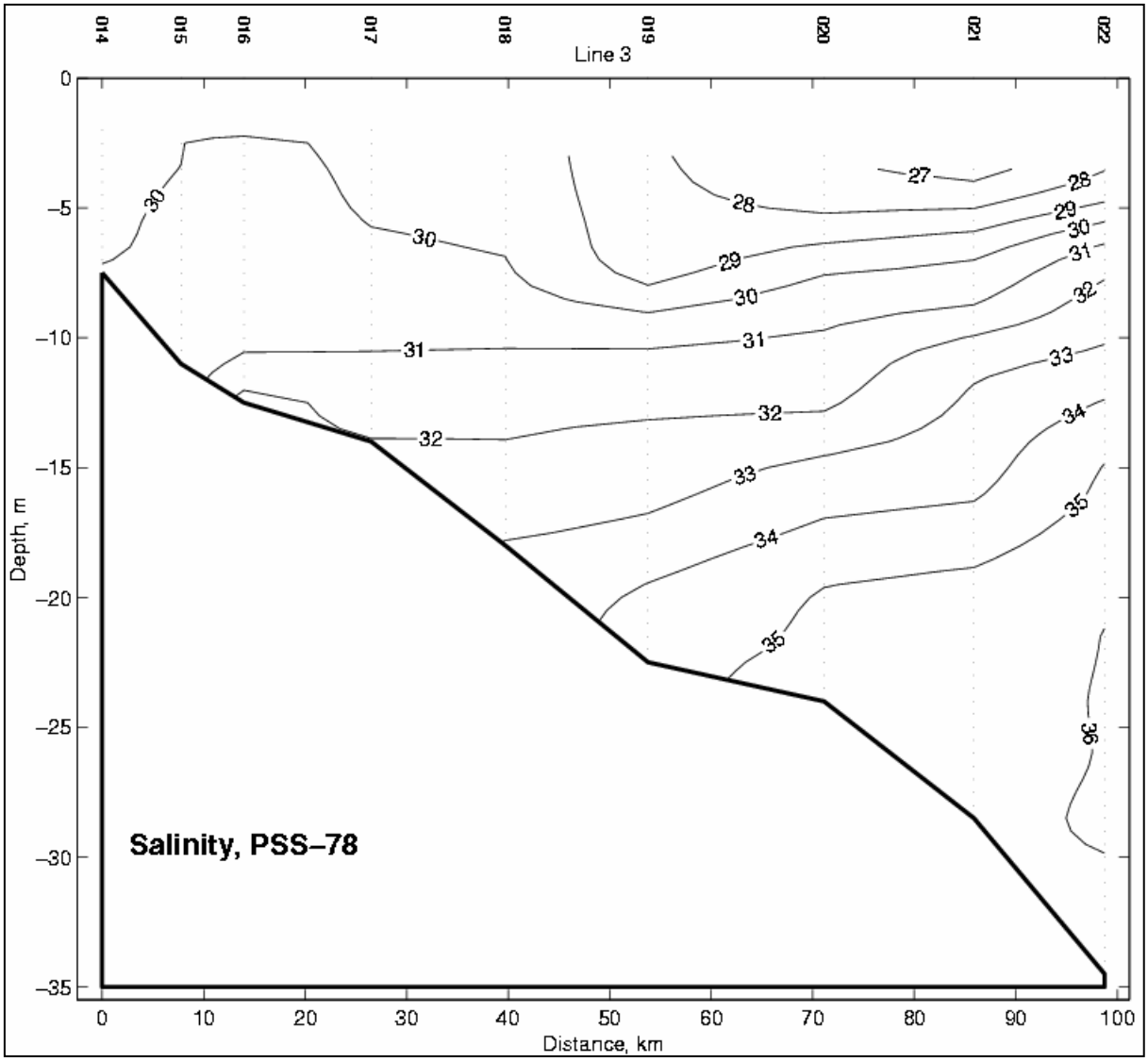

Figure 2.10 Vertical profile of salinity for Transect 3 (Figure 2.6, Stations 14 – 22). The contour interval is 1.0.

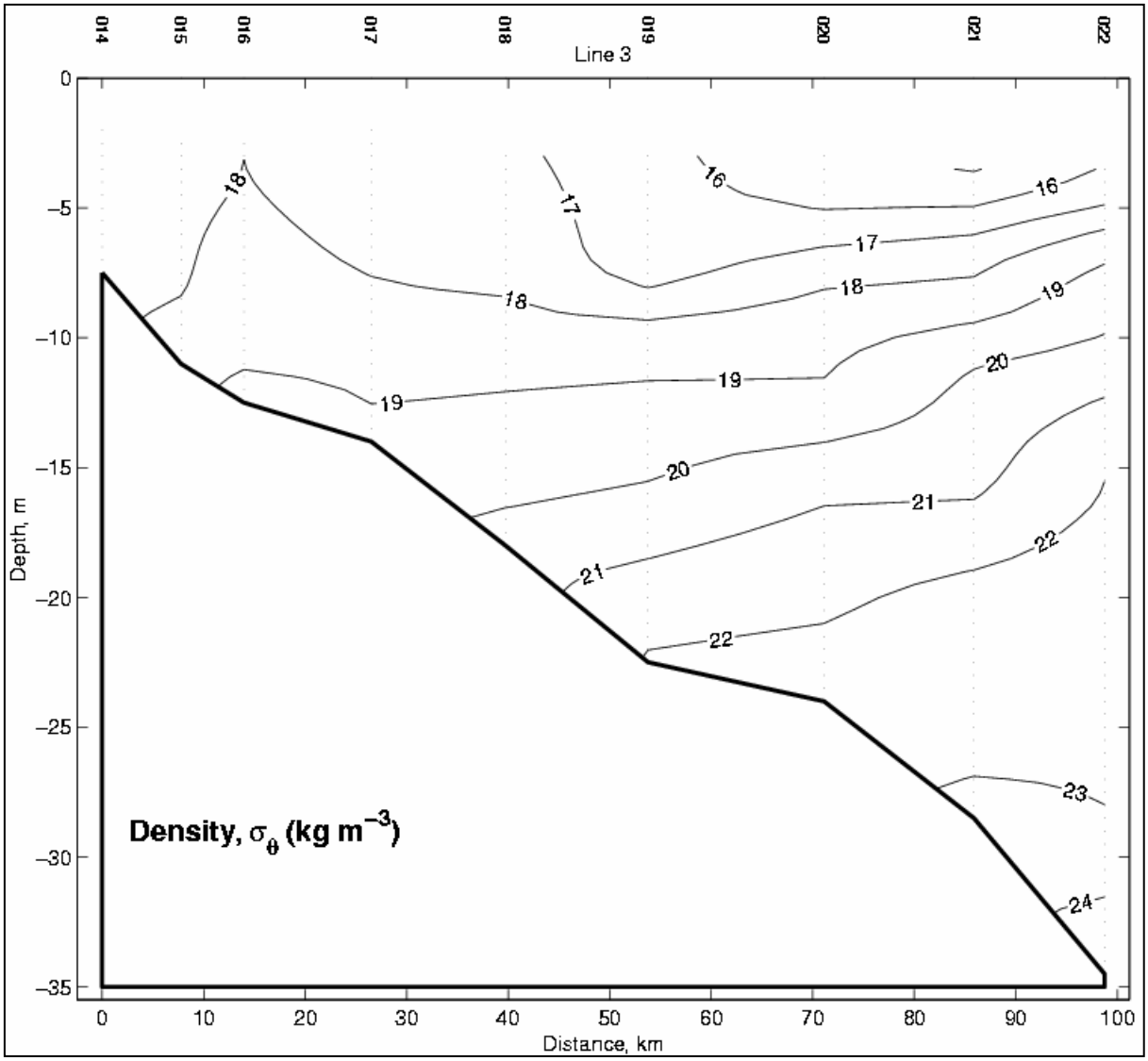

Figure 2.11 Vertical profile of density for Transect 3 (Figure 2.6, Stations 14 – 22). The contour interval is 1.0 σ_θ.

station locations are identified across the top of each figure, as well as the position of each data point. The data quality is high. The suggestion of coastal upwelling is, again, evident in this plot. A strong density gradient between transects 2 and 3 is quite evident. The minimum surface density is seen in transect 5.

2.2.3.4 Brunt-Vaisala Frequency

The Brunt-Vaisala frequency, in cycles per hour (cph), was computed from the temperature and salinity profiles. High values are typically found near the surface, where the vertical density gradient is the largest. Contours of the Brunt-Vaisala frequency transect 3 are shown in Figure 2.12. Contour plots of the Brunt-Vaisala frequency along other transects are presented in Appendix B. CTD stations locations are identified across the top of each figure, as well as the position of each data point.

2.2.3.5 Oxygen

Continuous profiles of dissolved oxygen were measured with a Beckman type polarographic *in situ* oxygen sensor, manufactured by Sensor-Medics, Inc. Mounted in the Sea-Bird SBE-911+ CTD, the oxygen sensor was attached to a manifold that permitted active pumping of water past the sensor membrane. To maintain sensor stability, care was taken to ensure that the dissolved oxygen membrane was not fouled with hydrocarbon contaminants. Between casts, the oxygen sensor was flushed and filled with clean water.

At all of the hydrography stations, with the exception of station 51, bottle titrations were performed to determine discrete dissolved oxygen values. This data served as an independent means of calibrating the oxygen sensor. Applying a non-linear least-squares regression technique, downcast oxygen sensor values were fit to the upcast bottle sample oxygen measurements. The calibration was effective for all but 15% of the stations (i.e., stations 35, 36, 38, 40, 41, 43, 44, and 45.) In these cases, it appears that the oxygen sensor was not properly equilibrated before the CTD package was lowered through the water column, resulting in oxygen sensor values significantly less than the bottle oxygen values over the top 30 m.

Contours of the calibrated dissolved oxygen concentration along transect 3 are shown in Figure 2.13. Contour plots of dissolved oxygen concentration for the other transects appear in Appendix B. CTD stations locations are identified across the top of each figure, as well as the position of each data point. Because there was no bottle data collected for station 51, that station is not included. For all other stations, the bottle value and its location are plotted on each figure as well.

2.2.3.6 Fluorescence

Continuous profiles of fluorescence were measured using a Chelsea fluorometer. Contoured data from transect 3 is shown in Figure 2.14, while that for the remaining transects appears in Appendix B. Units are μg/l of chlorophyll.

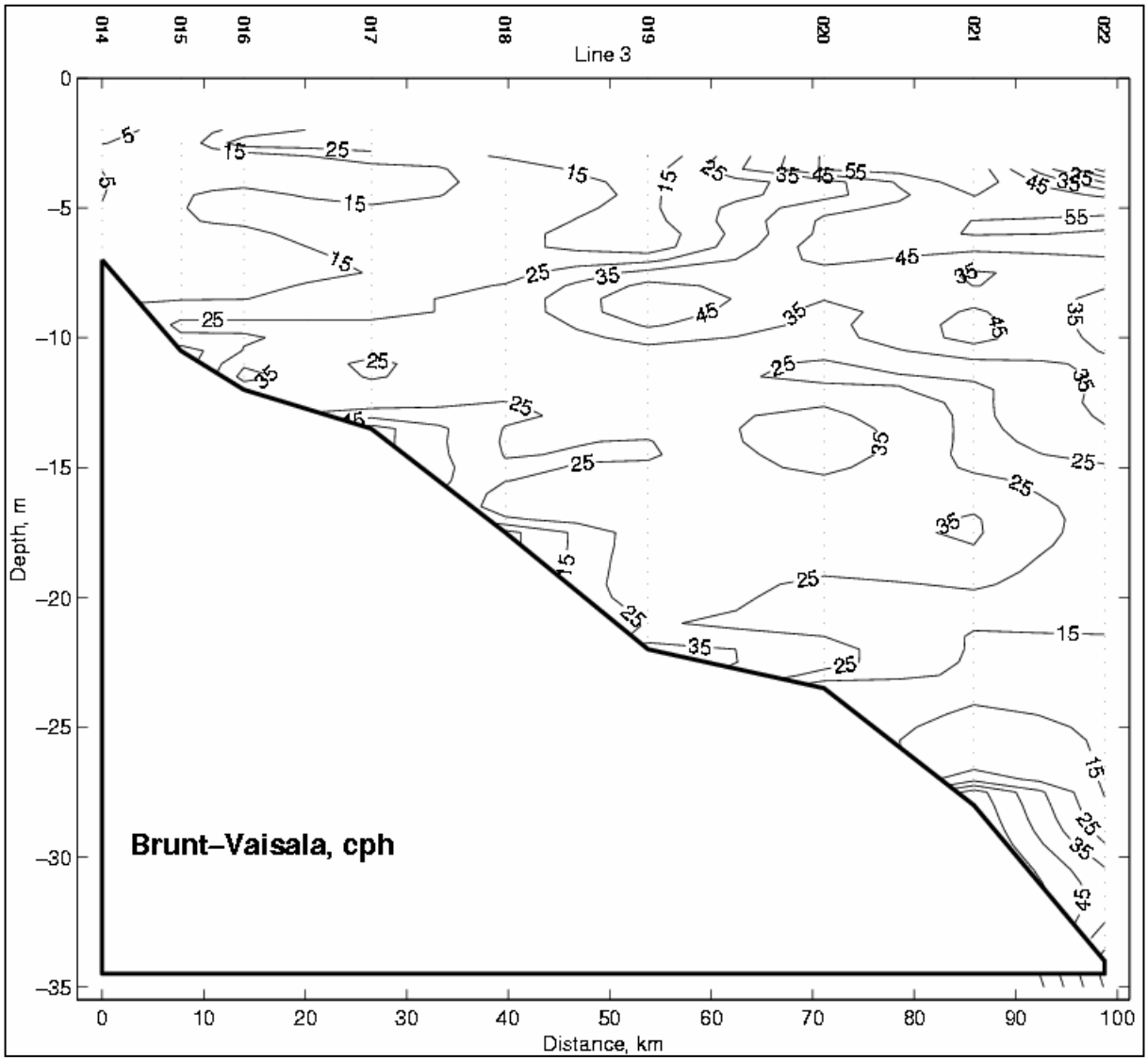

Figure 2.12 Vertical profile of Brunt-Vaisala frequency for Transect 3 (Figure 2.6, Stations 14 – 22). The contour interval is 10 cph.

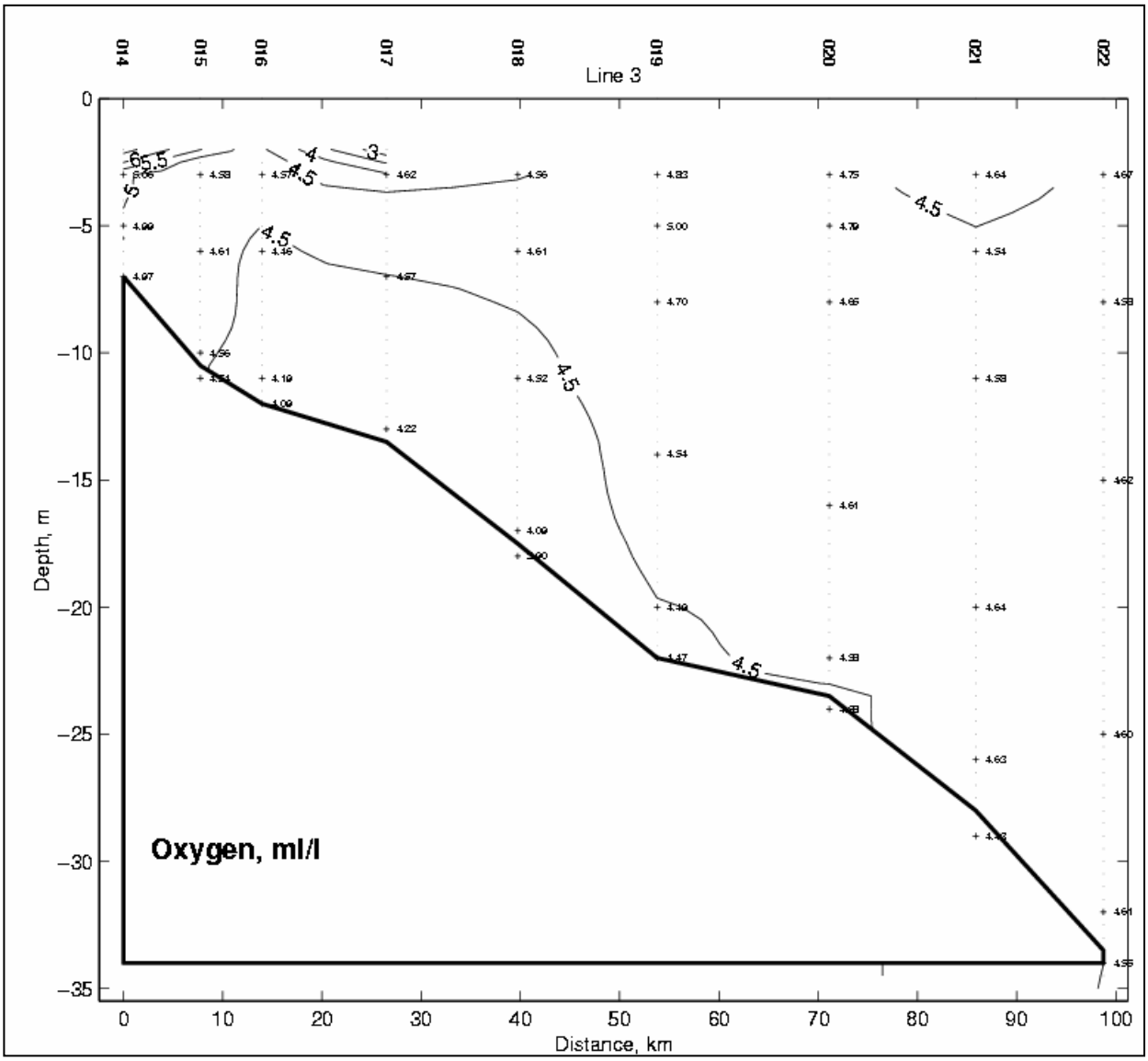

Figure 2.13 Vertical profile of dissolved oxygen for Transect 3. The contour interval is 0.5 ml l^{-1}.

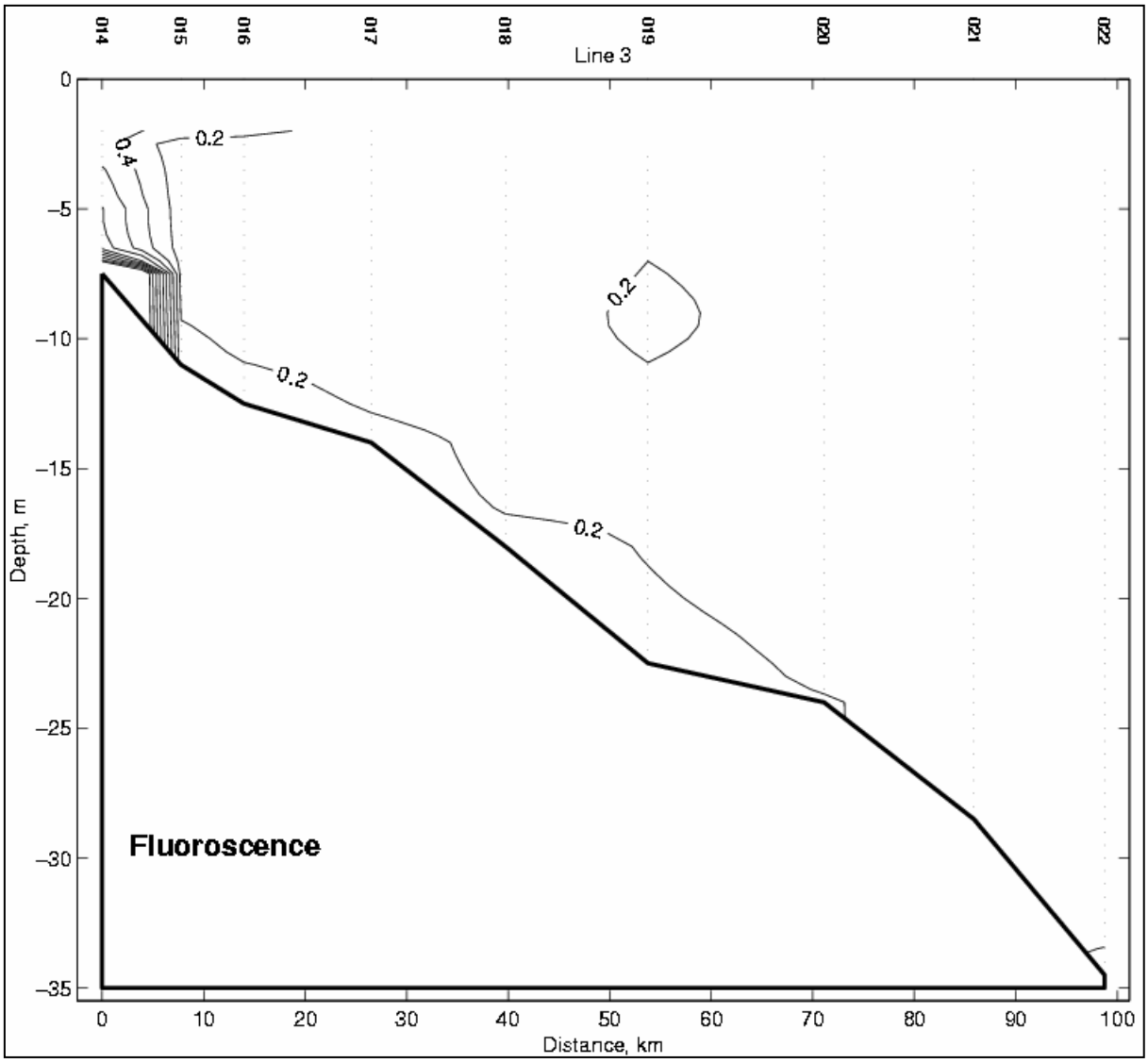

Figure 2.14 Vertical profile of fluorescence for Transect 3. The contour interval is 0.20.

2.2.3.7 Downwelling Irradiance

Continuous profiles of downwelling irradiance were measured using a Biospherical Instruments, Inc. Model QSP-200L irradiance profiling sensor. While the CTD package was on deck, the sensor was covered with an opaque cap for protection. Unfortunately, a review of the data reveals that the cap was probably not removed for stations 1-4, 8-13, 20-25, 31-36, 42-45, and 52-53. Contours of downwelling irradiance along transect 3 are presented in Figure 2.15 while contoured data from other transects are presented in Appendix B. In each of the figures, the following contour levels were used: 0.75, 1.0, 5.0, 10, 50, 100, 500, and 1000, $\mu E/(m^2 \bullet s)$.

2.2.3.8 Transmissivity

The CTD system was equipped with a SeaTech, Inc. 25-cm path length transmissometer to provide continuous profiles of percent transmission. The transmissometer lenses were cleaned every few stations using distilled water. Contours of transmissivity as recorded by the sensor along transect 3 are shown in Figure 2.16. Contours from other sections are presented in Appendix B.

2.2.4 ADCP

We used the opportunity of cruise 98-G-9 to operate a RDI 150 kHz Broadband ADCP and make continuous underway measurements of current velocities beneath the vessel down to a depth of about 150 – 200 m. Murphy et al. (1992) have described the mounting of the ADCP on the R/V *Gyre*. Shown in Figure 2.6 is the track line along which the ADCP was operated, though this does not imply useful data was obtained everywhere along the line.

The Broadband ADCP was a "direct reading" model with a four beam, downward looking, 30-degree convex head arrangement. The offset for the Broadband was set by visually aligning beam #3 transducer head with the ship's longitudinal axis. Any misalignment was corrected during post processing. The unit was operated in the bottom-tracking mode, which successfully tracked the bottom in depths up to 400 m. The ADCP was controlled by a personal computer that also processed and logged the data. Global positioning system navigation data, supplied by a separate system, were recorded by the RDI software in separate navigation files, but annotated with the ensemble number being collected. This easily allowed the navigation and raw data current files to be merged in post processing. The ship's Sperry gyrocompass was connected to the ADCP to provide heading information that was in addition to the GPS navigation data. The ADCP was configured as follows in Table 2.2.

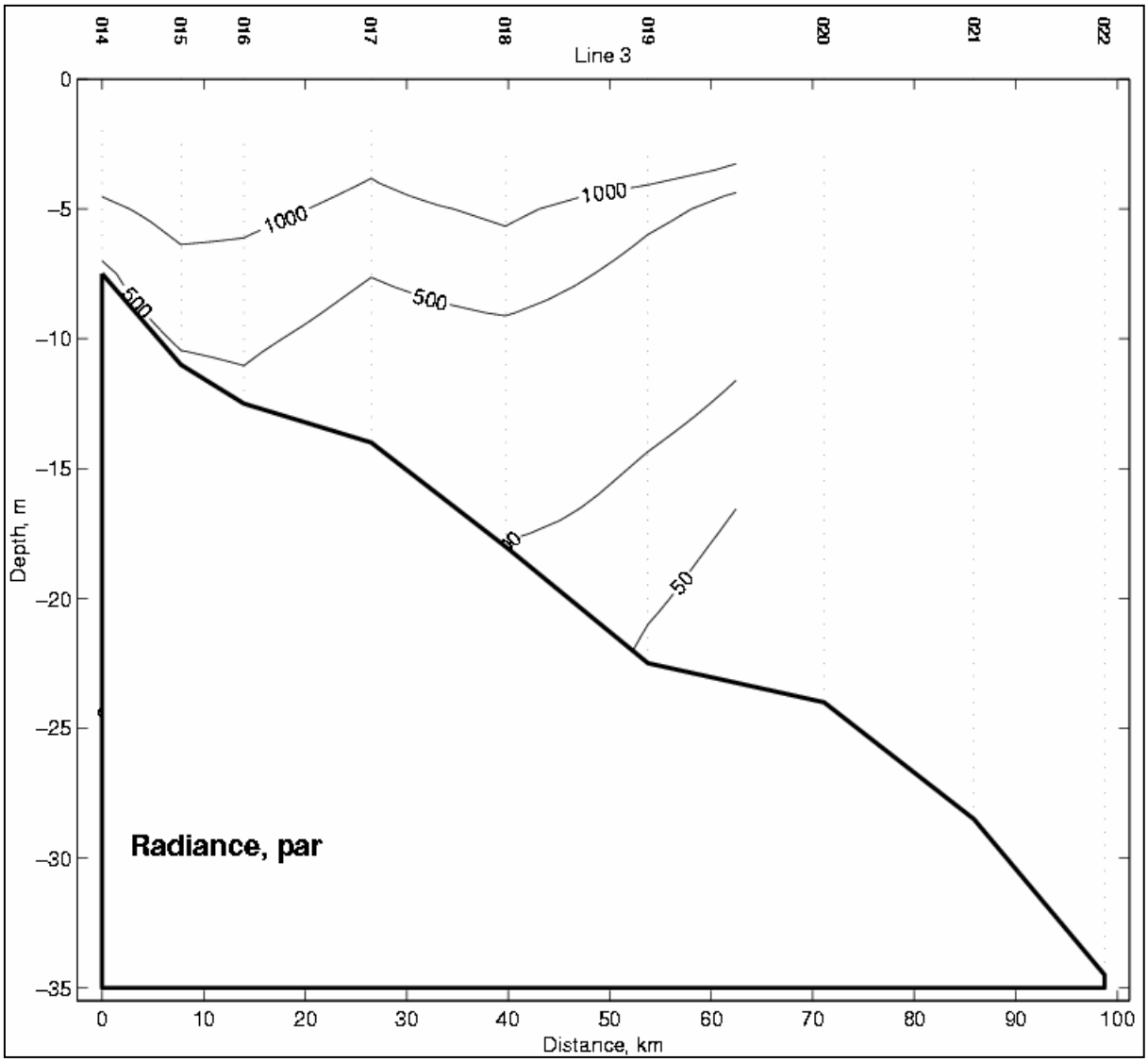

Figure 2.15 Vertical profile of radiance for Transect 3. The contour interval is defined in the text. There is no data for stations 020, 021, and 022.

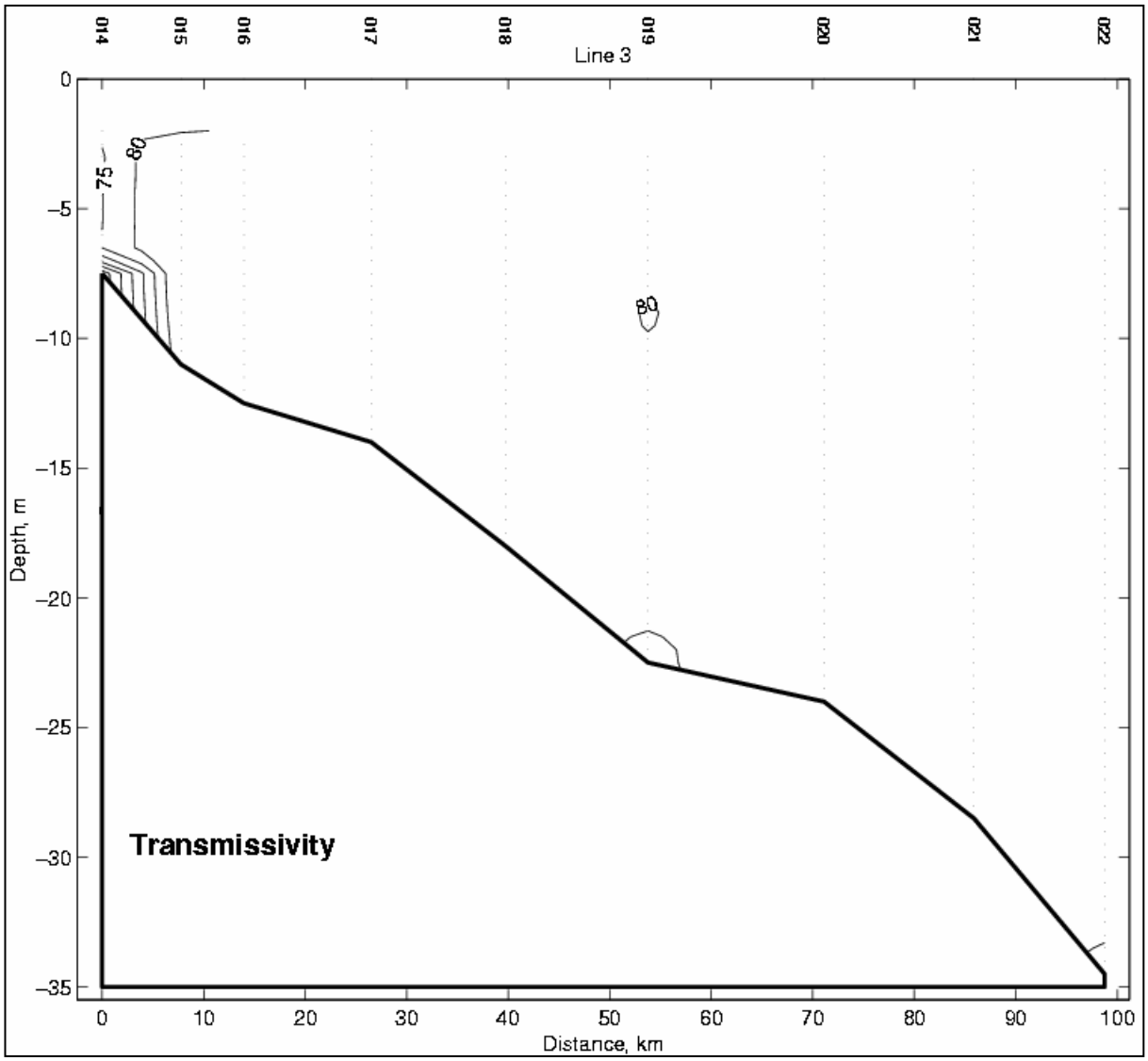

Figure 2.16 Vertical profile of transmissivity for Transect 3. The contour interval is 5%.

Table 2.2

ADCP Configuration Summary

Parameter	
Instrument Type	Broadband
Frequency (kHz)	153.6
Transducer pattern	Convex
Depth cell length (m)	4.00
Number of depth cells	90
Pings per ensemble	2 water track, 2 bottom track
Time between pings (s)	2
First bin depth (m)	14.11
Transmit pulse length (m)	6.15
Blank after transmit (m)	4.00
Navigation type	GPS, gyro heading
Data recorded	Raw, averaged, navigation

2.2.4.1 Post Processing

After collection, the undamaged raw data files were converted to a format suitable for post processing on a PC using MATLAB computer codes. All of the post processing described below was conducted on individual ensembles. We did not take advantage of the RDI processed average files. Examining each ensemble significantly increases the amount of data that can be used. Post processing required several levels of effort to merge navigation data, determine absolute ship velocity with respect to GPS positions, calibrate the offset and alignment of the ADCP, calculate current velocity, and remove outliers and suspicious data. The final step in this process is the production of ASCII data files containing the data and associated metadata, as well as plots of the resulting currents.

Merging of the Navigational Data

The first step of the post processing is to associate each ADCP ensemble with a valid GPS position fix. The RDI software annotates the incoming GPS stream with the current ensemble number, which conveniently allows each ensemble to be linked to a GPS position. Occasionally the GPS data stream is interrupted and not every ensemble has a valid GPS fix associated with it. Those ensembles were subsequently discarded. Of the 32,615 ensembles recorded by the ADCP prior to station 42, only 396 ensembles were rejected because they had no navigational data.

Ship's Velocity

For a given ensemble with a valid GPS fix, the great circle distance traveled during that ensemble is computed from the GPS fix at the beginning of that ensemble to the GPS fix at the beginning of the next ensemble. This step is critical in order to calculate the ship's velocity during an ensemble. The ship's velocity must be subtracted from the raw ADCP measurements

in order to obtain the current velocity. Errors in the ship velocity directly affect the variance in the current velocity.

The set of navigational ship velocities were inspected for any occurrence when the ship speed was less than 100 cm s^{-1}, when the ship speed was in excess of 650 cm s^{-1}, when the ship's acceleration exceeded 0.2 cm s^{-2}, or the ship was rapidly changing direction. Over the typical 10-second period needed to collect an ensemble, an acceleration of 0.2 cm s^{-2} corresponds to a 1 cm s^{-1} change in the ship speed. This variability is carried directly into the determination of the current velocity. The rapid change in direction criteria recognizes that the ship's gyrocompass is an electro-mechanical servo system with inertia and, therefore, exhibits lag. Consequently the gyro heading does not reflect the true ship's heading when the ship is rapidly turning. Each of these four criteria contributes errors to the final computed water velocity. Data that do not pass these requirements were rejected and any ensemble associated with it was rejected from further processing. Of the 32,219 ensembles that were processed through this step, 9,859 ensembles were rejected for failure to meet these four QC criteria. This left 22,360 ensembles of the original 32,615 ensembles that could be used in the following steps.

Offset and Alignment

The ADCP operated in bottom track mode also provides an estimate of the ship's velocity when the bottom is typically less than 400 m. The subset of data having both bottom-track and navigation velocities are used to perform a calibration of the ADCP after the manner of Joyce (1989). The errors are of two types: sensitivity and offset. Sensitivity errors arise because the orientation of the acoustic beam is not correct due to factors such as nonzero trim of the transducer and ship, small errors in the beam geometry, or an overall system bias. Alignment errors are caused by a misalignment between the reference frame of the ADCP and the ship's gyro. Joyce (1989) notes that these two errors arise from independent sources and are approximately orthogonal to each other. The misalignment causes errors that can be considerable in the velocity component perpendicular to the ship's longitudinal axis, while the sensitivity error occurs in the velocity component parallel to the ship. The mean alignment error is typically one to two degrees for the *R/V Gyre*. The mean sensitivity error is usually from 1.01 to 1.04, so the ADCP data is scaled up by this amount.

Only those ensembles with valid bottom track velocities and velocities that were sufficiently close to the navigational velocities were used in this step. Of the 22,360 ensembles that were processed through this step, 1,845 ensembles were not used. Results of the complex regression analysis for the bottom-track versus GPS navigation velocities are summarized in Table 2.3.

Table 2.3

Complex Regression Analysis

GPS vs. bottom-track velocity	
Ensembles utilized	20515
Clockwise regression angle, deg	4.1936
Sensitivity	0.99987
Average GPS ship speed, cm s^{-1}	433.97

Calculate Current Velocity

For each ensemble that passed through the ship's velocity step:

1. Extract beam velocities from raw data files.
2. Perform three-level screening: (a) Remove depth cells with bad data flags. (b) Remove depth cells with low correlations (< 64) and (c) cells with low percent good (< 25%).
3. Transform beam velocities to earth velocities using the ship's gyro heading.
4. Perform three-beam solutions where needed.
5. Correct earth velocities for alignment and sensitivity error.
6. Subtract navigational velocities from earth velocities to yield current velocities.

Ensemble Averaging

In order to reduce the large, but expected, variance in the individual ensemble velocities, 5-minute averages were constructed from individual, consecutive ensembles. Five minute averages, or segments, were constructed for the (a) water column velocities, (b) bottom track velocities, (c) navigational ship velocities, (d) ship's heading, and (e) GPS positions. Secondly the side lobe contamination depth for each segment was flagged and the velocities for all depth cells below that depth were summarily rejected.

It was possible to construct 644 5-minute segments from the 22,360 ensembles that were successfully processed through the previous step. On average, there were 31 ensembles per 5-minute segment, with a minimum of 15 and a maximum of 33. In the case of 180 segments, the side lobe contamination depth was less than the depth of the first good bin and the entire ensemble was rejected. This left 464 segments to process through final quality control.

Final Quality Control

The final step was to perform a cruise wide quality control check of the velocities. This entailed the following two steps:

1) Remove any segment if the current velocity exceeded 200 cm s^{-1}.
2) Compute the cruise-wide averaged standard deviation for each depth cell and then remove any segment if its velocity exceeded twice the cruise-wide average standard deviation.

Of the 464 segments processed through this step, 54 were rejected for failing the above two criteria. Consequently, of the 32,615 ensembles collected by the ADCP prior to data loss at CTD station 42, approximately 39% of the ensembles were acceptable.

2.2.4.2 Results

In order to show vertical profiles of velocity along different sections, Figure 2.17 defines 10 ADCP lines. These are called lines in order to distinguish them from the hydrography transects.

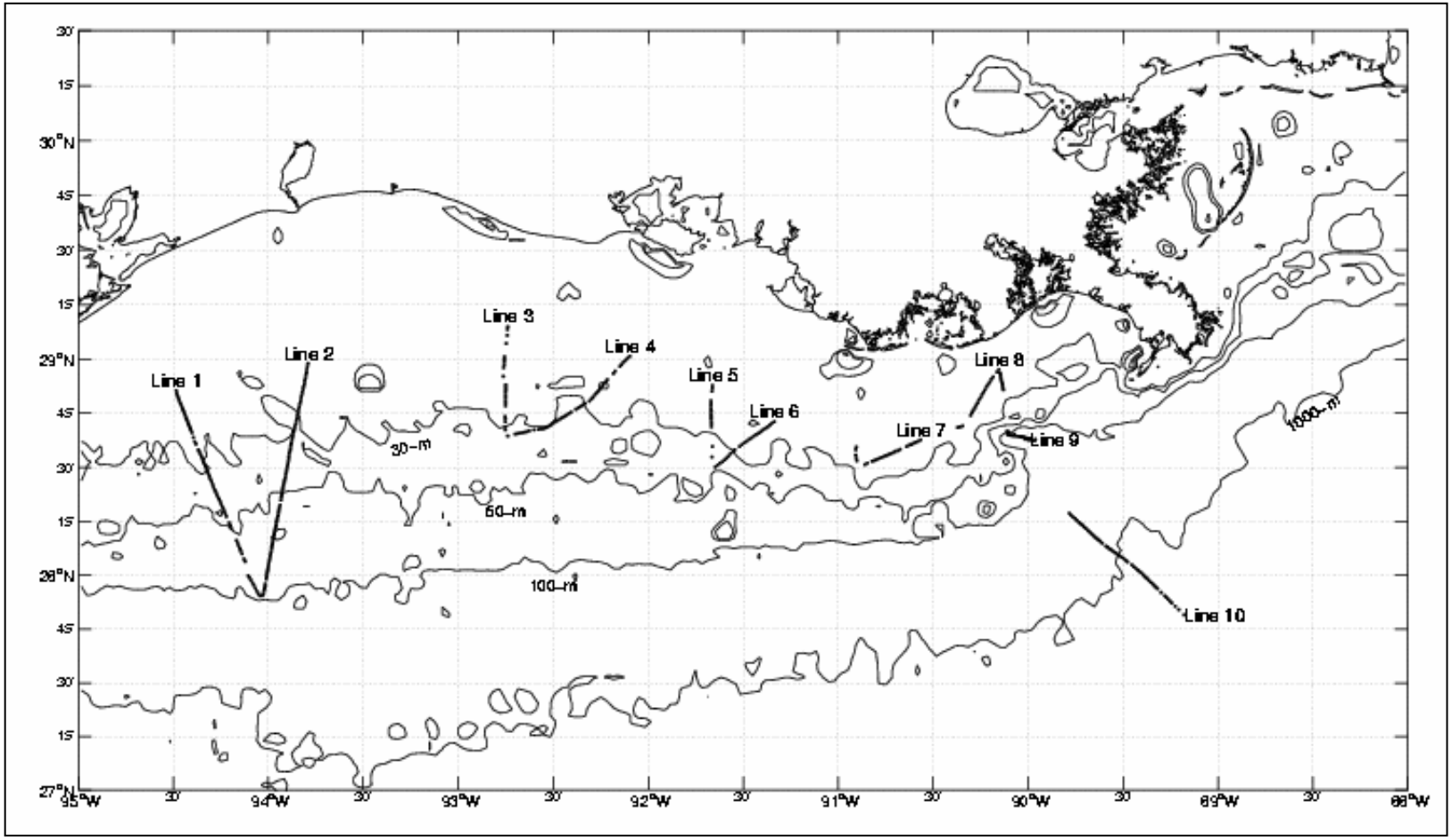

Figure 2.17 ADCP lines used to show vertical profiles. Bathymetric contours are shown for 30-, 50-, 100-, and 1,000-m depths.

Specifically, ADCP line 1 overlies hydrography transect 1, ADCP line 2 overlies hydrography transect 2, ADCP line 3 overlies hydrography transect 3, ADCP line 5 overlies hydrography transect 4, and ADCP line 9 overlies hydrography transect 6. In every case the inshore end of the ADCP line does not correspond to the inshore station of the hydrography transect, but actually occurs in deeper water. ADCP line 9 was transited three times, yielding results called lines 9A, 9B, and 9C.

Figure 2.18 shows the currents at 14 m. Maps of current vectors at 26, 50, and 102 m are in Appendix C. The normal velocity, parallel velocity, and speed for Line 3 are shown in Figures 2.19 to 2.21. Similar figures for the other lines are in Appendix C.

2.2.5 Collateral Data

Sea surface altimetry and computed geostrophic flows for the Gulf of Mexico were obtained from the University of Colorado's Center for Astrodynamics Research. The Center provides near real-time and archived maps of the sea surface height or height anomaly with superimposed velocity vectors. An analysis product is produced every weekday, based on the latest ten days of TOPEX and 17 days of ERS-2 sampling. The analysis TOPEX/ERS-2 for 15 July 1998 (Figure 2.22) shows an upcoast, geostrophic, flow across the outer shelf on the order of 25-50 cm s^{-1}. The TOPEX/ERS-2 satellite image for 1 August 1998 (Figure 2.23) shows the flow direction is essentially unchanged, but the velocity is less than 25 cm s^{-1}.

Sea surface temperatures for the Gulf of Mexico are made available by the Ocean Remote Sensing Group of the Johns Hopkins University Applied Physics Laboratory. The Ocean Remote Sensing Group records and processes imagery from the Advanced Very High Resolution Radiometer (AVHRR) on the NOAA polar orbiting satellites. Multi-day composites for specific periods of interest are made available on their website. The AVHRR 3-day composite for 21 July 1998 (Figure 2.24) clearly shows that the Atchafalaya River plume is turned towards the east.

The National Data Buoy Center (NDBC) owns and maintains a system of buoys and coastal monitoring stations that provides, among many other products, wind speed and direction. In Figure 2.25 we show the location of 10 specific buoys and the median wind speed and maximum likelihood direction for the month of July 1998. It is obvious that winds are upcoast near the Mississippi delta and on coast from Brownsville to Galveston.

2.3 MODELING THE BUOYANCY-DRIVEN FLOW DUE TO RIVER DISCHARGE ON THE TEXAS-LOUISIANA CONTINENTAL SHELF OF THE GULF OF MEXICO

The principal objective of the modeling effort was to investigate the basic physical mechanisms responsible for the development of the Mississippi-Atchafalaya River plume associated with surface wind forcing on the Texas-Louisiana continental shelf. It is well known that the upper layer ocean current responds to wind on a short time scale. In an analysis of the coherence between winds and sea surface currents on the Texas-Louisiana continental shelf, Cochrane and Kelly (1986) and Wang (1996) concluded that the inner-shelf current is strongly coherent with

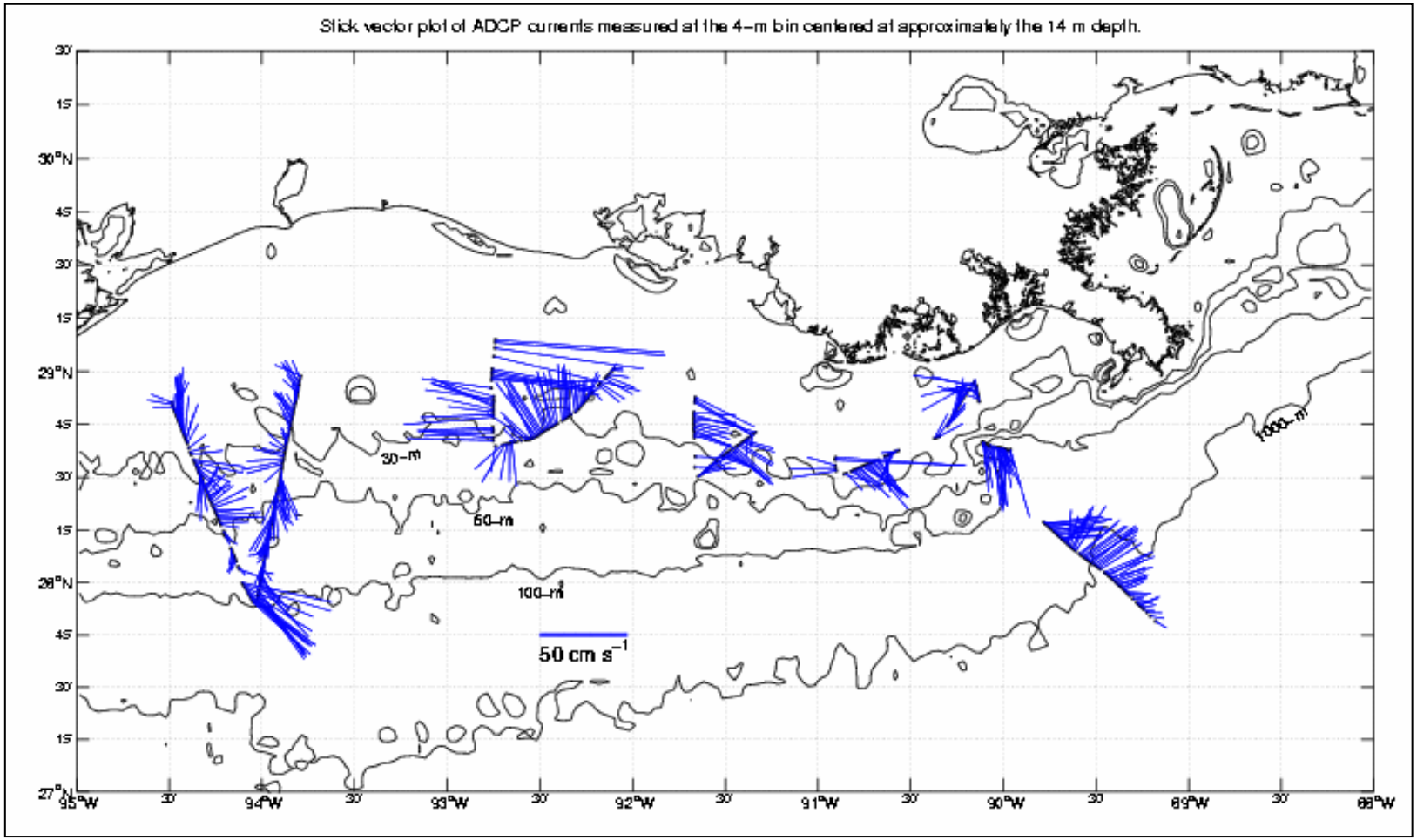

Figure 2.18 Stick vector plot of ADCP currents measured at the 4-m bin centered at approximately the 14 m depth. Bathymetric contours are shown for 30-, 50-, 100-, and 1,000-m depths.

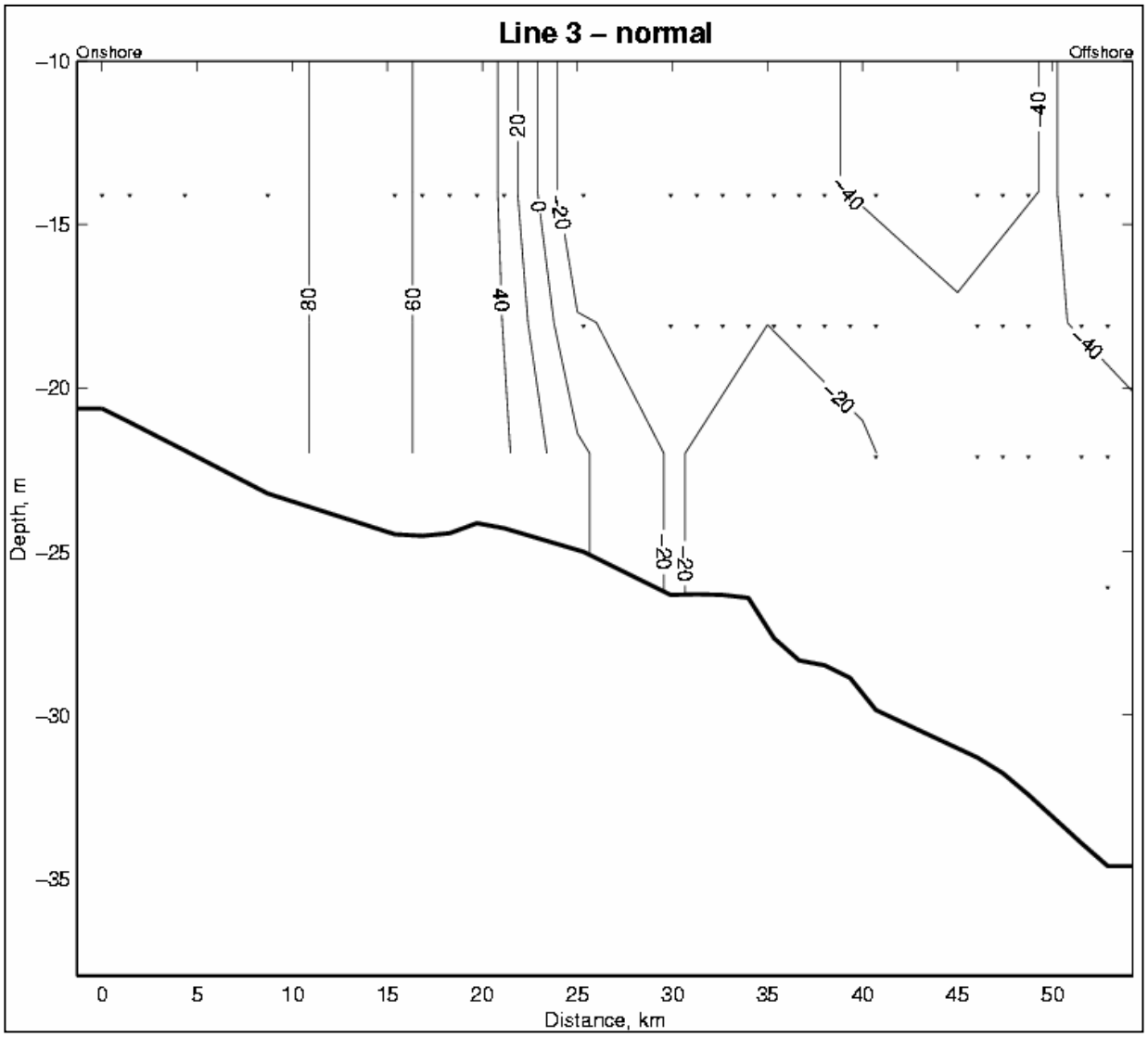

Figure 2.19 Vertical section of ADCP velocities (cm s^{-1}) normal to line 3 for cruise 98-G-9. Upcoast velocities are positive. Ensemble locations are marked with a small triangle.

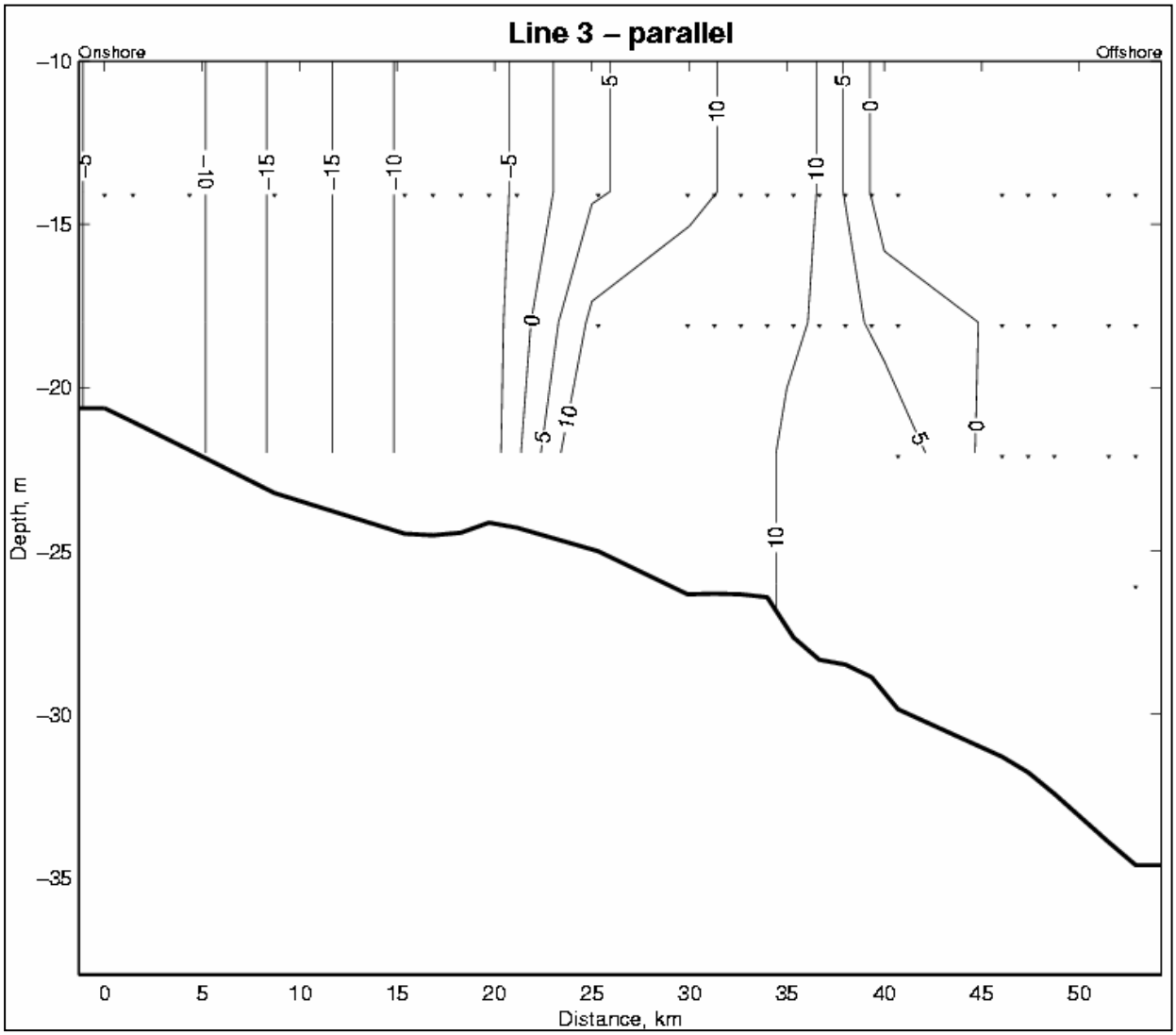

Figure 2.20 Vertical section of ADCP velocities (cm s^{-1}) parallel to line 3 for cruise 98-G-9. Onshore velocities are positive. Ensemble locations are marked with a small triangle.

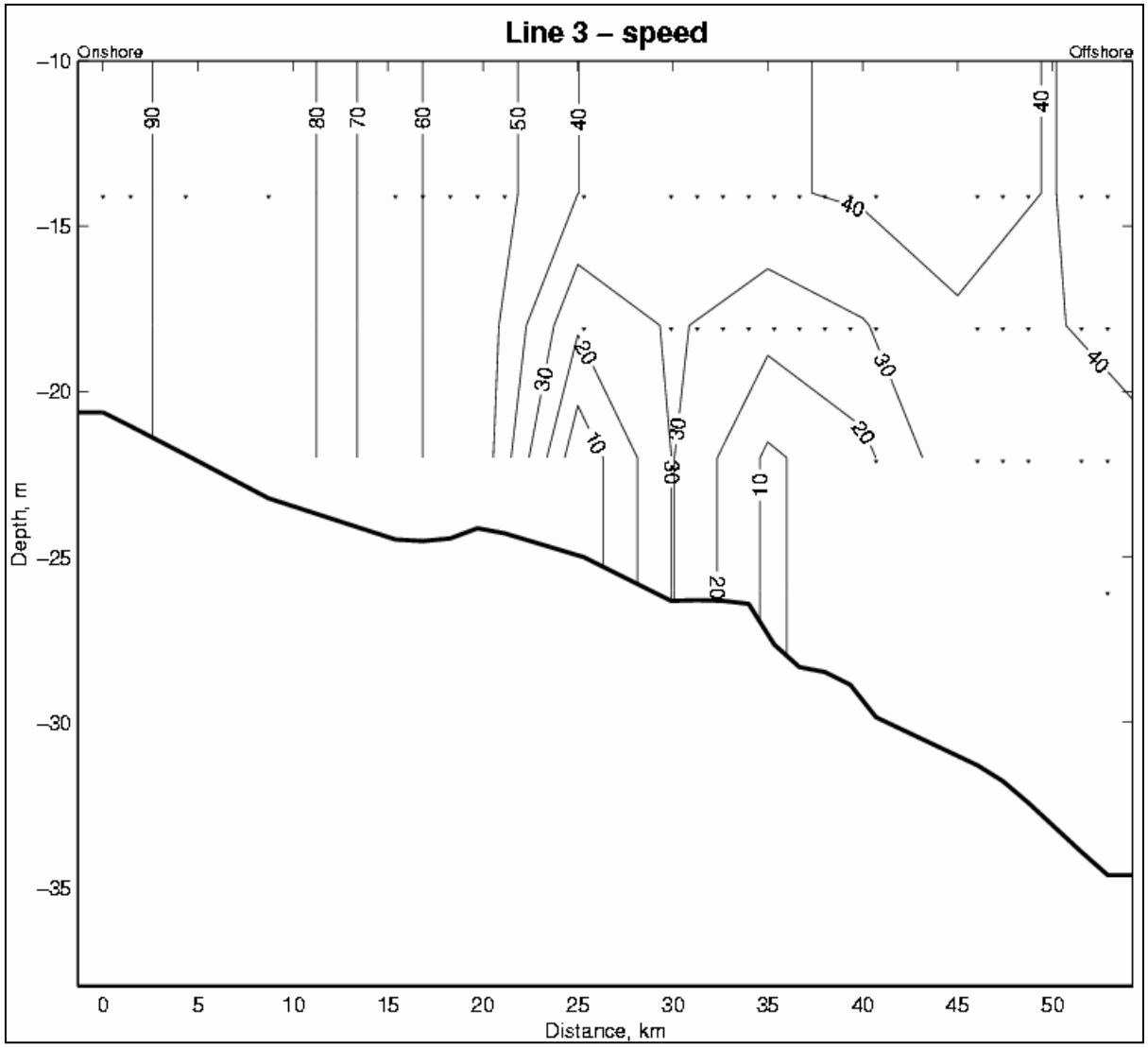

Figure 2.21 Vertical section of ADCP speeds (cm s^{-1}) for line 3 for cruise 98-G-9. Ensemble locations are marked with a small triangle.

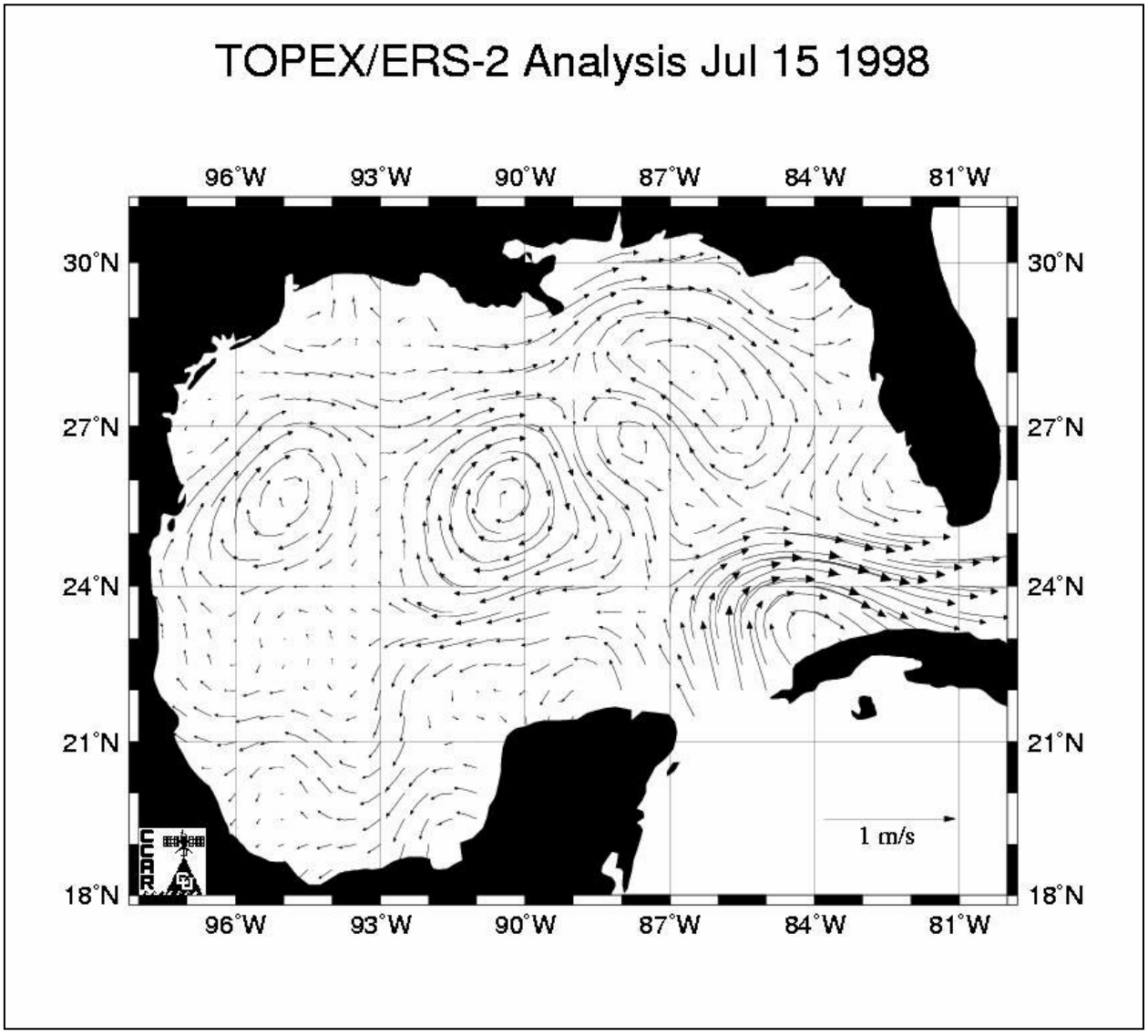

Figure 2.22 TOPEX/ERS-2 composite for 15 July 1998 shows an upcoast flow across the outer shelf on the order of 25-30 cm s^{-1}.

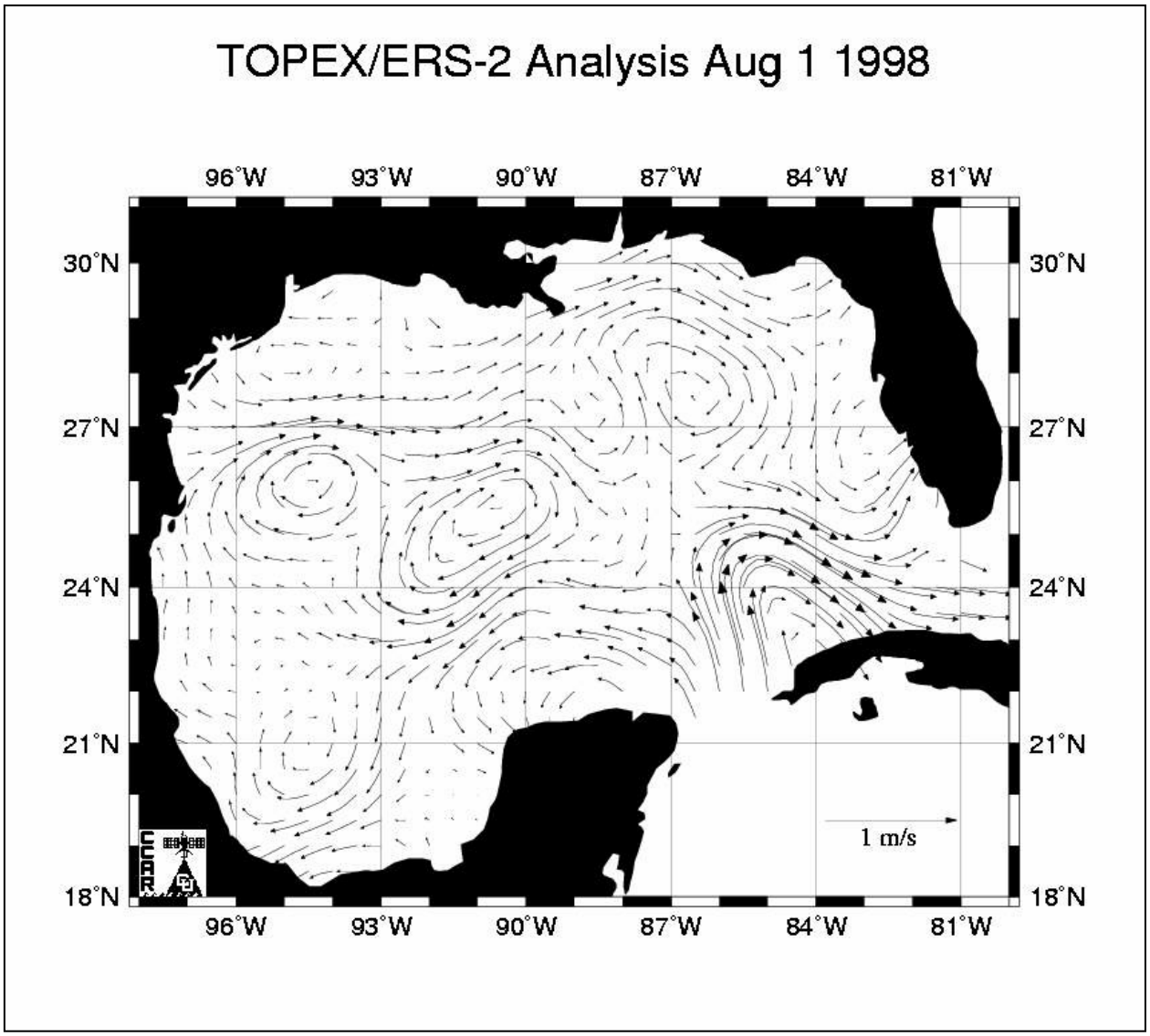

Figure 2.23 TOPEX/ERS-2 composite for 1 August 1998 shows an upcoast flow across the outer shelf on the order of 25 cm s^{-1}.

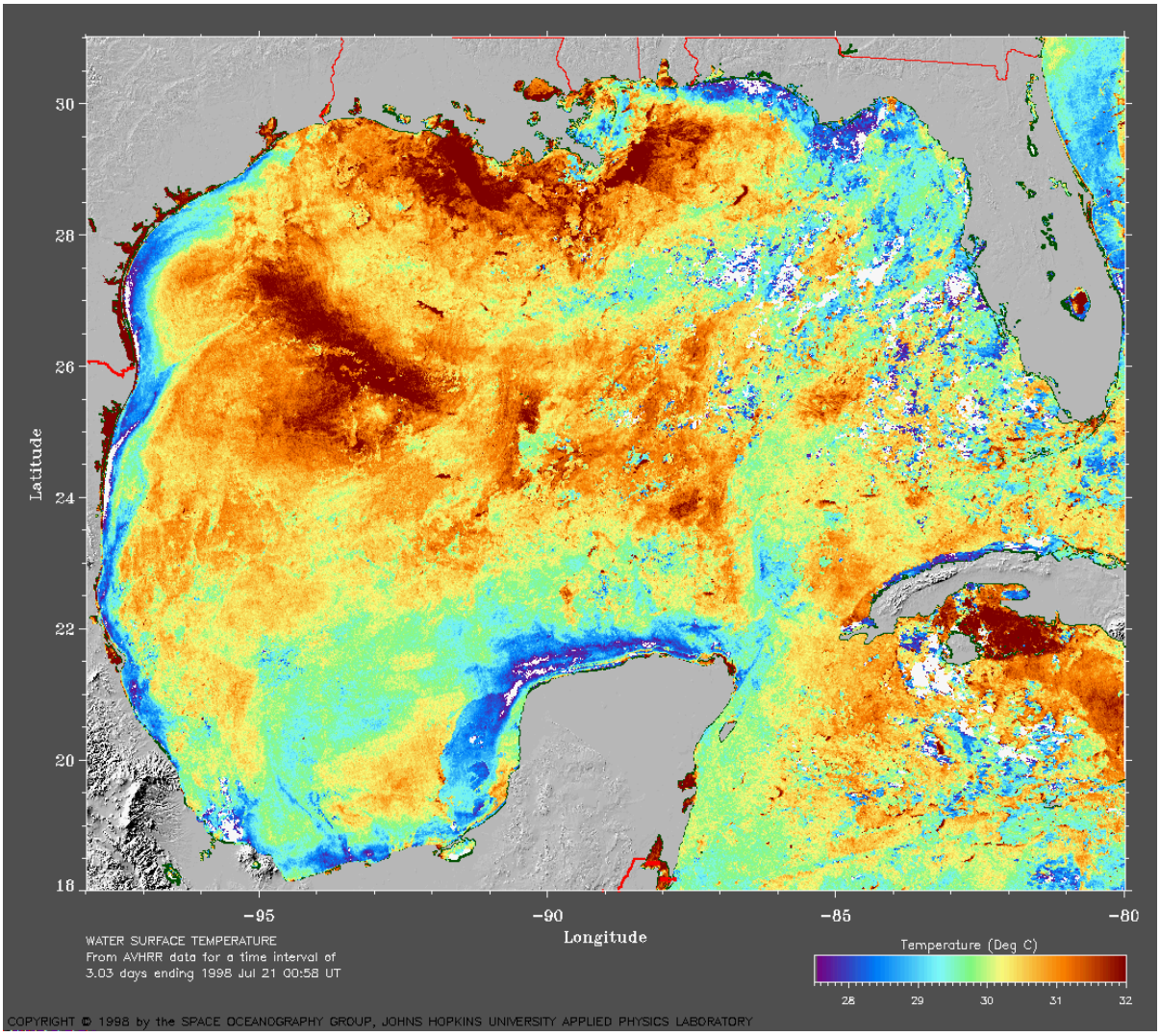

Figure 2.24 AVHRR 3-day composite of the Gulf of Mexico for 21 July 1998 shows that the Atchafalaya River plume is turned towards the east, due to upcoast winds. This image was produced by the Space Oceanography Group, Johns Hopkins University, Applied Physics Laboratory.

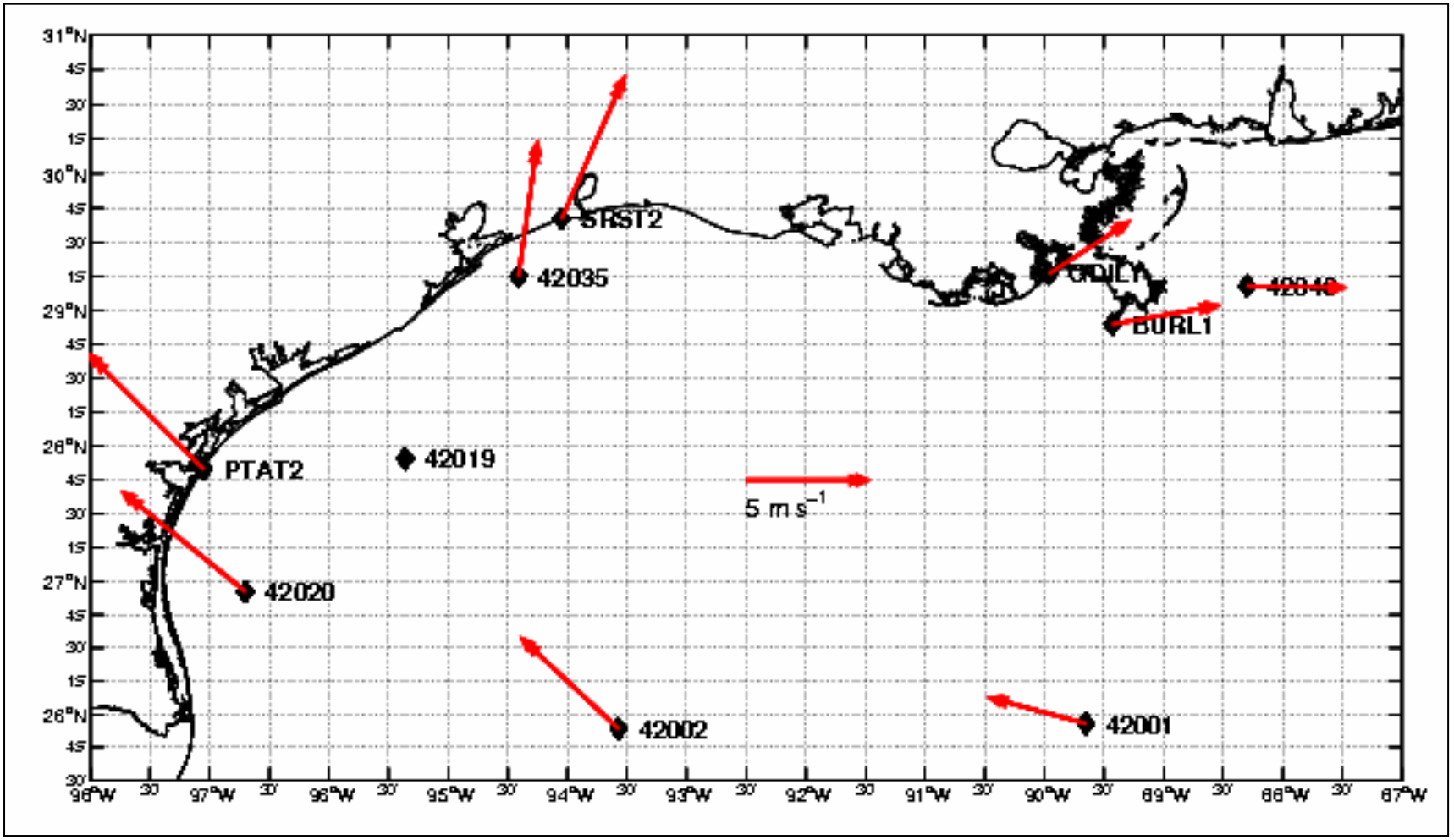

Figure 2.25 Median wind speed and maximum likelihood direction wind vectors for the month of July 1998 for 10 NDBC meteorological stations. NDBC buoy 42019 was not operating during this time period. The winds in the Mississippi delta region are clearly upcoast.

the along-shore wind component. When the along-shore wind turns upcoast (in the direction from the Rio Grande to the Mississippi Delta) from late-June through mid-August, the coastal current on the southwestern part of the shelf also turns upcoast and an anticyclonic circulation forms over the mid shelf. The right-bounded coastal current near the Mississippi Delta, on occasion, disappears during the upcoast wind period. With regards to the data used by Cochrane and Kelly (1986) to make their conclusions, it should be mentioned that Dinnel and Wiseman (1986) pointed out that the Mississippi and Atchafalaya Rivers had relatively small discharges during the 1963-1965 period. It is of interest to study the variability of the summer circulation pattern caused by unusual river discharge events such as the summer flood of 1993. In particular, the following questions were addressed:

> What is the spatial and temporal structure of the Mississippi-Atchafalaya River plumes under different regimes? What physical mechanisms are important in the plume front near the river mouth and downstream?
>
> What is the physical mechanism by which the cross-shelf density front is influenced by winds over the inner shelf?
>
> Does the southwestward along-shore coastal current persist due to the large river fluxes during the upcoast wind period during flood conditions? Specifically, how did the summer flood of 1993 affect the model-predicted summer circulation pattern on the Texas-Louisiana continental shelf?

To answer these questions, a set of model experiments was conducted to investigate the basic physical mechanisms responsible for formation and evolution of the Mississippi-Atchafalaya River plumes on the Texas-Louisiana continental shelf. The methods and results are fully discussed in Lo (1999); here we present a summary of the relevant findings.

The numerical model used in this study was a modified version of the Princeton Ocean Model (POM), which is a three-dimensional, primitive-equation, estuarine and coastal ocean circulation model. The present model applies a 170×64 curvilinear orthogonal grid in the horizontal as shown in Figure 2.26 and 21 levels with irregular spacing in the vertical direction. In order to examine the influence of variable bathymetry on the river plume and buoyancy-driven flow in the shelf sea region, the present model utilizes realistic bottom topography and irregular coastline geometry for model simulation.

In summary, the model results of the present study demonstrate that the buoyancy flow induced by the river inflow from the Mississippi and Atchafalaya Rivers has a significant impact on the circulation over the Texas-Louisiana continental shelf. The major findings of this study are given as follows: (1) Consistent with previous studies, such as Chao and Boicourt (1986) and Oey and Mellor (1993), freshened bulges are formed near the river mouths and a baroclinic boundary current, propagating as a coastal Kelvin-like wave, is developed along the coast toward the west. (2) The model results show that the near bottom current flows, opposite to the surface current, toward the east in the region near the river mouths, indicating a first baroclinic mode structure. (3) An anticyclonic eddy associated with upwelling is found near the head of the Mississippi Canyon. The generation mechanism of this eddy is in accordance with the linear

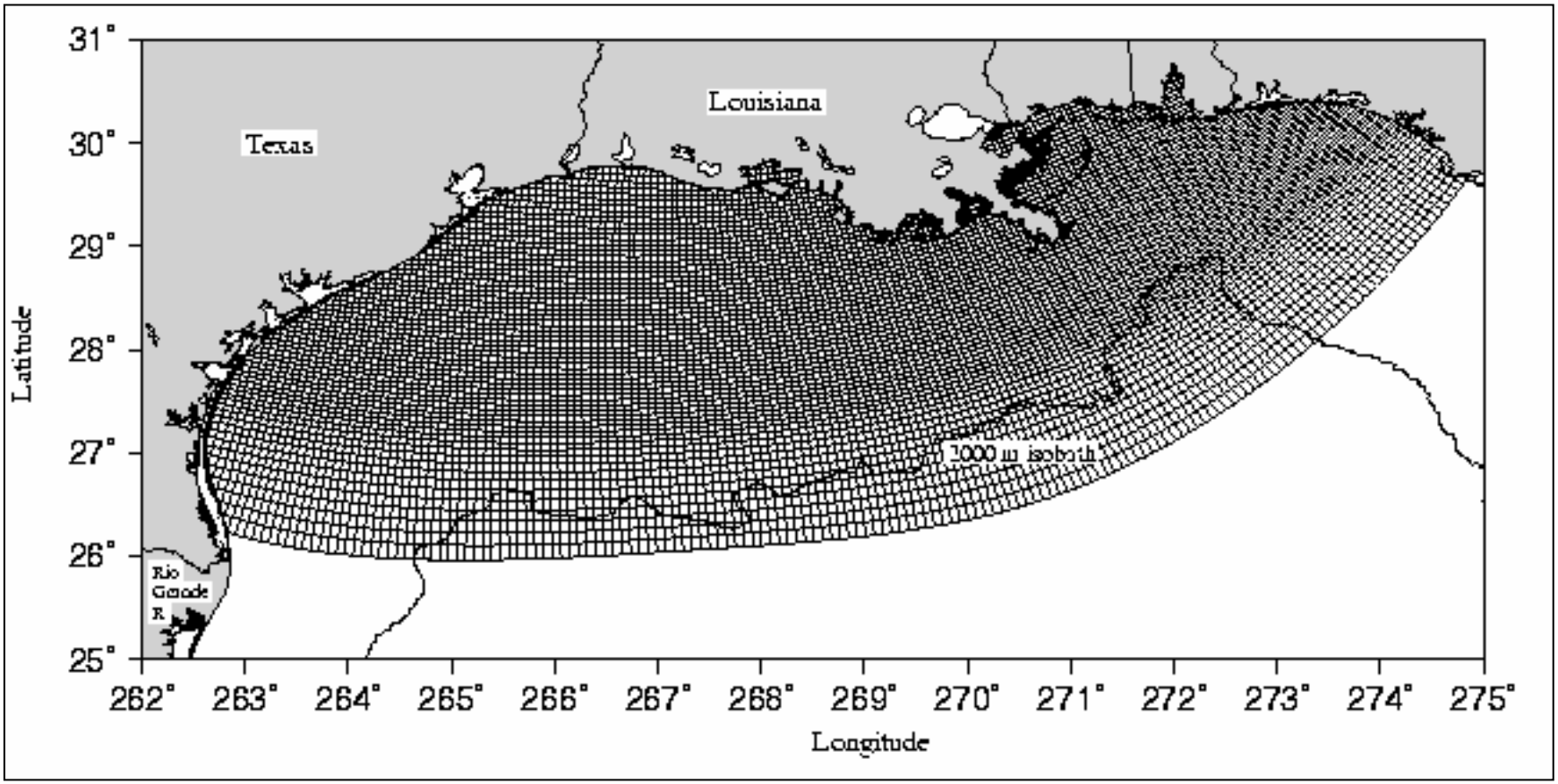

Figure 2.26 The 172 x 66 curvilinear orthogonal model grid of the Texas-Louisiana shelf. The mesh resolution varies from 2.8 km on the inner shelf to 19.7 km near the open boundary.

theory of geostrophic adjustment. (4) The dynamics of the plume front near the river mouths are strongly nonlinear, but the flow in the downstream region is geostrophic. (5) The bottom boundary layer is an important region in the adjustment of the structure of the cross-shelf front, where buoyancy is transported across the shelf near the bottom. (6) The river plume is significantly altered by the surface wind stress, especially the along-shore component of wind stress. (7) The surface current is primarily dominated by the surface wind stress. The model predicts that the right-bounded coastal current completely vanishes during an upcoast wind period even where both rivers have extreme inflow such as during the summer flood of 1993.

To better understand and characterize the basic physical mechanisms and the evolution of the Mississippi-Atchafalaya River plume, the first group of model experiments was performed with initially homogeneous conditions and the current was mainly driven by the buoyancy or potential energy induced by river discharge. Similar to the previous studies, without considering other forcing factors such as tides or winds, the model also shows that the effects of the Coriolis force play an important role in the river plume dynamics. As freshwater discharges from the river mouths onto the shelf, the surface flow turns anticyclonically within the freshened bulge due to the Coriolis force. A right-bounded coastal current leaking from the bulge is formed in the downstream region, with a width of about 60 km, or about 2~3 Rossby radii. This is shown in Figure 2.27. From a diagnostic analysis of the momentum balance, the river plume in the cross-shelf direction can be described by linear dynamics in which the flow is a balance between the pressure gradient and the Coriolis force terms; i.e., a geostrophic balance. In contrast, in the along-shelf direction the flow becomes strongly non-linear within the frontal zone near the river mouths in the model.

The model also reveals the importance of the bottom boundary layer in adjusting the vertical structure of the density fields in the cross-shelf direction. The cross-shelf transport near the bottom, generated due to bottom friction, is known to be an important mechanism in driving the density front across the shelf. The model results illustrate that the vertical structures of the density and velocity fields in the region near the river mouths and in the downstream regions are very different because of the different direction of the cross-shelf transport produced by bottom friction in the bottom boundary layer. In the downstream region, an offshore transport is generated in the bottom Ekman layer and causes the water column to be vertically homogeneous in the inner shelf. In contrast, in the region near the river mouths, onshore transport is generated in the model near the bottom, which is in partial compensation of the offshore transport above the bottom boundary layer; the onshore near-bottom flow has a tendency to tilt the density contours seaward from bottom to surface.

One of the important findings of this present study is that the model illustrates a significant interaction between the river plume and the Mississippi Canyon. The pressure gradient is built up as the offshore current, propagating from the east, approaches the transverse canyon, where high pressure occurs in the deep region of the canyon and drives an up-canyon flow. An anticyclonic eddy, therefore, is formed near the head of the canyon as a result of geostrophic adjustment (Figure 2.28). Although there is no observation to support the model results that an anticyclonic circulation is trapped by the Mississippi Canyon, the dynamics of the flow around the canyon is generally consistent with other studies of the interaction between a current and a canyon (Freeland and Denman 1982; Klinck 1988; Howard 1992). Based on a diagnostic

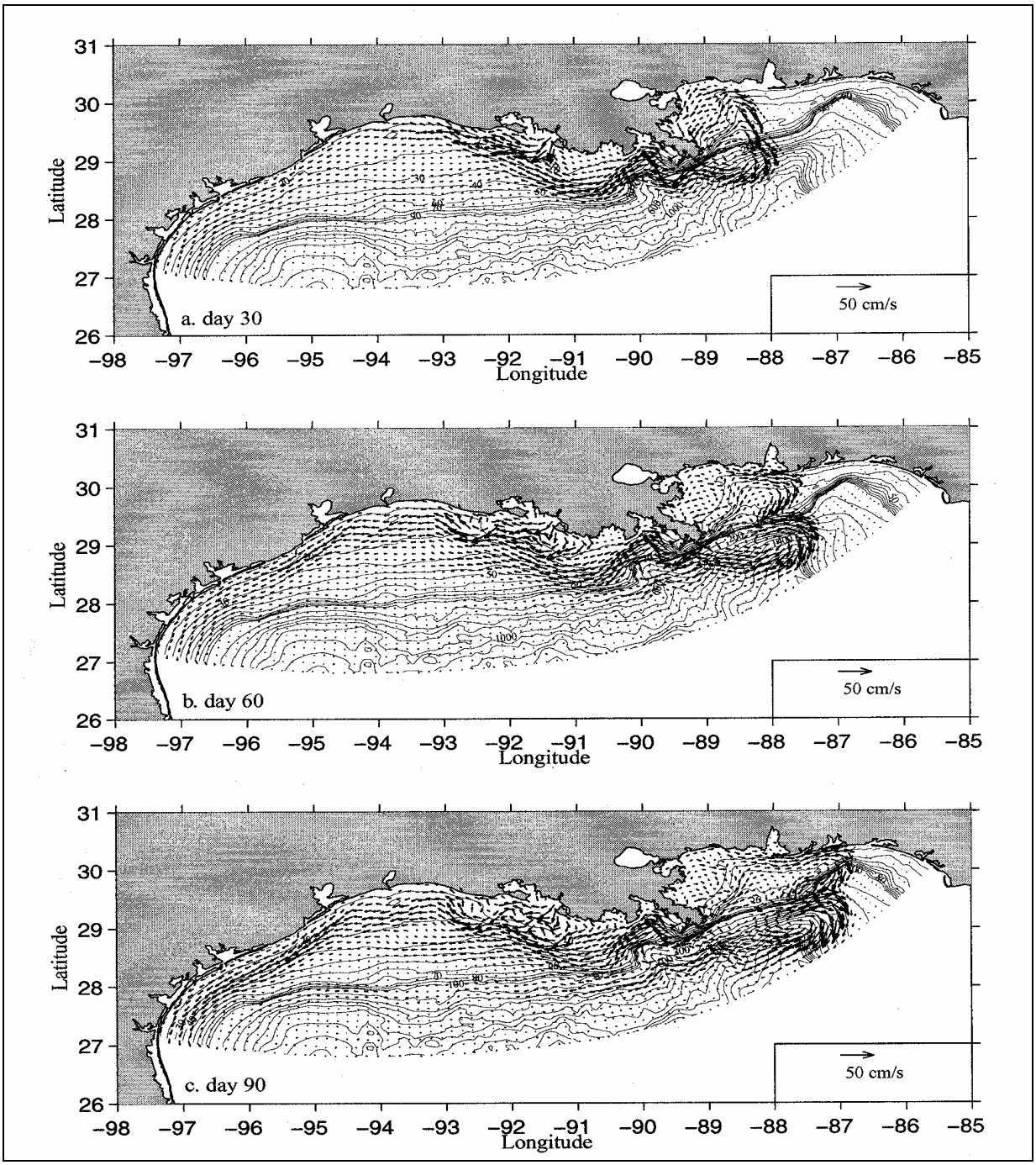

Figure 2.27 Plan views of the near-surface velocity fields with constant river discharge. Snapshots are taken at times (a) 30, (b) 60, and (c) 90 days. For clarity, current arrows are plotted at every other grid point. Contours represent bottom topography. The sponge layer is not shown.

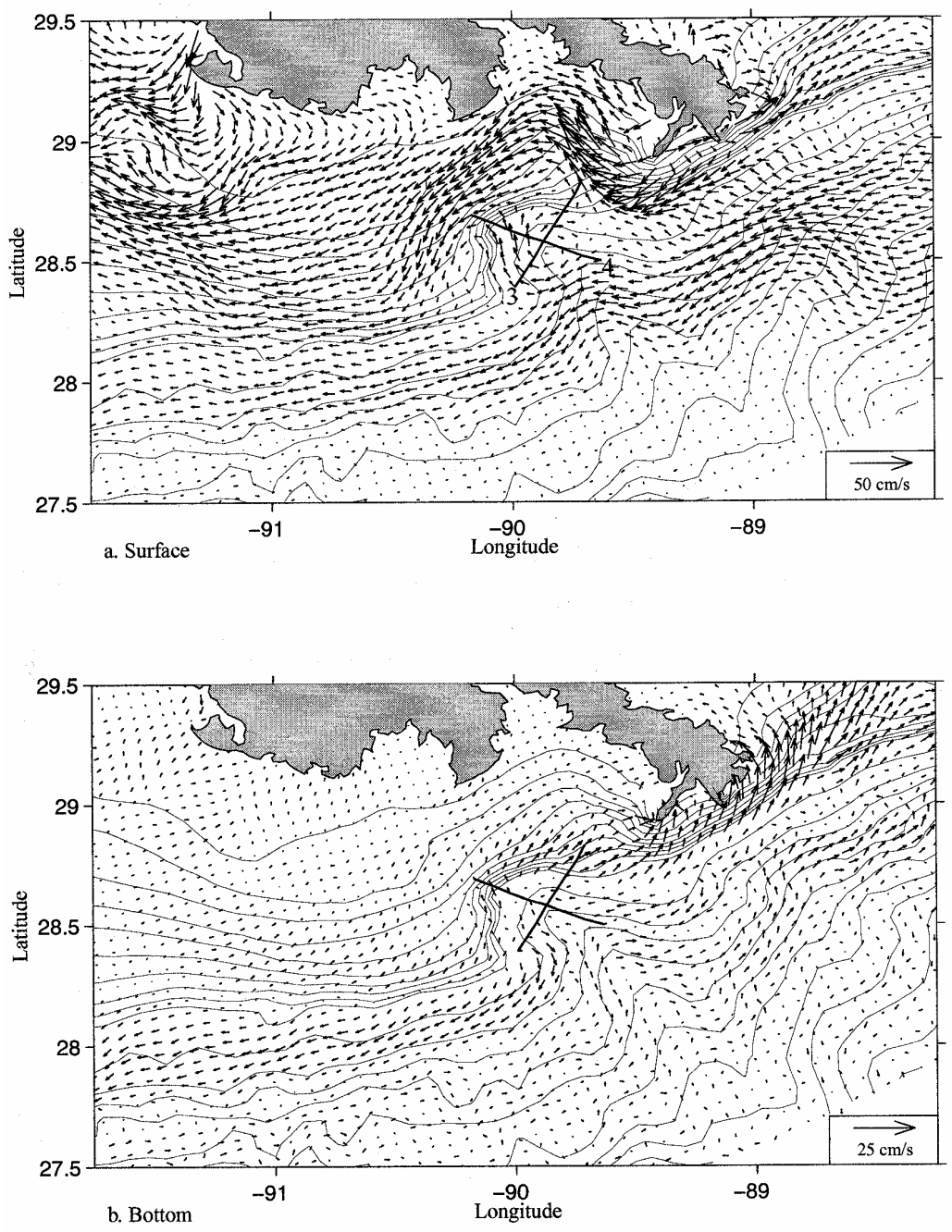

Figure 2.28 Plan view of detailed information of (a) the near surface and (b) the near bottom velocity fields in the region between the Mississippi Canyon and the Atchafalaya Bay at 90 days. Contours represent bottom topography. Heavy solids lines indicate the locations of Sections 3 and 4.

analysis of the vertically integrated vorticity balance, we found that the vortex stretching or compression of the water columns mainly determines the vertical motion within the canyon. The model predicts that the anticyclonic eddy induces upwelling at the head of the canyon as the flow moves from depth onto the shelf along the canyon axis.

The influence of spatially uniform winds on the preexisting river plume on the Texas-Louisiana continental shelf also has been examined. The model results suggest that the river plume is significantly altered by the surface wind stress. This is especially so for the along-shore component of wind, which generates surface Ekman transport across the shelf and induces strong downwelling or upwelling near the shore. For a downwelling-favorable wind, the right-bounded coastal current is intensified by converging surface onshore Ekman transport, and the water column over the inner shelf becomes vertically homogeneous. In contrast, if the wind is upwelling-favorable, the right-bounded coastal current completely vanishes as shown in Figure 2.29. In addition, a large amount of the plume water is moved across the shelf by the surface offshore Ekman transport and a shoreward transport is generated underneath the surface Ekman layer to compensate the surface offshore transport. As a result, the stratification of the water column in the inner shelf becomes stabilized. The vertical distributions of the salinity and velocity fields at Sections 1 and 2 (Figure 2.30) at time t = 30 days after application of the downcoast and upcoast wind forcing are presented in Figures 2.31 and 2.32. The model salinity results for the upcoast wind (upwelling favorable wind) are consistent with the vertical sections of salinity measured during the late July 1998 cruise (Figure 2.10 and Figures B.16 to B.22).

It is of interest that the model shows the interaction between the buoyancy-drive flow and the surface wind stress. First, in the downstream region, the surface current is in agreement with the typical Ekman theory, but the surface flow in the region near the river mouths becomes more complex because of the interaction of the pressure gradient induced by the river inflow. Secondly, the structure of the nearshore vertical velocity in the near field is dominated by the buoyancy-driven flow. The model indicates that the nearshore water moves upward in the near field for a downwelling-favorable wind.

An attempt at a short-term model prediction of the circulation on the Texas-Louisiana continental shelf during the summer of 1993 was made. The monthly mean surface circulation of August shows some differences between the model predictions under spatially uniform winds (Figure 2.33) and hourly gridded wind conditions (Figures 2.34 and 2.35). The gridded wind set was derived from hourly surface meteorological data taken from 16 NDBC stations during the period from July 31 to September 30, 1993, when upcoast winds occur. In comparison with the low-frequency circulation scheme given by Cochrane and Kelly (1986), the model result with gridded wind forcing is more consistent with past observations. Furthermore, in comparison with Figure 2.18, the stick vector plot of ADCP currents measured during late July 1998 at the 14m depth, the model derived, near-surface velocity field driven by gridded winds, as shown in panel (b) of Figure 2.32, is surprisingly consistent. This suggests that the right-bounded coastal current completely vanishes during an upcoast wind period, even when both rivers have extreme inflow such as caused by the summer flood of 1993.

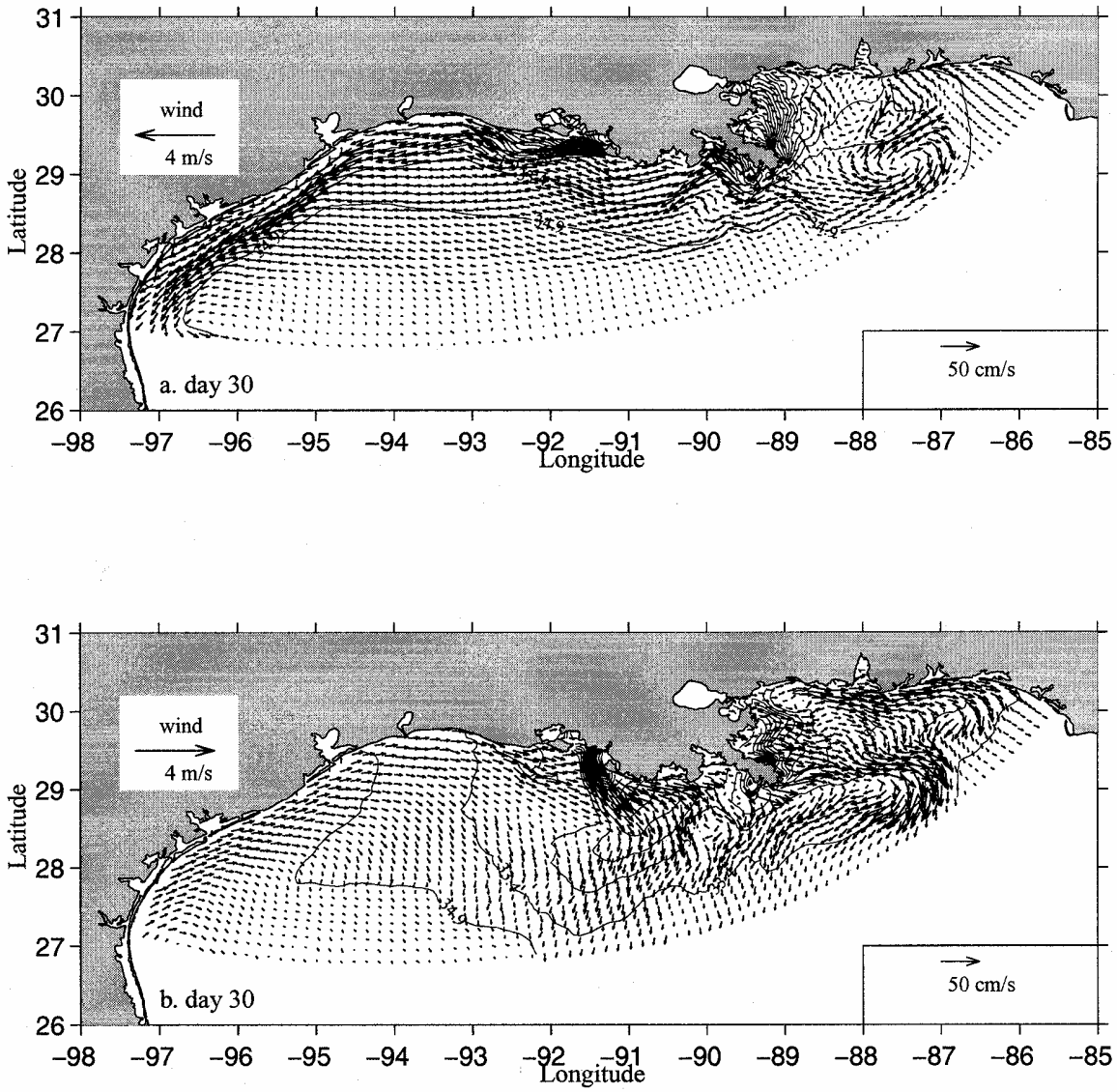

Figure 2.29 Plan views of the near-surface velocity and salinity fields with constant river discharge and winds. Snapshots are taken at time t=30 days after adding (a) downcoast and (b) upcoast winds. For clarity, current arrows are plotted at every other grid point. Salinity contours are shown at intervals of 1.5‰. The sponge layer is not shown.

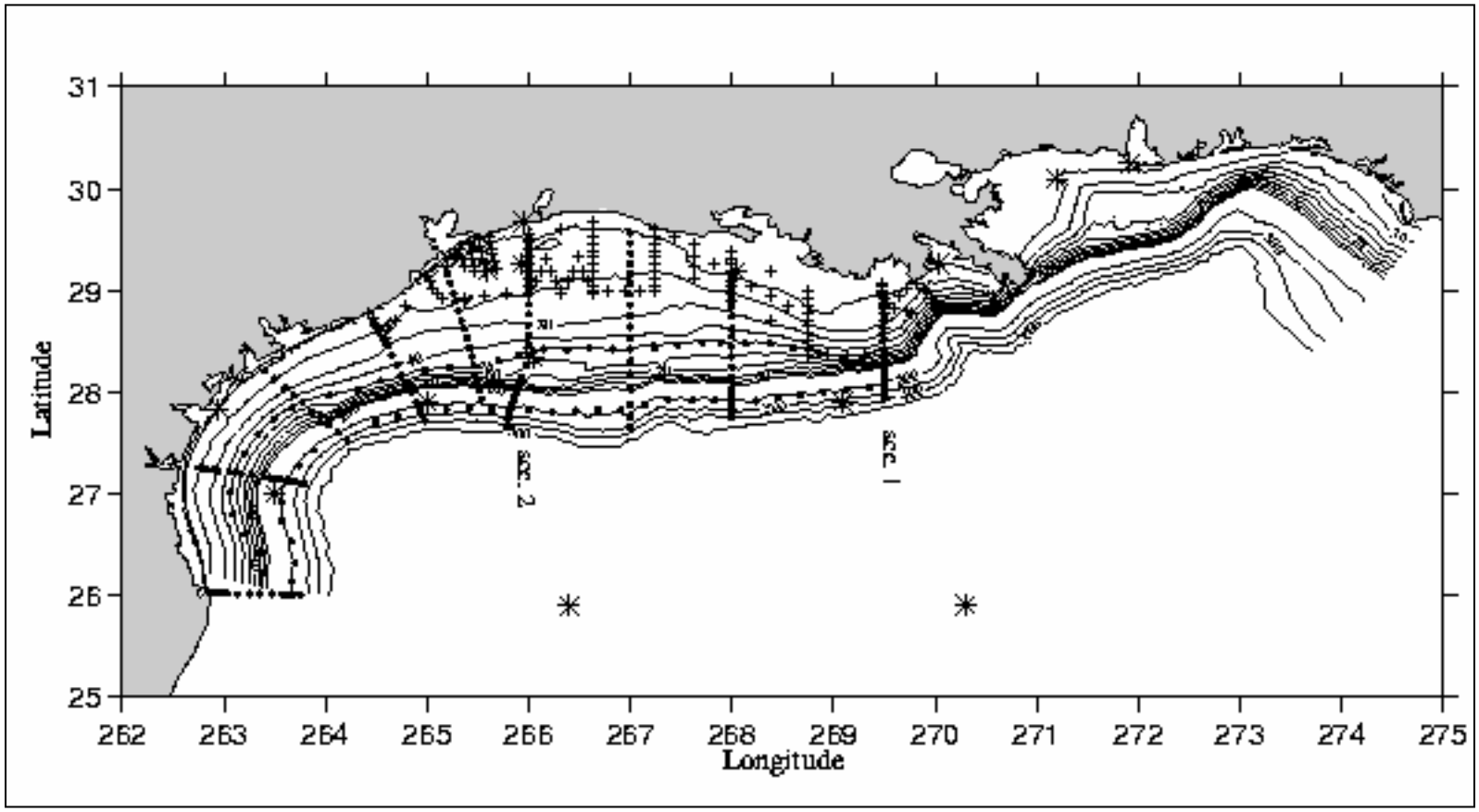

Figure 2.30 Smoothed bottom topography. Depth contours are in meters. The circles indicate the hydrographic stations of LATEX A cruise H06; crosses indicate the hydrographic stations of LATEX B cruise 4; stars indicate the wind observing stations.

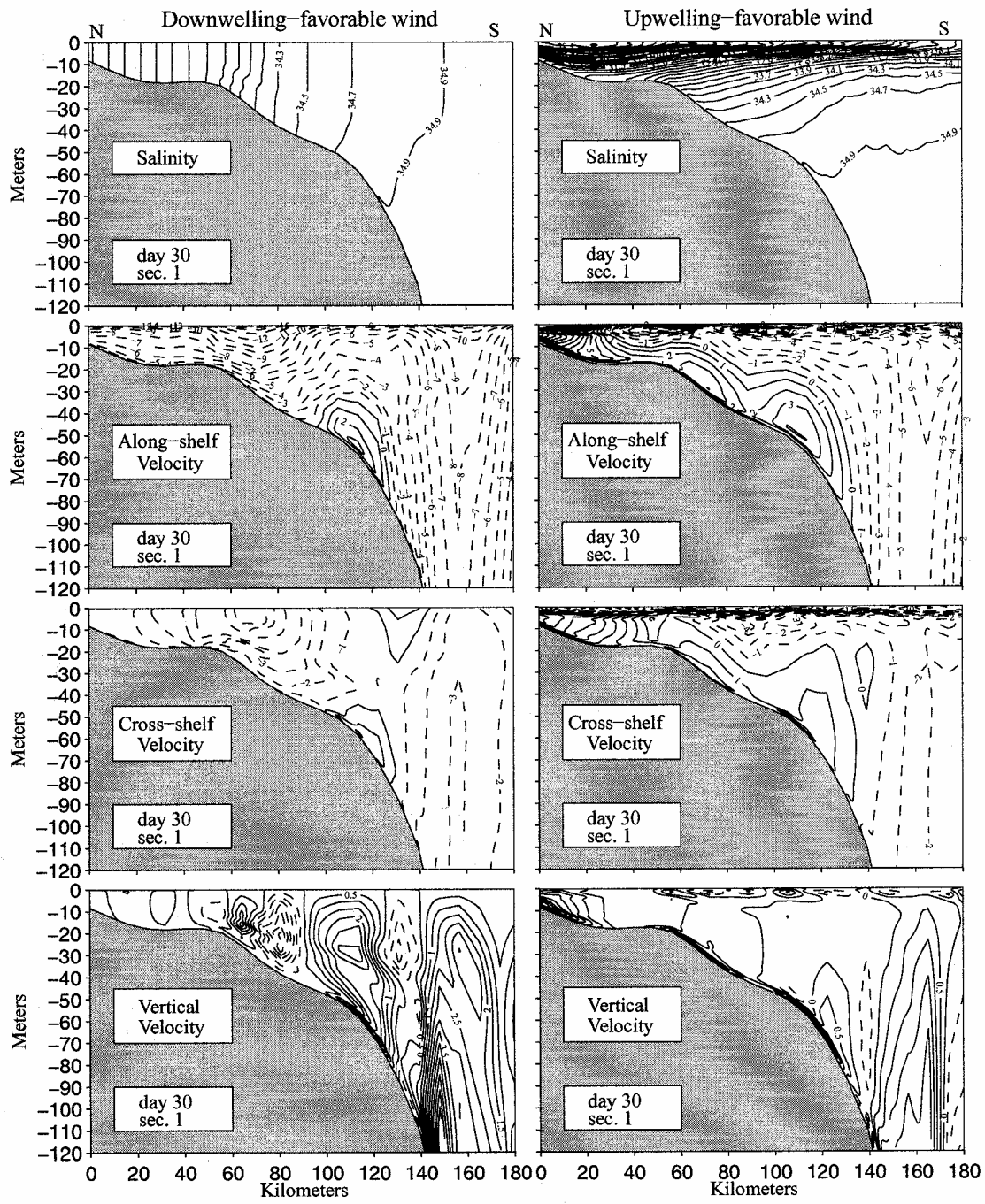

Figure 2.31 Vertical distributions of salinity (top), along-shelf (second), cross-shelf (third), and vertical (bottom) velocities at section 1 at time t=30 days after downcoast (left) and upcoast (right) wind forcings. Solid (dashed) contours represent upcoast (downcoast) flow in the second panels, shoreward (seaward) flow in the third panels, and upward (downward) flow in the bottom panels.

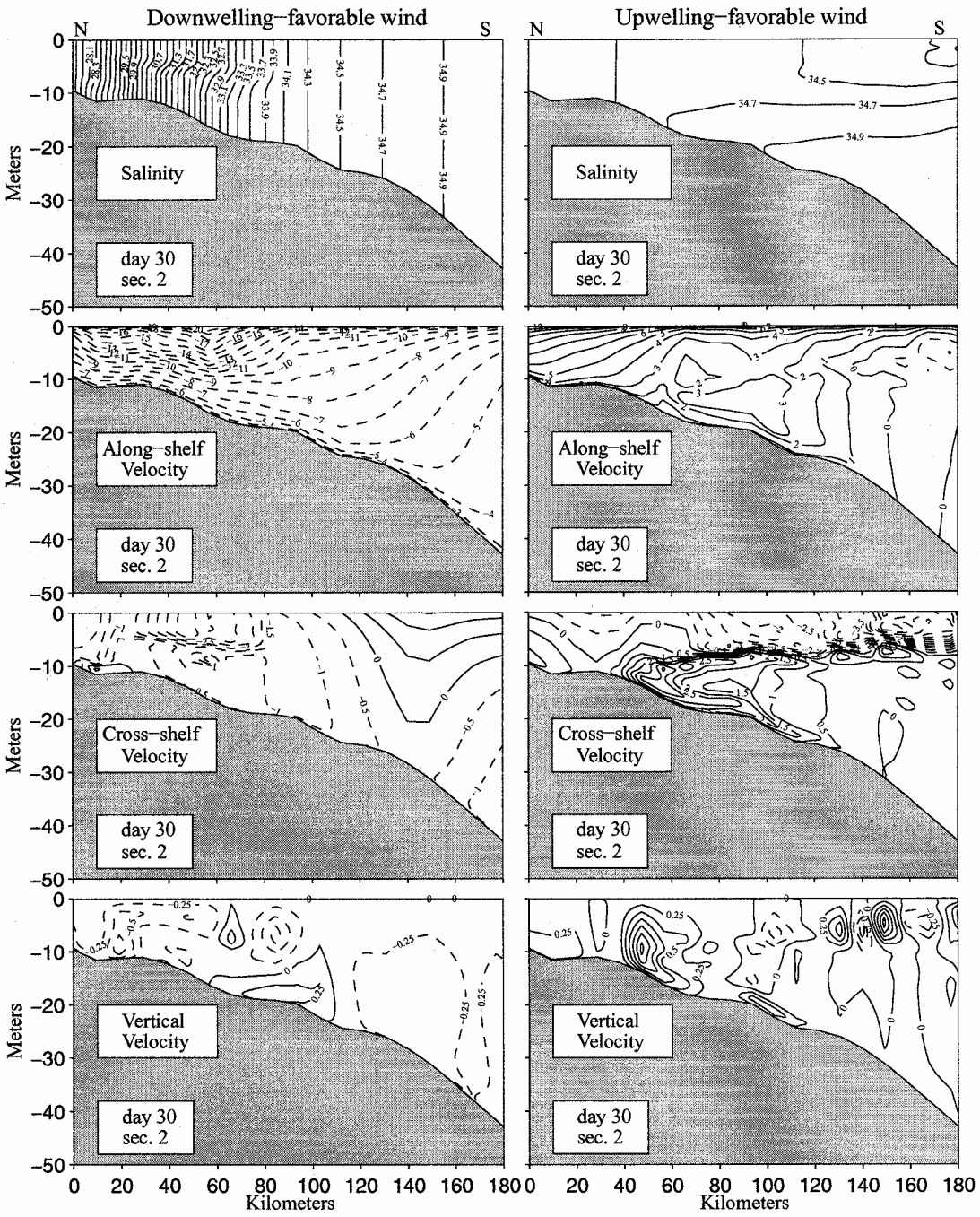

Figure 2.32 Vertical distributions of salinity (top), along-shelf (second), cross-shelf (third), and vertical (bottom) velocities at section 2 at time t=30 days after downcoast (left) and upcoast (right) wind forcings. Solid (dashed) contours represent upcoast (downcoast) flow in the second panels, shoreward (seaward) flow in the third panels, and upward (downward) flow in the bottom panels.

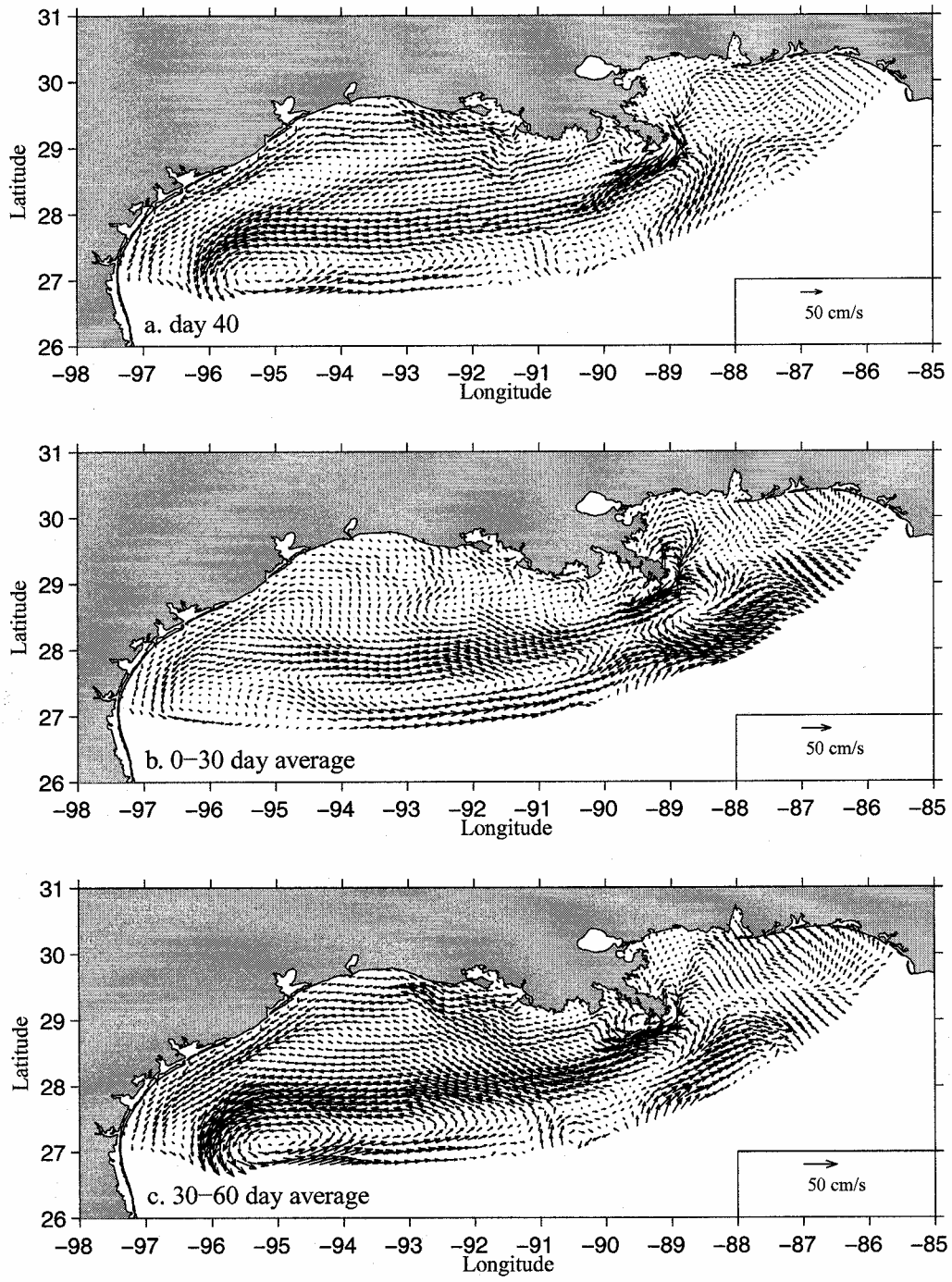

Figure 2.33 Plan views of the near-surface velocity fields with spatially uniform winds at (a) time t=40 days, of (b) the first 30-day mean (0-30 days) and (c) the second 30-day mean (30-60 days). For clarity, current arrows are plotted at every other grid point. The sponge layer is not shown.

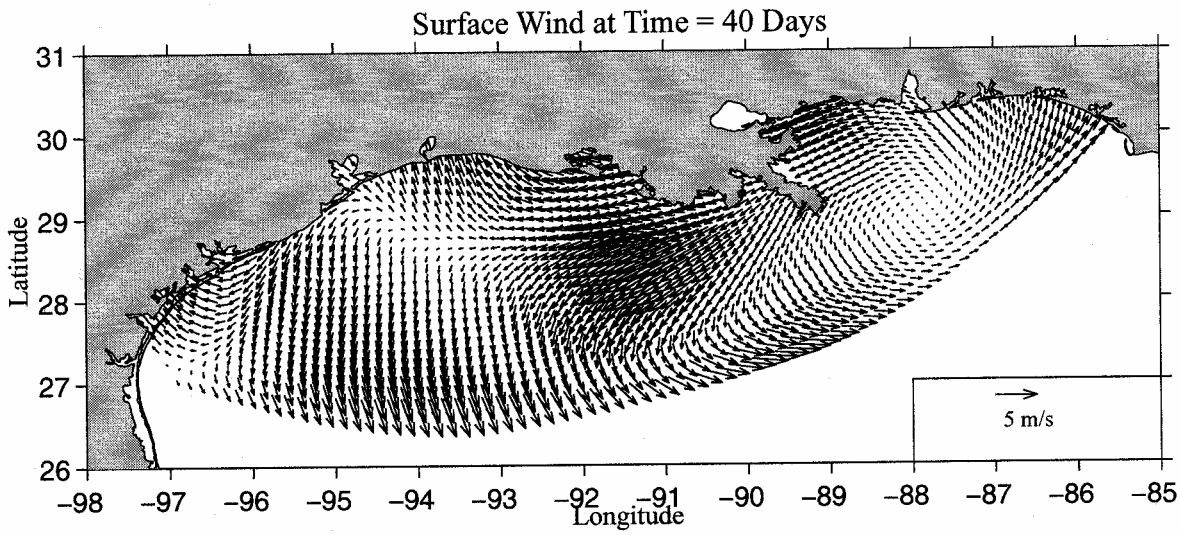

Figure 2.34 Plan view of the surface wind field at time t=40 days. The gridded winds are interpolated by using the observed meteorological data of NBDC. For clarity, wind vectors are plotted at every other grid point.

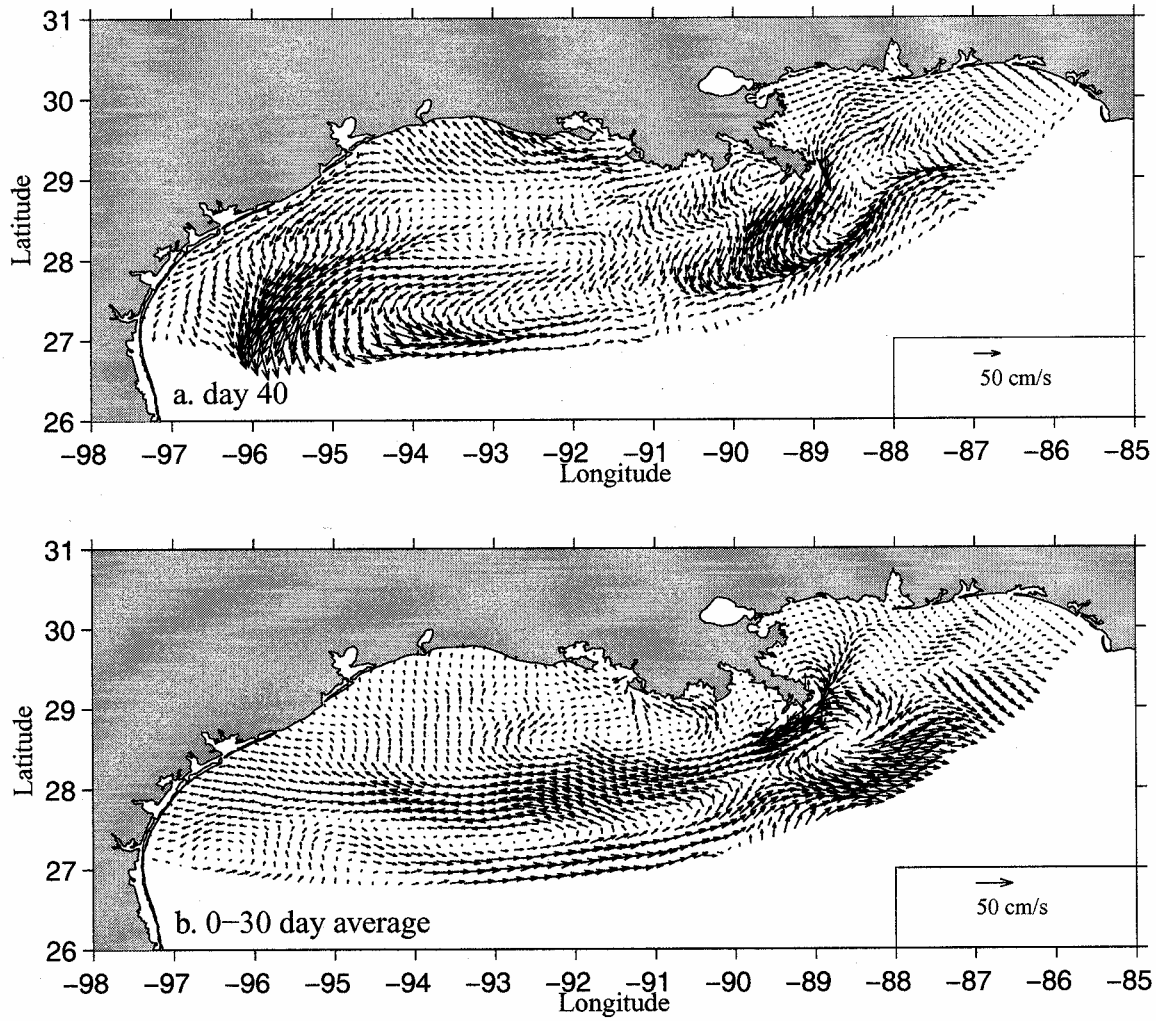

Figure 2.35 Plan views of the near-surface velocity fields with gridded winds at (a) time t=40 days and of (b) the first 30-day mean. For clarity, current arrows are plotted at every other grid point. The sponge layer is not shown.

In general, the model results of the present study are in considerable agreement with past and present observations and previous model studies. The model results support the hypothesis that the river plume structure is primarily modified by local winds. The model experiments with spatially and temporally uniform wind indicate that the surface wind stress has a first-order impact on the surface current. The river plume structure is significantly altered by the surface wind stress, especially the along-shore component of the wind stress.

Chapter 3

3.0 INTRODUCTION

The Texas-Louisiana shelf is an area with a constant risk of oil spills. Therefore, knowledge of the surface circulation in this area is of particular value. Previous works (Cochrane and Kelly, 1986; Oey, 1995, Li et al., 1997; Cho et al., 1998) mainly focus on the mid- and outer Texas-Louisiana shelf while the Texas-Louisiana inner shelf (shallower than 20 m) has not been fully explored. The alongshore current is mainly wind-driven, particularly during winter, and the response time of the alongshore current to the alongshore wind is less than one day. Recent work (Nowlin et al., 1998) indicates that the variation of the inner shelf circulation is very complicated. The coherence between local alongshore wind and alongshore current has large spatial and temporal variability, though significant coherence is found in both the weather band (2-10 days) and the diurnal band. In general, in the cross-shore direction, the coherence decreases with the distance from the coast; in the alongshore direction, the coherence over the eastern region of study is lower than over the western region; seasonally, the coherence is higher in winter than in the summer stratified season.

Despite the above findings, several issues involving the relationship of wind and inner shelf flow have not been elucidated. One is the structure of the inner shelf circulation: is it simply a downcoast (from Louisiana to Texas) branch of the offshore circulation gyre in winter and upcoast branch in summer (e.g., Cochrane and Kelly, 1986) or of more complicated structure? The second issue is that the mechanisms by which the inner-shelf flow is driven have not been fully studied. It is widely regarded that the inner-shelf alongshore flow is dominated by alongshore wind forcing. During winter the inner shelf water is well mixed and the balance between alongshore wind stress and bottom friction controls the volume of the alongshore flow. The balance mechanism was used by Cochrane and Kelly (1986) and Chuang and Wiseman (1983) to explain the relationship between observed alongshore wind and current or water level, respectively. Linear bottom friction coefficients were estimated. In addition to the local wind-friction balance, there are other important mechanisms such as coastal-trapped waves and wind-induced downwelling/upwelling. The former is a principle way to propagate non-local effects and the latter dominates the cross-shore flow and vertical transport. Current (1996) developed a coastal-trapped wave model to simulate the inner-shelf current variability with a scale of 2-10 days. On average, the model could explain 46% of the total variance of observed alongshore current. Thus, there is a large part of the total variance that still cannot be explained by the barotropic wind forcing. Spring floods result in a density front, strong along-front geostrophic currents, and inhibition of vertical mixing. The resultant strong stratification is enhanced by solar heating during summer. The existence of the stratification can significantly influence the inner shelf circulation. Wiseman et al. (1997) studied the seasonal and interannual variation of stratification over the east Texas-Louisiana shelf (93.5°W-89°W). Strongest stratification is observed in spring and summer. In winter, the stratification is disrupted by strong mixing caused by storms. The stratification greatly influences the vertical shear of inner shelf currents, especially when alongshore wind stress is weak (in summer). This also impacts the coherence between wind and current in different seasons (Nowlin et al, 1998). Last, but not least, Loop Current rings may have an influence on the inner shelf flow as a boundary forcing.

The influences of these factors are all reflected in the current observations. However, it is a great challenge to quantify them. Recent wind and current velocity measurements from the Texas Automated Buoy System (TABS) provide a new source of data to study inner-shelf current variability in space and time. The subsequent examination of the TABS data shall extend existing knowledge, provide new findings, and suggest dynamic explanations of the inner-shelf flow variability in this area.

The objectives of this report are therefore to use TABS data, re-examining previous findings of wind-current coherence variability over the Texas-Louisiana inner shelf and exploring the spatial structures of the inner shelf circulation (including both mean circulation and coastal trapped waves) and the momentum balance. Since wind variations over the Texas-Louisiana inner shelf have been well documented (Wang et al., 1996; Nowlin et al., 1998), this chapter will omit description of the wind spectrum analyses. The rest of the chapter is organized as follows: Chapter 3.1 describes data sources and pre-processing; Chapter 3.2 examines the monthly mean inner shelf circulation variability; wind-current coherence analysis is discussed in Chapter 3.3 and the spatial coherence of currents in Chapter 5. Conclusions and discussions are presented in Chapter 3.5.

3.1 DATA

Locations of wind and current stations are shown in Figure 3.1. Wind measurements were taken from stations SRST2, PTAT2 and 42035 (Figure 3.1). The first two are C-MAN stations and the third one is a buoy station maintained by the National Data Buoy Center (NDBC). The heights of the anemometers are 14.5 m, 12.5 m and 5.0 m at SRST2, PTAT2, and 42035, respectively. Surface current measurements (at 2m depth) were taken from five TABS sites: A, B, C, D and F (Figure 3.1). All current meters and wind velocity stations are located near or over the inner-shelf.

Daily surface current and wind velocities from 1 April 1995 through 1 April 1998 were used in this study. The original data consists of hourly winds and half-hourly currents, downloaded from the TABS web site. A 71h low-pass filter (Thompson, 1983) has been applied to the wind and current data to remove the tidal and inertial currents. The daily winds and currents are then produced by sampling the low-passed data at the middle of each day. The results are shown in Figure 3.2a and Figure 3.2b. We interpolate across data gaps shorter than 3 days in the daily time series. Larger gaps at wind stations SRST2 and PTAT2 are filled with data from the other, since the spatial scale of the wind is large enough to include both stations (Nowlin et al., 1998) and the amount of filled data constitutes less than 5% of the total amount of data (Figures 3.2a and 3.2b). Minor errors introduced by this data substitution do not influence the results in this paper. After the preprocessing there is only one gap in wind data in the record of station 42035 but still several gaps in the currents. Continuous data segments shorter than 60 days are not used in this study.

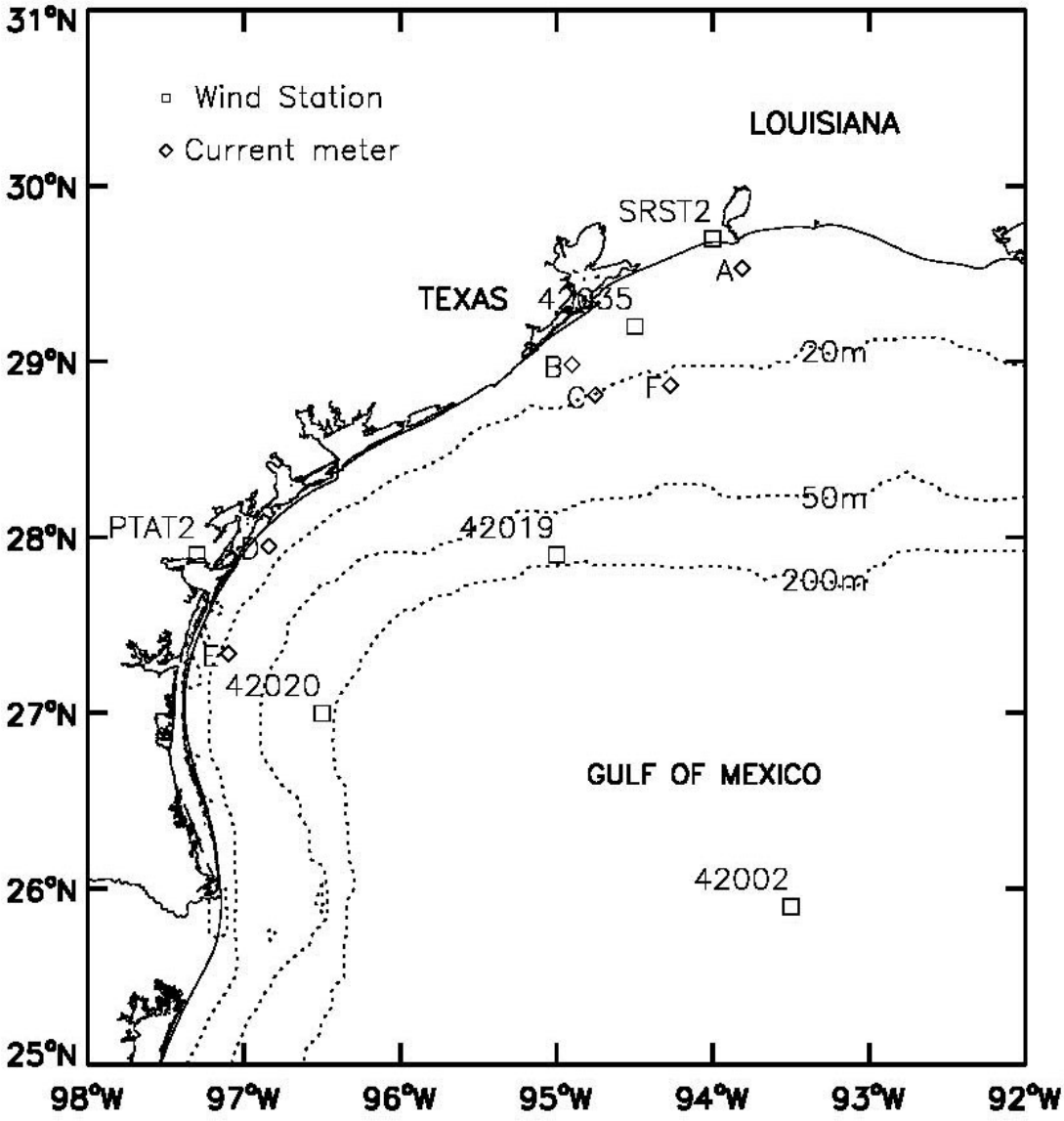

Figure 3.1 TABS current-meter mooring and NDBC/CMAN buoy sites over the Texas-Louisiana inner shelf.

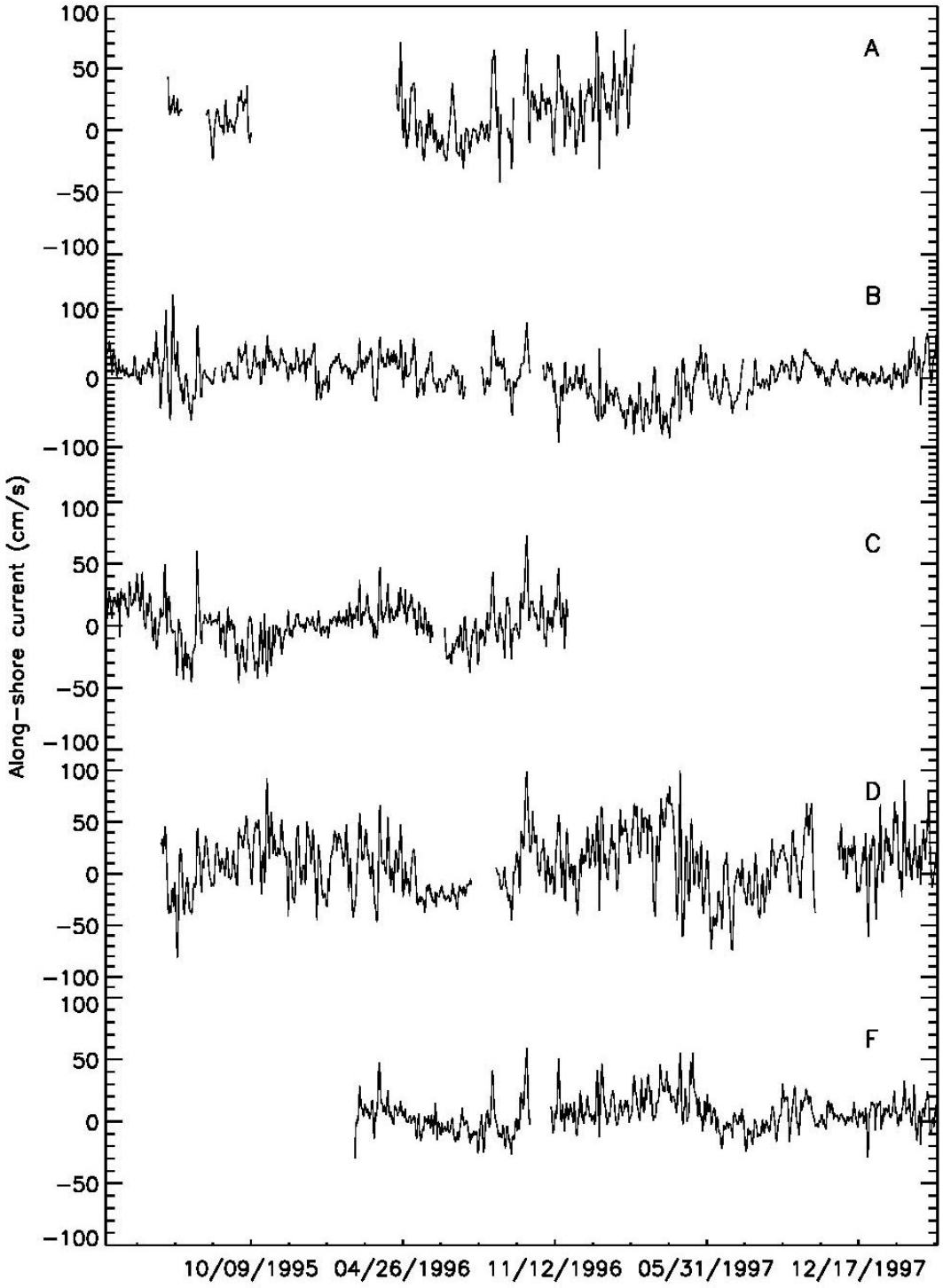

Figure 3.2a Time series of low-passed daily alongshore currents.

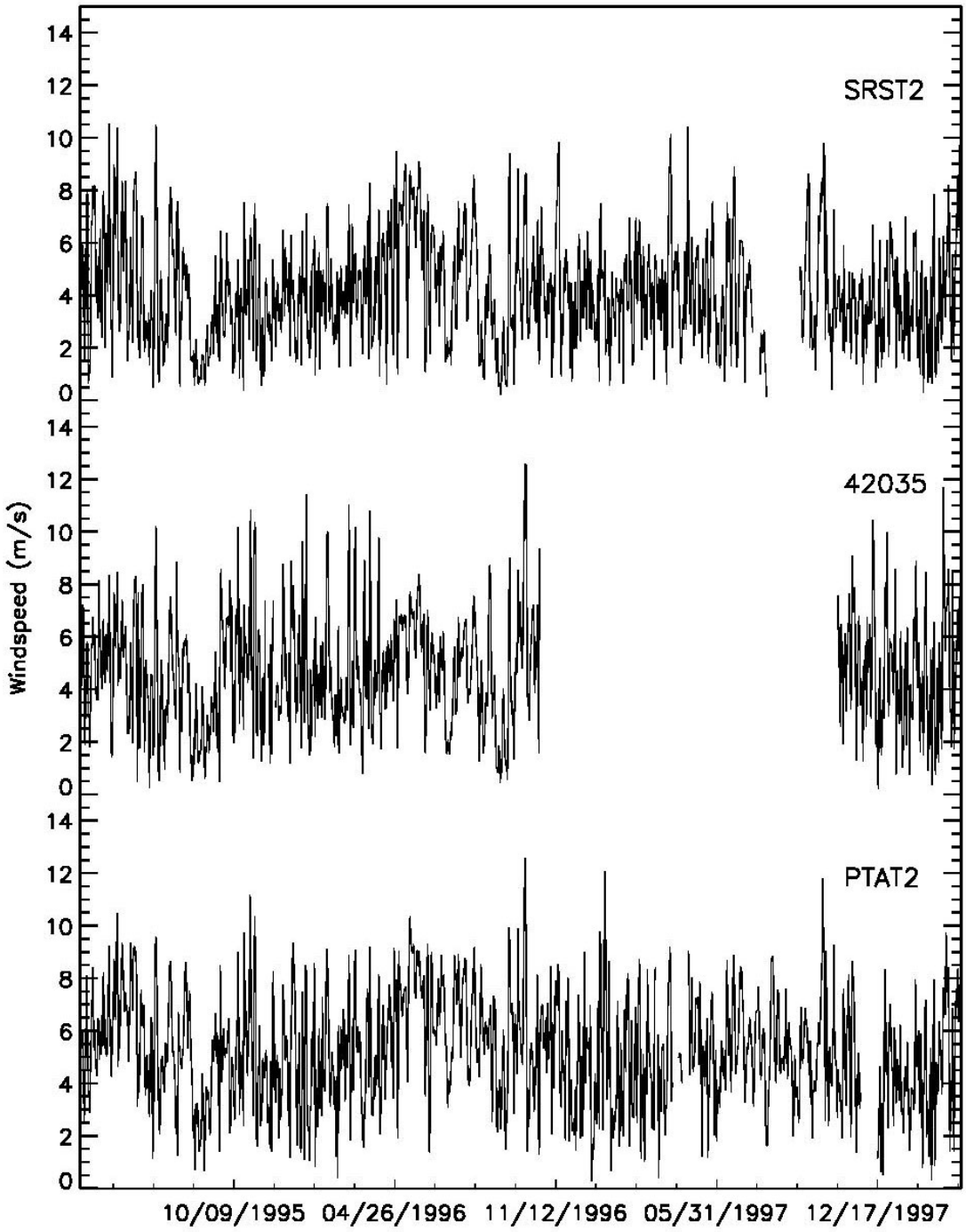

Figure 3.2b Time series of low-passed daily wind speeds.

Local alongshore and cross-shore coordinate systems are defined as follows: the *x* axis is parallel to the local coastline or isobath and the y axis is directed offshore, thus the positive x axis is directed down-coast from Louisiana to Texas. This local coordinate system is applied to both the winds and the currents. For currents at A, B and F, winds at SRST2 are assumed to be "local winds" and 42035 winds for currents at C and PTAT2 winds for currents at D.

3.2 SUB-TIDAL INNER-SHELF FLOW VARIABILTY

3.2.1 Monthly Mean Currents

3.2.1.1 Alongshore Current

The 31-day running average of the low-passed alongshore winds and currents is shown in Figure 3.3. Substantial spatial variability is observed. Alongshore flow at D is always in phase with the alongshore wind. At stations A, B and C, an upcoast wind is associated with downcoast currents in April, May and even June in some years. Monthly mean upcoast flow commences 2-3 months later than the upcoast wind. This is likely caused by the downcoast pressure gradient force related to a suggested geopotential high at 93.5°W and the discharge from the Mississippi-Atchafalaya River system. The south-southeasterly wind during this season combines with the curvature of the coastline to cause an alongshore wind stress convergence, as pointed out by Cochrane and Kelly (1986). The convergence of the alongshore wind stress leads to a convergence of the alongshore wind driven flow and, consequently, the development of a geopotential high. The upcoast wind must overcome the downcoast pressure gradient force before upcoast flow can occur.

Downcoast flow commences, in the records, around late August or the beginning of September, in phase with the downcoast wind. The downcoast wind and flow are in phase until mid-March or April when alongshore winds begin to change direction. For the monthly low-passed inner-shelf alongshore flow at A, 46% of its variance can be explained by the alongshore wind forcing; this value is 79% at D and 38% at F.

There are extended periods when the alongshore flow is out of phase with the alongshore wind, such as autumn 1995 at C and mid-November 1996 until the end of May 1997 at B. During these periods, alongshore flow at other stations is still in phase with the alongshore wind. This suggests a local circulation around A, B, C and F during these times. It is very interesting that starting from mid-November 1996, alongshore flow at A, which is upstream of B, increases significantly. This is not due to the local wind forcing (Figure 3.3). The strong alongshore flow, however, can result in convergence in a coastal area with converging isobaths, such as around B and C, thus provoking local circulations. It is worthwhile to explore whether this alongshore flow at A could cause the flow at B moving in the opposite direction to the wind.

3.2.1.2 Cross-Shore Current

The 31-day running average of the low-passed alongshore winds and cross-shore currents are shown in Figure 3.4. In general the cross-shore flow is out of phase with the alongshore wind at

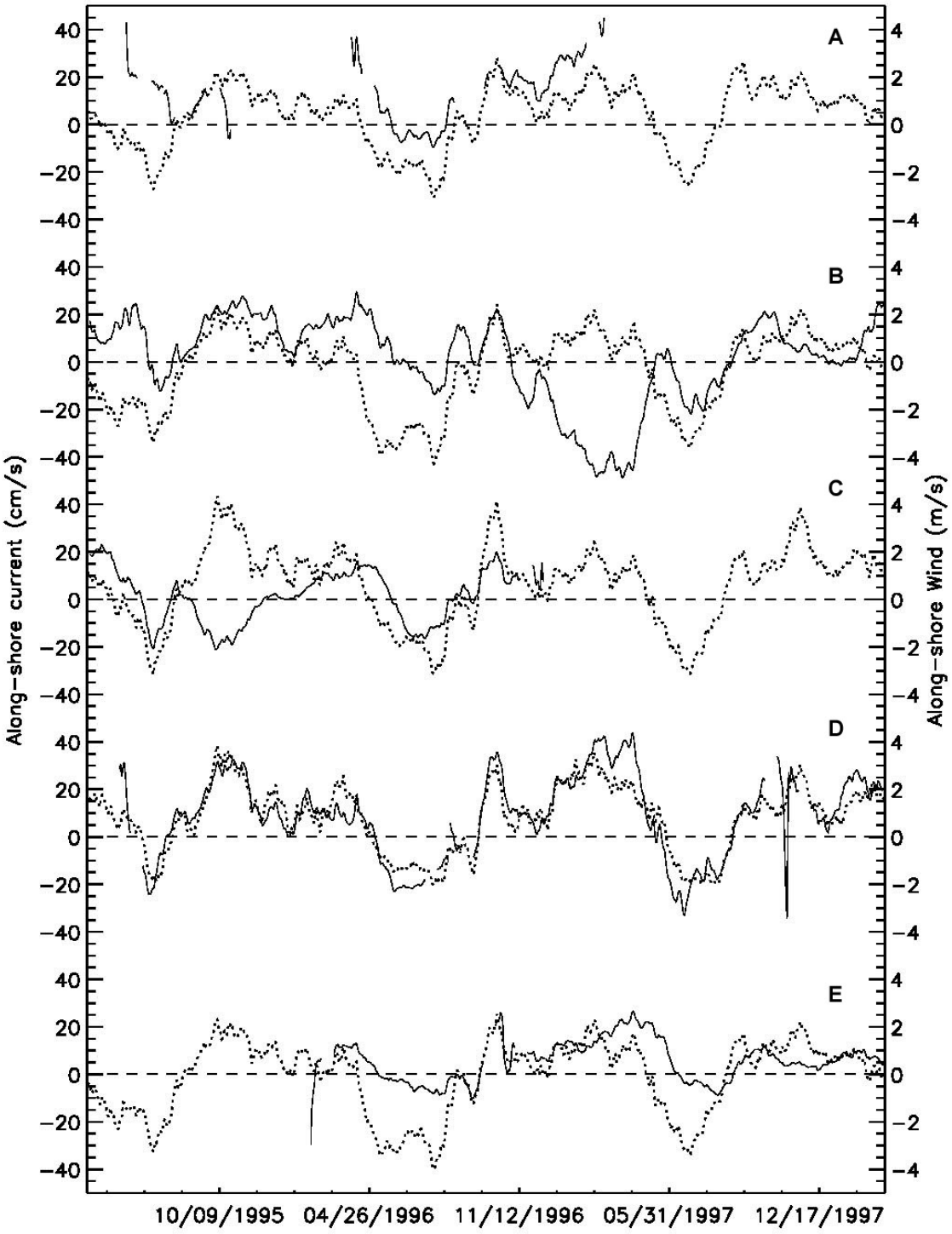

Figure 3.3 31-day running-average of the alongshore currents (solid line) and alongshore winds (dotted line).

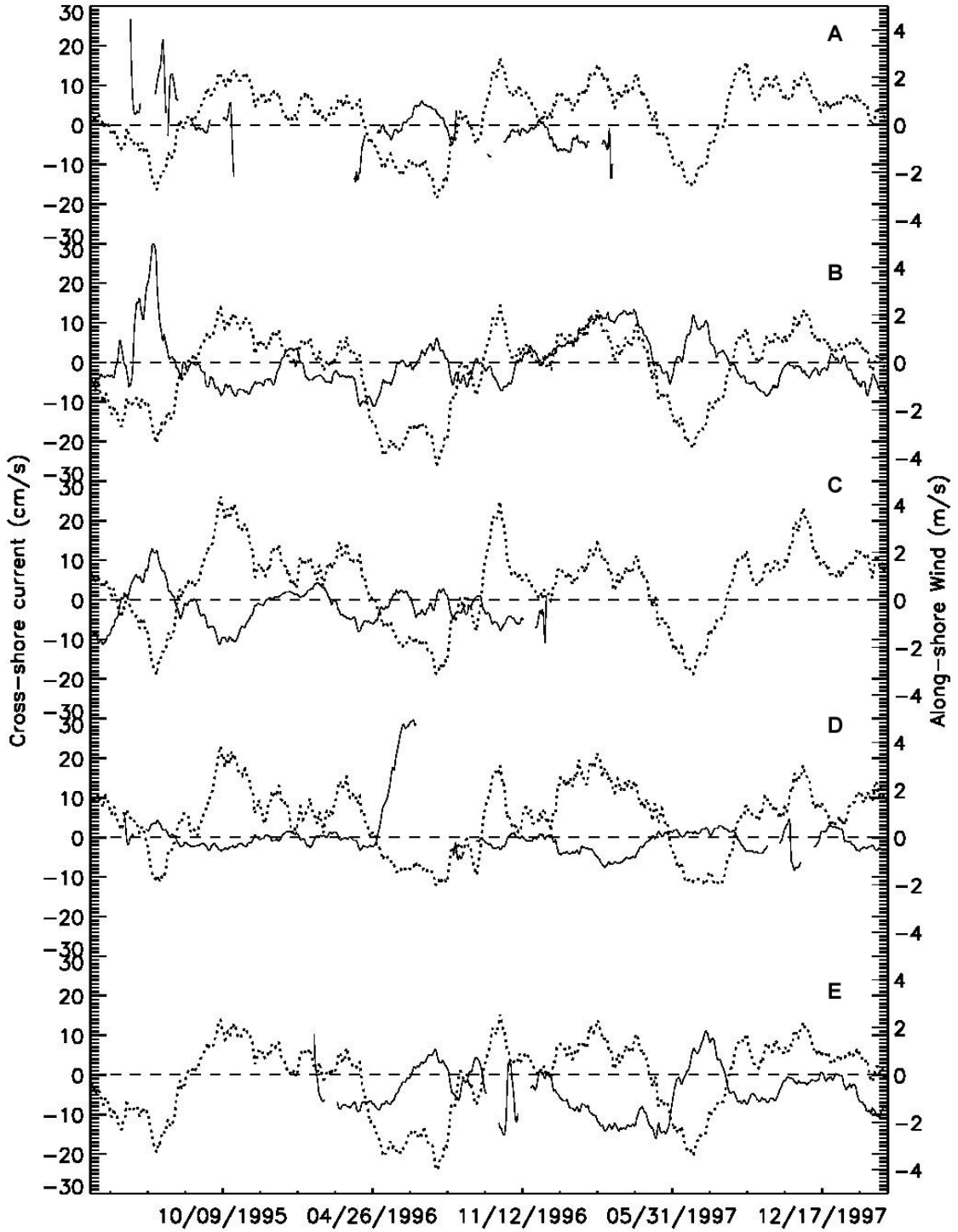

Figure 3.4 31-day running-average of the cross-shore currents (solid line) and alongshore winds (dotted line).

all stations, i.e., offshore flow from May to August and onshore flow from September to April. This is consistent with wind-forced upwelling and downwelling (Gill, 1982). During April-August, the cross-shore flow response to the upcoast wind is less than during the downcoast wind periods at B and F. The reason is that there exists an onshore component of the flow in balance with the downcoast pressure gradient force. This will be further discussed in Chapter 3.3.

3.3 WIND-CURRENT COHERENCE ANALYSIS

3.3.1 Alongshore Wind-Current Correlation

3.3.1.1 Dominant Correlation Patterns

Bimonthly linear correlation coefficients are estimated at each station between the low-passed alongshore winds and alongshore currents (Figure 3.5). The 95% significance level is also shown. The number of equivalent degrees of freedom is 29. The dominant feature in Figure 3.5 is the difference between winter and summer correlation patterns. Downcoast currents driven by downcoast winds characterize the winter pattern. The winds and flow are positively correlated. While this pattern is mainly found in winter, it sometimes occurs in spring and autumn. The summer pattern is characterized by upcoast flow driven by an upcoast wind, again resulting in positive correlation. It is apparent, in Figure 3.5, that the correlation during summer is weaker than during the winter at most stations. This is partly due to the effects of strong stratification. This is consistent with previous findings (Nowlin et al., 1998). The pattern is strongest at station D and weakest at B. No significant correlation is found from October 1997 until April 1998 at B (Figure 3.5).

3.3.1.2 Transient Correlation Patterns

In addition to the two principle patterns some new features have been found. One is a transition correlation pattern, which is characterized by mean upcoast winds together with mean downcoast currents (Figure 3.3). The alongshore winds and currents are positively correlated, which means that the downcoast wind variations always strengthen the downcoast flow variations. This pattern, mainly found during the transient months between winter and summer, i.e., April, May and August, suggests a non-locally wind-driven downcoast mean flow over the inner shelf. The downcoast flow is consistent with a geopotential high around 93.5°W, related to the alongshore wind stress convergence and associated flow convergence, as suggested in Chapter 3.2. The transition pattern is found at A, B, C, and F, but not D. This suggests that the hypothesized non-locally wind-driven downcoast flow does not extend to the down-stream area around station D.

3.3.1.3 Negative Correlation Patterns

Another feature is the occasional occurrence of negative correlations at B, C, and D. The alongshore winds are negatively correlated with the alongshore currents from November 1996 thru May 1997 at B, September 1995 thru November 1995 at C, and June 1996 thru July 1996 at

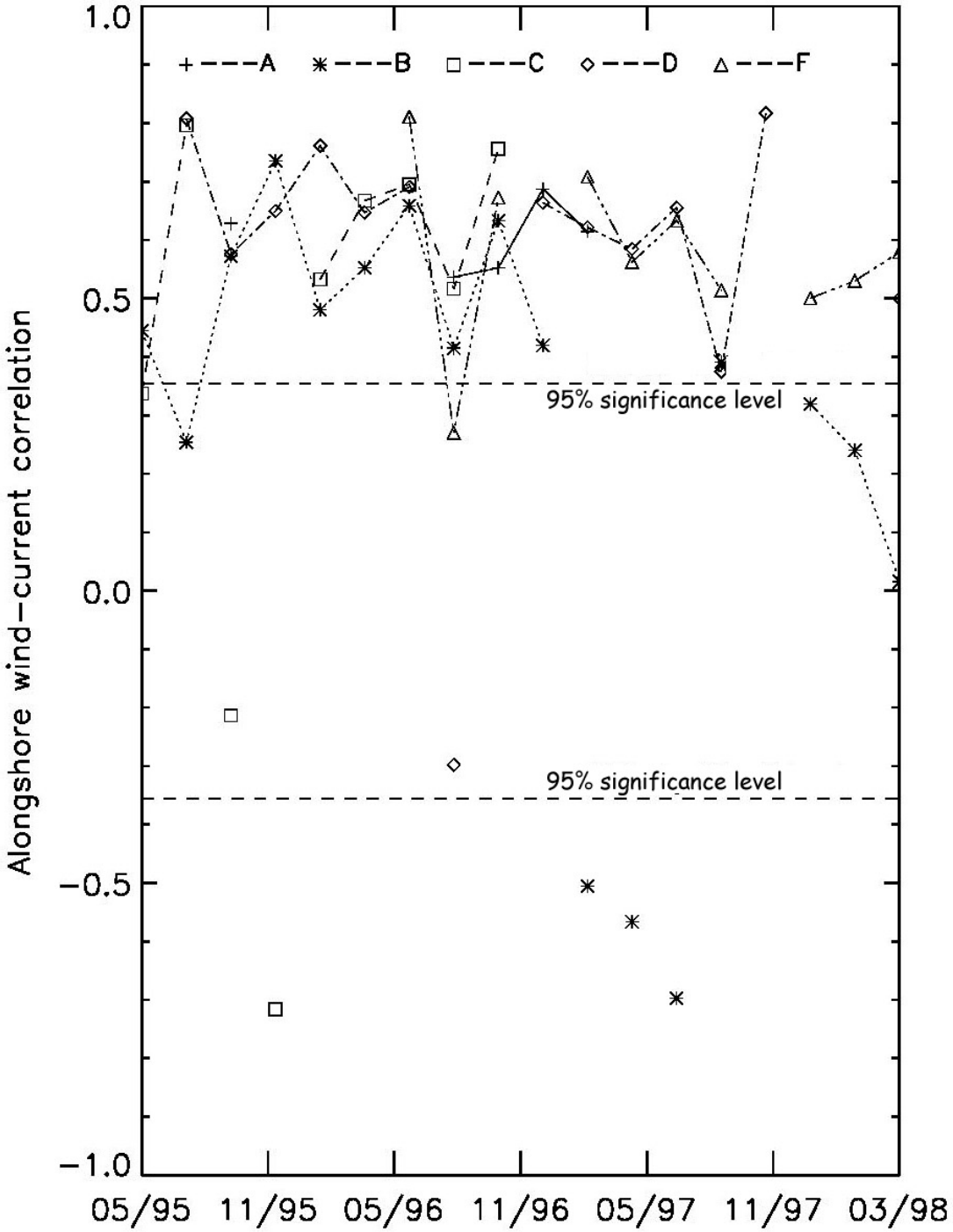

Figure 3.5 Bimonthly correlation coefficients between alongshore winds and alongshore currents for five current meter stations.

D. The time scale of the negative correlation varies from 1 month at D to 6 months at B. The correlation coefficients are -0.57, -0.71 and -0.56 at B, C and D, respectively. The correlations are significant at a level of 99.9% at B and C, and at 95% at D. Negative correlation is only found locally; other stations still exhibit normal positive correlation. At B and C, the alongshore flow moves in the opposite direction to the wind, i.e., the stronger the downcoast wind, the stronger the upcoast flow. A local circulation around A, C, F and B is suggested during the negative correlation periods. A possible forcing mechanism has been discussed above. At D, the stronger upcoast flow is related to a weaker upcoast wind, which is contrary to a local wind forcing mechanism. Isolation of the cause of this response is not possible given the present limited data coverage.

3.4 ALONGSHORE WIND – CROSS-SHORE CURRENT CORRELATION

Significant correlation is found between the alongshore winds and cross-shore currents at all stations. This is in contrast with Nowlin et al. (1998), who found no significant coherence between the alongshore winds and cross-shore currents in the weather band. Figure 3.6 shows the bimonthly correlation coefficients for the current stations. The correlations shown in Figure 3.6 are even greater than that between the alongshore wind and current (Figure 3.3) during some periods. For example, at B, the correlation between alongshore wind and cross-shore current is significant from October 1997 through April 1998, though the alongshore wind-current correlation is not.

3.4.1 Dominant Correlation Patterns

Similar to the correlations between alongshore wind and alongshore current, winter and summer patterns are identified as two distinct principal correlation patterns. The former is characterized by downcoast winds and onshore currents and the latter by upcoast winds and offshore currents (Figure 3.4). The alongshore winds and cross-shore currents are negatively correlated, which means that the downcoast winds always strengthen the onshore currents and upcoast winds strengthen the offshore currents, consistent with wind-forced down/upwelling near shore (Gill, 1982). The winter pattern prevails in non-summer months and the summer pattern prevails only in the summer months (June - July).

3.4.2 Transition Correlation Patterns

In the transition months between the winter and the summer, the correlation is still negative but mean cross-shore currents are onshore while mean winds are upcoast. This pattern is particularly clear at B during April, May, August and September. This is because the negative alongshore wind stress has to overcome the alongshore pressure gradient force associated with the hypothesized geopotential high near 93.5°W and the buoyancy-driven flow from the Mississippi-Atchafalaya River system before generating the offshore flow.

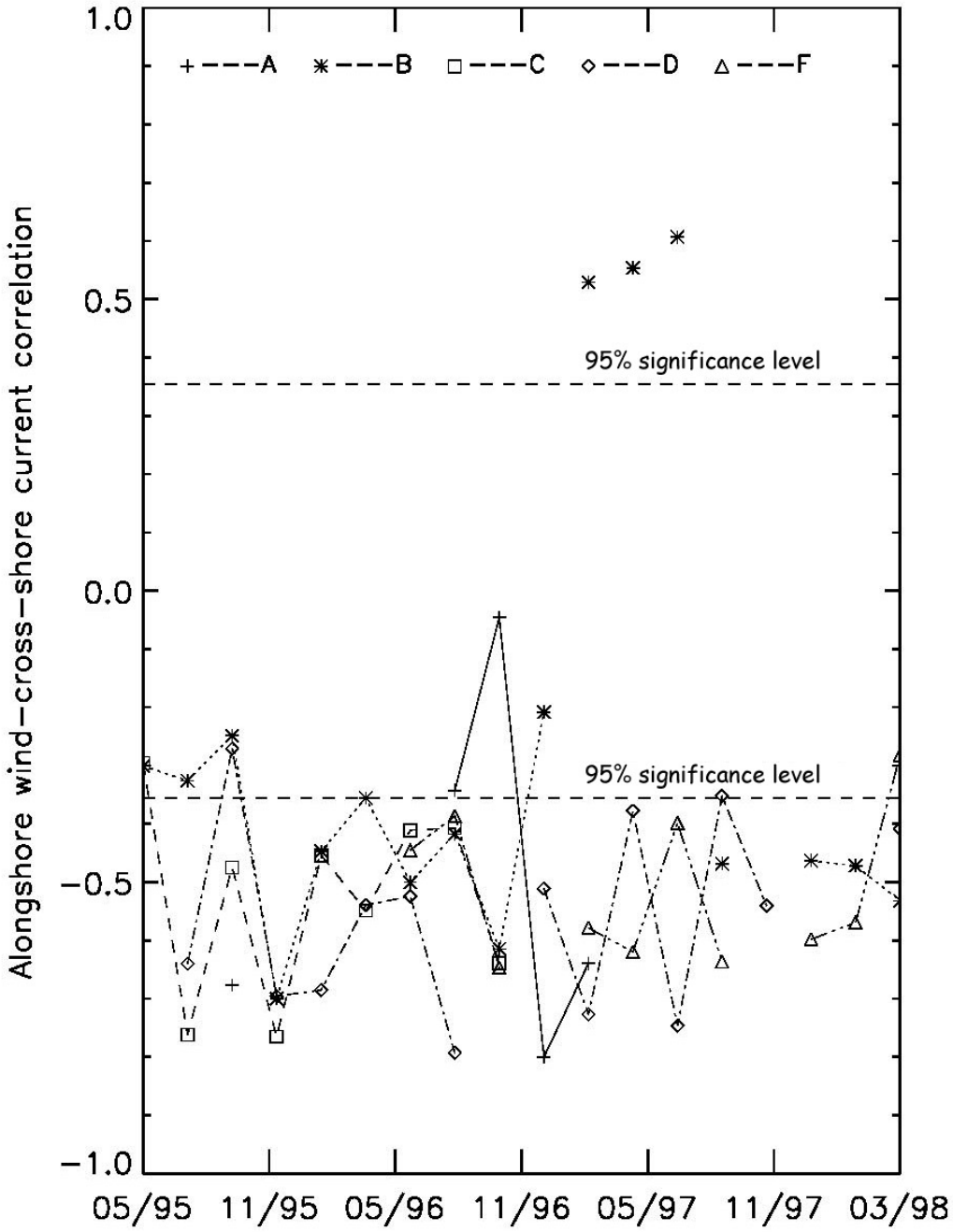

Figure 3.6 Same as in Figure 3.5 but for alongshore winds and cross-shore currents.

3.4.3 Positive Correlation Patterns

Positive correlation between the alongshore winds and cross-shore currents is found at B during the same period as the negative correlation between alongshore wind and alongshore current. This means that downcoast winds always strengthen the offshore currents at B, in contrast to a local wind forcing mechanism. The possible reason for this has been discussed in Chapter 3.2.

3.5 COHERENCE STUDY

The wind-current relationship can also be studied in the frequency domain. Coherence squared estimates between alongshore wind and alongshore and cross-shelf flow are estimated for summer (June-August), winter (October-March) and transition seasons (April, May, August and September). A block-averaging method (Emery and Thompson, 1997) is used. For a given station, the current time-series is first divided into 3 categories, i.e., summer, winter and transition. Then the data in each category are divided into several blocks, with 90-day data blocks for the winter and the summer and 60-day blocks for the transient season. Up to 50% data overlap is applied to some winter and summer data. The coherence squared is estimated by using averaged covariance spectra and energy density spectra of the two components. A Hanning window is applied in the computation. The 95% significance level for the coherence-squared estimates is calculated as:

$$\gamma = 1 - \alpha^{[1/(EDOF - 1]}$$

where $\alpha = 0.05$ and EDOF is the equivalent degrees of freedom, determined by the number of blocks and the method of spectrum smoothing (Emery and Thompson, 1997). In the calculation, the periods of negative correlation between alongshore wind and current (Chapter 3.3.1.3) were not used.

Figure 3.7 shows examples of the block-averaged coherence squared between alongshore wind and alongshore currents in summer, winter and the transition season at B and D. Figure 3.8 shows the same but for alongshore wind stress and cross-shore currents. Since a 71-h low-pass filter has been used to produce daily time series, the coherence analysis should only focus on the time scale longer than 3 days. Considering that the current response time scale to alongshore winds is less than one day, the coherence phases are not shown here.

3.6 COHERENCE BETWEEN ALONGSHORE WINDS AND ALONGSHORE CURRENTS

During winter (Figure 3.7), significant coherence between alongshore winds and alongshore currents is found in all bands between 3 and 30 days for D and F. At A, B and C, however, the bands of significant coherence are gappy. The coherence is only significant in the 6-20 day band at A, the 4-7 and 13-30 day bands at B, and the 4-7 and 9-30 day bands at C. The peak coherence is around 5-6 days and 10 days, i.e. within the weather band. A common feature, though, is that

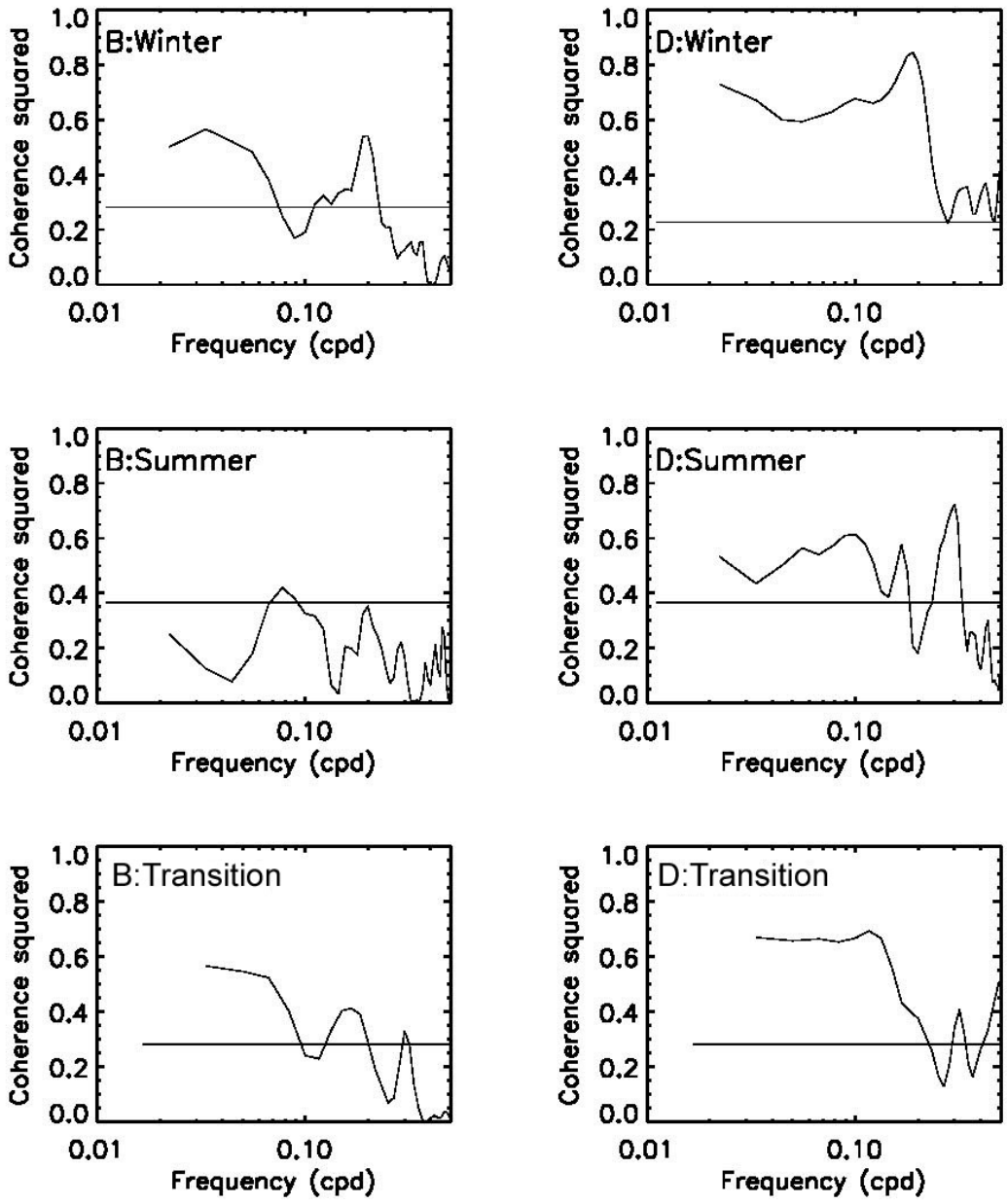

Figure 3.7 Block-averaged coherence-squared between alongshore flow and alongshore winds in different seasons at B and D. The solid line is the 95% significance level.

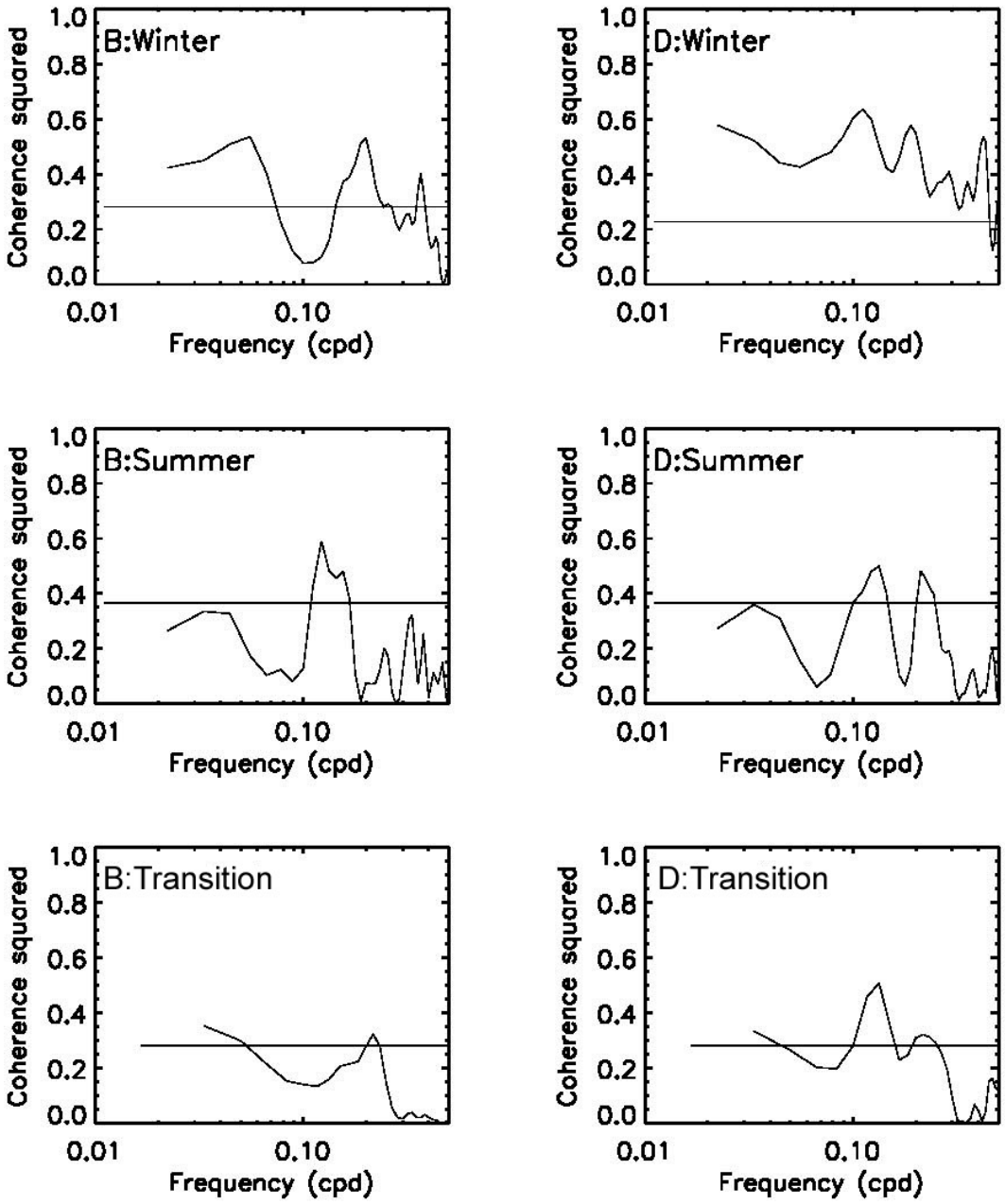

Figure 3.8 Same as in Figure 3.7 except for alongshore winds and cross-shore currents.

the significant coherence extends outside the weather band to low frequency. In summer, the coherence decreases and significant coherence bands become narrow and lower at all stations except C. Significant coherence is found in the 4-9 day band at A, the 6-9 day band at B, the 4-5 day and 6-13 day bands at C, the 4-5 and 8-10 day bands at D, and the 4 day and 7-9 day bands at F. Coherence peaks are found around 4 days and 9 days at most stations. The coherence in the transition season is also weaker than in the winter. In this season, station F exhibits the strongest coherence, which is significant in all bands longer than 3 days. Significant coherence is also found in the 3-10 day band at C, the 4-10 day band at D, around 5 days at A and B, and at periods longer than 12 days at A.

3.7 COHERENCE BETWEEN ALONGSHORE WINDS AND CROSS-SHORE CURRENTS

Significant coherence between alongshore winds and cross-shore currents in winter (Figure 3.8) occurs in all bands longer than 3 days at station D, in the 5-20 day band at A, the 4-9 and 13-30 day bands at B, the 4 and 9 day bands at C, and the 3-11 day band at F. In summer, the coherence varies greatly with location. At D, all bands except near five-day periods exhibit significant coherence. At B no significant coherence is found except for a narrow band around 12 day periods. At C, significant coherence occurs at periods longer than 10 days, and at F at periods of 8-14 days. Reduced gravity wave theory in a two-layer stratified ocean (Gill, 1982) predicts that cross-shore flow induced by alongshore winds is related to distance from the coastline and the stratification. The space-dependent coherence between alongshore winds and cross-shore flow over the Texas-Louisiana inner shelf should be related to the local stratification, which is very complicated (Wiseman, et al., 1997) and beyond the scope of this work.

3.8 SPATIAL COHERENCE OF CURRENTS

One way to isolate possible coastal trapped wave signals and other kinds of alongshore propagating signals is to have recourse to the spatial coherence of the alongshore flow. We chose to compare stations B and D. These stations have the longest time series and both are located along the 18m isobath. Figure 3.9 presents the coherence squared and phase estimates between alongshore flow at B and D. In winter, alongshore flow at B is highly coherent with the alongshore flow at D at periods longer than 4.5 days. The phase relationship shows that alongshore flow at D leads that at B. The lead is about 1.3 days at the coherence peak near 30 days and about zero at the other peak near 7 days. The in-phase coherence at seven days is caused by large scale wind forcing, but an upcoast propagation with a scale of 30 days is hard to explain. The phase relationship is contrary to that predicted by coastal-trapped wave theory.

There are two coherence peaks in summer. One, near 10-day periods, exhibits an in-phase relationship and the other, very weak, peak occurs near 4.3 days, where alongshore flow at B leads that at D by about 50°, i.e., 14 hours. Again, the in-phase relationship at 10 days is caused by the large scale wind forcing. The downcoast propagation at 4.3 day periods has a phase speed of 3.7 m/s. This speed is similar to that of the first mode of a wind-forced barotropic coastal trapped wave (Brink and Allen, 1978), which is about 4.3 m/s.

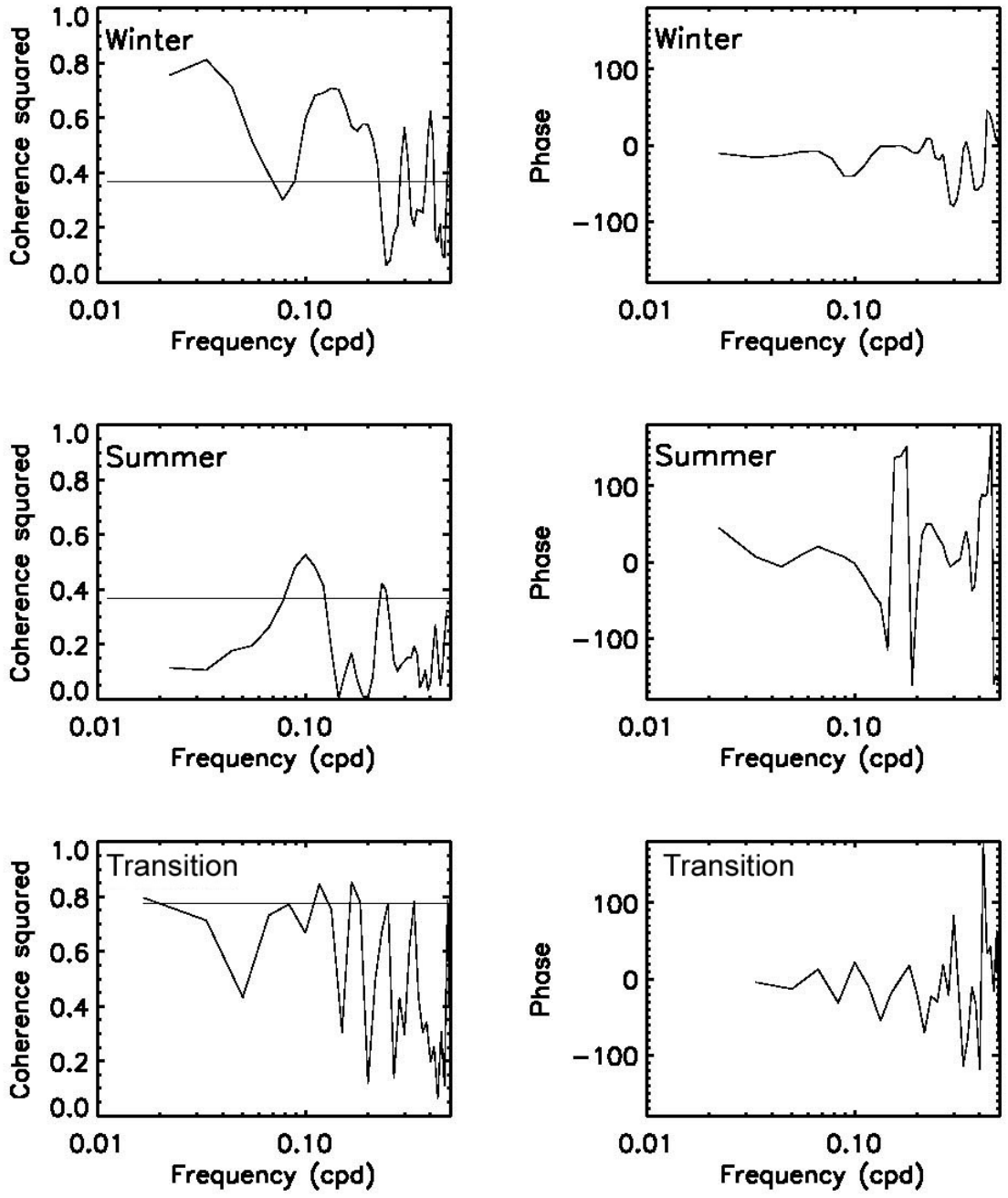

Figure 3.9 Coherence-squared and phase relationship of alongshore flow between B and D during the winter, summer and transition seasons, positive phase means B leads D. The solid line is the 95% significance level.

The coherence in the transition season also exhibits two weak peaks: one at about 8.5 days with D leading B by about 5.4 hours and the other at 5.5 days with B leading D by about 6.4 hours. The former is, again, difficult to explain as the phase propagation is opposite to long coastally trapped waves. The latter suggests a phase speed of 1.7 m/s, which is comparable to that of a second mode wind-forced barotropic coastal-trapped wave (Brink and Allen, 1978). As with the summer coherence peak near 4.3 day periods, the significance of these coherence peaks is small. Longer records will be required to establish the existence of important propagating signals in this highly frictional environment. It should be noted, though, that Current (1996) successfully modeled a significant percentage of the inner shelf low-frequency flow using a wind-driven coastal trapped wave model.

3.9 CONCLUSIONS AND DISCUSSIONS

TABS buoy data obtained from April 1995 to March 1998 have been used to verify previous findings and explore new features of the subtidal circulation over the Texas-Louisiana inner-shelf and its response to wind forcing. General winter and summer coherence/correlation patterns are consistent with prior conclusions. From September to March, downcoast wind and downcoast flow prevail. These are positively correlated. During summer, upcoast wind and flow prevail. They are also positively correlated. In the upstream area near the Texas-Louisiana border, about 42% of the monthly alongshore flow variance can be explained by the alongshore wind forcing, but 79% at station D further south. In general, correlation between the two signals is weaker in summer than that in winter.

Some additional points have been suggested. During the upcoast wind period, i.e., April-August, the upcoast flow starts rather late (July) near the Texas-Louisiana border. We suggest that this is because the upcoast wind must overcome a downcoast pressure gradient force related to riverine discharge in Louisiana waters and a suggested geopotential high near 93.5°W. The high is mainly caused by the alongshore wind-driven convergence due to the curvature of the coastline. Alongshore flow at station D further south, however, is in-phase with the upcoast wind. Significant negative correlation is observed, during some periods, between the alongshore wind and current, implying flow variations moving in opposition to the wind variations. These correlations are local. The case at station B is of particular interest because positive correlation is found between the alongshore wind and cross-shore current during the same period and because of the extended duration of the event. This suggests a local circulation near station B. Simultaneous, strong alongshore flow at A, interacting with converging isobaths, can cause convergence and enhancement of the suggested local geopotential high , which drives a local circulation.

Significant negative correlation exists between alongshore wind and cross-shore flow, consistent with wind-induced upwelling/downwelling theory (Gill, 1982). The spatial variation of this correlation is large in the summer and transition seasons, suggesting the importance of local stratification.

Alongshore spatial coherence was analyzed to investigate the alongshore propagation of the coastal waves. Three kinds of coherence/phase relations were found. One is an in-phase relationship at 7 day periods in winter and 10 day periods in summer, resulting from the alongshore flow response to large scale alongshore wind forcing. The second is an apparent upcoast propagation near 30-day periods in winter and 8.5-day periods in the transition season. The reason for the apparent upcoast propagation is not clear. The third is downcoast propagation near 4.3 day periods in summer and 5.5 day periods during the transition season. The coherence is barely significant at the 95% level and further analysis has not been pursued, although it is noted that the inferred phase speeds are consistent with barotropic coastal trapped wave theory (Brink and Allen, 1978).

For the alongshore wind and alongshore flow, significant coherence occurred at most periods longer than 3 days in winter. The coherence peaks occurred near 5-6 days and 10 days. The coherence in summer and the transition seasons was lower and the bands of significant coherence became narrower. Coherence peaks occurred near 4 and 9 day periods in summer. The spatial variability of the coherence in summer was large.

Significant coherence was also found between the alongshore wind and the cross-shore flow in bands from 3-30 day periods at different stations. In winter, a 4-9 day band of significant coherence was common. In summer, more spatial variability of the coherence was found than in winter.

The results of these analyses, thus, indicate both significant spatial and temporal variability in the response of currents along the Texas-Louisiana inner shelf to wind forcing and the fact that a local, linear relationship between the two fields does not explain all the observed variability in the currents. The role of upstream river discharge and local flow convergence have been suggested as important contributors to this variability. The importance of local upwelling/downwelling was confirmed. Further advancement in understanding of the shelf flows in this complex environment awaits the acquisition of longer time-series and data from more focused process experiments.

Chapter 4

4.0 CONCLUSIONS

The efforts of the scientists at Texas A&M's Geochemical Environmental Research Group resulted in the deployment of a TABS buoy over the inner shelf of Louisiana and its maintenance from July 1998 to February 2000. Despite typical problems with biofouling and instrument failure, extended periods of quality controlled data recovery occurred and the data reported from this buoy through the TABS communication network were posted on the TABS web site in real time.

These data add to the growing database of inner shelf flows that are available for the study of pollutant transport along this important region of U.S. coastline. Furthermore, the ancillary data collected during the cruise of the *R/V Gyre* used to deploy the buoy also add to the data set. Texas A&M has a long history of modeling the circulation in the Gulf of Mexico and over its shelves, e.g. Lewis and Reid (1985). The spectral model developed by Current (1996) clearly demonstrates the skill that a model of inner shelf currents might produce in forecasting flows when upstream boundary conditions, such as could be produced by an array of current meter moorings reporting in real time are provided. The excellent results produced by this model were, though, confined to the barotropic flows. The strong stratification present over the LATEX shelf region during much of the year suggests the importance of fully three-dimensional effects. The initial modeling results presented at the end of Chapter 2 represent the first steps towards development of such a model, which would then be able to assimilate the real time data provided by observing arrays such as TABS.

The usefulness of such observing arrays for operational programs is already demonstrated and justifies the continued maintenance of the system by the Texas General Land Office. The usefulness of the data sets being collected and stored at Texas A&M for scientific studies is demonstrated by the analyses of historical TABS data presented in Chapter 3. These analyses have allowed:

- Confirmation of the findings of Nowlin et al. (1998) regarding the seasonal coherence relationships between local winds and currents.
- Identification of strong cross-shore flow patterns consistent with upwelling theory. (Previous studies had been unable to identify such strong signals because of the depths at which moored inner shelf current meters are typically deployed.)
- Identification of marginally significant signatures of longshore propagating flow features consistent with coastally-trapped wave theory (Brink and Allen, 1978).
- Development of the hypothesis that there exists a seasonal geopotential high near 93º W, forced by the convergence of wind-driven flows from the southwest and riverine-driven flows from the east, which is used to explain the very low-frequency patterns of flow.

When this effort was initially proposed, it was the intention that the results would be used to promote continued funding of an extended TABS array into coastal Louisiana waters. Since that time, the WAVCIS array of anemometers, pressure cells, and bottom-mounted acoustic Doppler current meters (http://wavcis.csi.lsu.edu/introd.html; Stone and Zhang, 2000) has been developed and planned expansions include western Louisiana waters. The full water column coverage available from this program, as well as the ability to obtain wave characteristics (the purpose for which it was originally designed), have convinced us that expansion of this array should be pursued for Louisiana waters. The data from the two systems, both of which report in real-time, can be easily coupled in any coastal ocean observing network and assimilated into developing models.

4.1 ACKNOWLEDGMENTS

This work was supported by the Minerals Management Service, U.S. Department of the Interior, under MMS agreement No. 14-12-0001-30660, Task Order 19943. Computer facilities and support were provided by the Center for Coastal Physical Oceanography, Old Dominion University. Data were kindly made available by the Geochemical and Environmental Research Group at Texas A&M University, College Station, TX.

REFERENCES

Brink, K.H. and J.S. Allen. 1978. On the effect of bottom friction on barotropic motion over the continental shelf. J. Phys. Oceanogr. 8:919-922.

Chao, S.-Y. and W. C. Boicourt. 1986. Onset of estuarine plumes. J. Phys. Oceanogr. 16:2137-2149.

Chaplin, G.F. and F.J. Kelly. 1995. Surface current measurement network using cellular telephone telemetry. Proceedings of the IEEE Fifth Working Conference on Current Measurement. Feb. 7-9, 1995, St. Petersburg, FL.

Cho, K., R.O. Reid, and W.D. Nowlin Jr. 1998. Objectively mapped stream function fields on the Texas-Louisiana shelf based on 32 months of moored current meter data. J. Geophys. Res. 103:10,377-10,390.

Cochrane, J.D. and F.J. Kelly. 1986. Low-frequency circulation on the Texas-Louisiana continental shelf. J. Geophys. Res. 91:10,645-10,659.

Chuang, W.S. and W.J. Wiseman, Jr. 1983. Coastal sea-level response to front passage on the Louisiana-Texas Shelf. J. Geophys. Res. 88: 2,615-2,620.

Current, C.L. 1996. Spectral model simulation of wind driven subinertial circulation on the inner Texas-Louisiana Shelf, Ph.D. Thesis, Tex. A&M University, College Station. 144 pp.

DiMego, G.J., L.F. Bosart, and G.W. Endersen. 1976. An examination of the frequency and mean conditions surrounding frontal incursions into the Gulf of Mexico and Caribbean Sea. Monthly Weather Review. 104:709-718.

Fernandez-Partegas, J. and C.N.K. Mooers. 1975. A synoptic study of winter cold fronts in Florida. Monthly Weather Review 103:742-744.

Dinnel, S.P. and W.J. Wiseman, Jr. 1986. Fresh water on the Louisiana and Texas shelf. Continental Shelf Res. 6:765-784.

Emery, W.J. and R.E. Thompson. 1997. Data analysis method in physical oceanography. New York: Elsevier Science Inc. 634 pp.

Freeland, H.J. and K.L. Denman. 1982. A topographically controlled upwelling contour of southern Vancouver Island. J. Mar. Res. 40:1069-1093.

Gill, A.E. 1982. Atmosphere-ocean dynamics, New York: Academic Press. 666 pp.

Howard, M.K. 1992. Flow over a shelf-submarine canyon system: A numerical study. Ph.D. dissertation, Texas A&M University, College Station, TX. 117 pp.

Huh, O.K., L.J. Rouse, Jr. and N.D. Walker. 1984. Cold air outbreaks over the northwest Florida continental shelf: Heat flux processes and hydrographic changes. J. Geophys. Res. 89:717-726.

Joyce, T.M. 1989. On in-situ 'calibration' of shipboard ADCPs. J. Atmos. Ocean. Tech., 6:169-172.

Kelly, F.J., N.L. Guinasso, Jr., L.L. Lee III, G.F. Chaplin, B.A. Magnell and R.D. Martin, Jr. 1998. Texas Automated Buoy System (TABS): A public resource. Proceedings of the Oceanology International 98 Exhibition and Conference, 10-13 March 1998, Brighton UK, Vol. 1. P. 103-112.

Klinck, J.M. 1988. The influence of a narrow transverse canyon on initially geostrophic flow. J. Geophys. Res. 93:509-515.

Lee, L.L., F.J. Kelly, and N.L. Guinasso, Jr. 1996. Armchair currents using TABS (Texas Automated Buoy System). EOS Trans. AGU, 76(3). (suppl.).

Lewis, J.K. and R.O. Reid. 1985. Local wind forcing of a sea at subinertial frequencies. J. Geophys. Res. 94:8163-8178.

Li, Y., W.D. Nowlin, Jr., and R.O. Reid. 1997. Mean hydrographic fields and their interannual variability over the Texas-Louisiana continental shelf in spring, summer, and fall, J. Geophys. Res. 102:1027-1049.

Lo, Y.-T. 1999. Modeling the buoyancy-driven flow due to river discharge on the Texas-Louisiana continental shelf of the Gulf of Mexico. Ph.D. Dissertation, Texas A&M University. 154 pp.

Magnell, B.A., F.J. Kelly, and R.A. Arthur. 1998. A new telemetering environmental buoy for offshore applications. Proceedings of the Oceanology International 98 Exhibition and Conference, 10-13 March 1998, Brighton UK, Vol. 1. P. 179-197.

Martin, R.A., F.J. Kelly, L.L. Lee III, and N.L. Guinasso, Jr. 1997. Texas Automated Buoy System: Real-time currents for oil spill response. Proceedings of the 1997 International Oil Spill Conference, April 7-10, 1997, Fort Lauderdale, FL.

Murphy, D.J., D.C. Biggs, and M.L. Cooke. 1992. Mounting and calibration of an acoustic Doppler current profiler. MTS Jour. 26(3):34-38.

Nowlin, W.D., Jr., A.E. Jochens, R.O.Reid, and S.F. DiMarco. 1998. Texas-Louisiana shelf circulation and transport processes study: Synthesis report. Volume I:Technical Report. U.S. Dept. of the Interior, Minerals Management Service, Gulf of Mexico Region, New Orleans, LA. OCS Study MMS 98-0035. 502 pp.

Oey, L.-Y. and G.L. Mellor. 1993. Subtidal variability of estuarine outflow, plume, and coastal current: A model study. J. Phys. Oceanogr. 13:1798-1808.

Oey, L.-Y. 1995. Eddy- and wind-forced shelf circulation. J. Geophys. Res. 100:8621-8637.

Stone, G.W. and X.P. Zhang. 2000. Wave-current online information system for oil spill contingency planning. Spill Science and Technology Bulletin.

Thompson, R.O.R.Y. 1983. Low-pass filters to suppress inertial and tidal frequencies. J. Phys. Oceanogr. 13:1077-1083.

Wang, W., W.D. Nowlin, Jr., and R.O. Reid. 1996. Analyzed surface meteorological fields over the northwestern Gulf of Mexico for 1992-1994: Mean, seasonal, and monthly patterns. Mon. Wea. Rev. 126:2864-2883.

Wang, W. 1996. Analysis of surface meteorological fields over the northwestern Gulf of Mexico and wind effects on the circulation over the LATEX shelf. Ph.D. dissertation, Texas A&M University, College Station, TX. 122 pp.

Wiseman, W.J., Jr. and F.J. Kelly. 1994. Salinity variability within the Louisiana Coastal Current during the 1982 flood season. Estuaries 17:732-739.

Wiseman W.J., N.N. Rabalais, R.E. Turner, S.P. Dinnel, and A. MacNaughton. 1997. Seasonal and interannual variability within the Louisiana coastal current: Stratification and hypoxia. J. Mar. Sys. 12:237-248.

Appendix A

Time Series Plots of Data Collected at TABS Buoy Site P

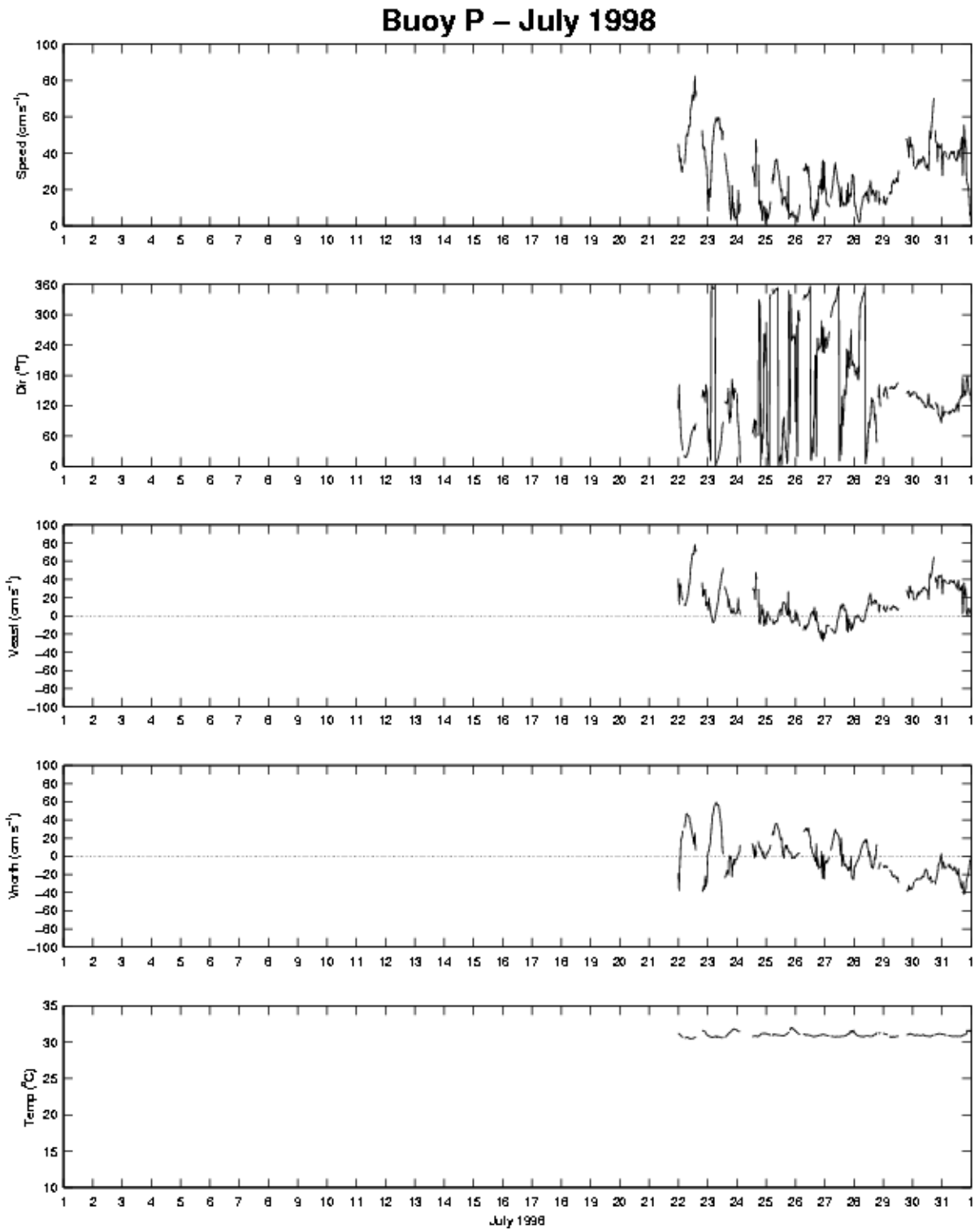

Figure A.1. Time series plot of Buoy P current velocity and water temperature collected during July 1998.

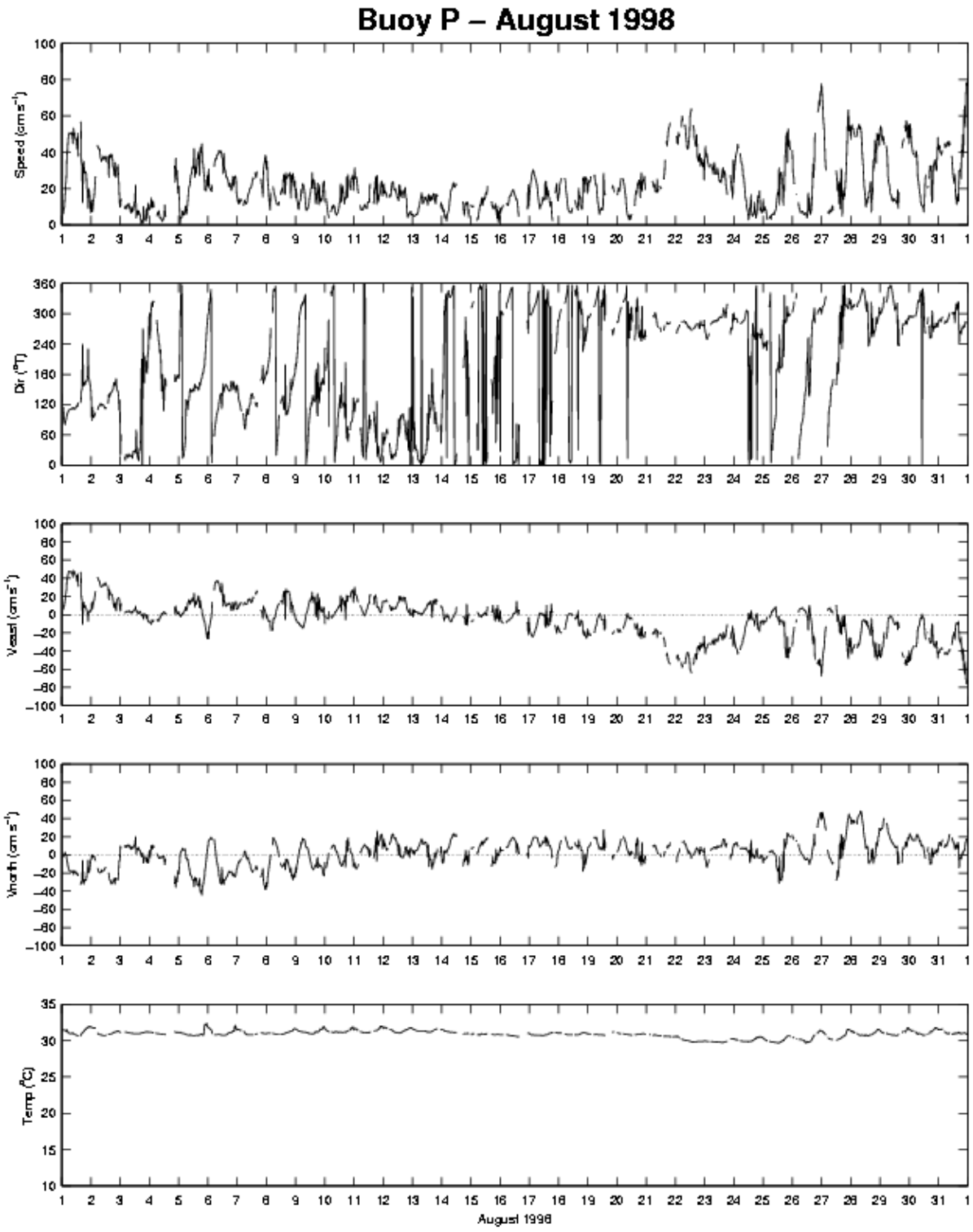

Figure A.2 Time series plot of Buoy P current velocity and water temperature collected during August 1998.

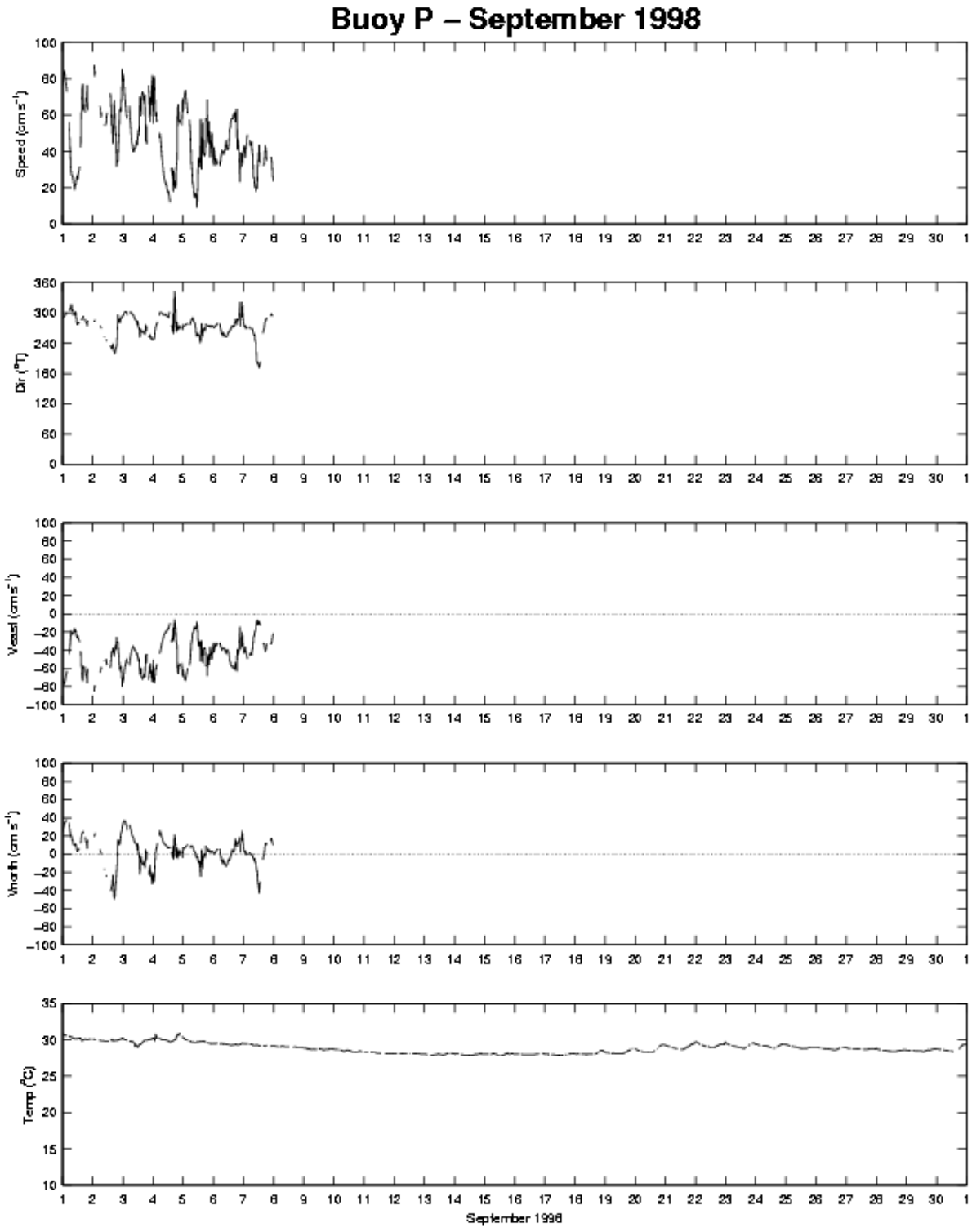

Figure A.3 Time series plot of Buoy P current velocity and water temperature collected during September 1998. Velocity data after 8 September 1998 are considered bad, though the temperature record is still reliable.

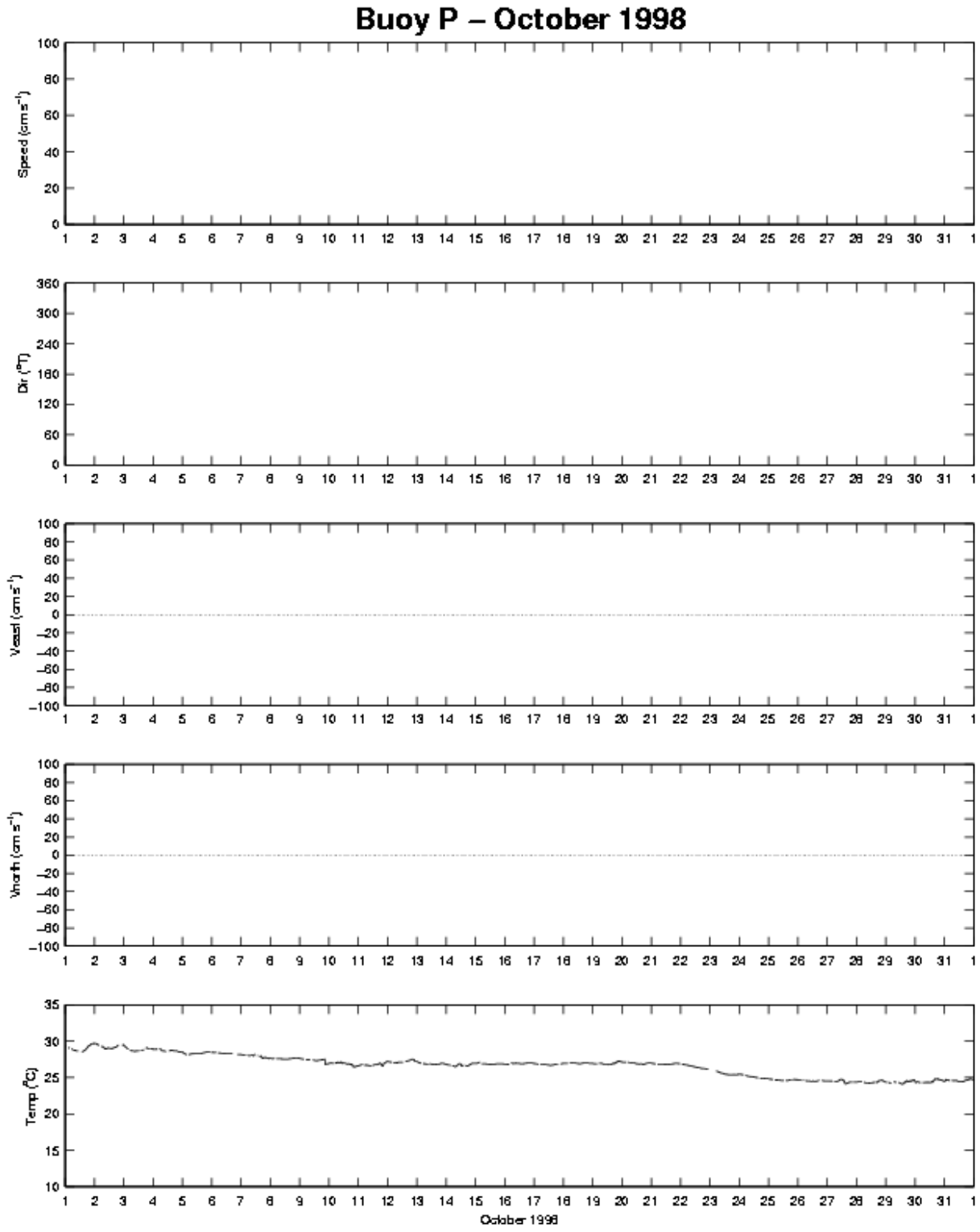

Figure A.4 Time series plot of Buoy P current velocity and water temperature collected during October 1998. Velocity data after 8 September 1998 are considered bad, though the temperature record is still reliable.

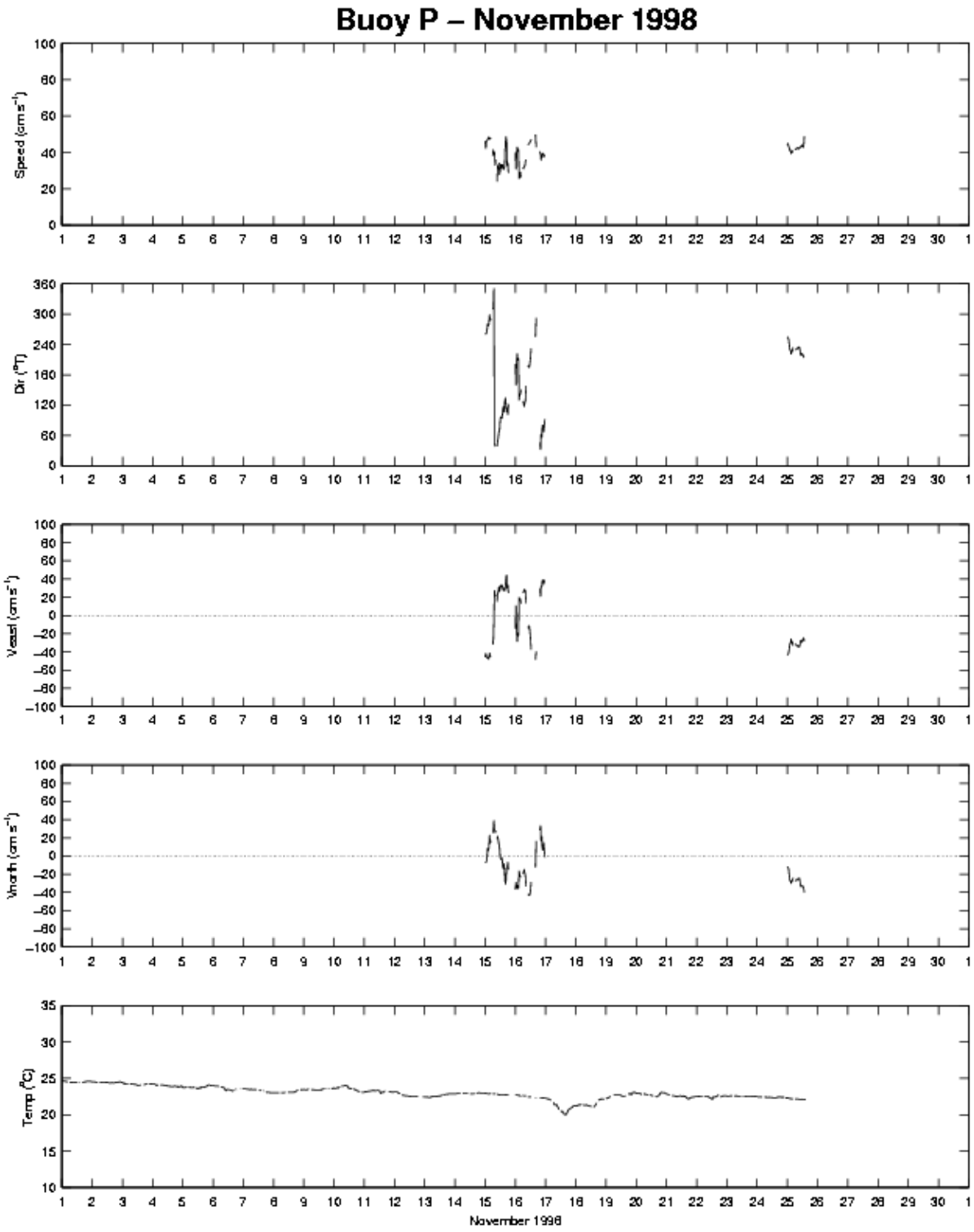

Figure A.5 Time series plot of current velocity and water temperature from Buoy P during November 1998. Except for brief periods, velocity data after 8 September 1998 are considered bad, though the temperature record is still reliable.

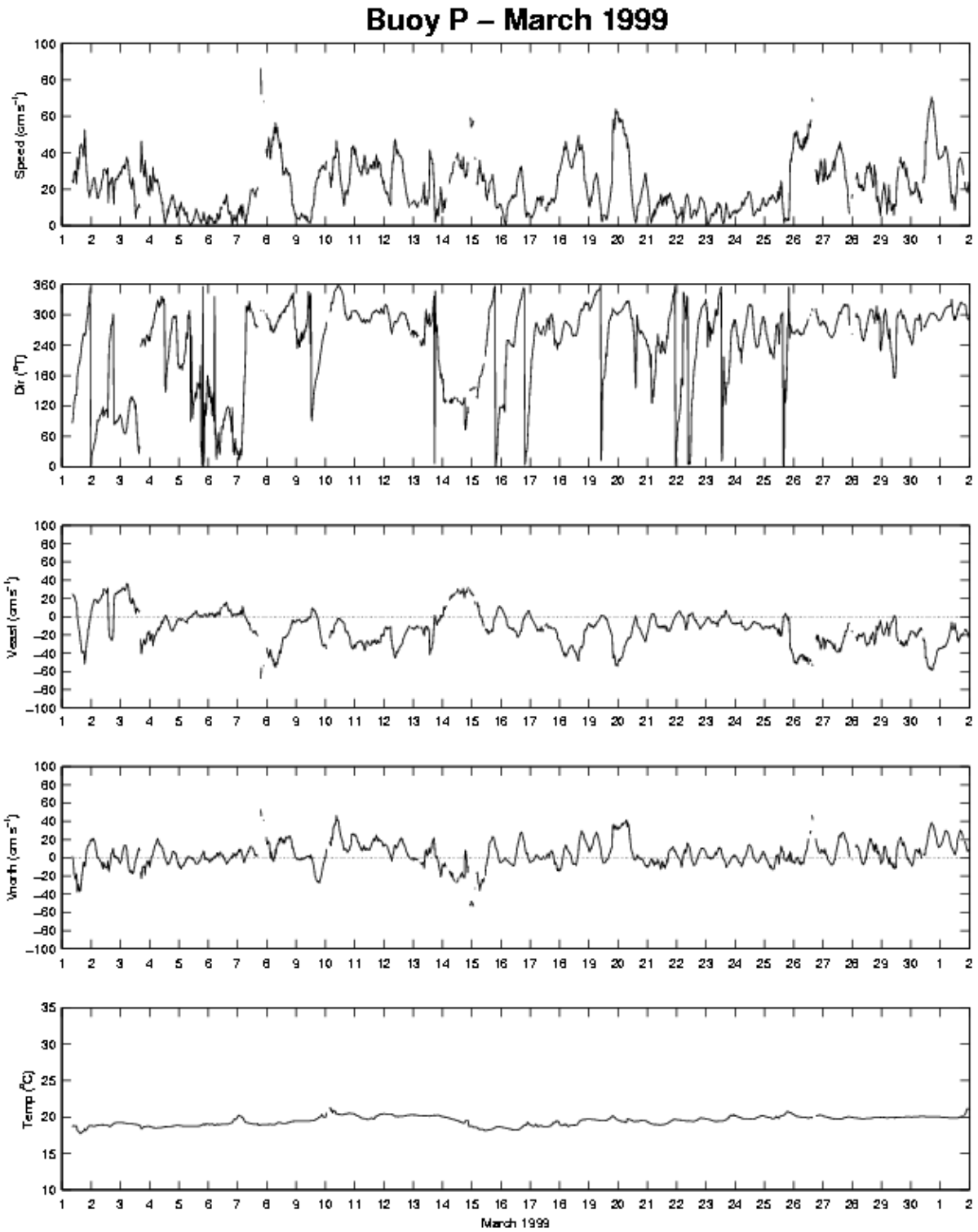

Figure A.6 Time series plot of current velocity and water temperature from Buoy P during March 1999.

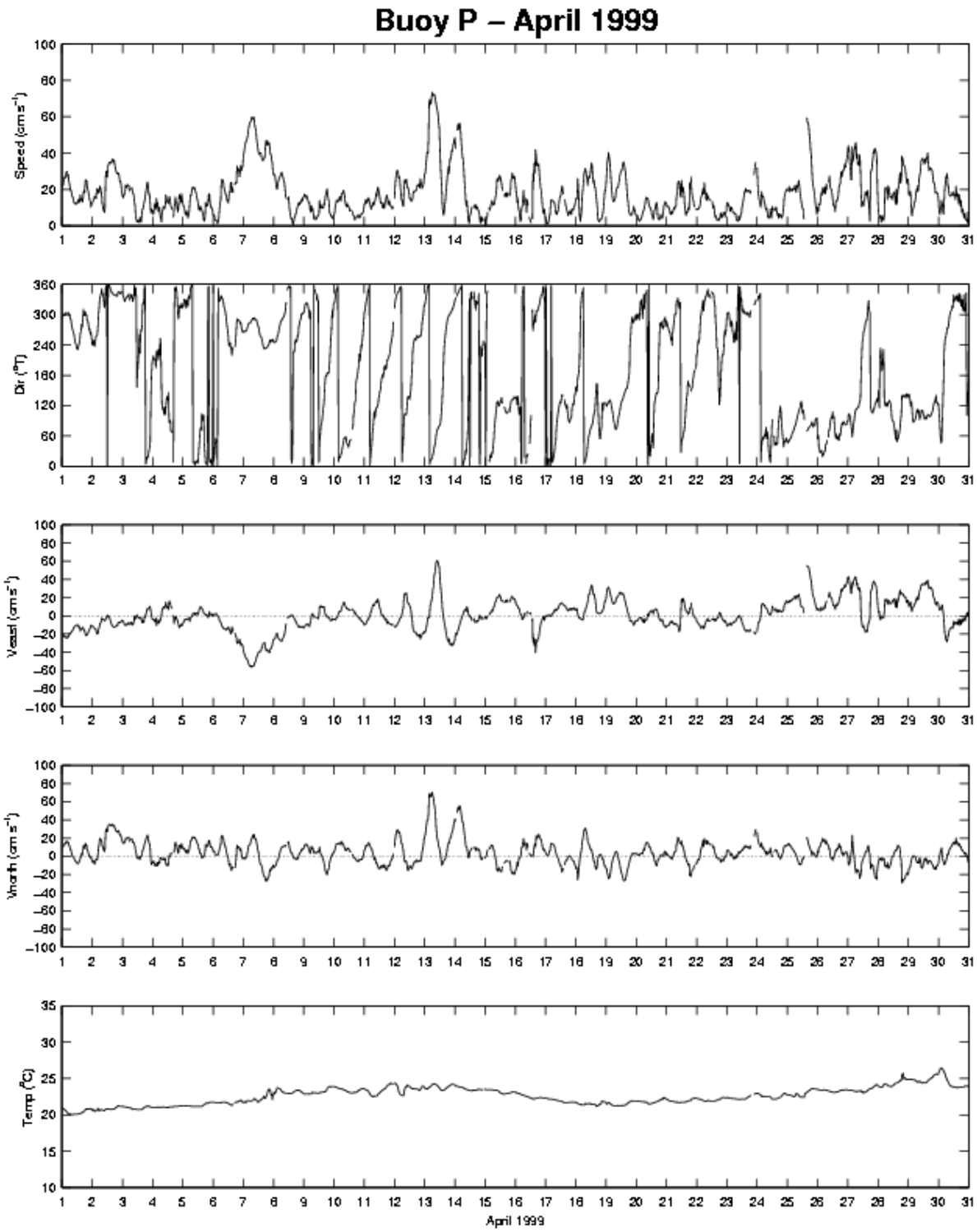

Figure A.7 Time series plot of current velocity and water temperature from Buoy P during April 1999.

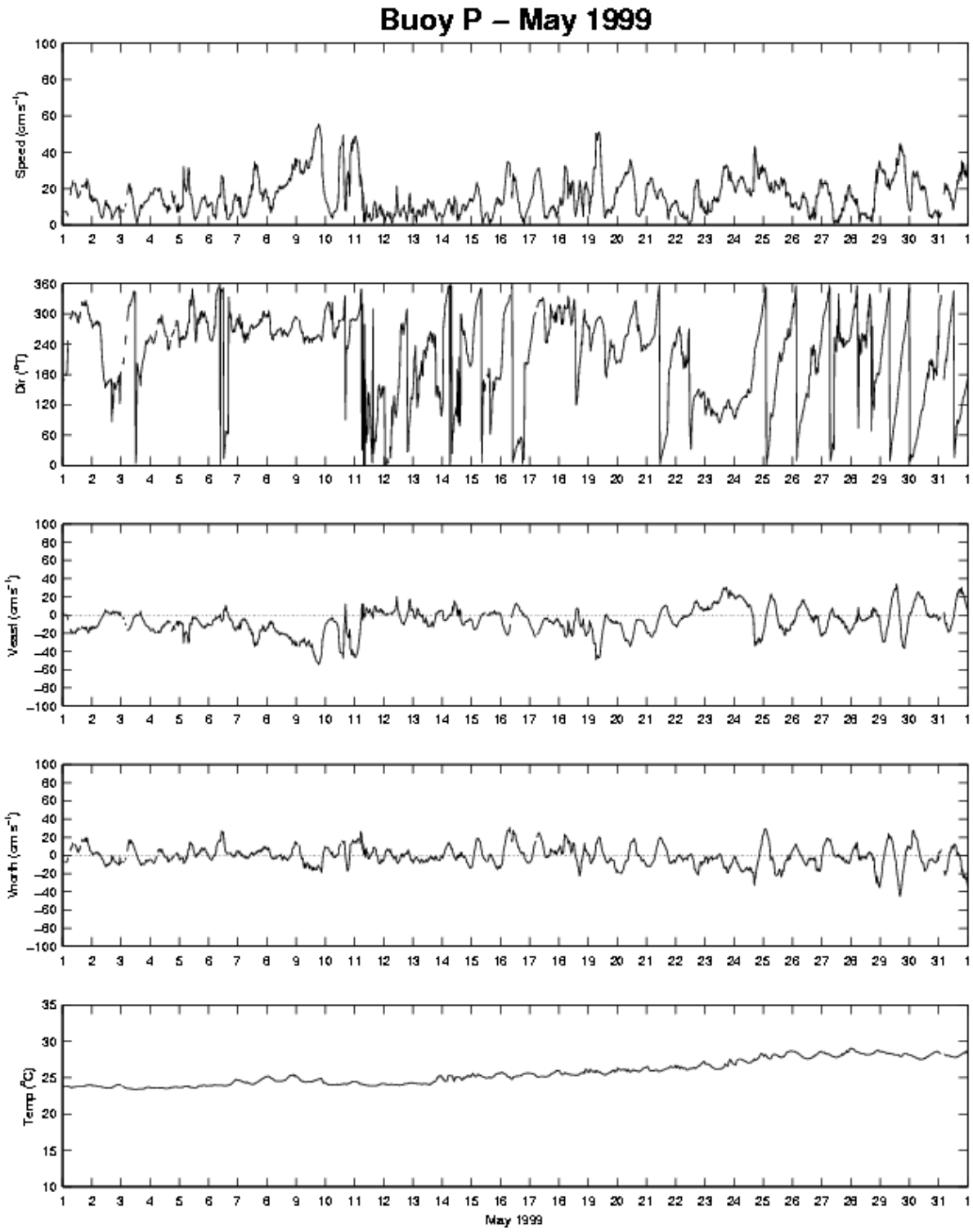

Figure A.8 Time series plot of current velocity and water temperature from Buoy P during May 1999.

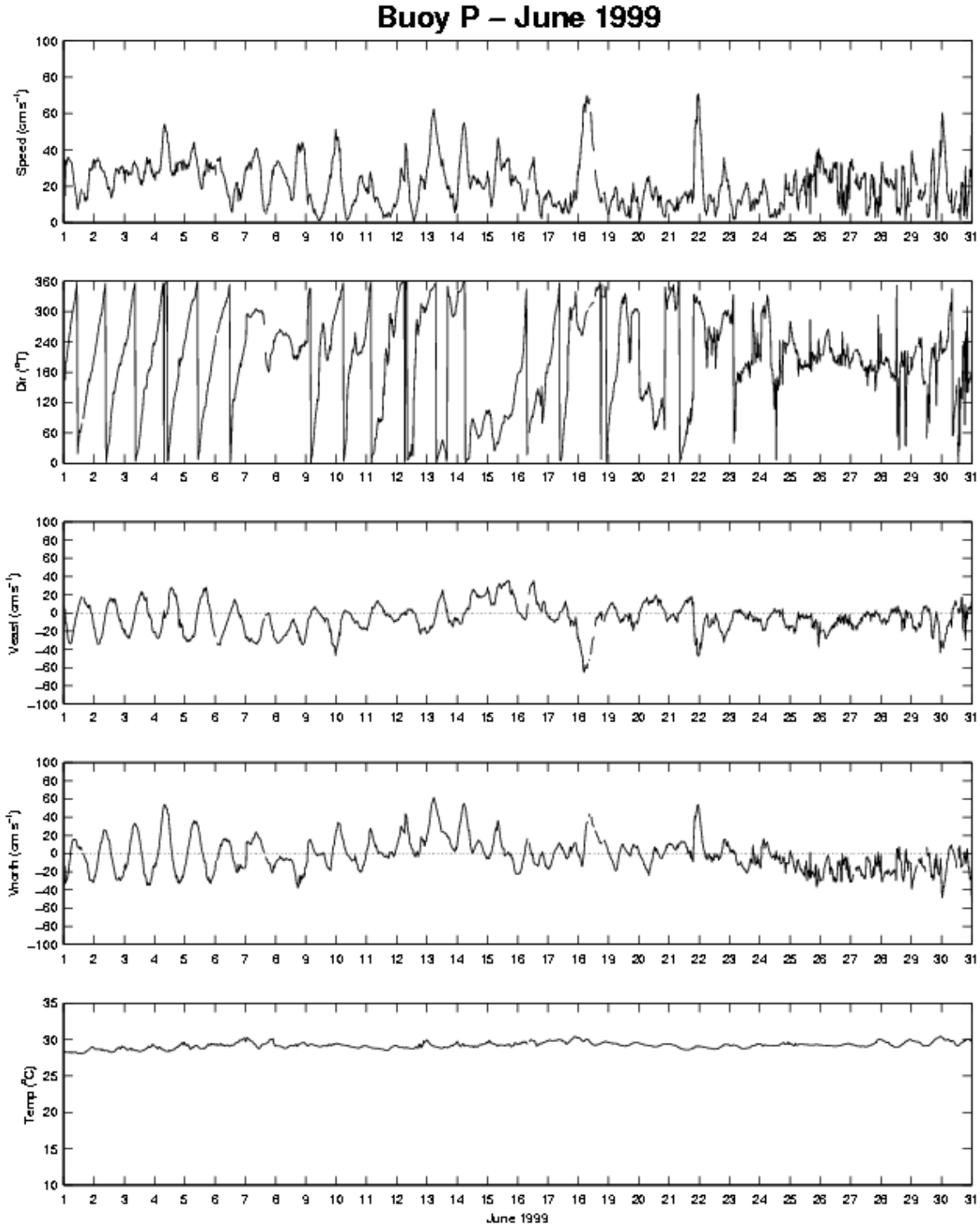

Figure A.9 Time series plot of current velocity and water temperature from Buoy P during June 1999.

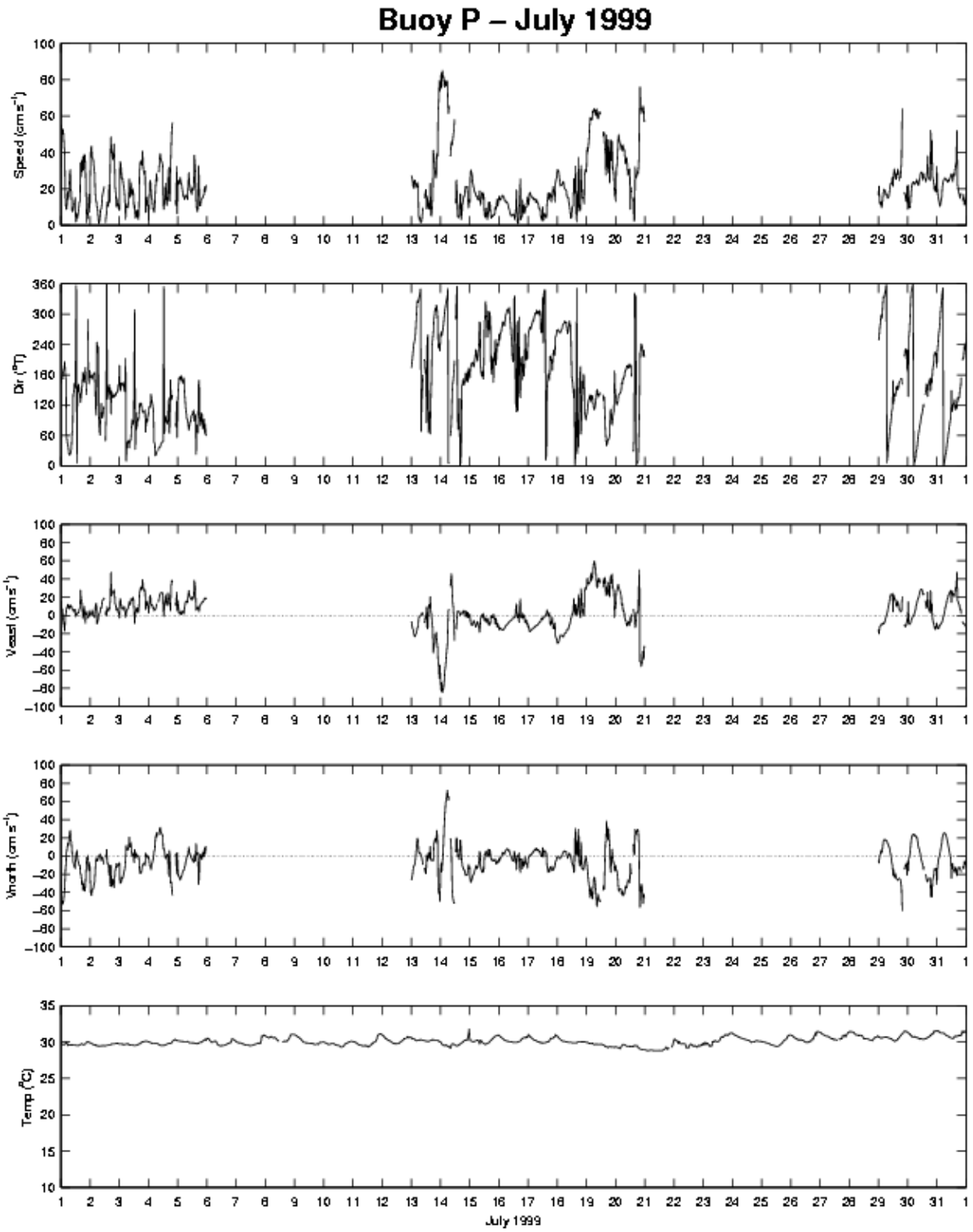

Figure A.10 Time series plot of current velocity and water temperature from Buoy P during July 1999. Gaps in the velocity record are due to bad data.

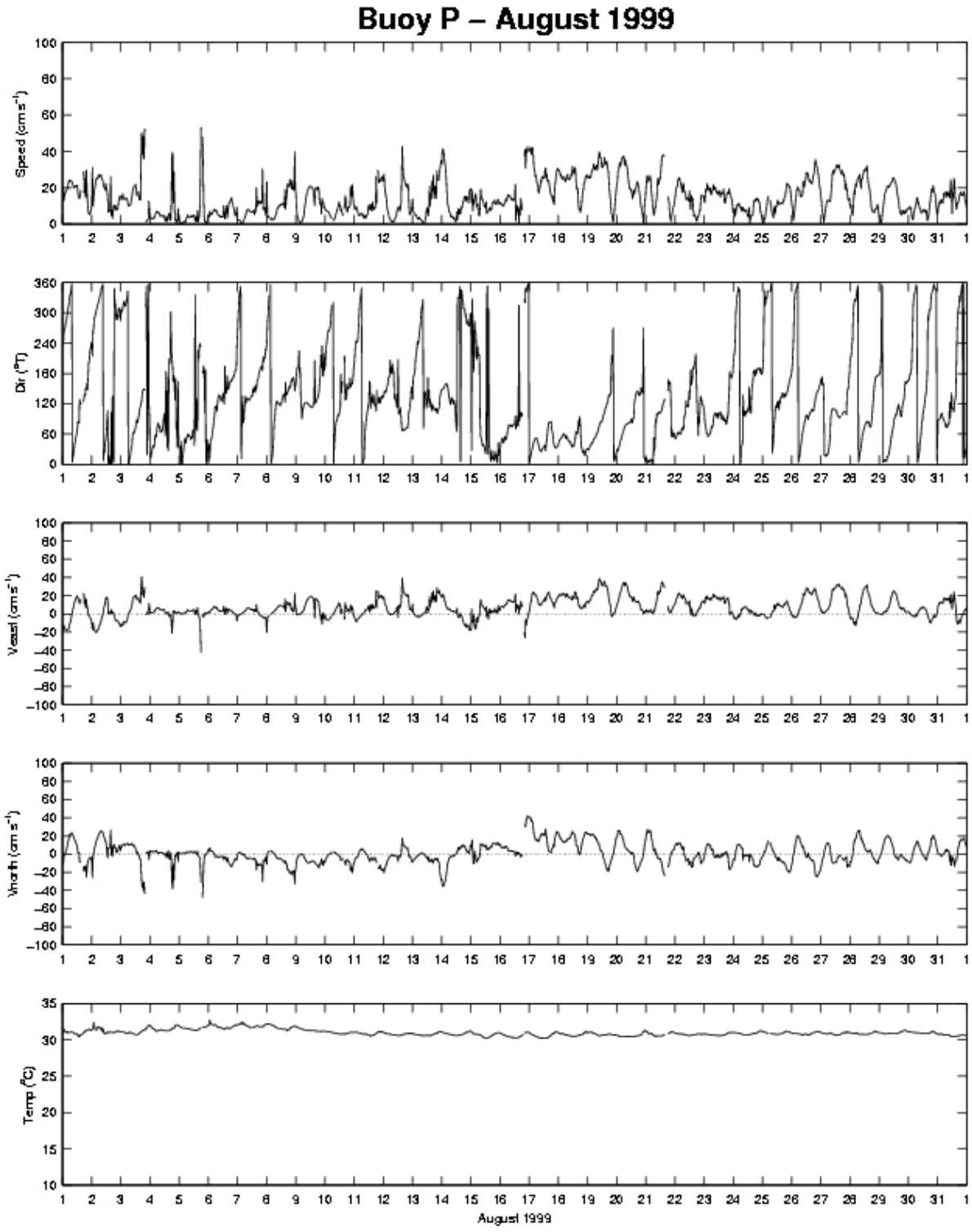

Figure A.11 Time series plot of current velocity and water temperature from Buoy P during August 1999.

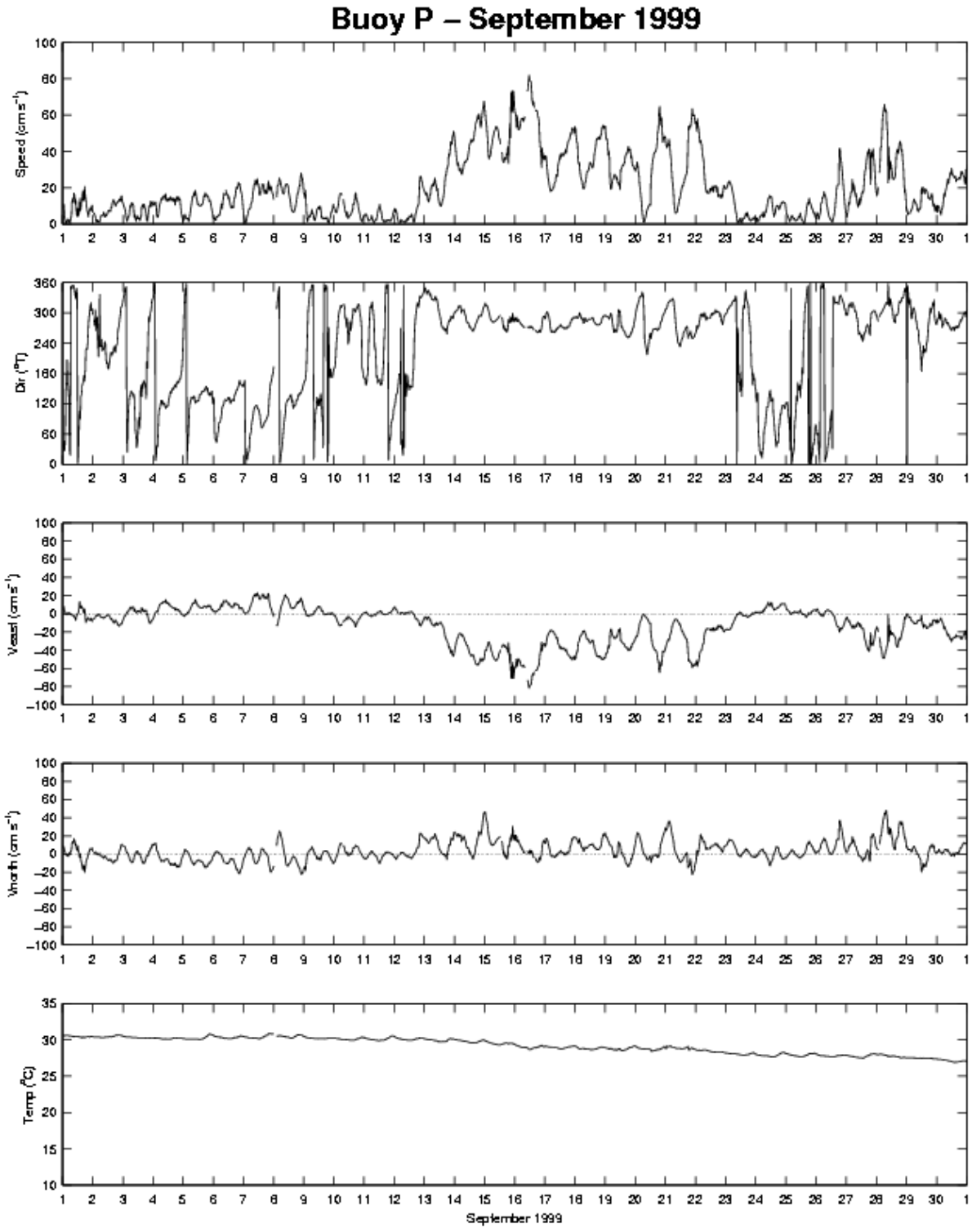

Figure A.12 Time series plot of current velocity and water temperature from Buoy P during September 1999.

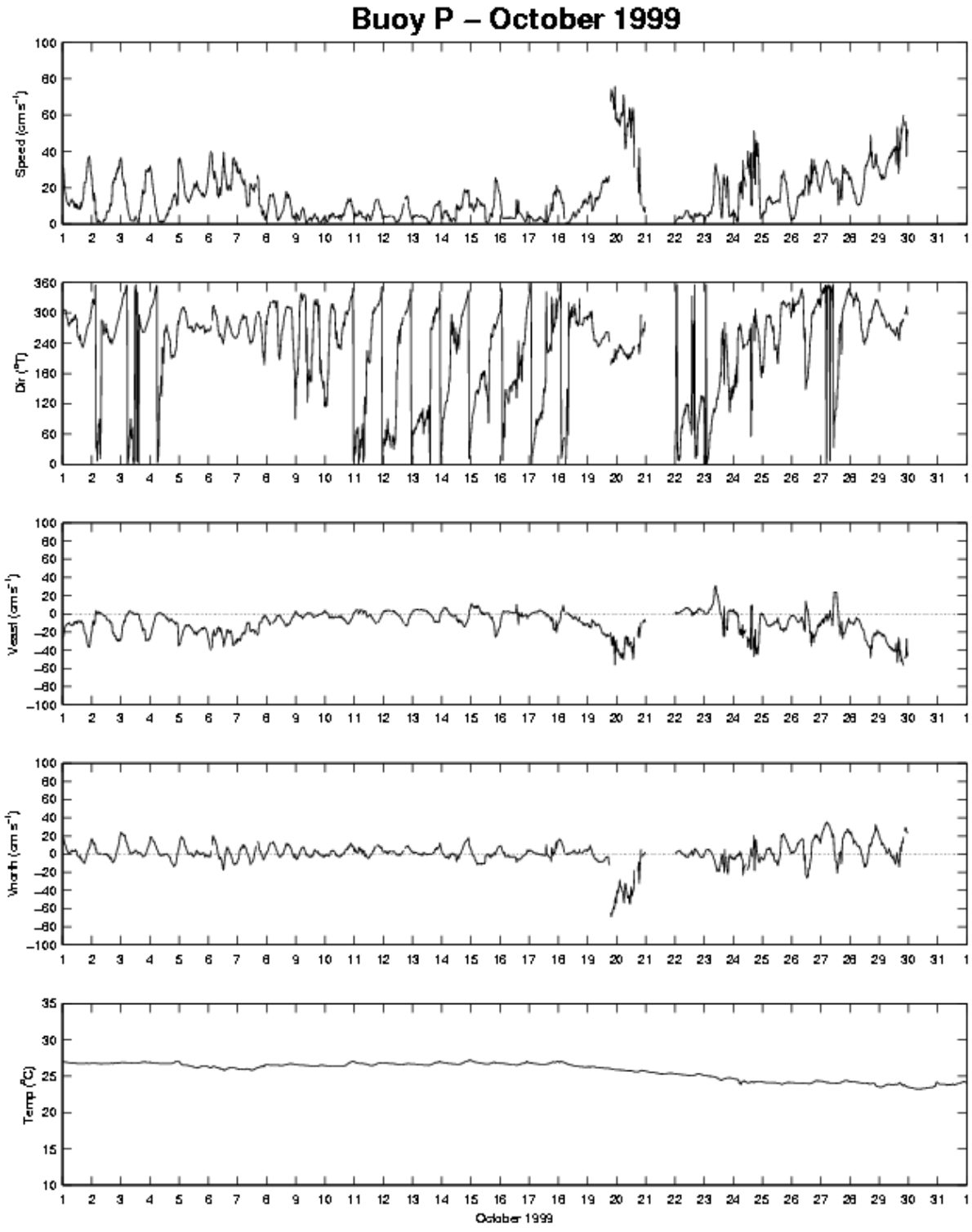

Figure A.13 Time series plot of current velocity and water temperature from Buoy P during October 1999.

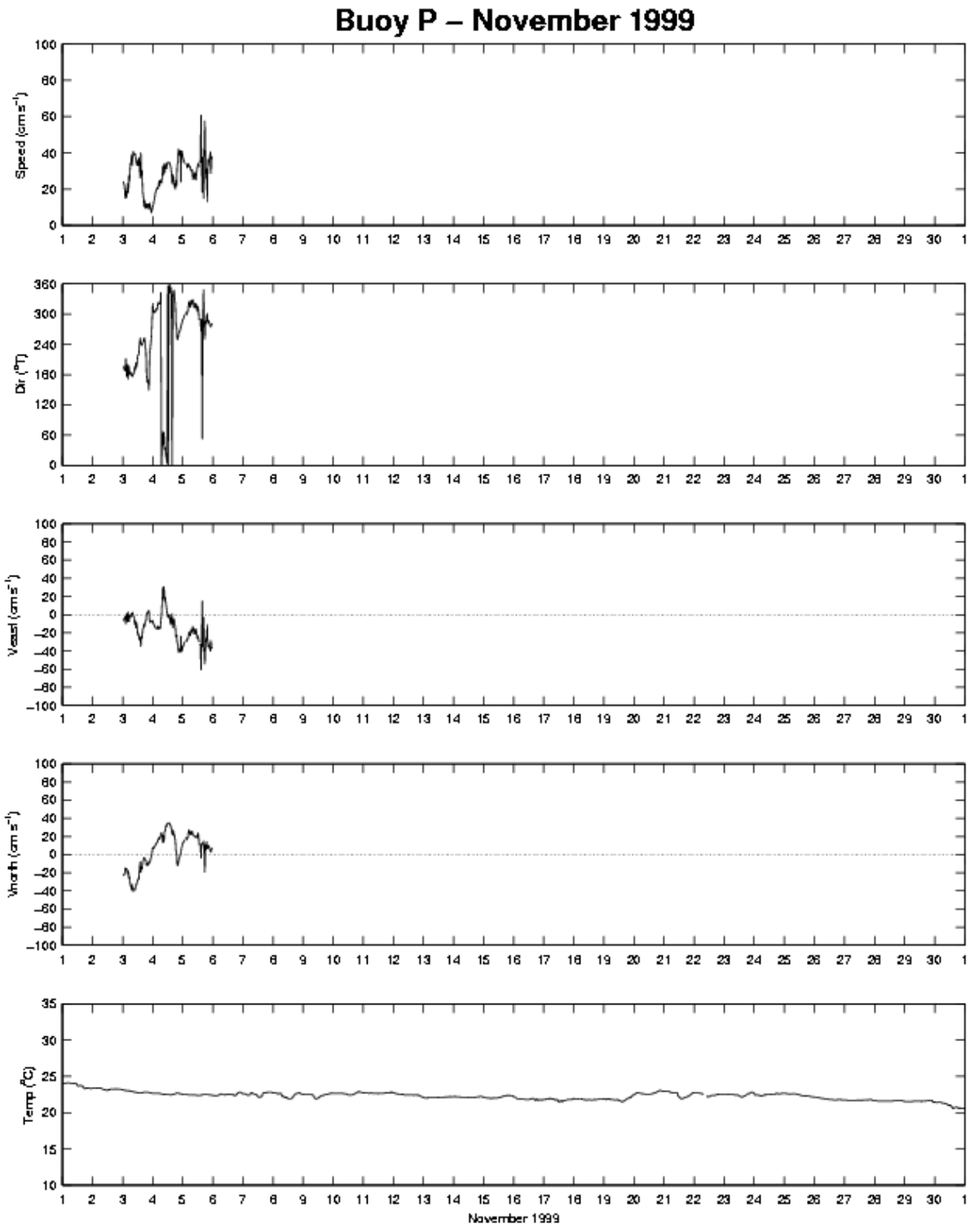

Figure A.14 Time series plot of current velocity and water temperature from Buoy P during November 1999. Gaps in the velocity record are due to bad data.

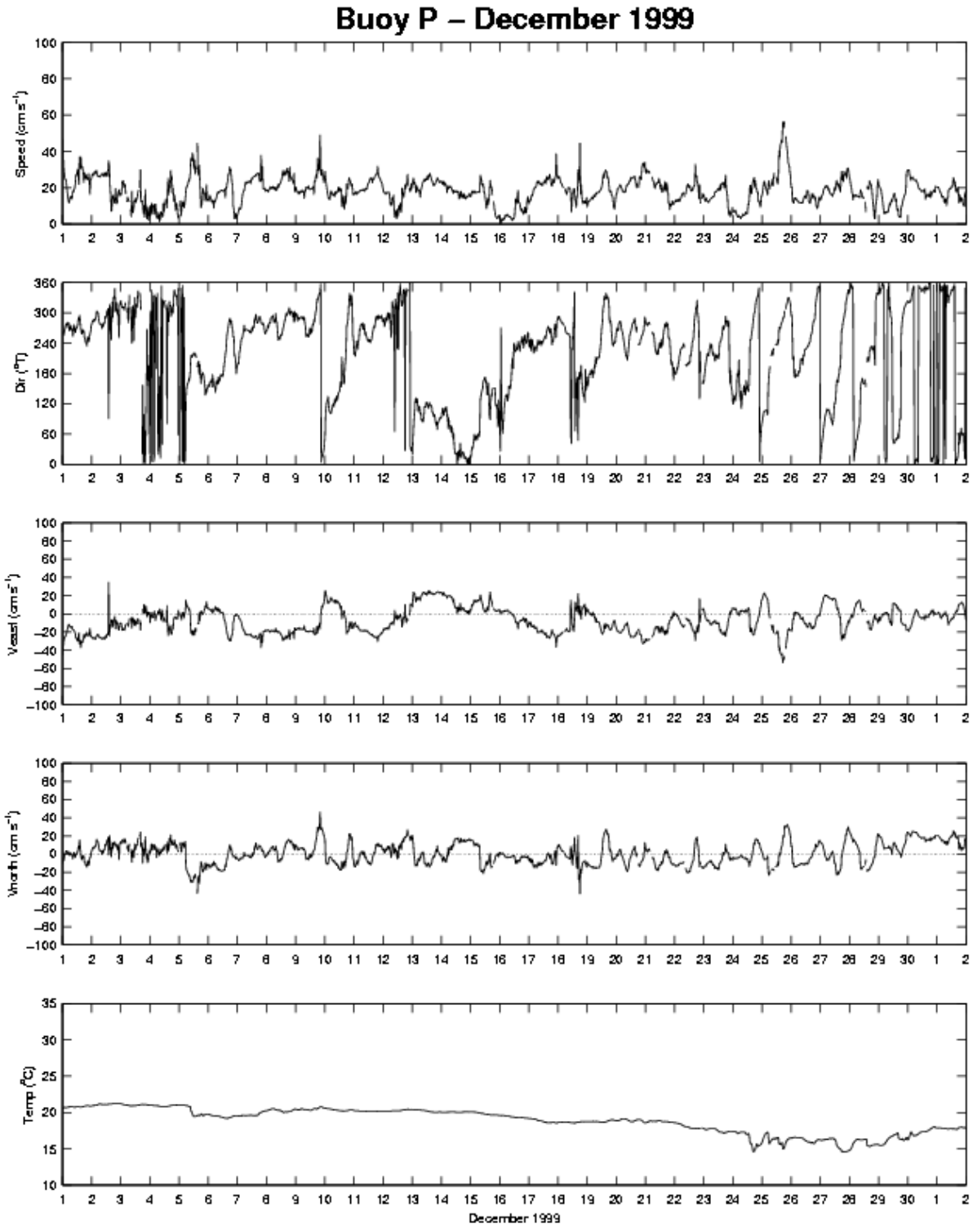

Figure A.15 Time series plot of current velocity and water temperature from Buoy P during December 1999.

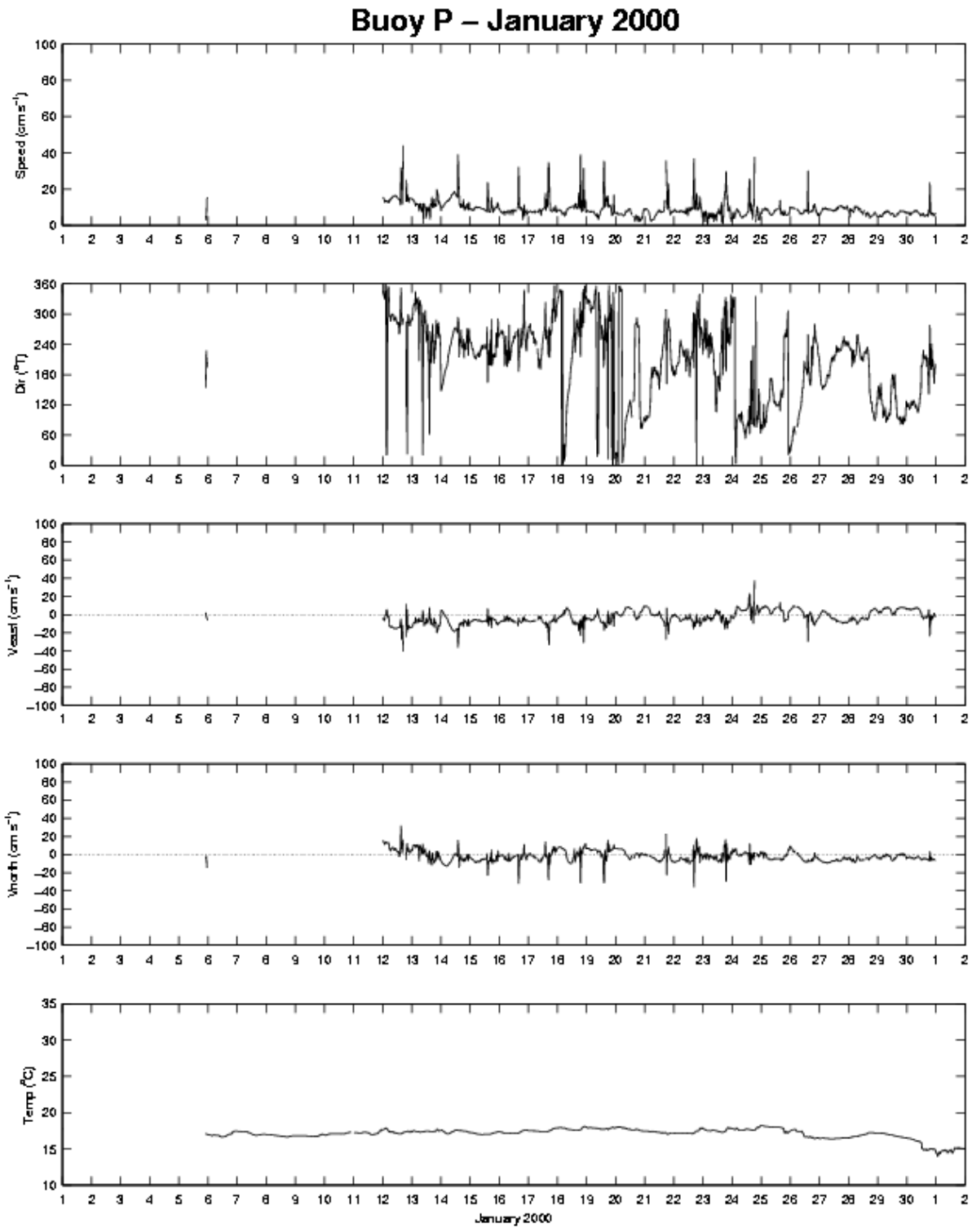

Figure A.16 Time series plot of Buoy P current velocity and water temperature collected during January 2000. Gaps in the velocity record are due to bad data.

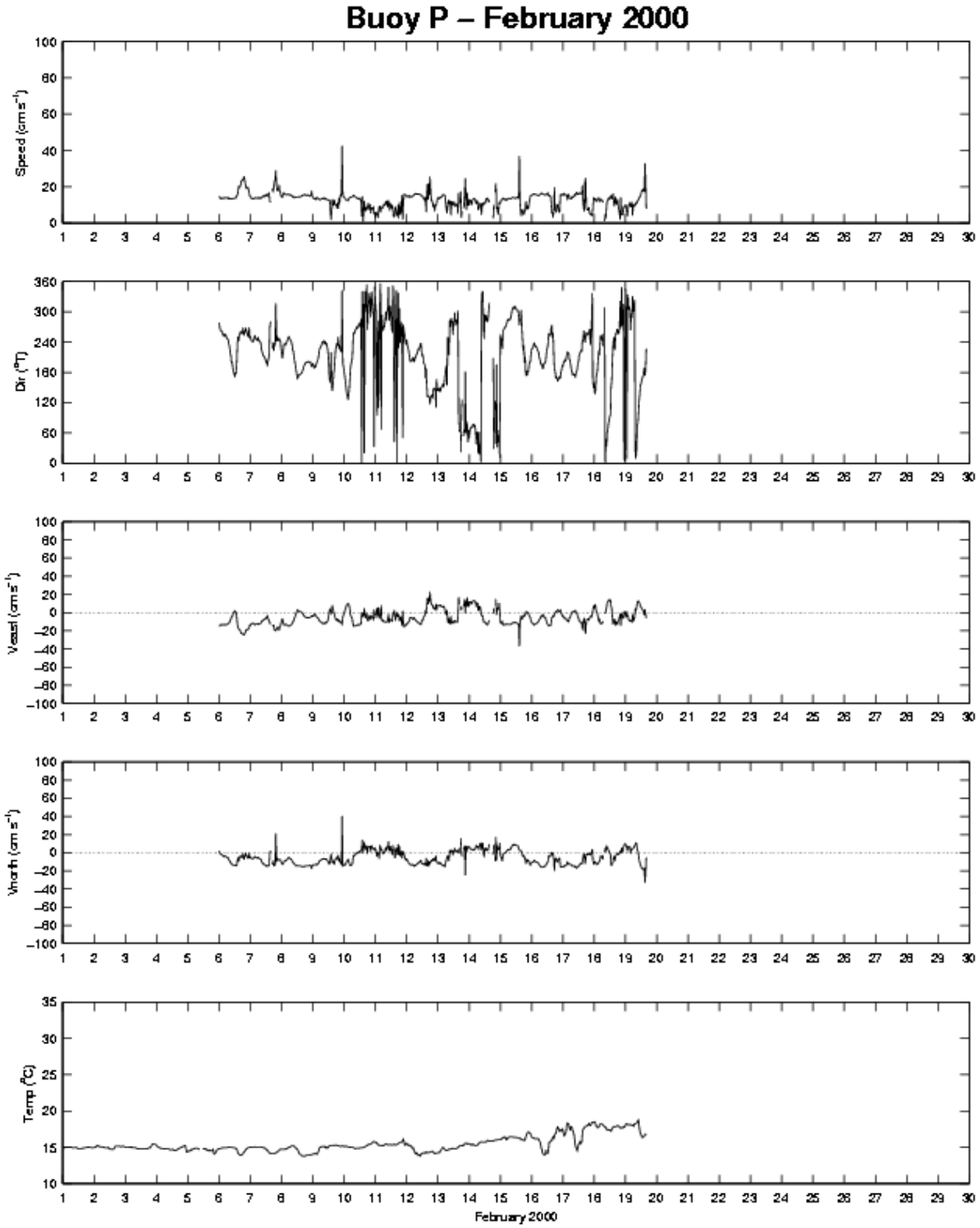

Figure A.17 Time series plot of Buoy P current velocity and water temperature collected during February 2000. Gaps in the velocity record are due to bad data.

Appendix B

Hydrographic Data Collected During *R/V Gyre* Cruise 98-G-9: Temperature-Salinity Plots and Vertical Sections

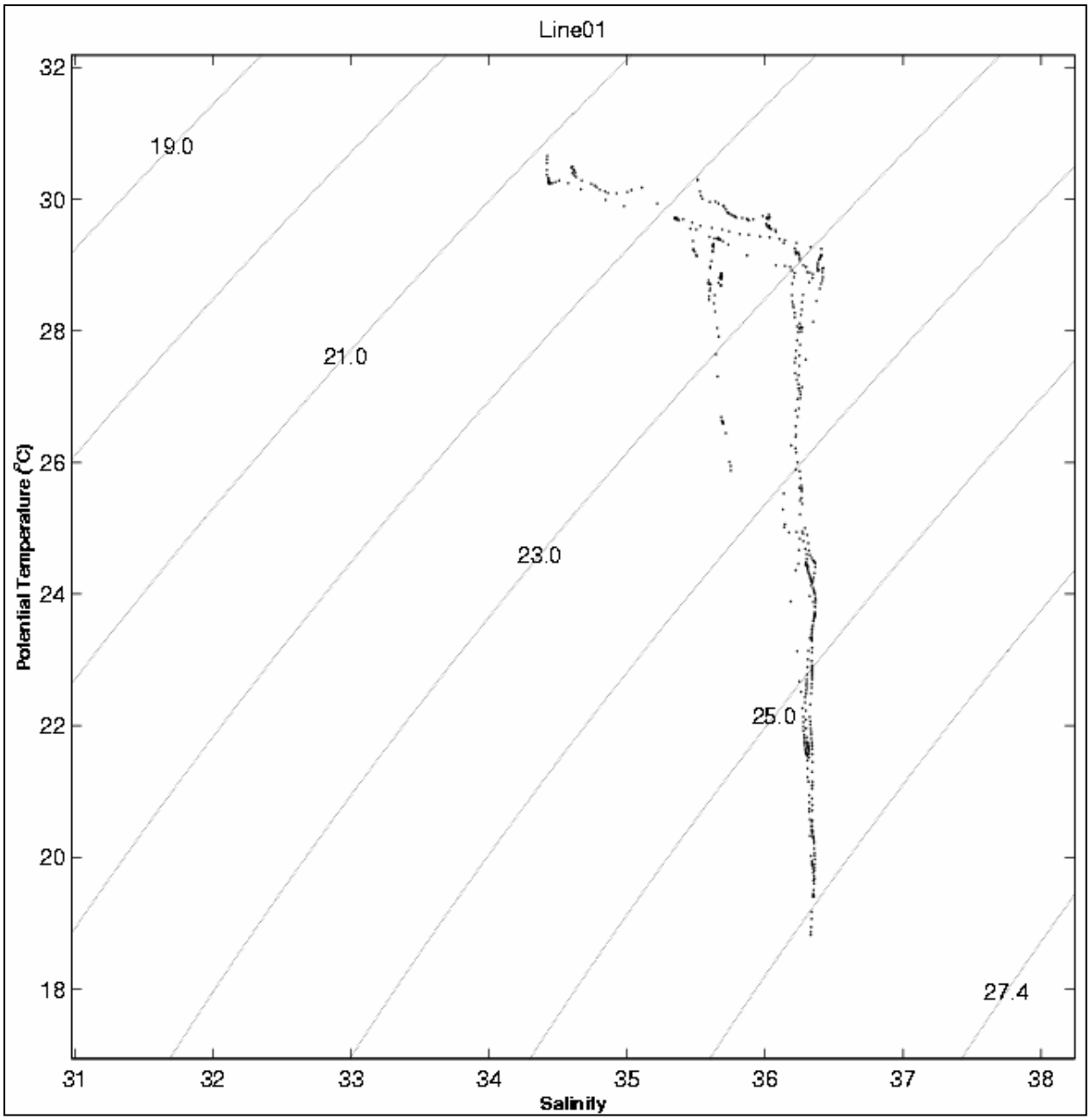

Figure B.1 Temperature Salinity relationship for CTD stations along Transect 1 sampled during *R/V Gyre* cruise 98-G-9.

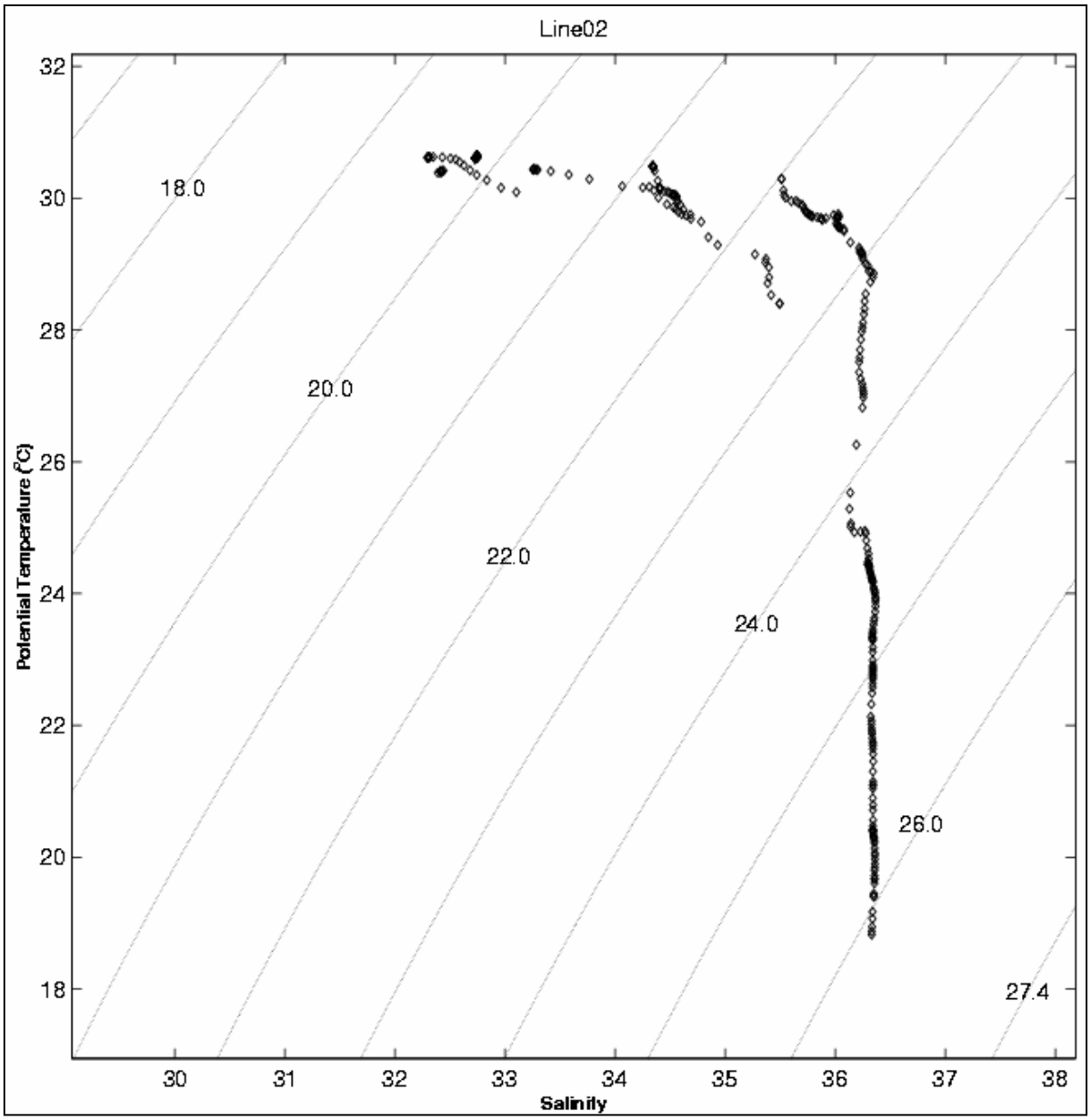

Figure B.2 Temperature Salinity relationship for CTD stations along Transect 2 sampled during *R/V Gyre* cruise 98-G-9.

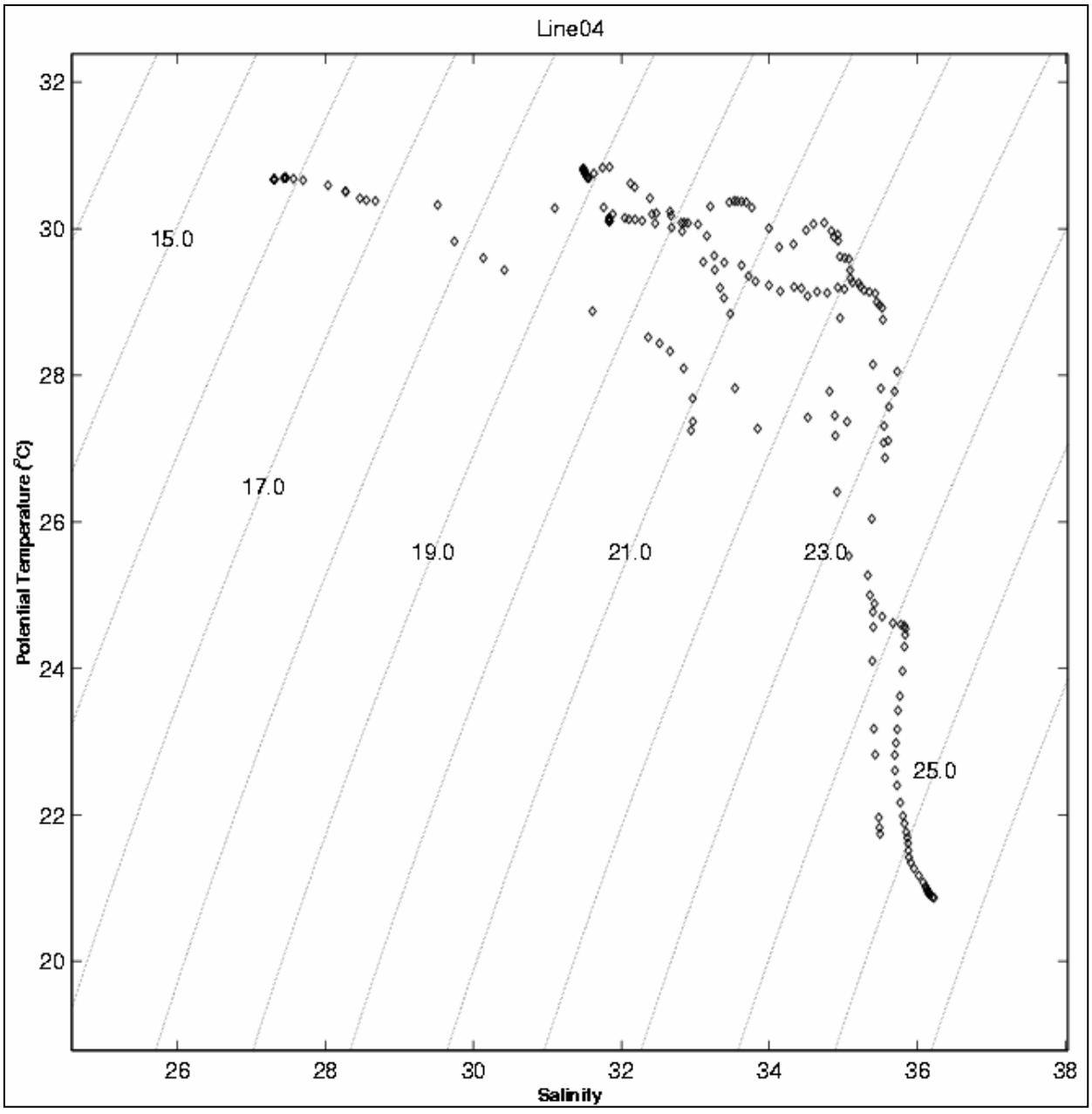

Figure B.3 Temperature Salinity relationship for CTD stations along Transect 4 sampled during *R/V Gyre* cruise 98-G-9.

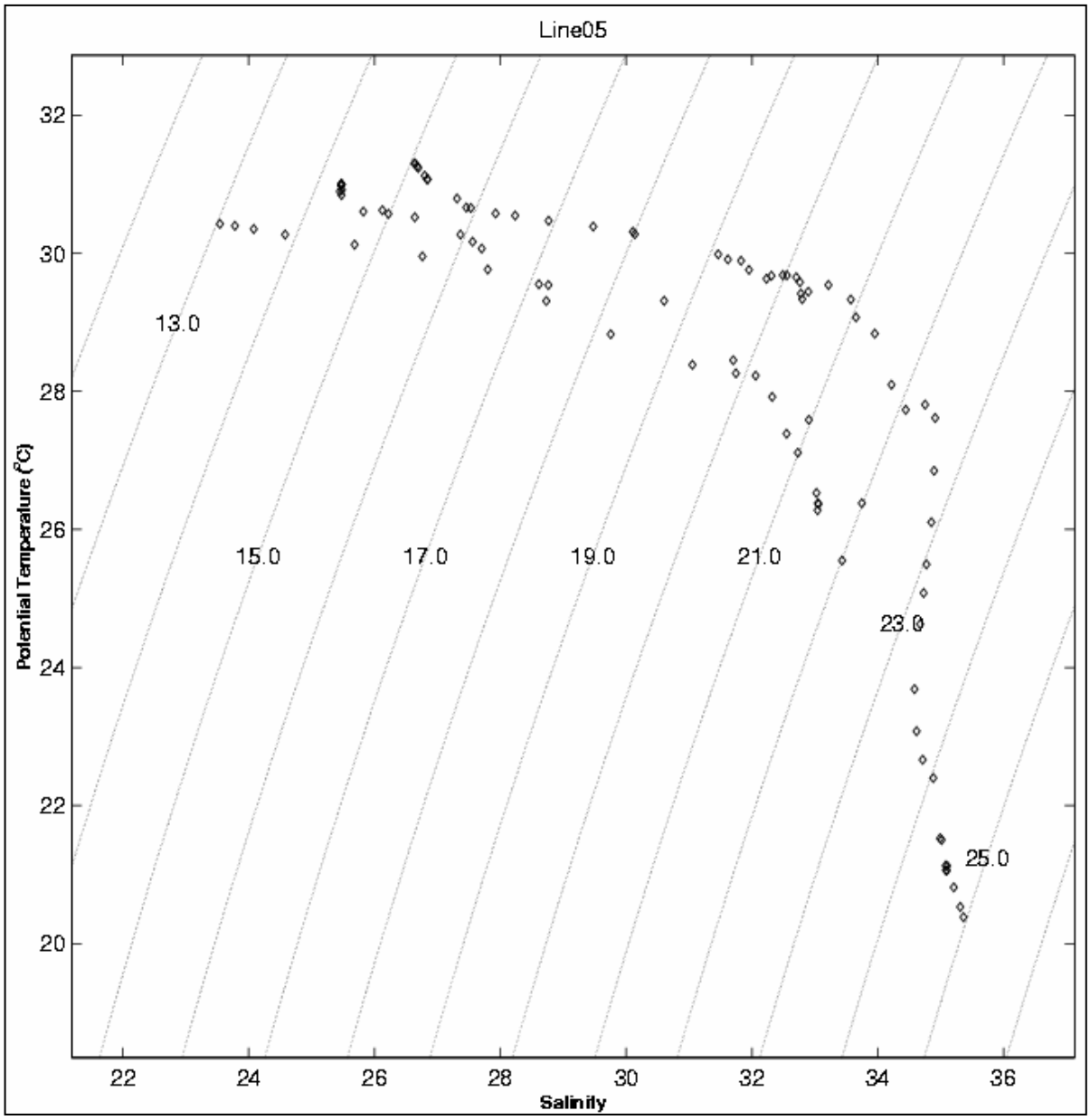

Figure B.4 Temperature Salinity relationship for CTD stations along Transect 5 sampled during *R/V Gyre* cruise 98-G-9.

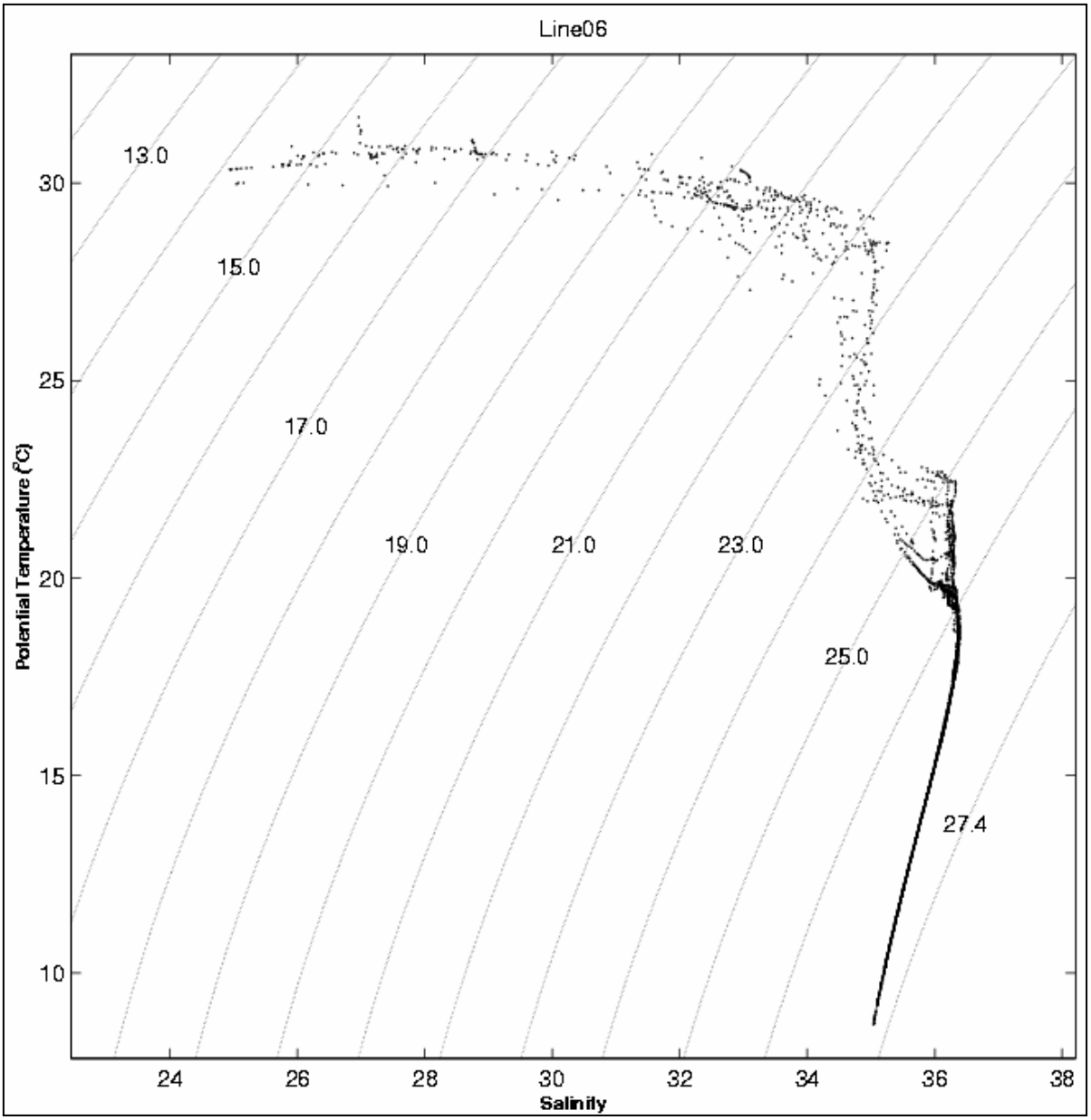

Figure B.5 Temperature Salinity relationship for CTD stations along Transect 6 sampled during *R/V Gyre* cruise 98-G-9.

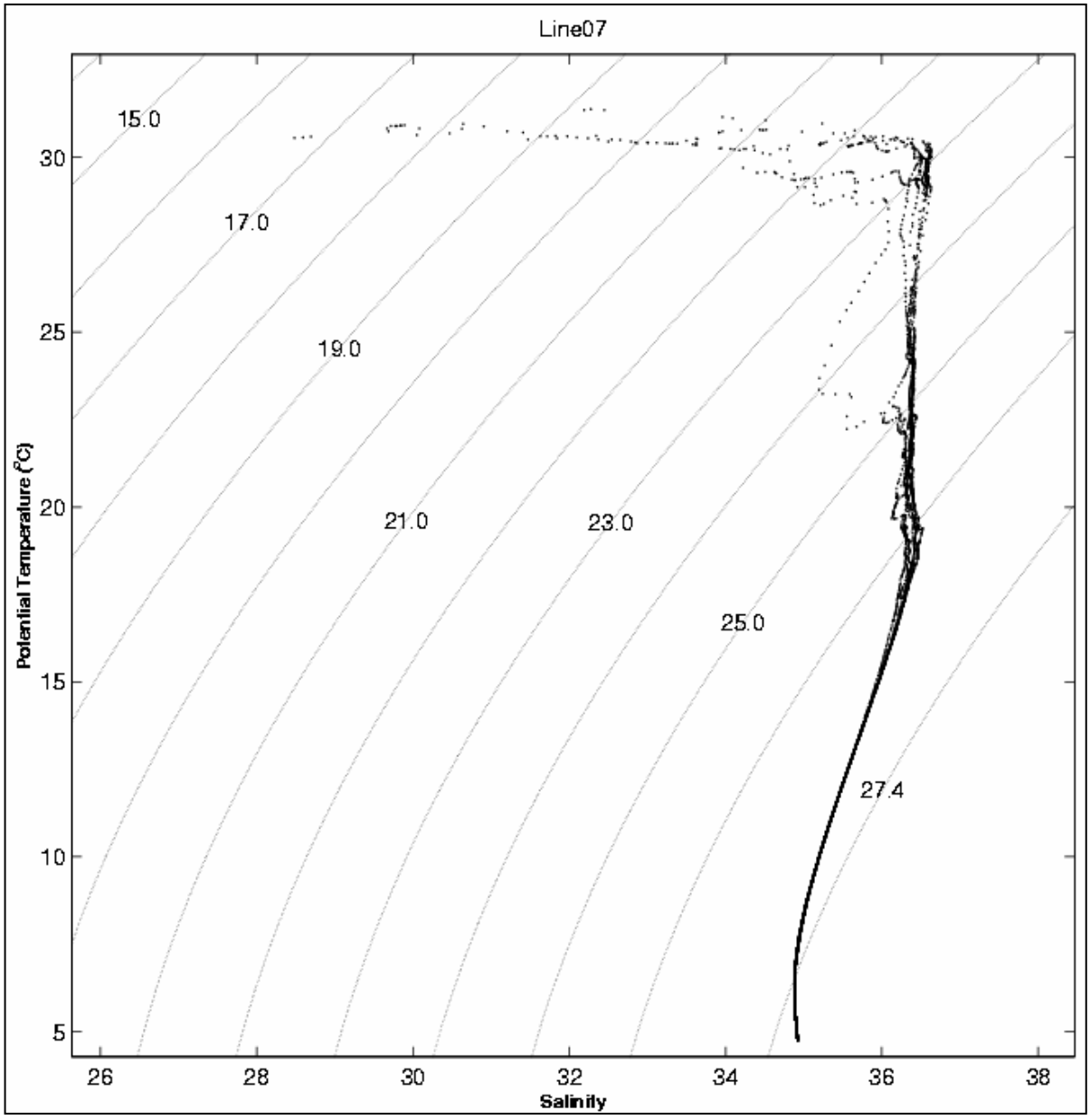

Figure B.6 Temperature Salinity relationship for CTD stations along Transect 7A sampled during *R/V Gyre* cruise 98-G-9.

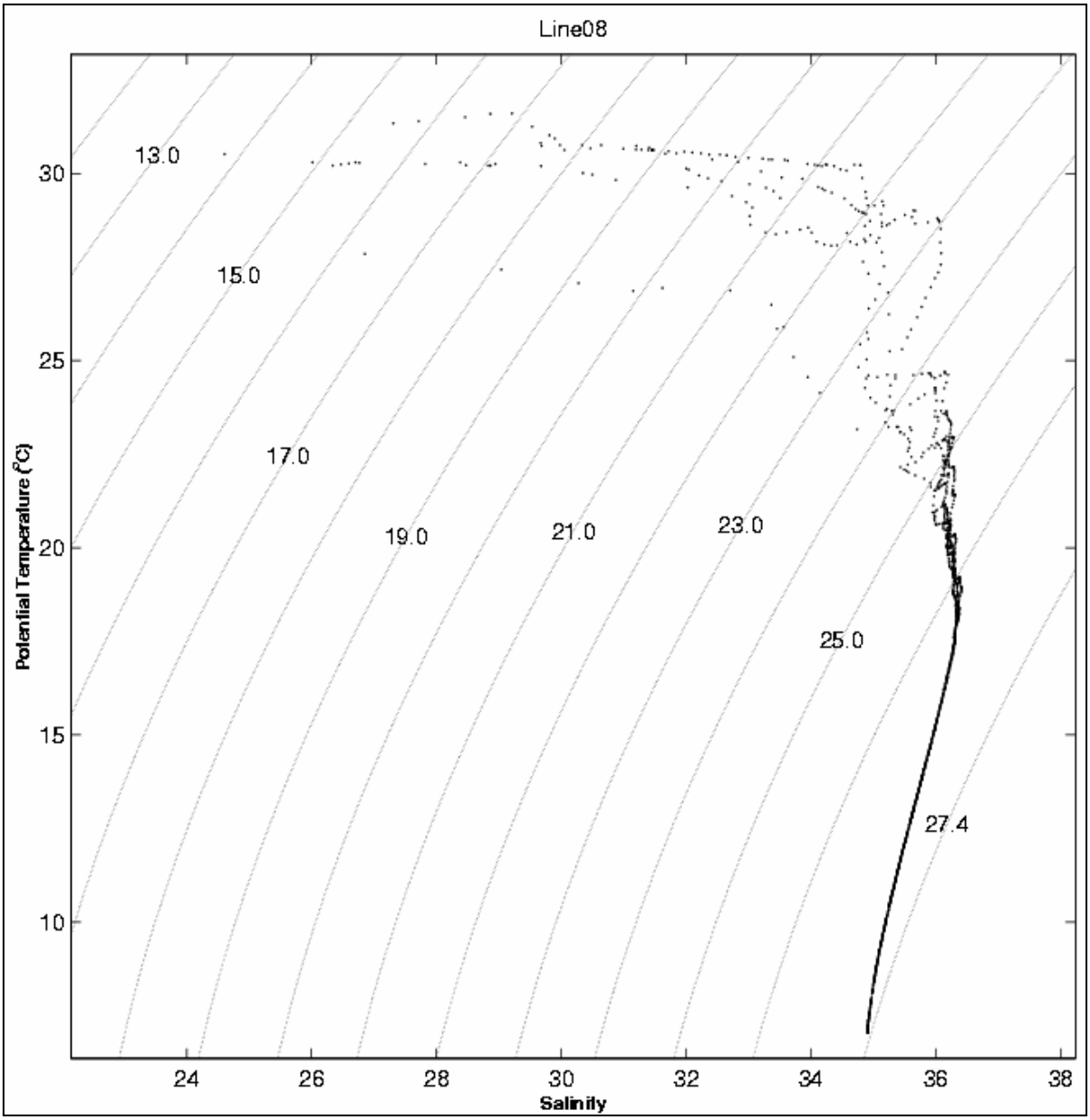

Figure B.7 Temperature Salinity relationship for CTD stations along Transect 7B sampled during *R/V Gyre* cruise 98-G-9.

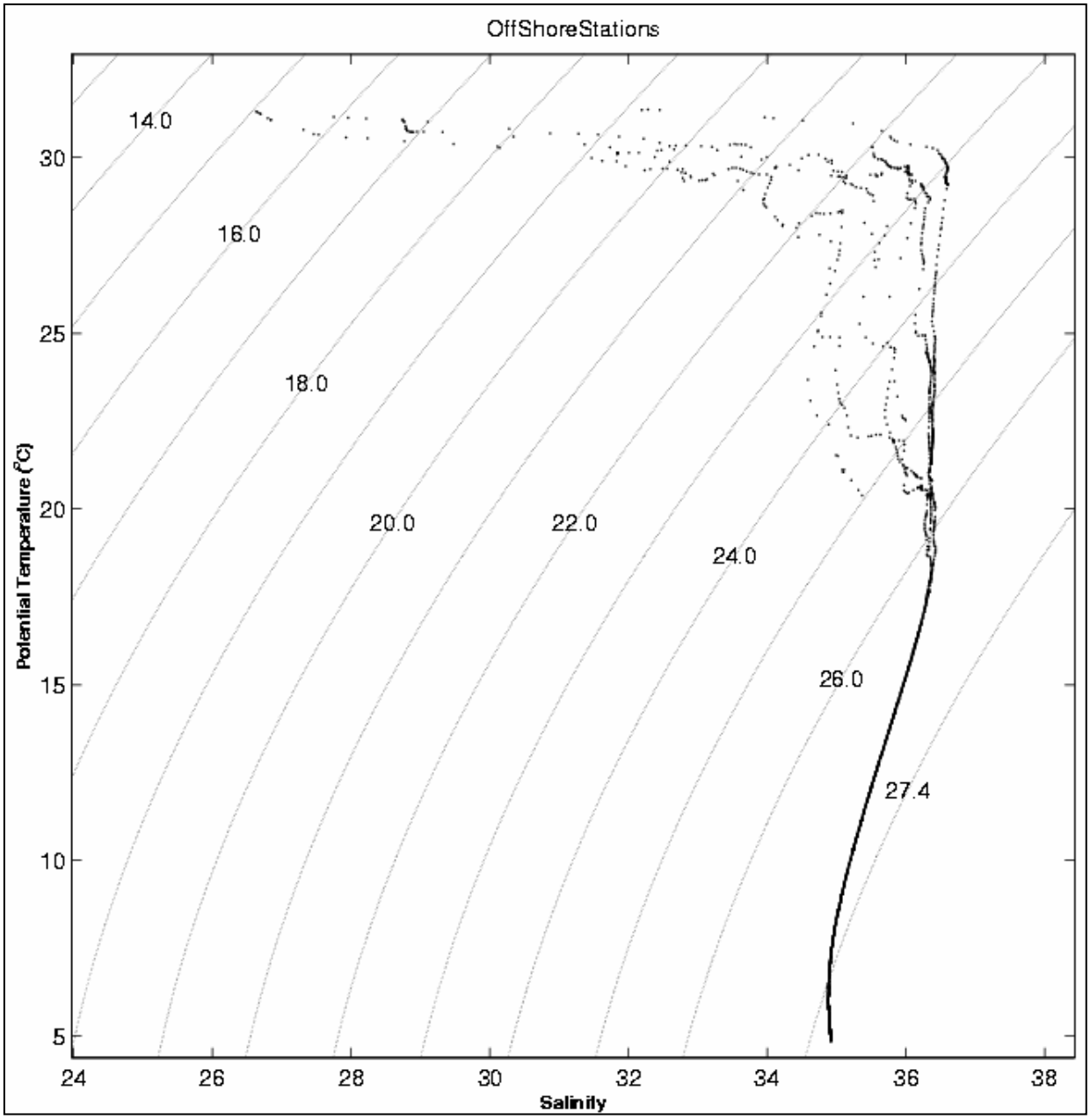

Figure B.8 Temperature Salinity relationship for offshore CTD stations sampled during *R/V Gyre* cruise 98-G-9.

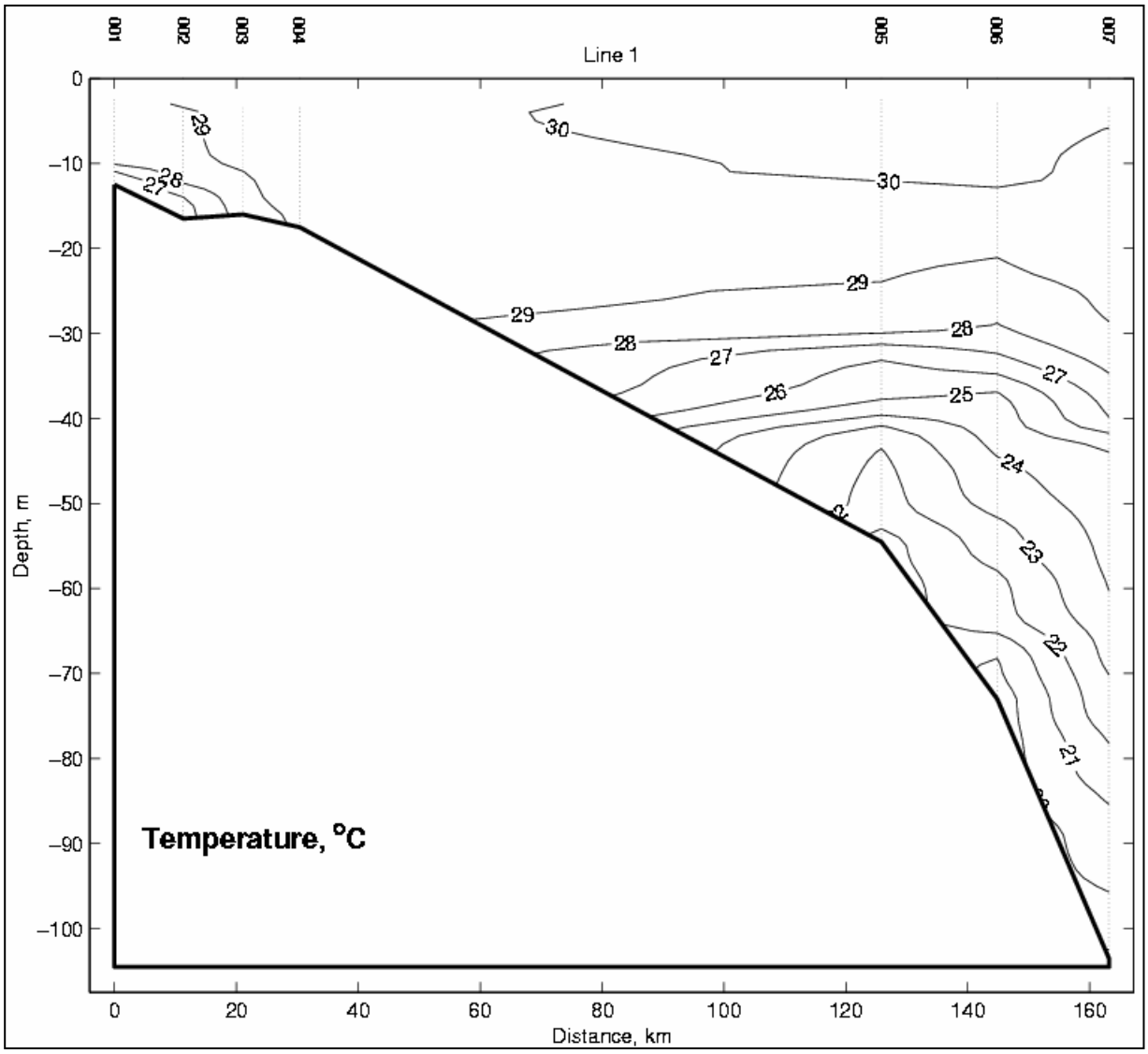

Figure B.9 Vertical profile of temperature for Transect 1. The contour interval is 1°C.

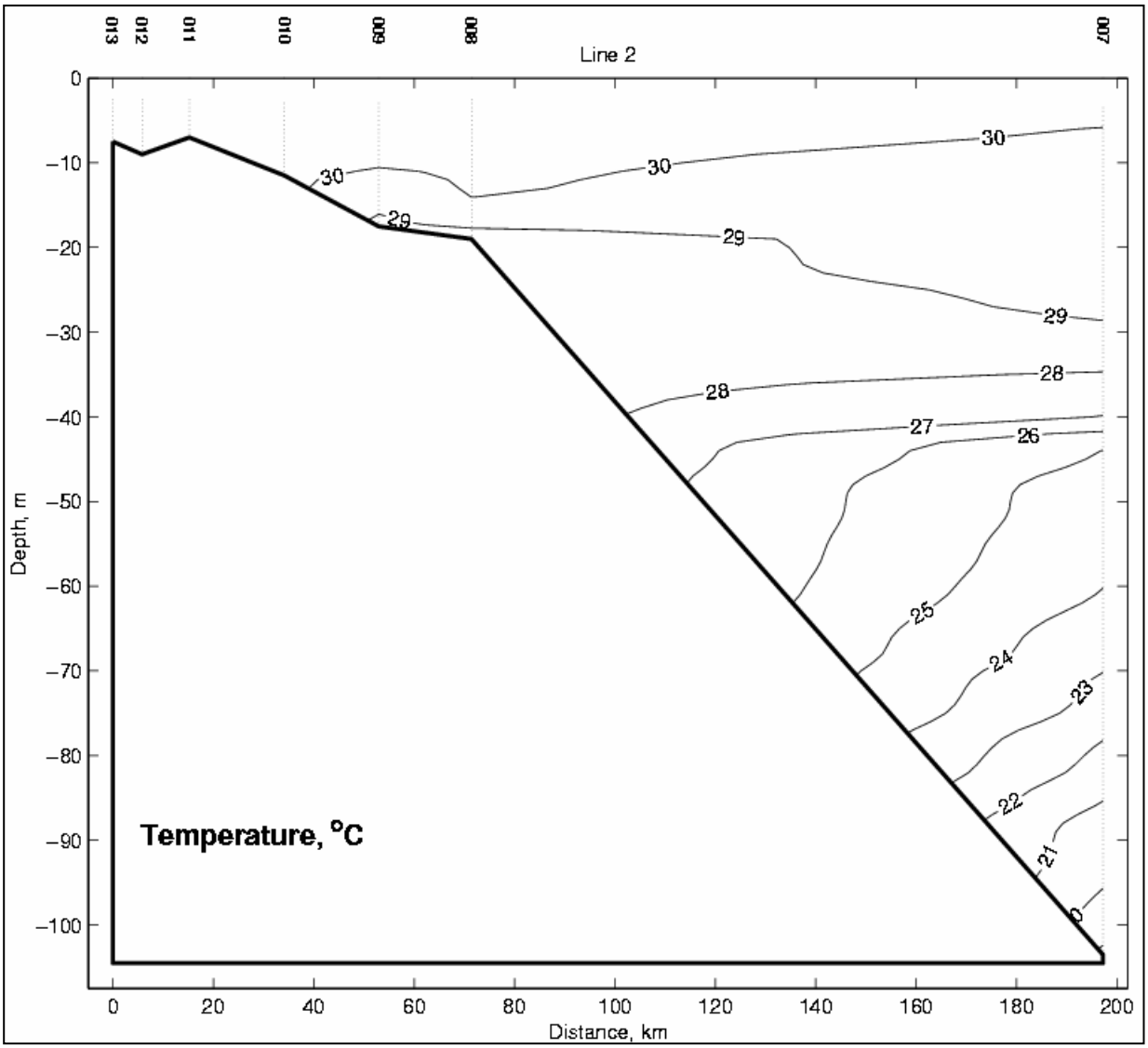

Figure B.10 Vertical profile of temperature for Transect 2. The contour interval is 1°C.

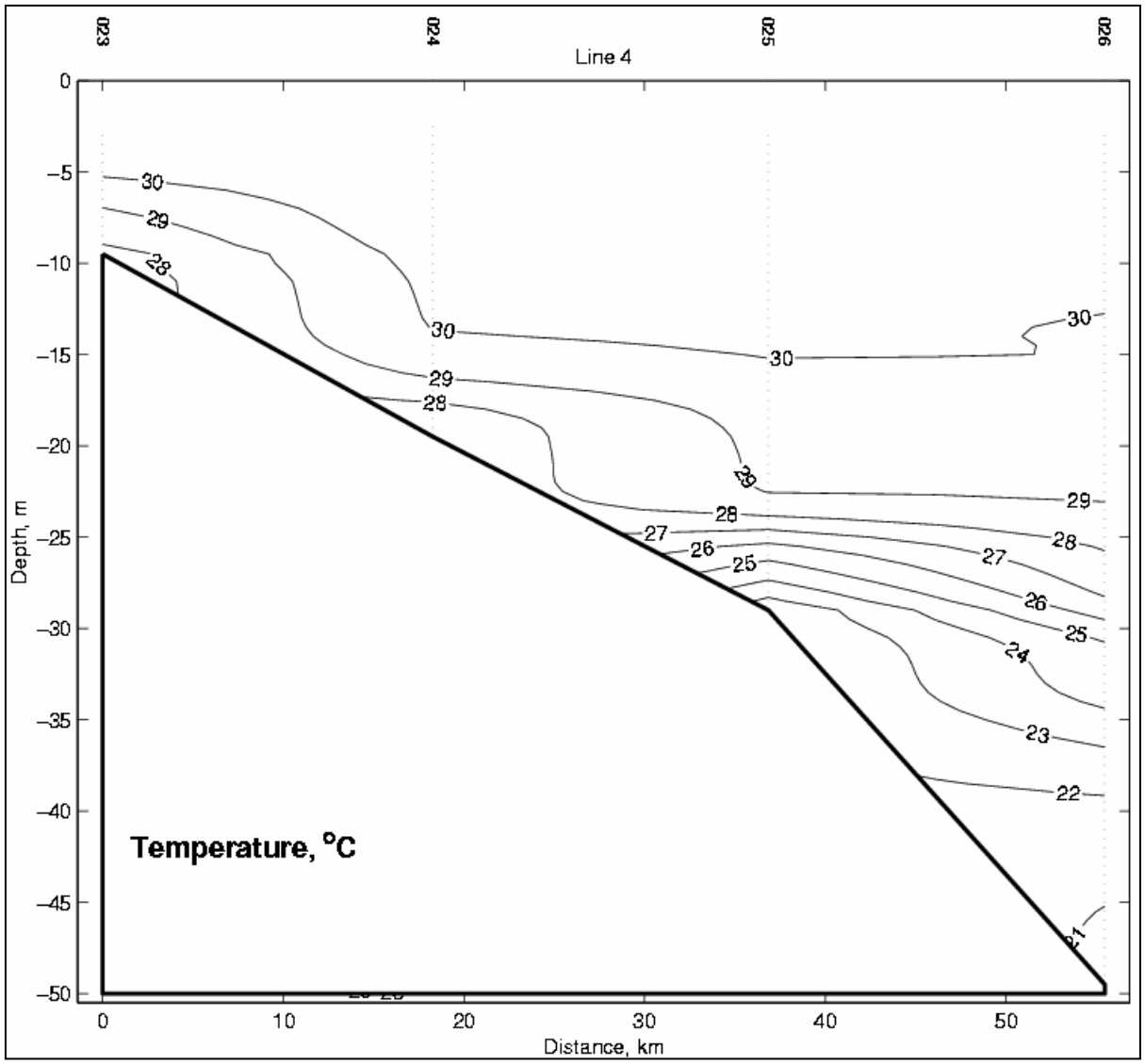

Figure B.11 Vertical profile of temperature for Transect 4. The contour interval is 1°C.

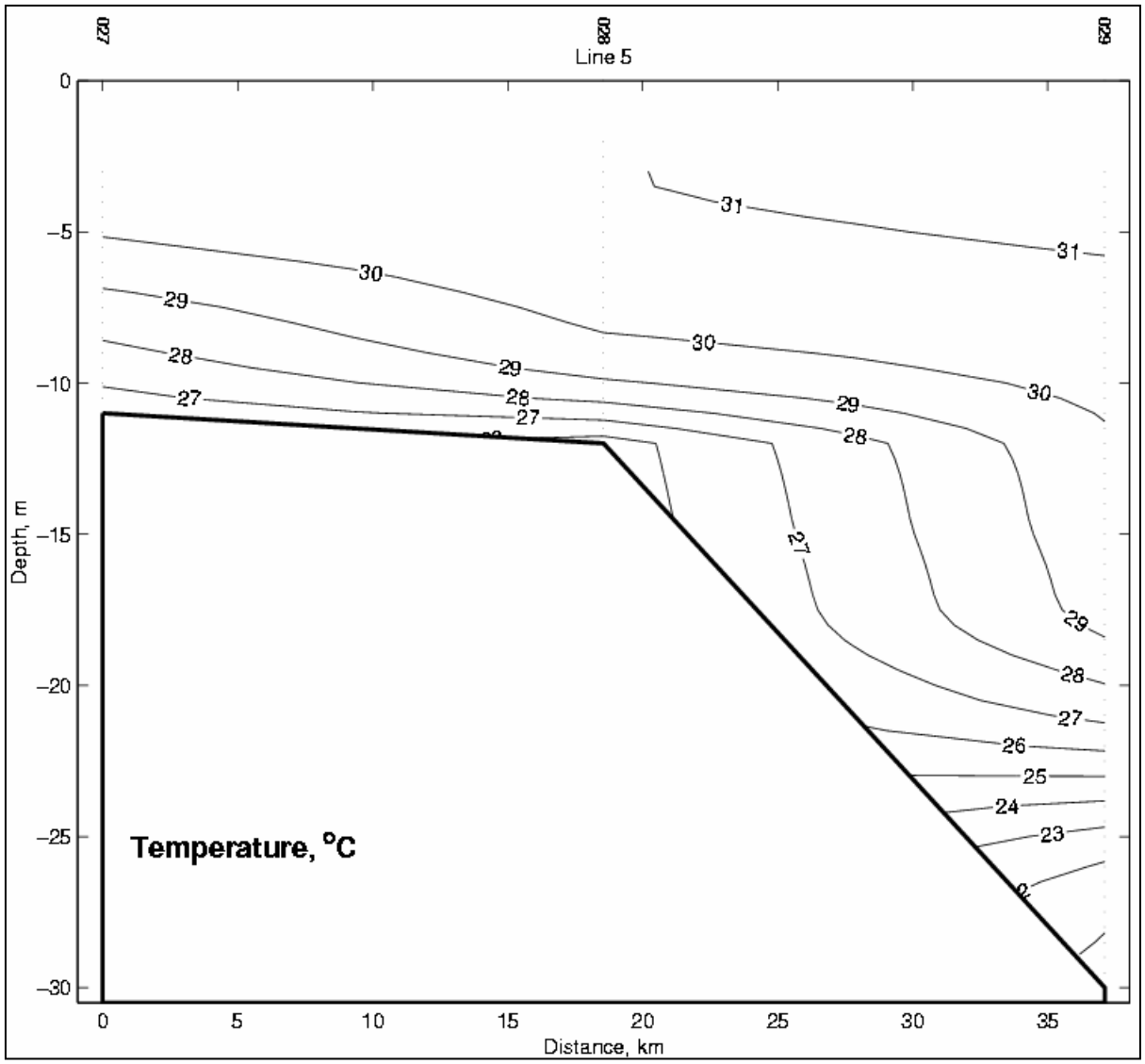

Figure B.12 Vertical profile of temperature for Transect 5. The contour interval is 1°C.

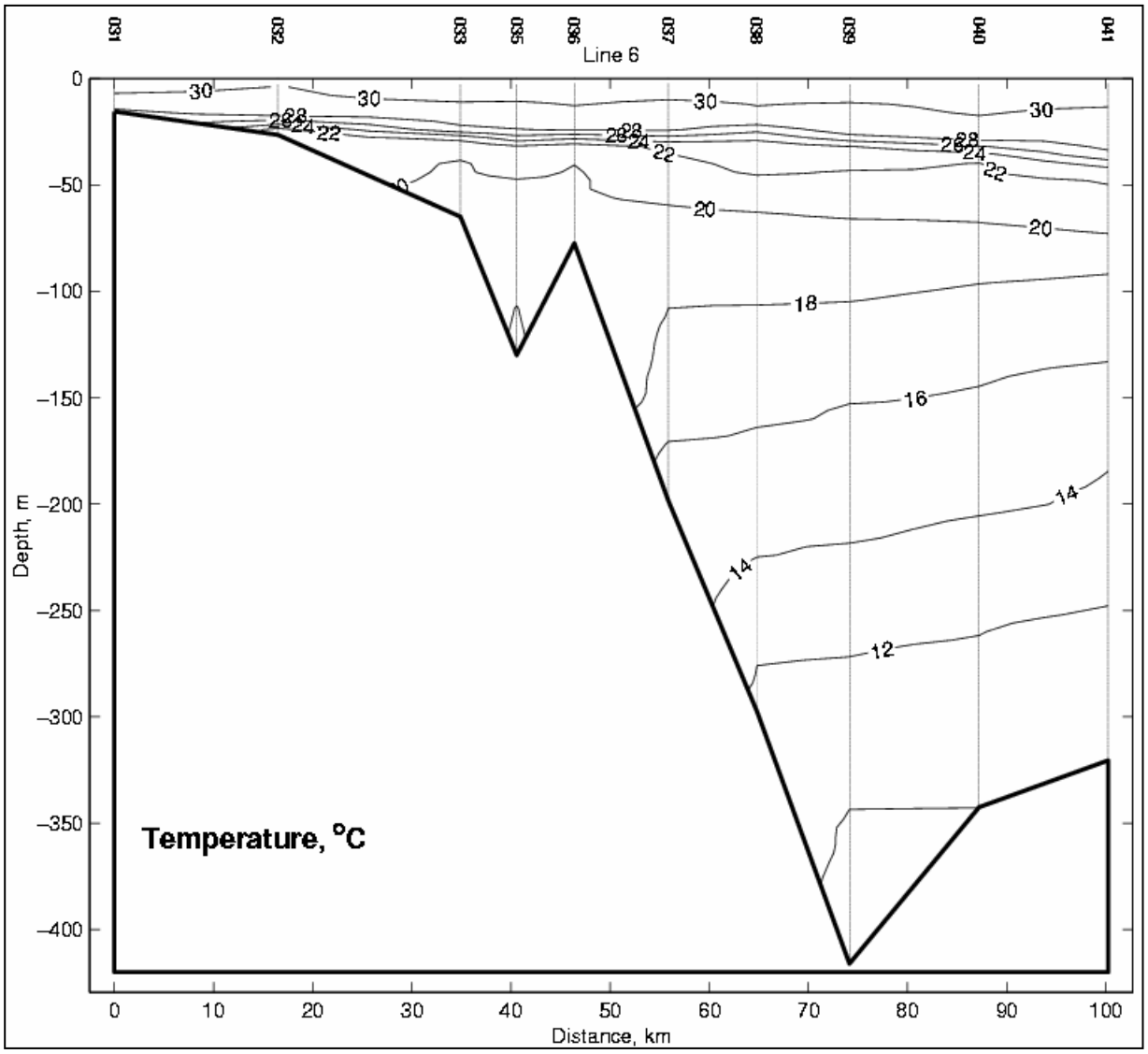

Figure B.13 Vertical profile of temperature for Transect 6. The contour interval is 2°C. Note the strong thermocline between the 30 and 50m depth.

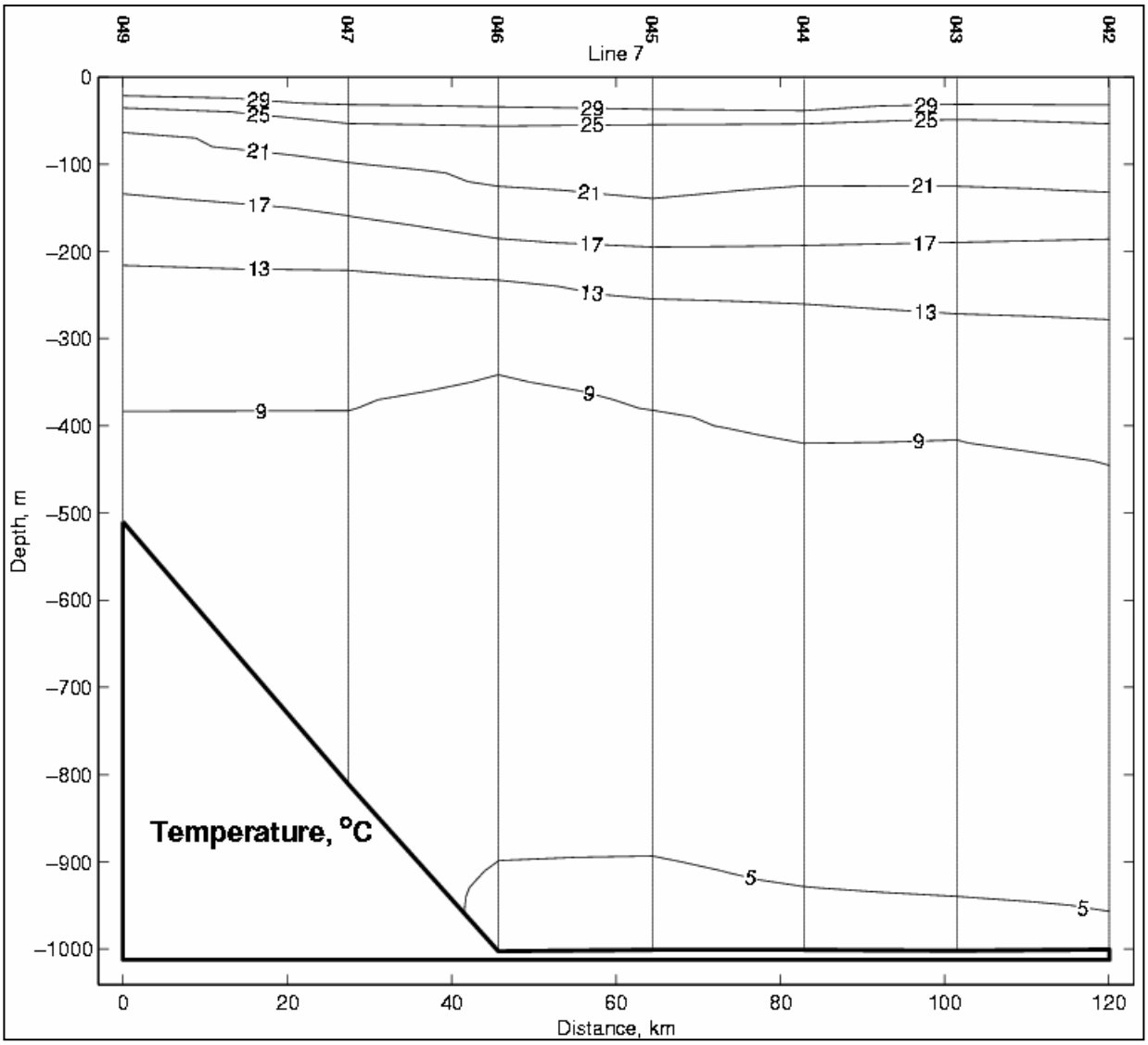

Figure B.14 Vertical profile of temperature for Transect 7A. The contour interval is 4°C. Note the strong thermocline between the 30 and 50m depth.

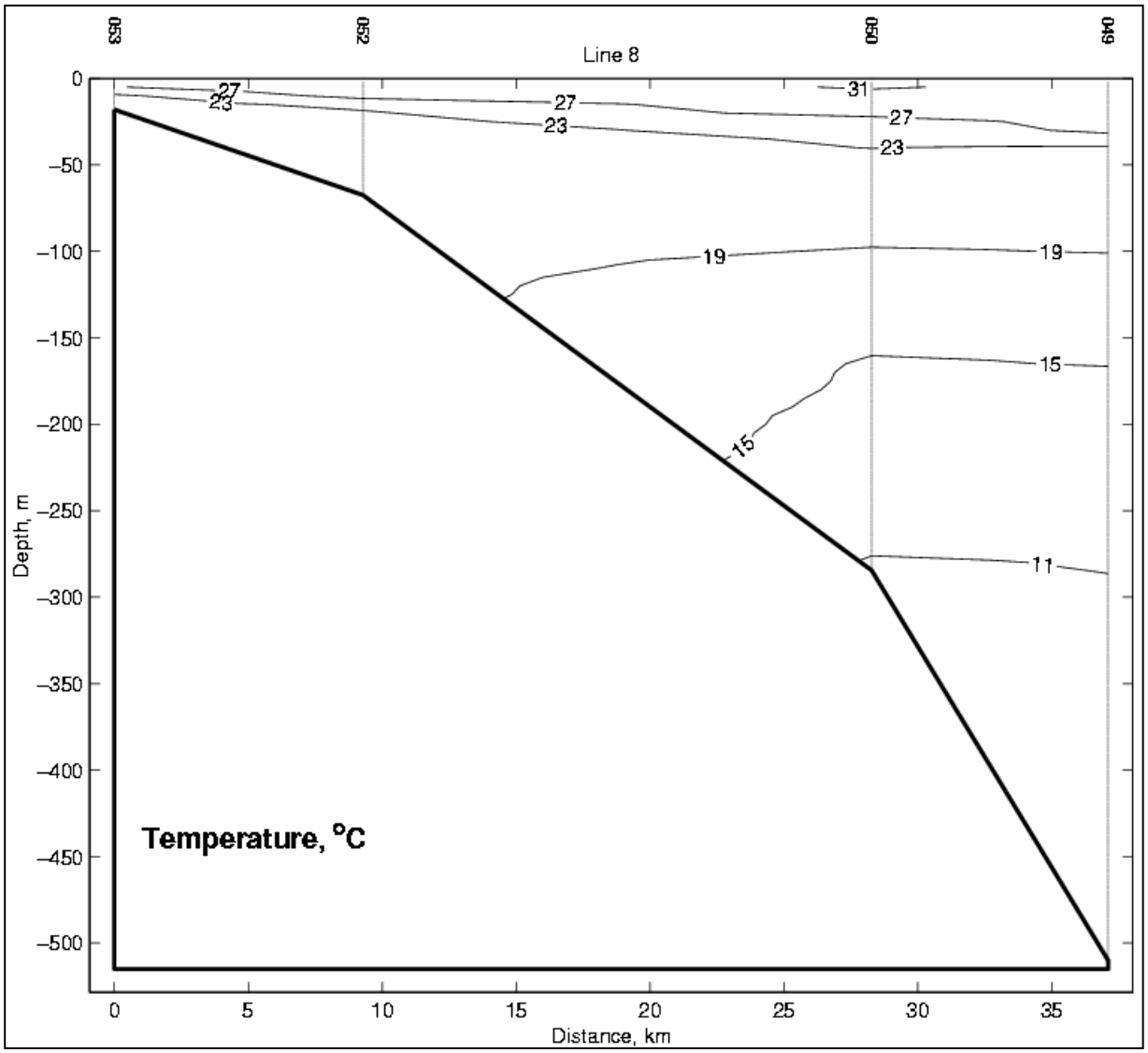

Figure B.15 Vertical profile of temperature for Transect 7B. The contour interval is 4°C.

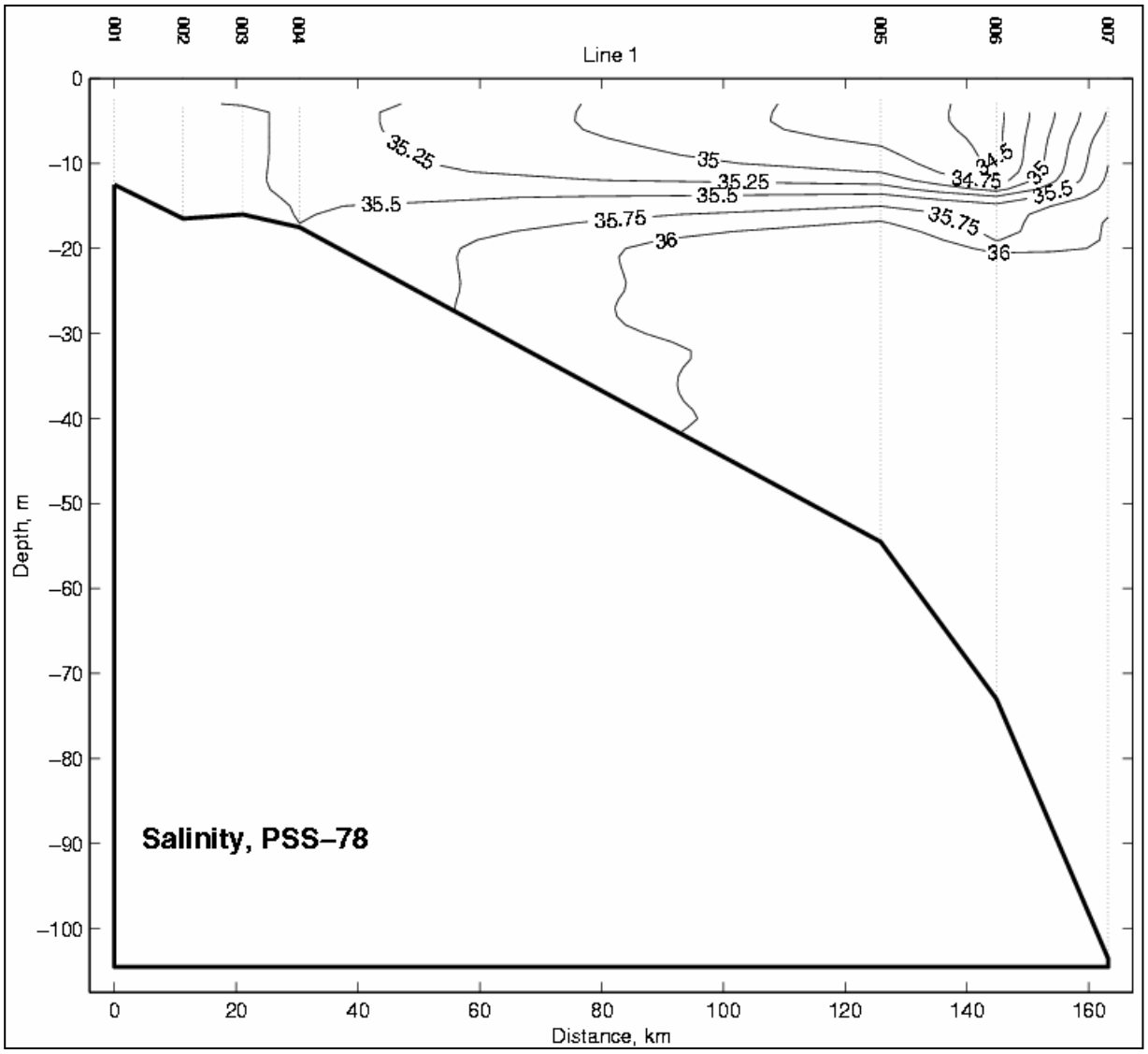

Figure B.16 Vertical profile of salinity for Transect 1. The contour interval is 0.25. Note the indication of a possible surface salinity front between stations 005

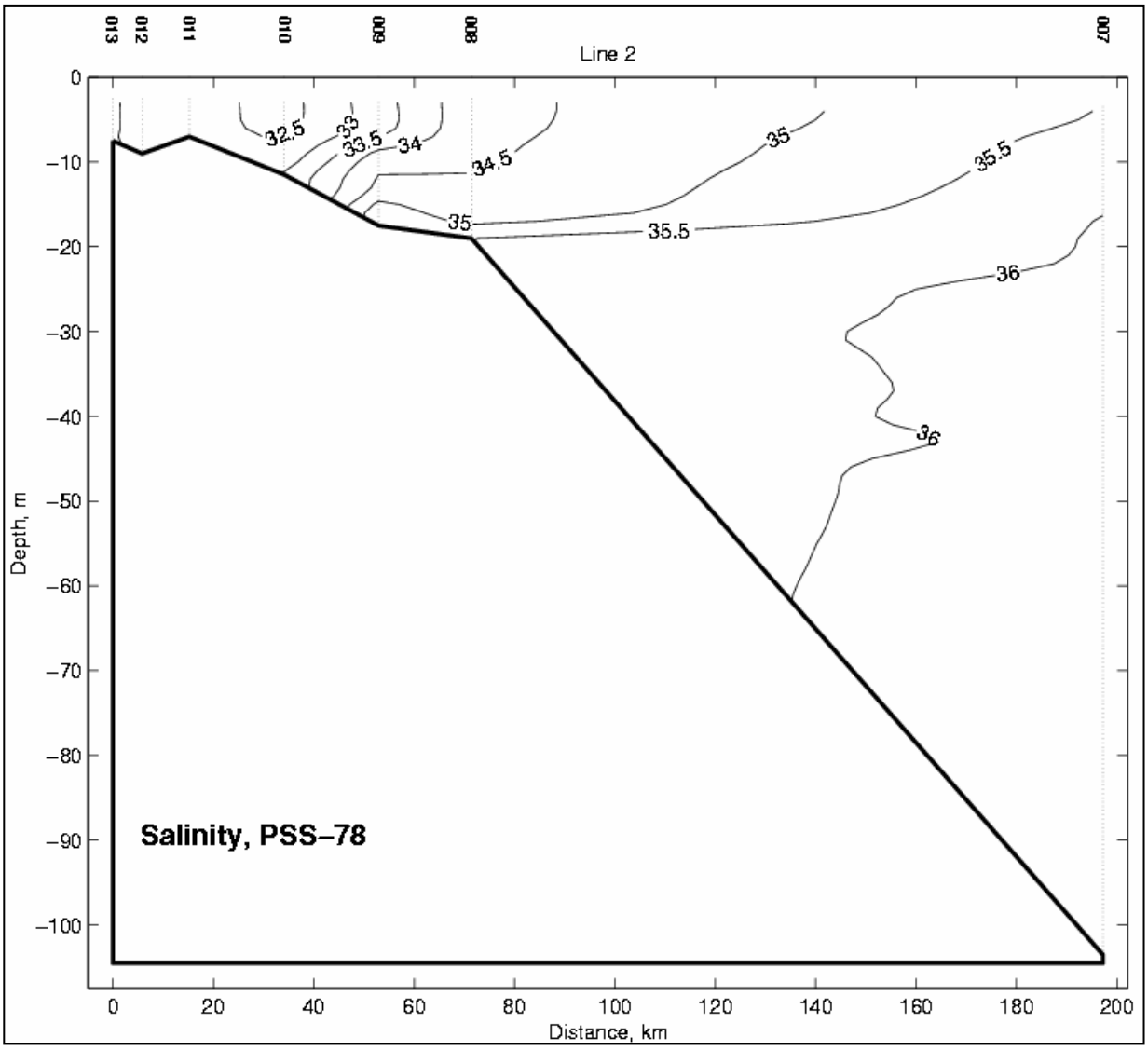

Figure B.17 Vertical profile of salinity for Transect 2. The contour interval is 0.50.

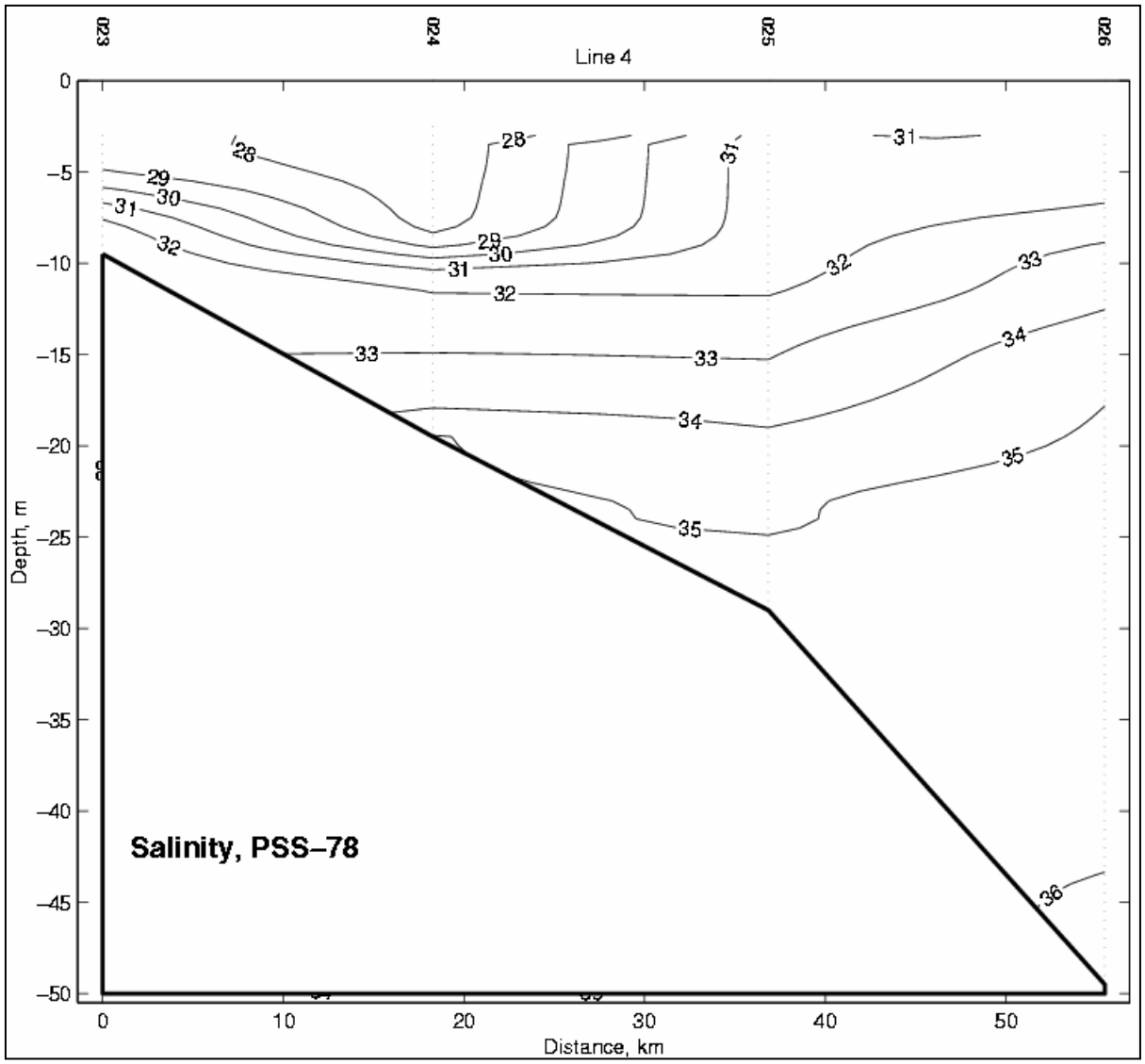

Figure B.18 Vertical profile of salinity for Transect 4. The contour interval is 1.0.

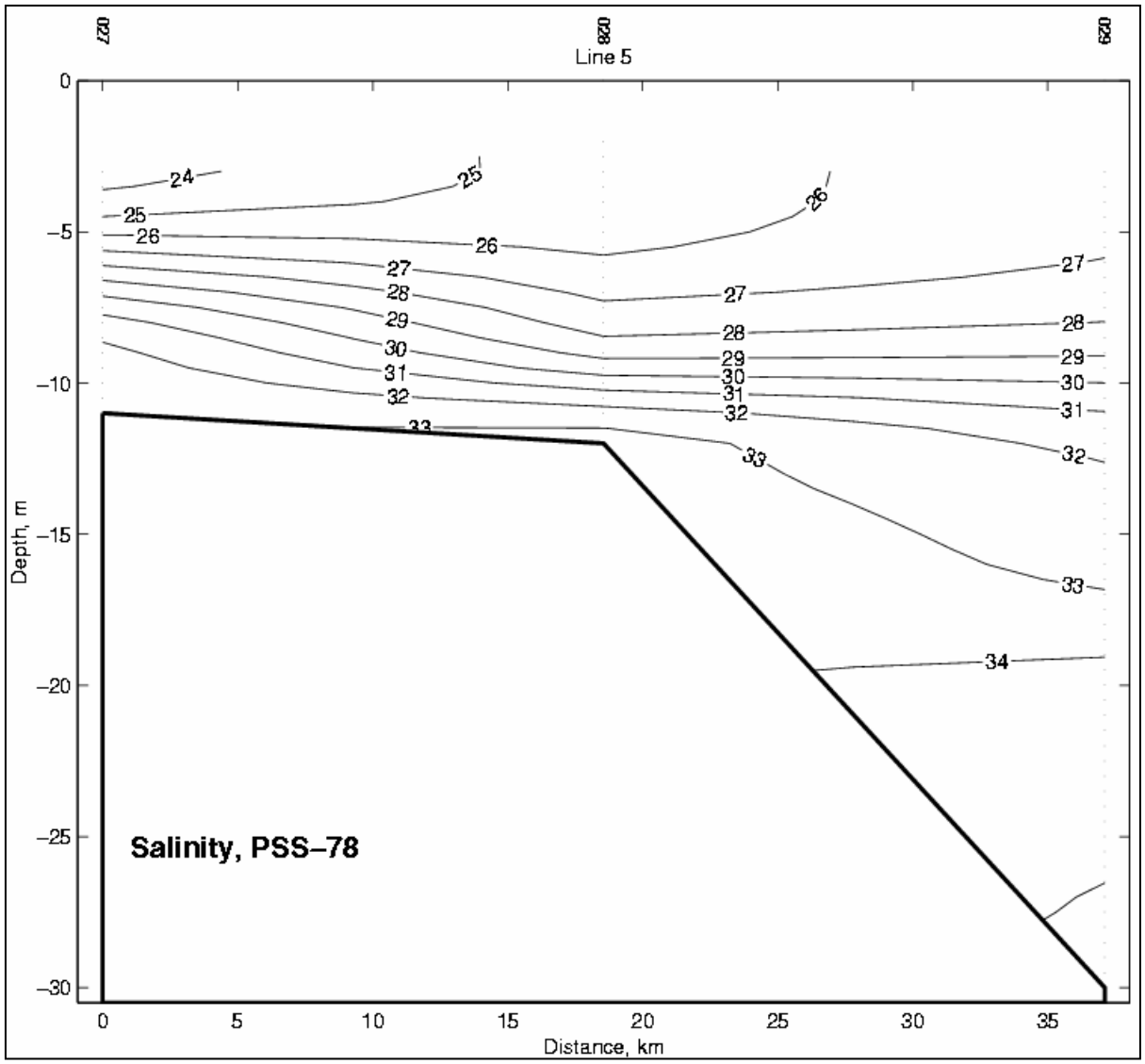

Figure B.19 Vertical profile of salinity for Transect 5. The contour interval is 1.0.

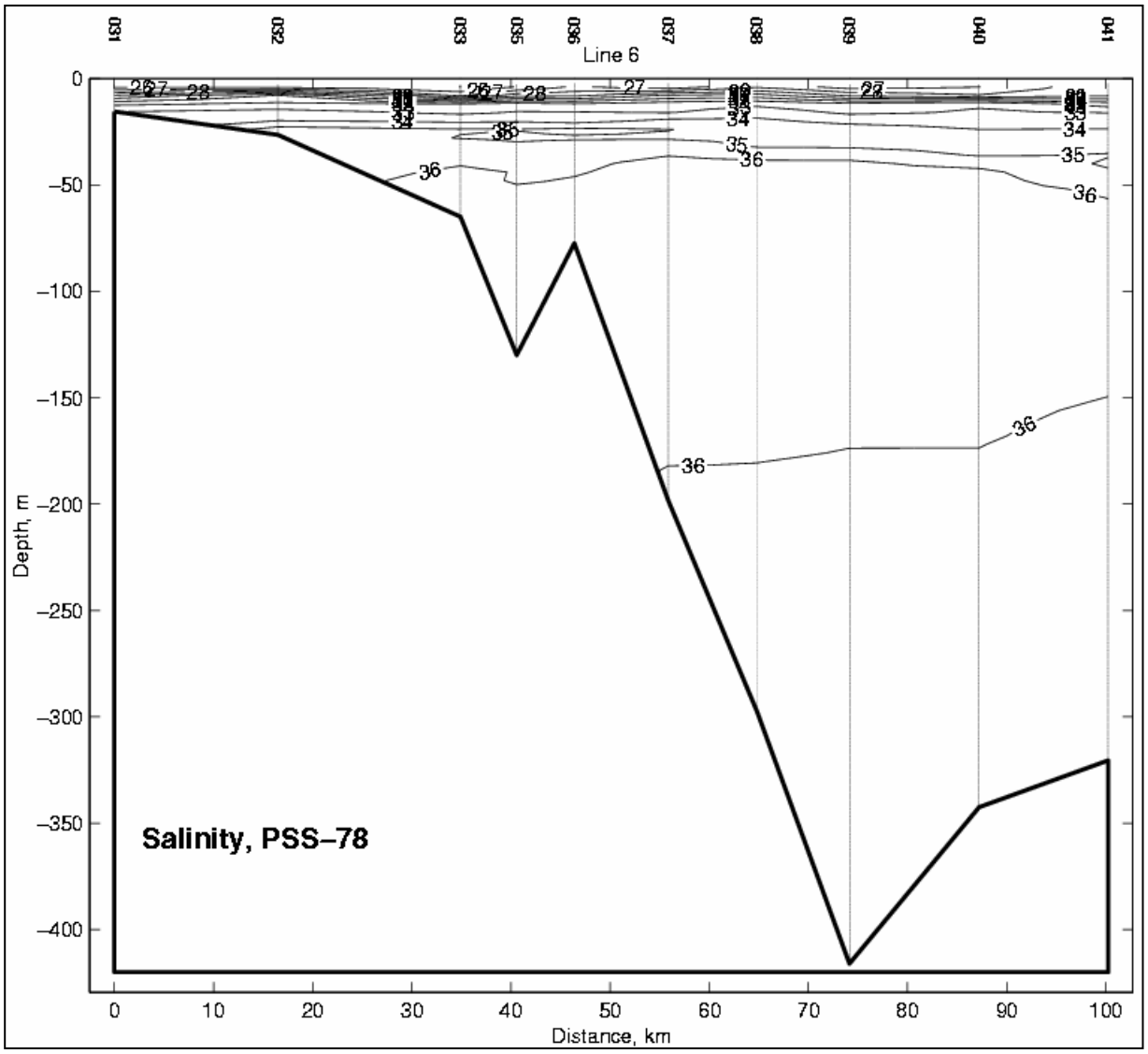

Figure B.20 Vertical profile of salinity for Transect 6. The contour interval is 1.0.

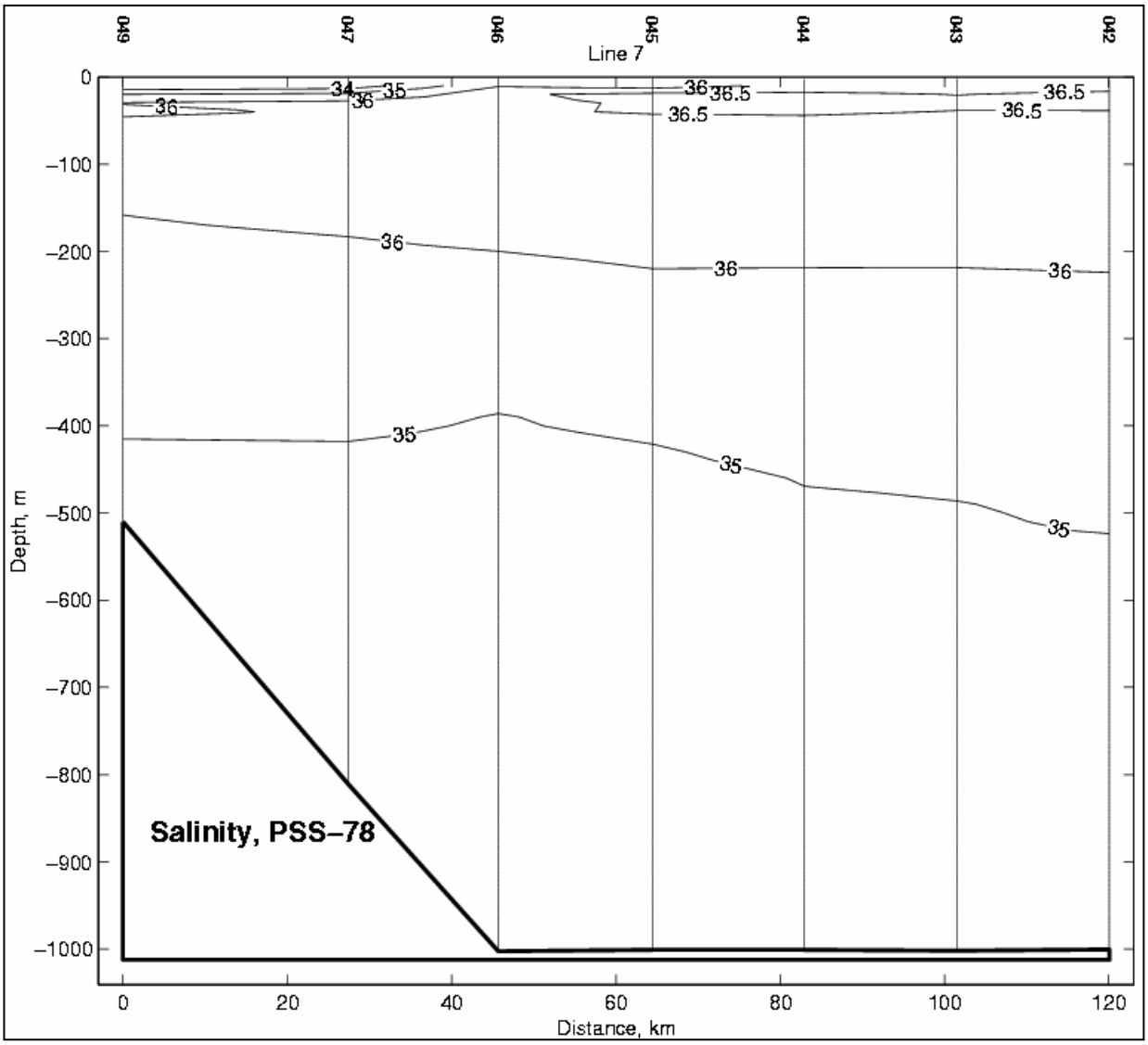

Figure B.21 Vertical profile of salinity for Transect 7A. The contour interval is 1.0. Note the presence of a Loop Current intrusion, S > 36.5.

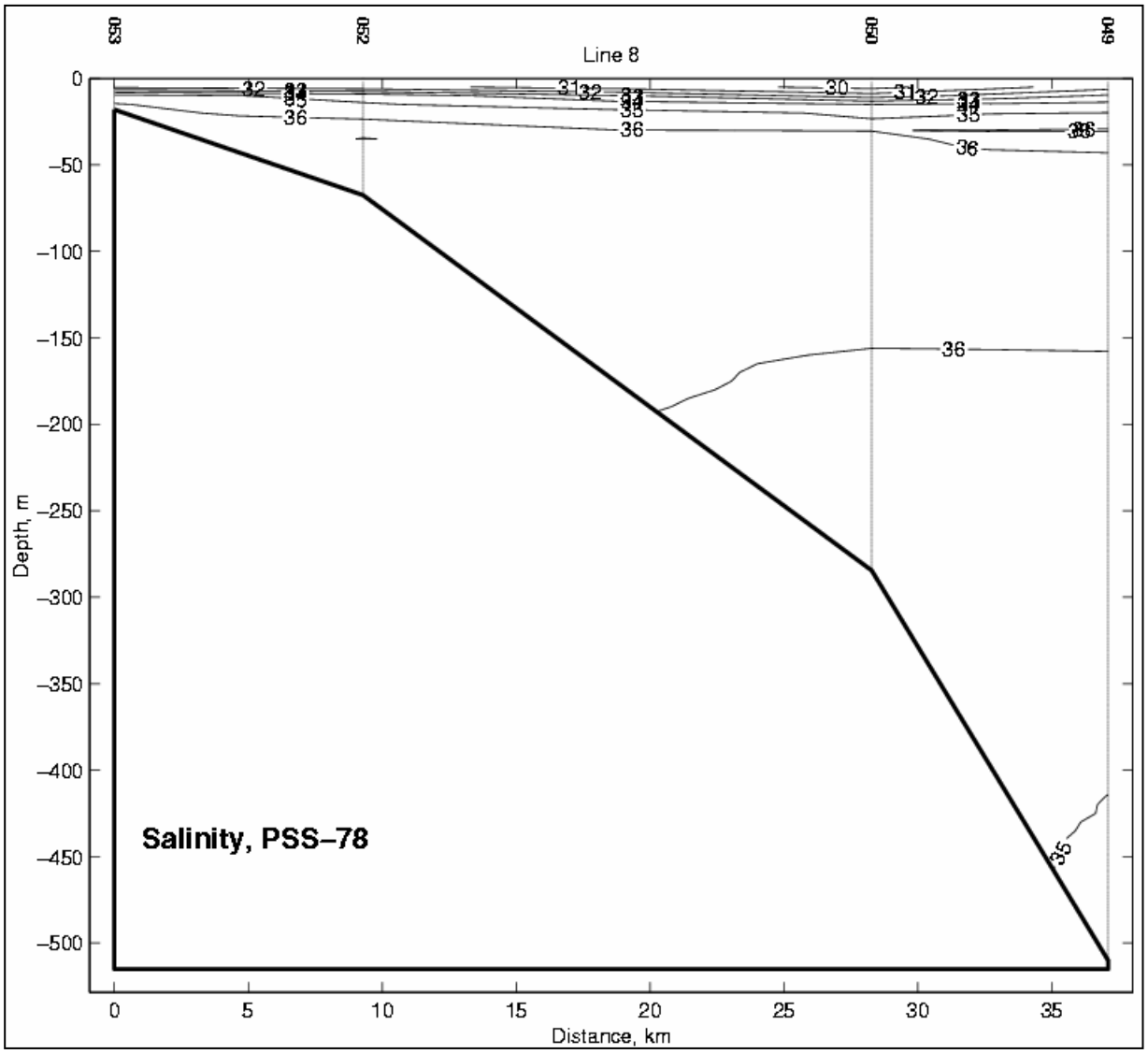

Figure B.22 Vertical profile of salinity for Transect 7B. The contour interval is 1.0.

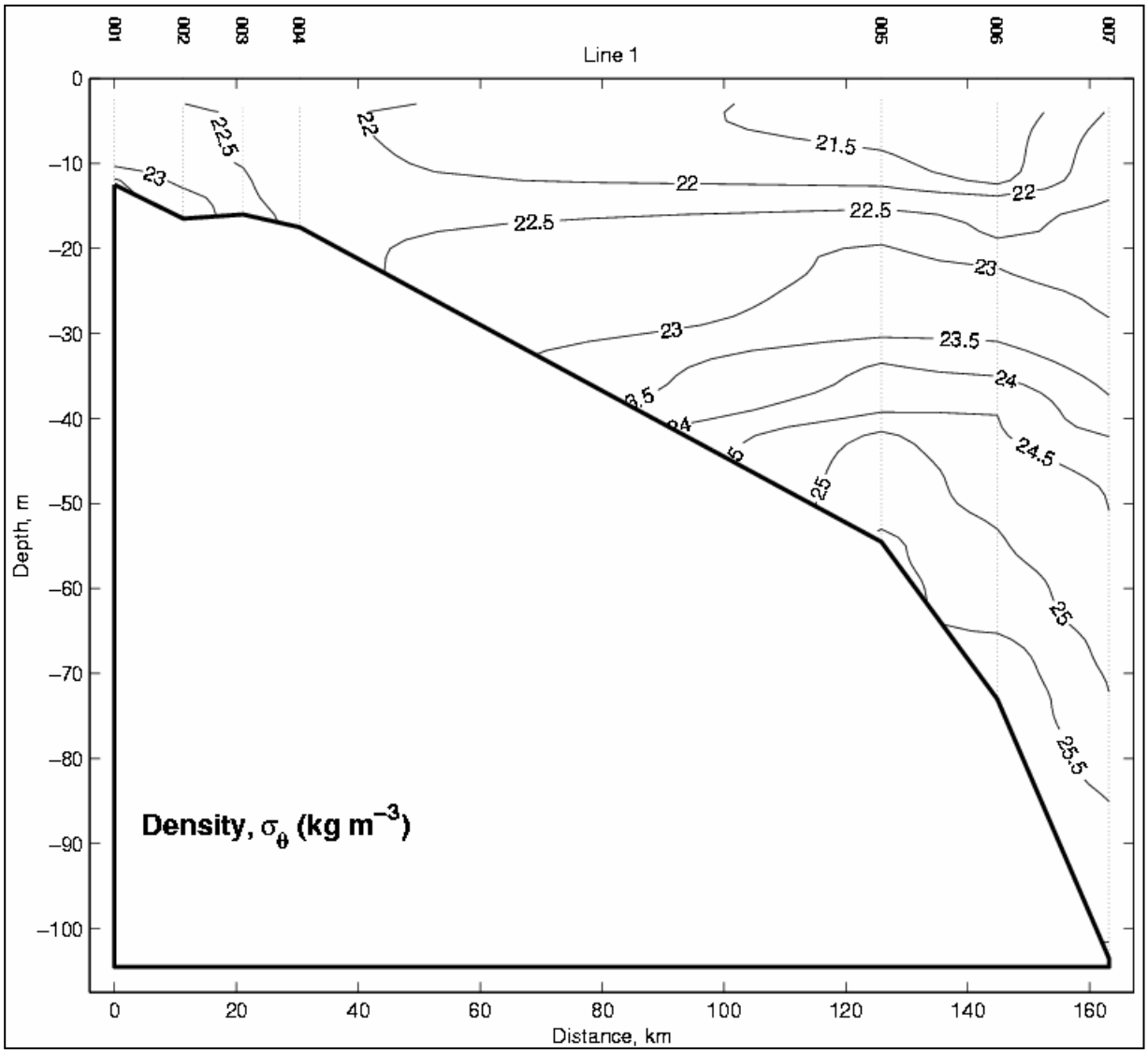

Figure B.23 Vertical profile of density for Transect 1. The contour interval is 0.5 σ_θ.

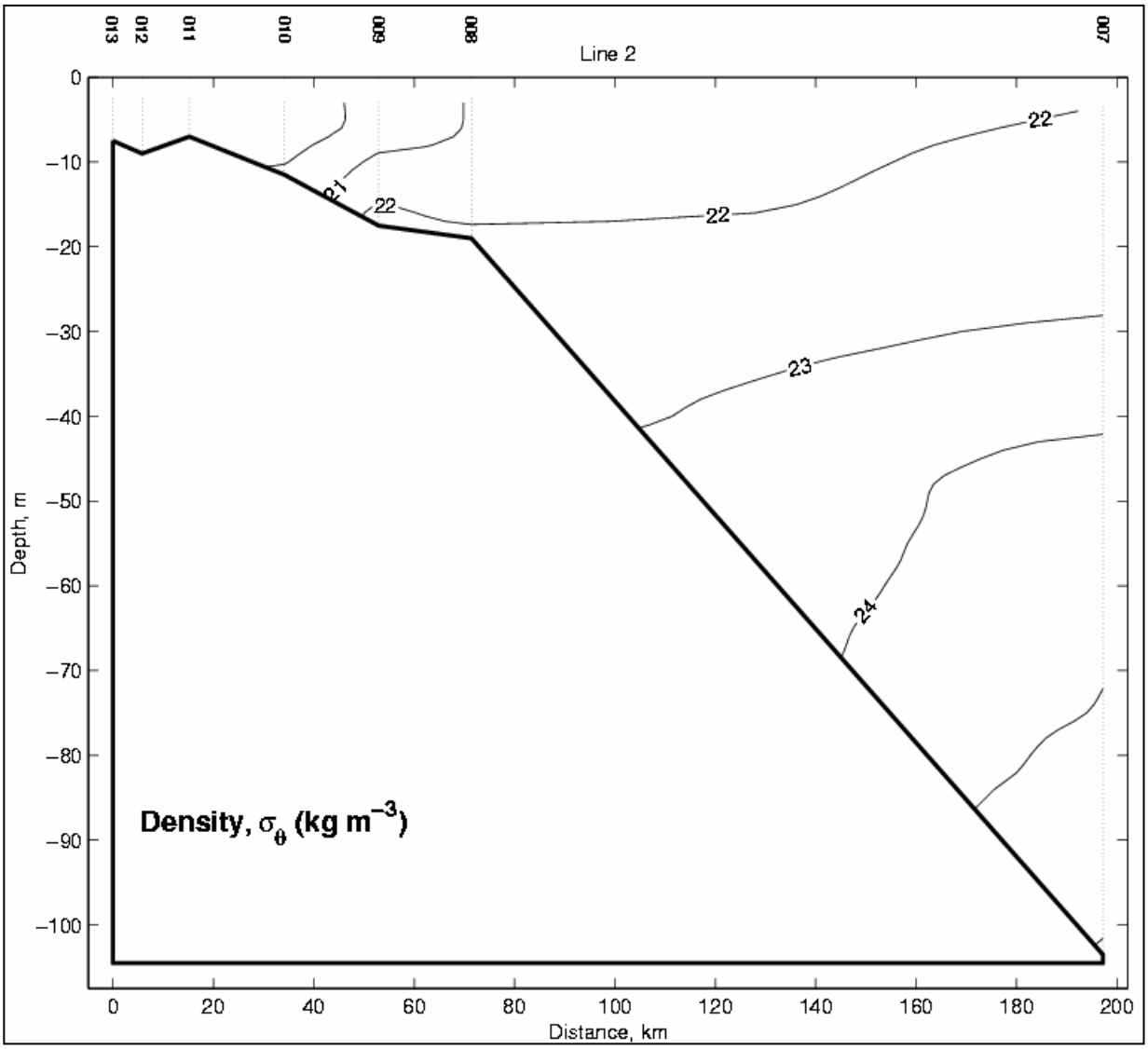

Figure B.24 Vertical profile of density for Transect 2. The contour interval is 1.0 σ_θ.

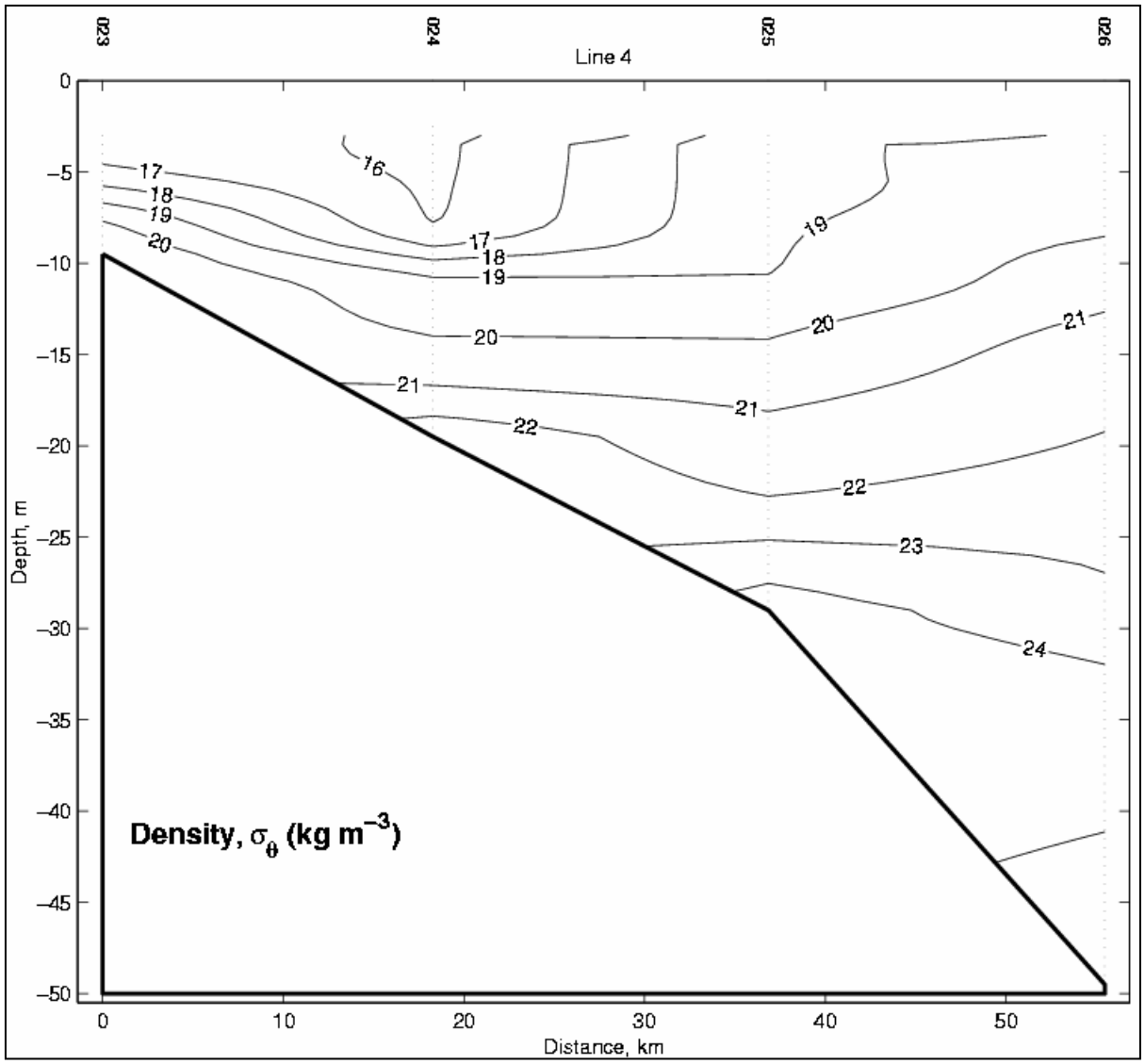

Figure B.25 Vertical profile of density for Transect 4. The contour interval is 1.0 σ_θ.

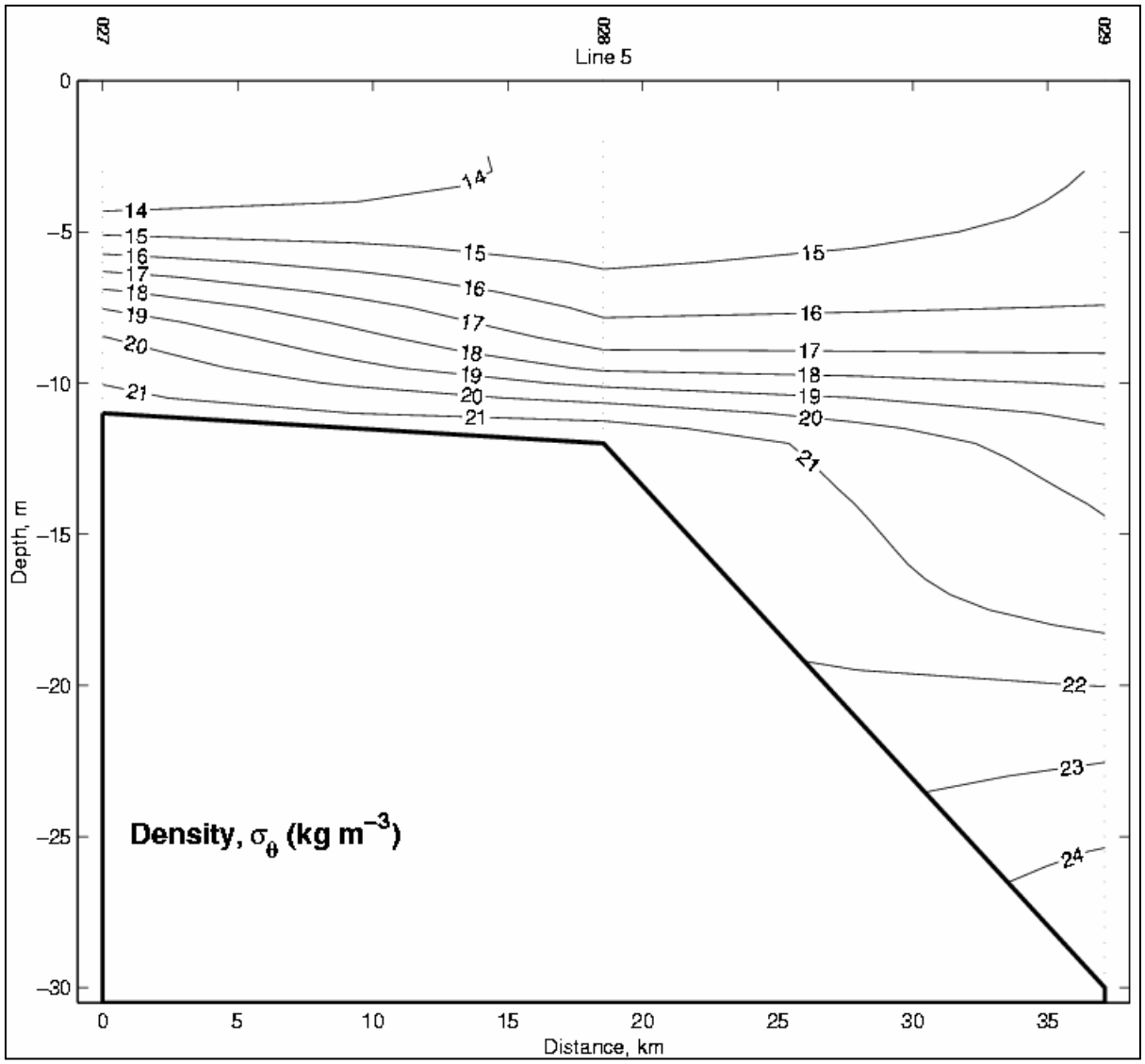

Figure B.26 Vertical profile of density for Transect 5. The contour interval is 1.0 σ_θ.

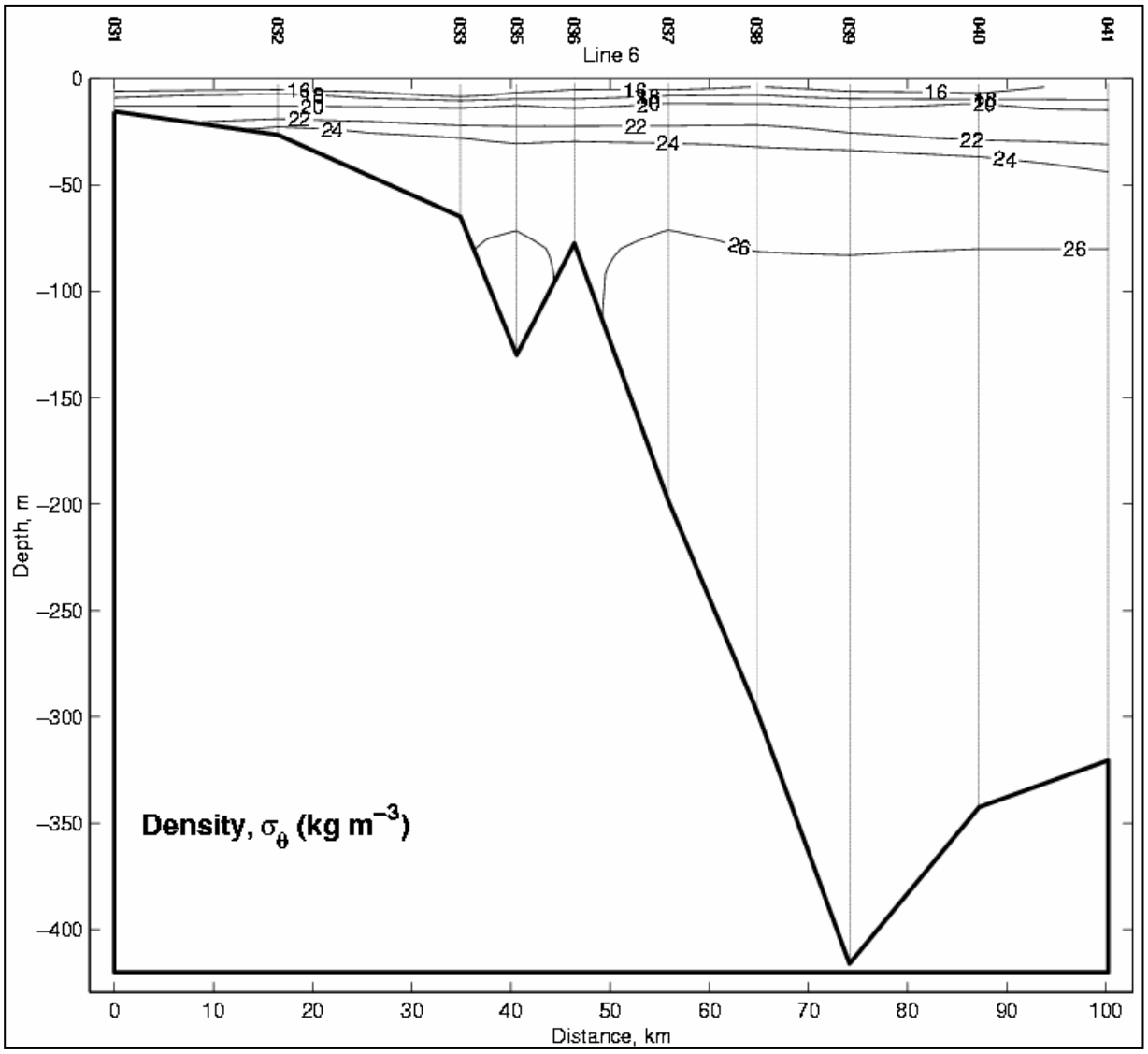

Figure B.27 Vertical profile of density for Transect 6. The contour interval is 2.0 σ_θ.

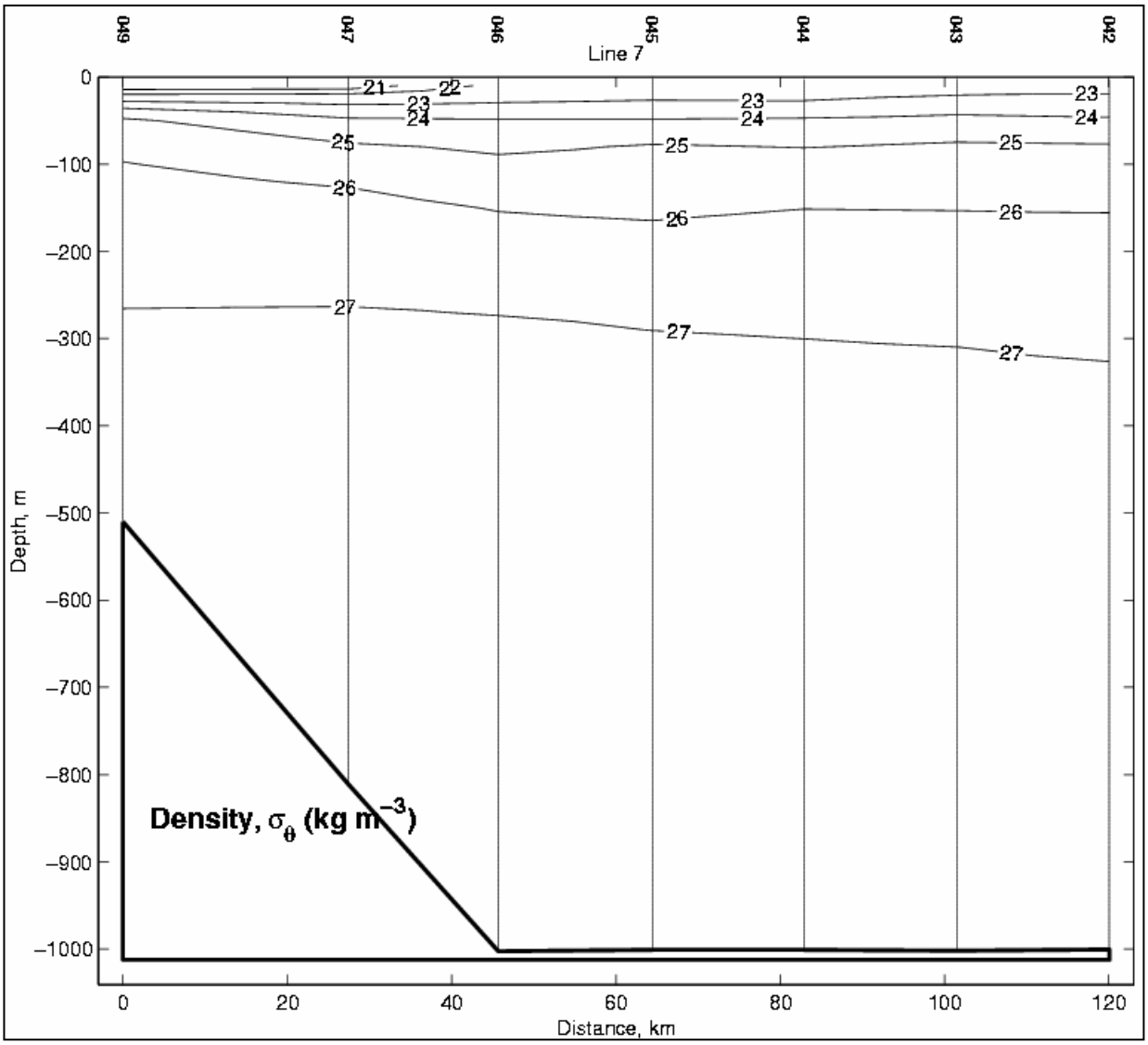

Figure B.28 Vertical profile of density for Transect 7A. The contour interval is 1.0 σ_θ.

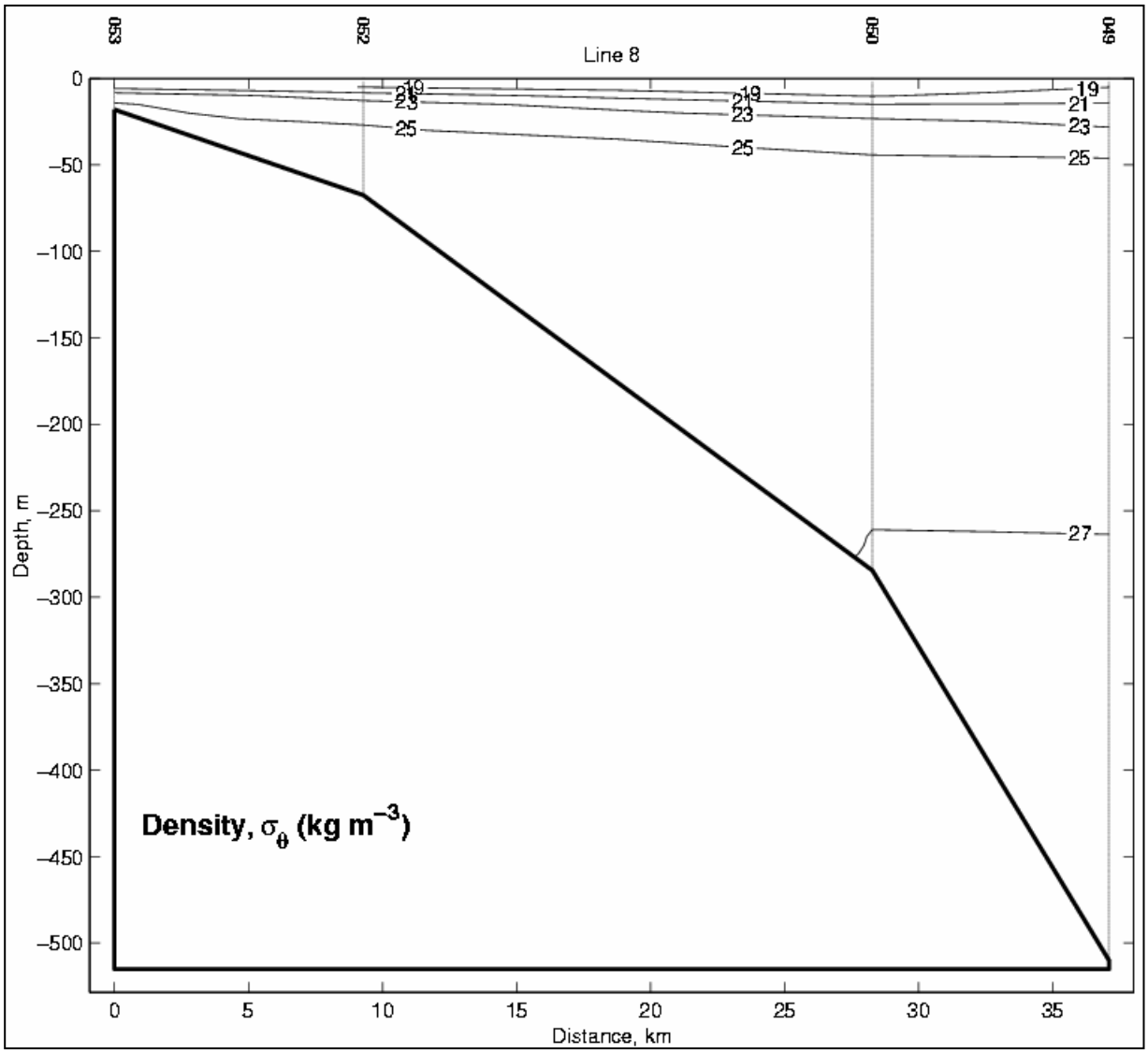

Figure B.29 Vertical profile of density for Transect 7B. The contour interval is 2.0 σ_θ.

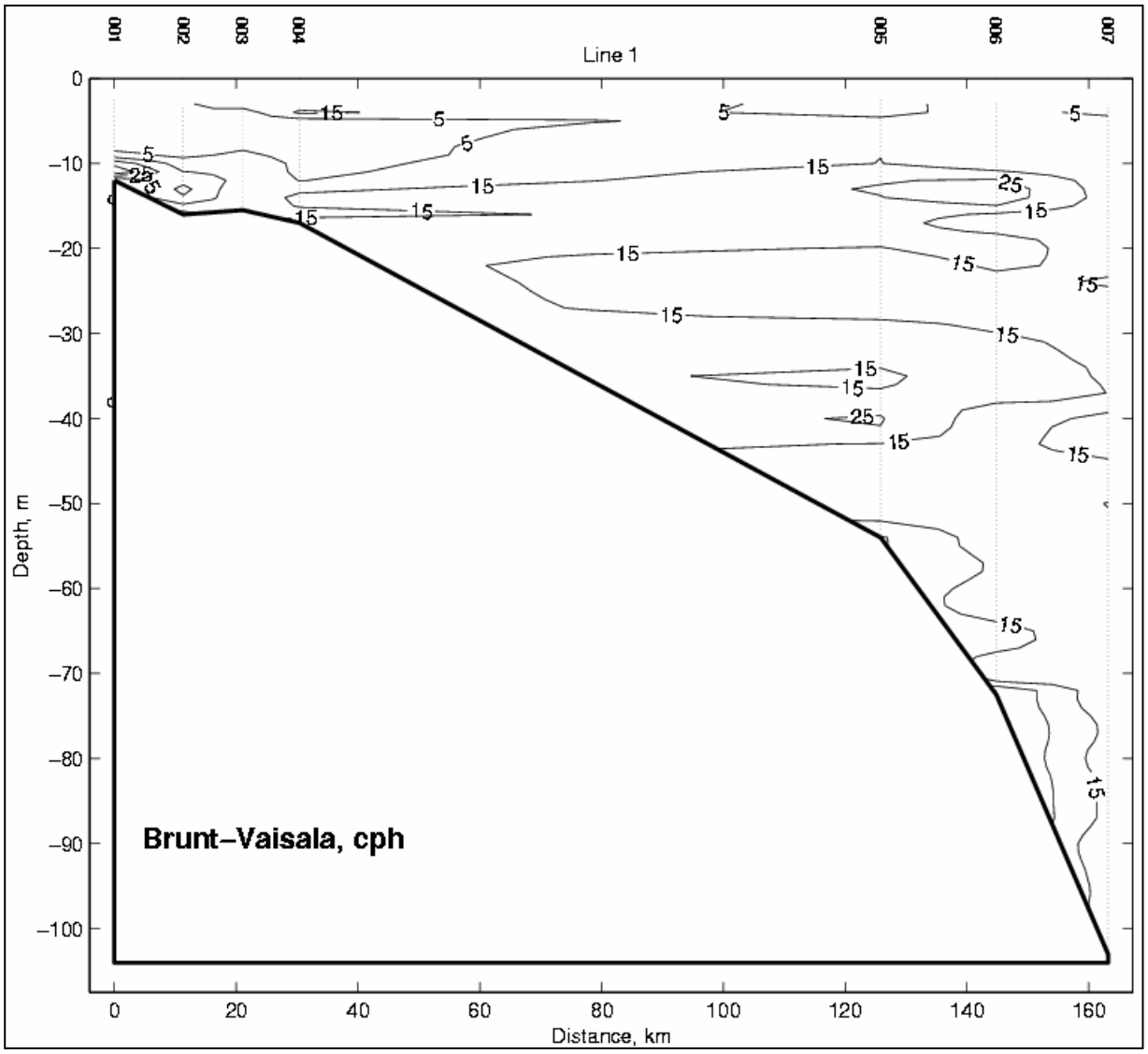

Figure B.30 Vertical profile of Brunt-Vaisala frequency for Transect 1. The contour interval is 5 cph. Evidence of a strong stability layer is seen at 10m.

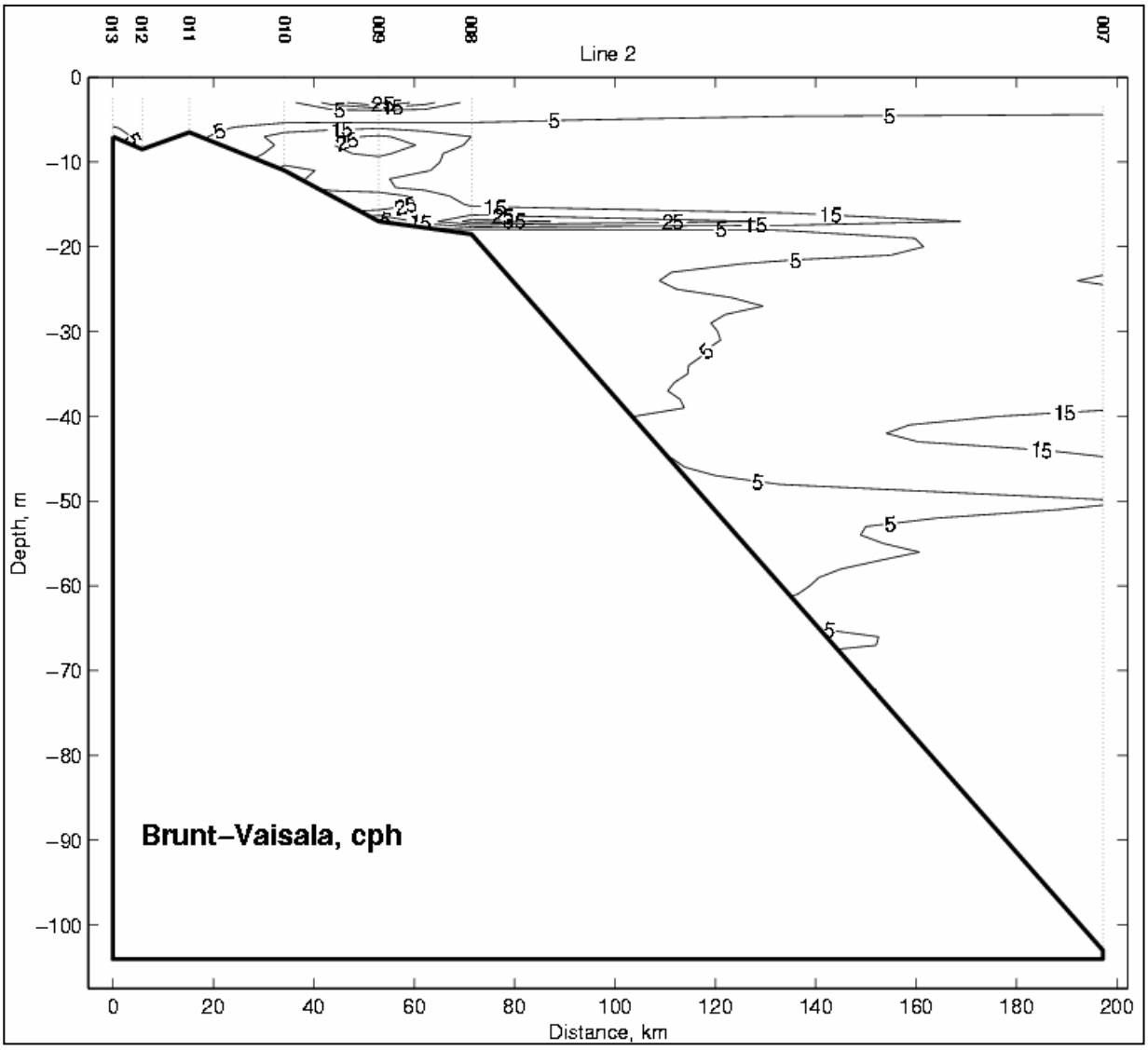

Figure B.31. Vertical profile of Brunt-Vaisala frequency for Transect 2. The contour interval is 10 cph. Evidence of a strong stability layer is seen at 15m.

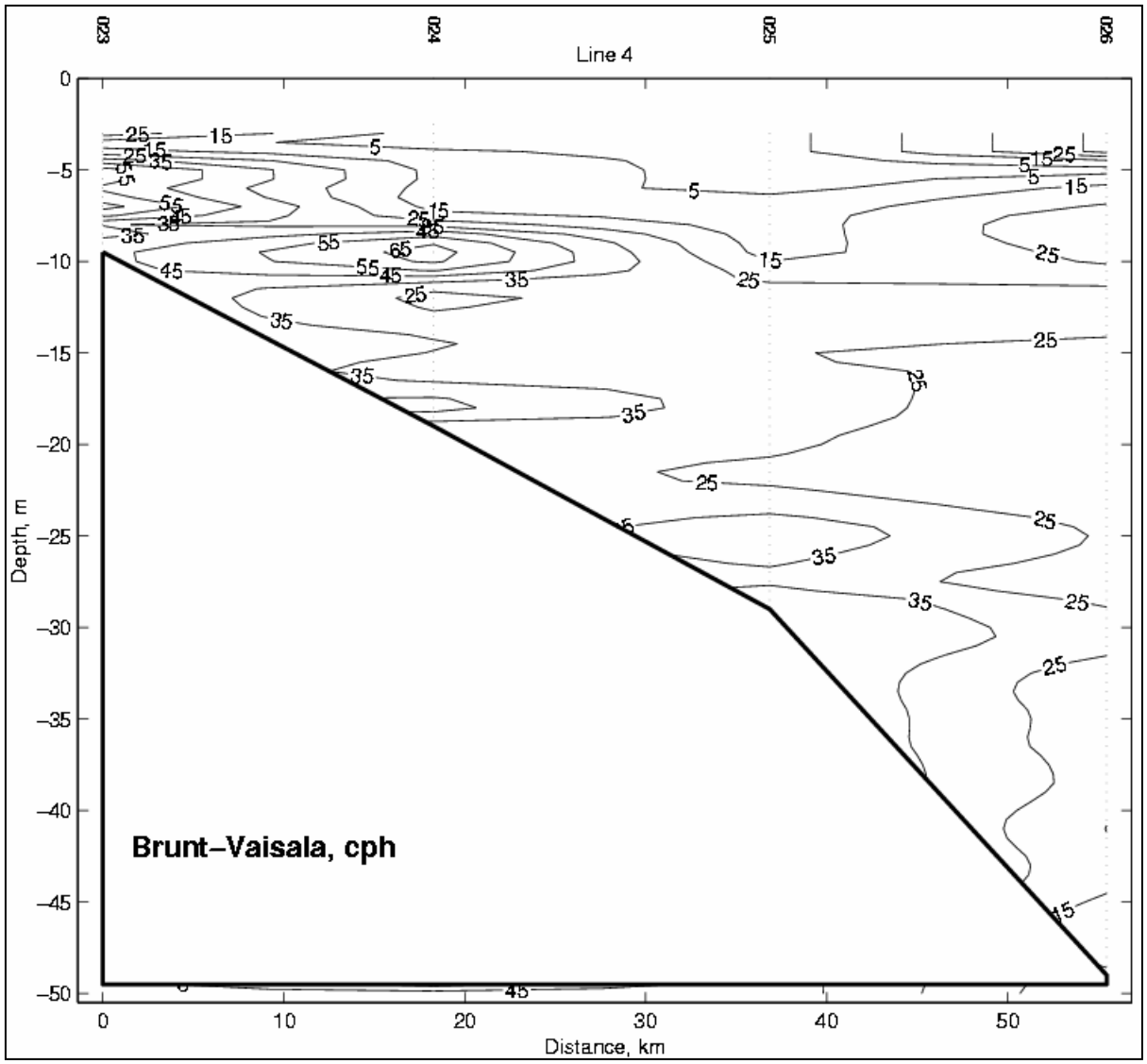

Figure B.32 Vertical profile of Brunt-Vaisala frequency for Transect 4. The contour interval is 10 cph.

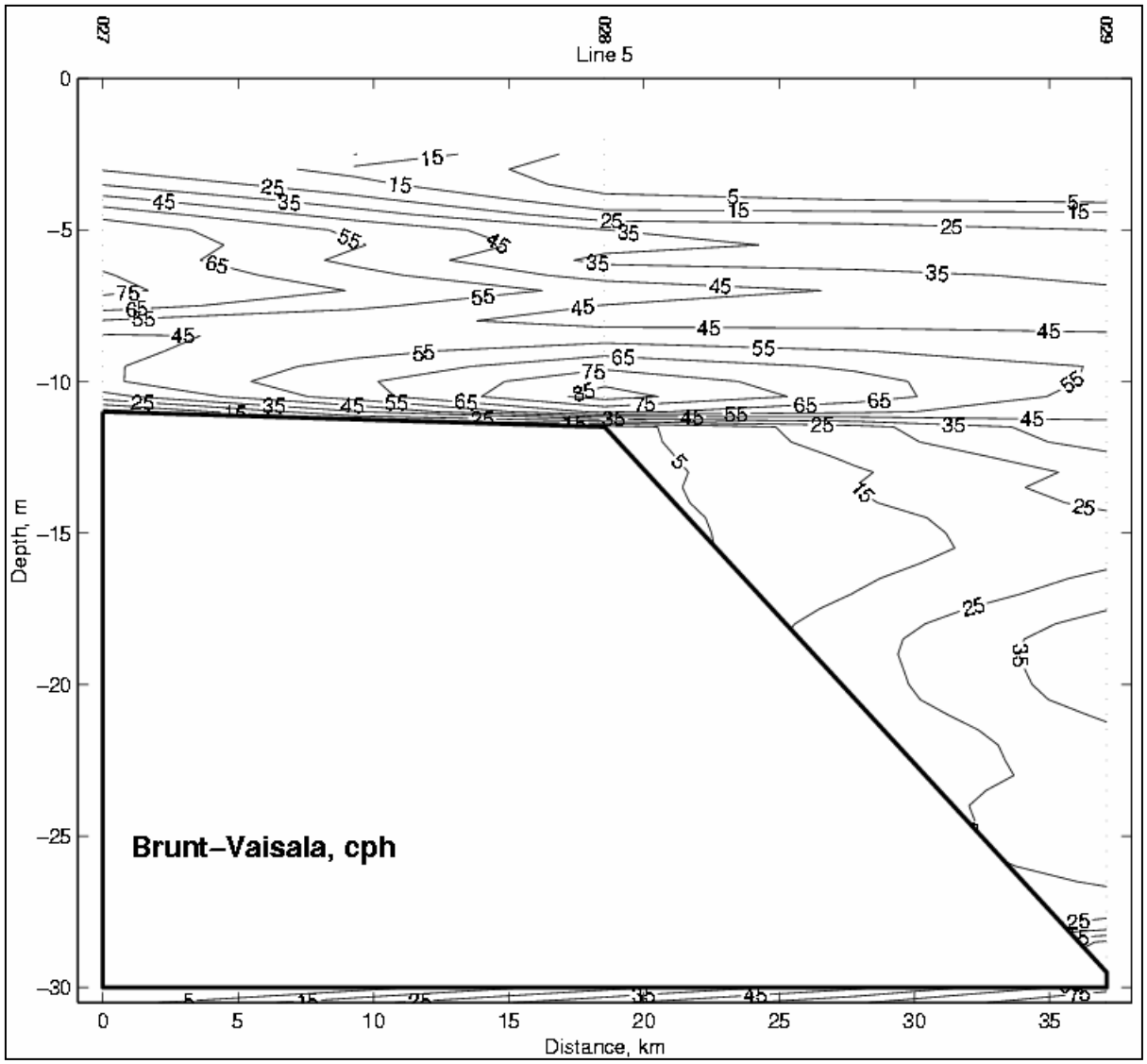

Figure B.33 Vertical profile of Brunt-Vaisala frequency for Transect 5. The contour interval is 10 cph.

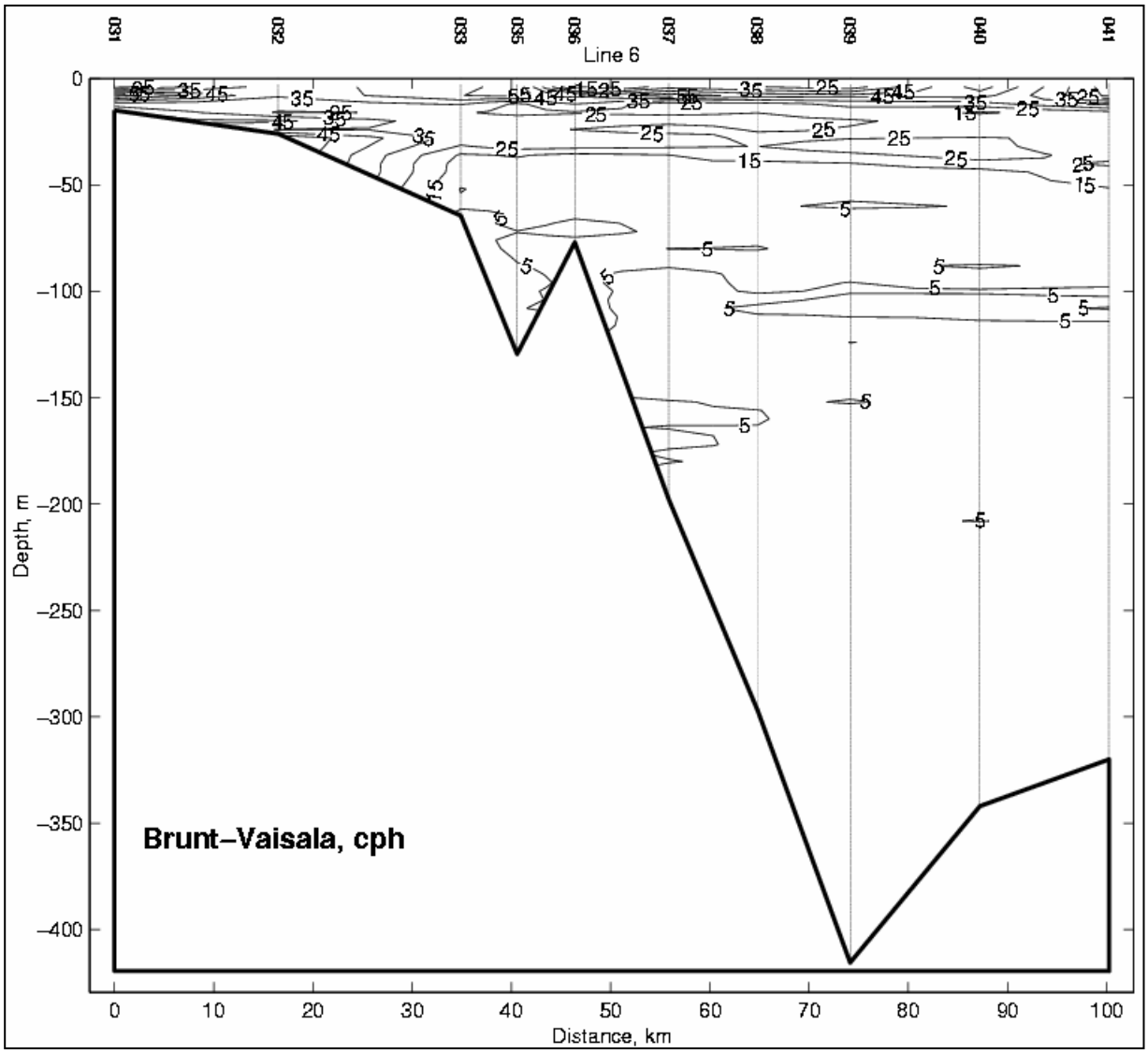

Figure B.34 Vertical profile of Brunt-Vaisala frequency for Trsansect 6. The contour interval is 10 cph.

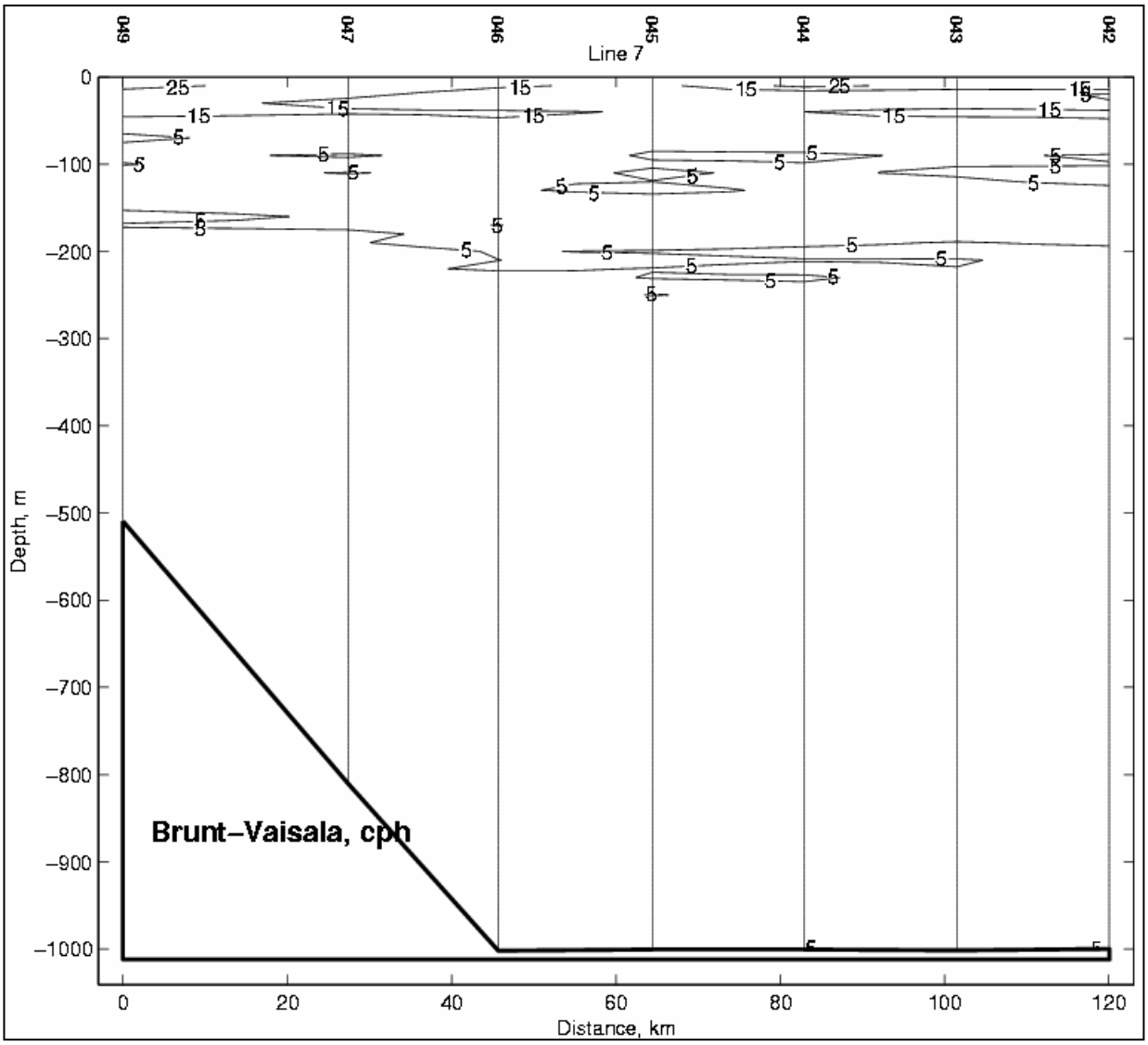

Figure B.35 Vertical profile of Brunt-Vaisala frequency for Transect 7A. The contour interval is 5 cph.

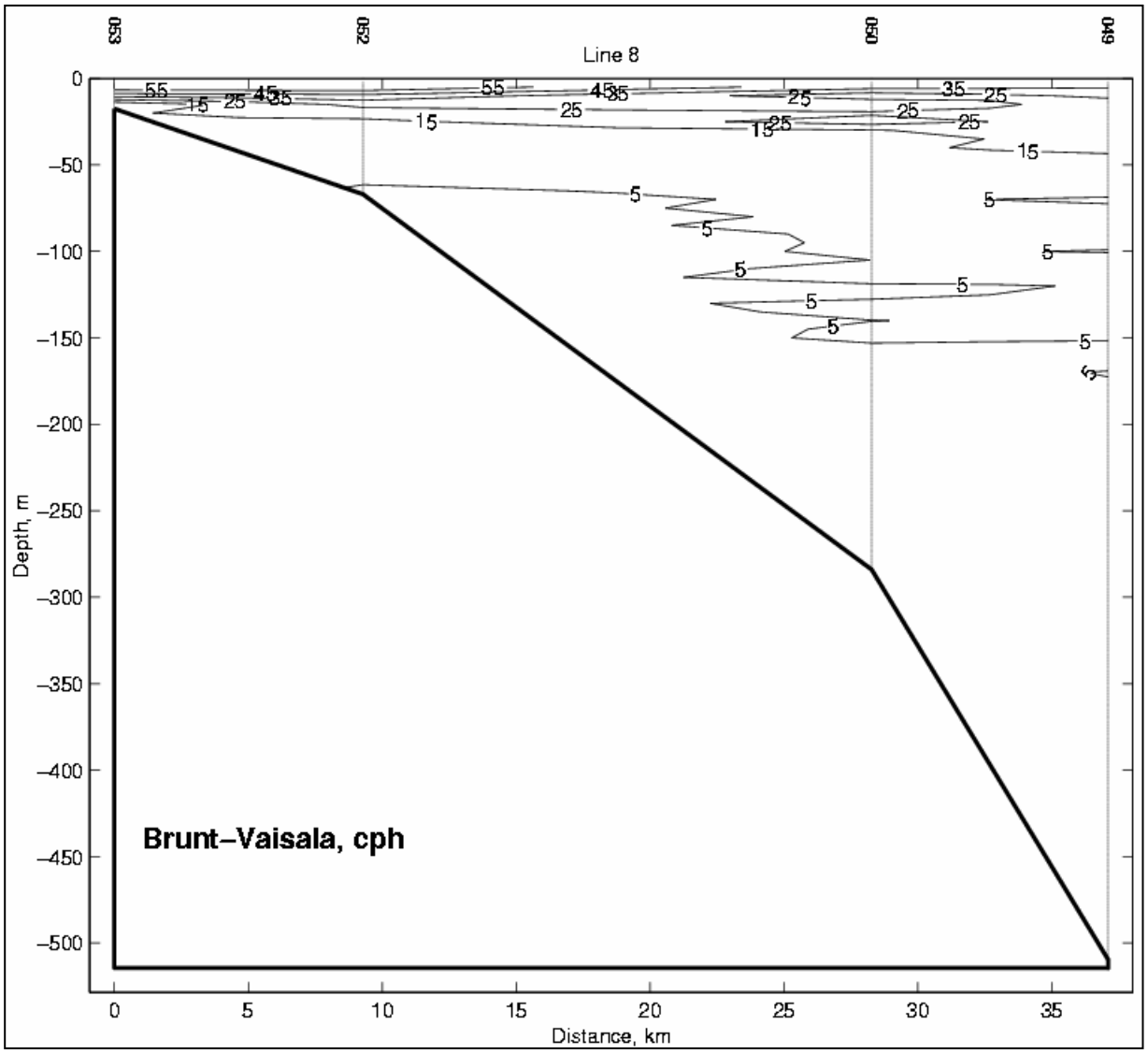

Figure B.36 Vertical profile of Brunt-Vaisala frequency for Transect 7B. The contour interval is 10 cph. Evidence of a strong stability layer is seen at the surface.

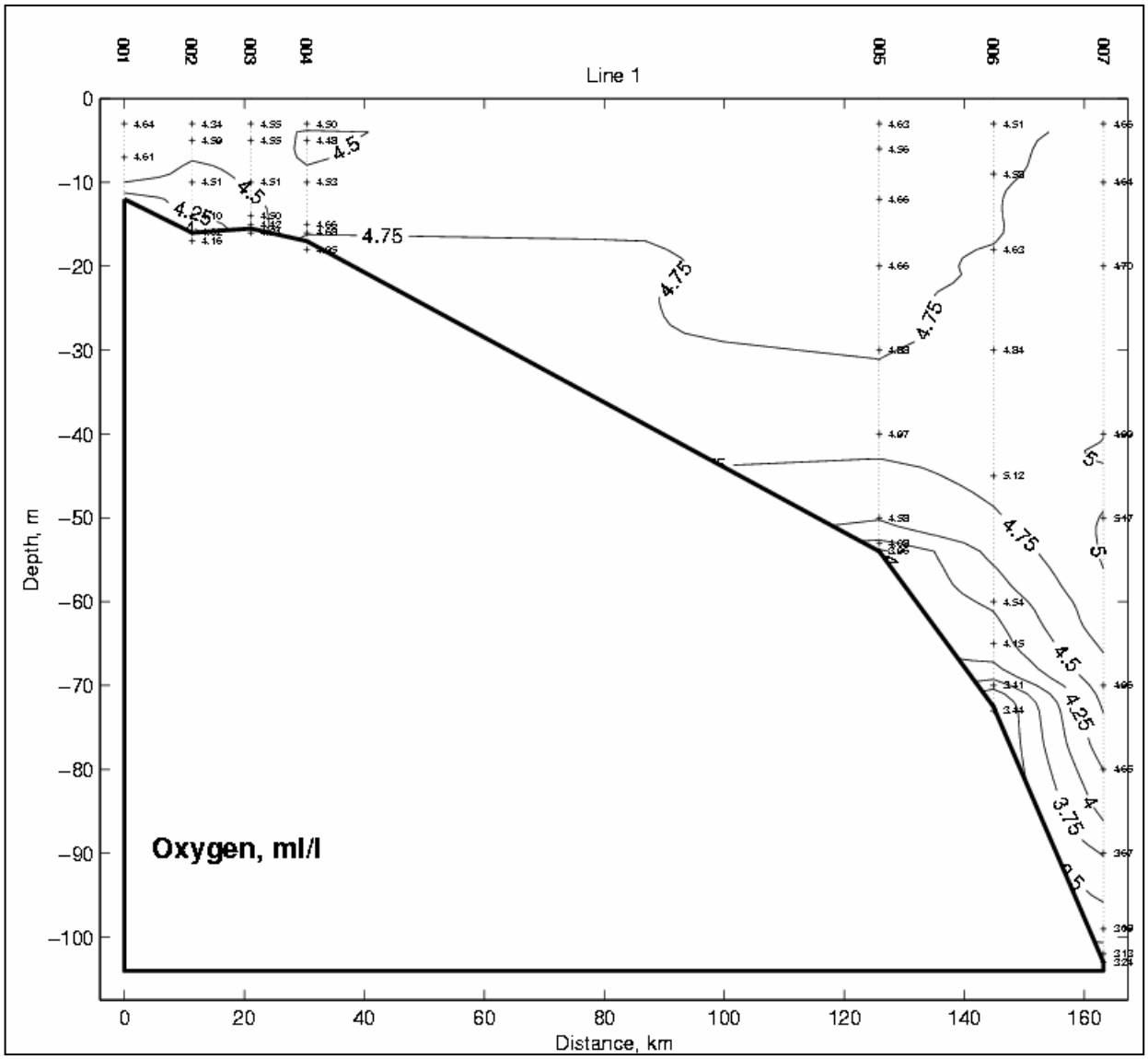

Figure B.37 Vertical profile of dissolved oxygen for Transect 1. The contour interval is 0.25 ml l^{-1}.

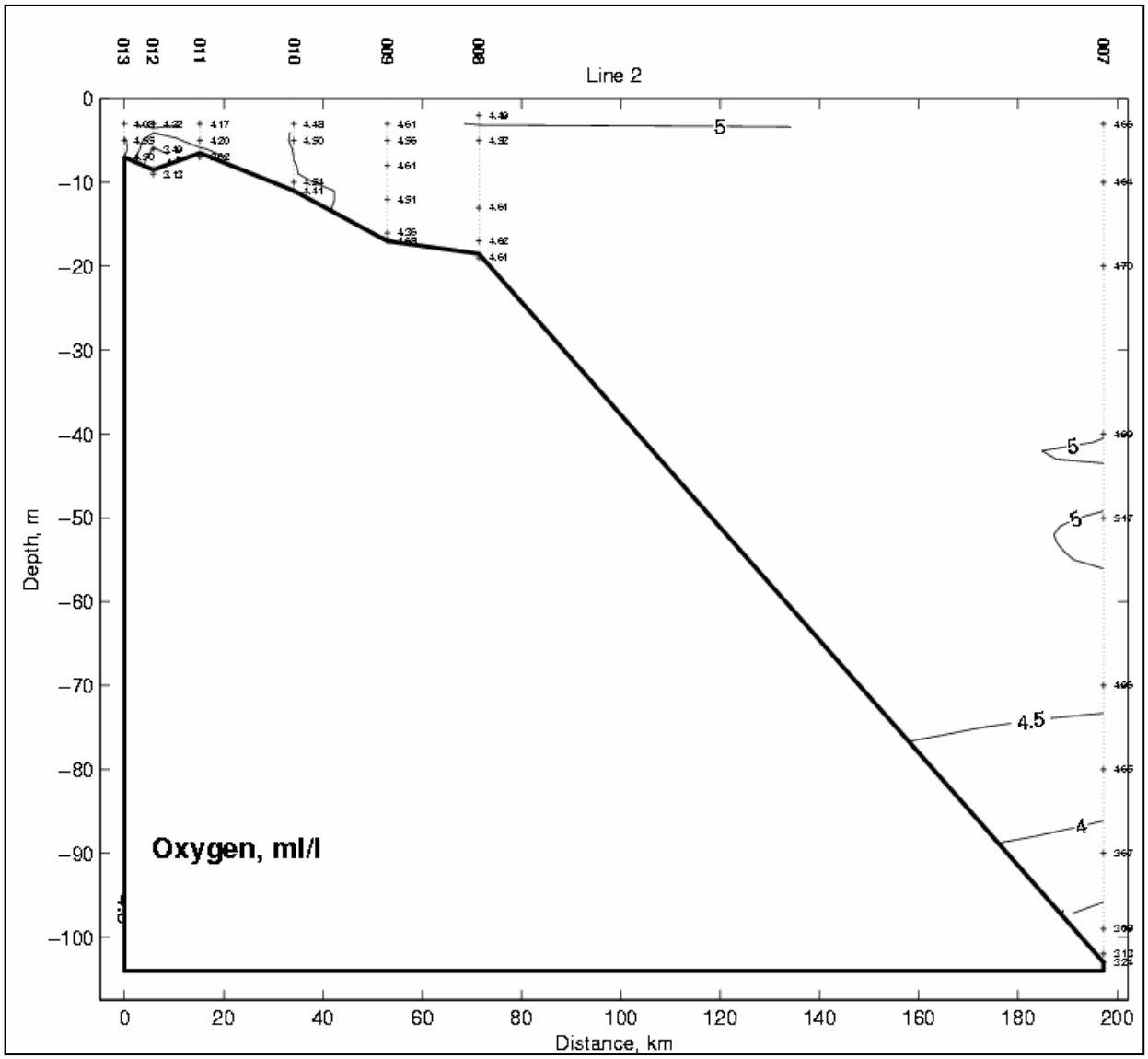

Figure B.38 Vertical profile of dissolved oxygen for Transect 2. The contour interval is 0.5 ml l^{-1}.

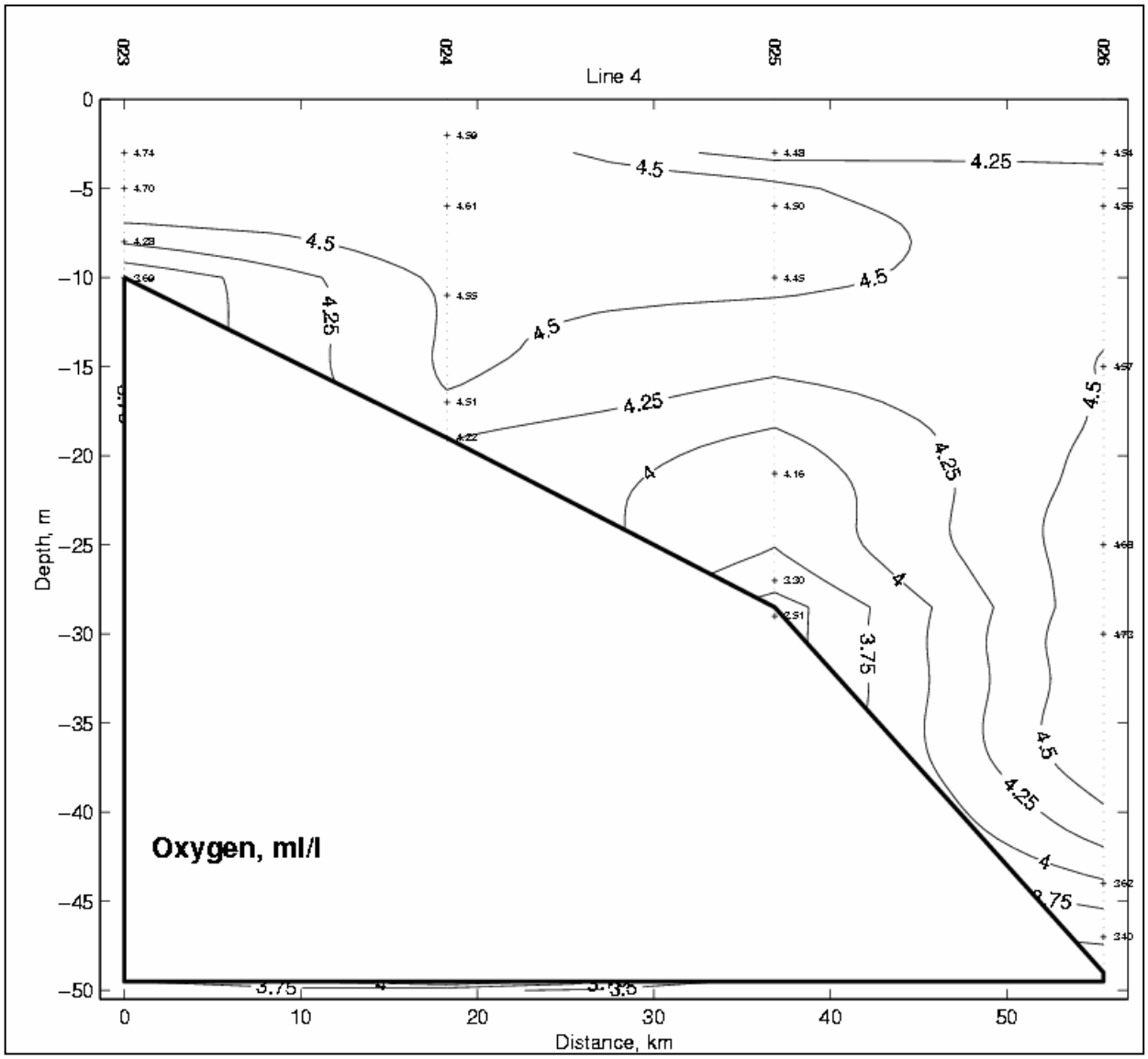

Figure B.39 Vertical profile of dissolved oxygen for Transect 4. The contour interval is 0.25 ml l^{-1}.

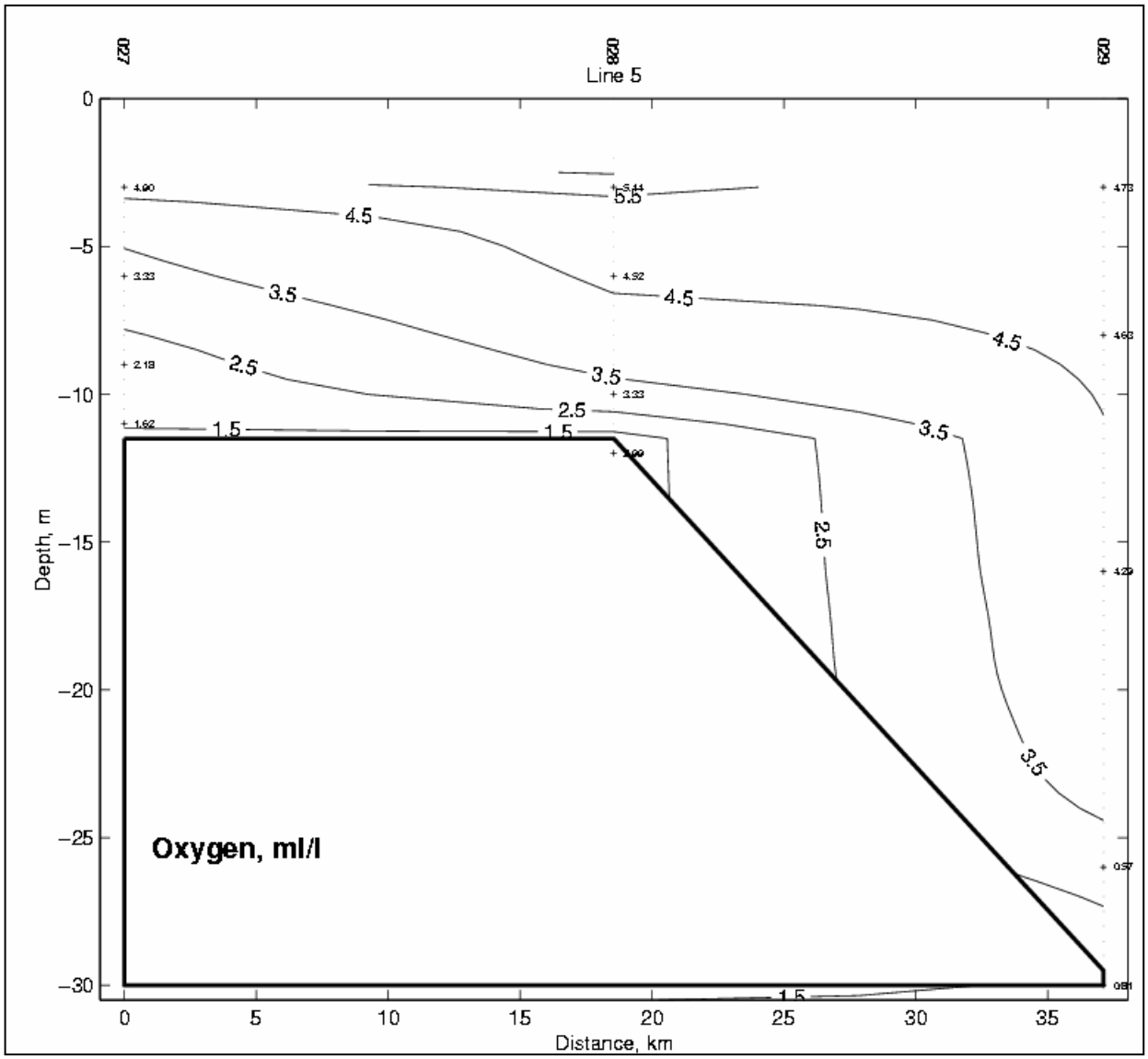

Figure B.40 Vertical profile of dissolved oxygen for Transect 5. The contour interval is 1.0 ml l^{-1}.

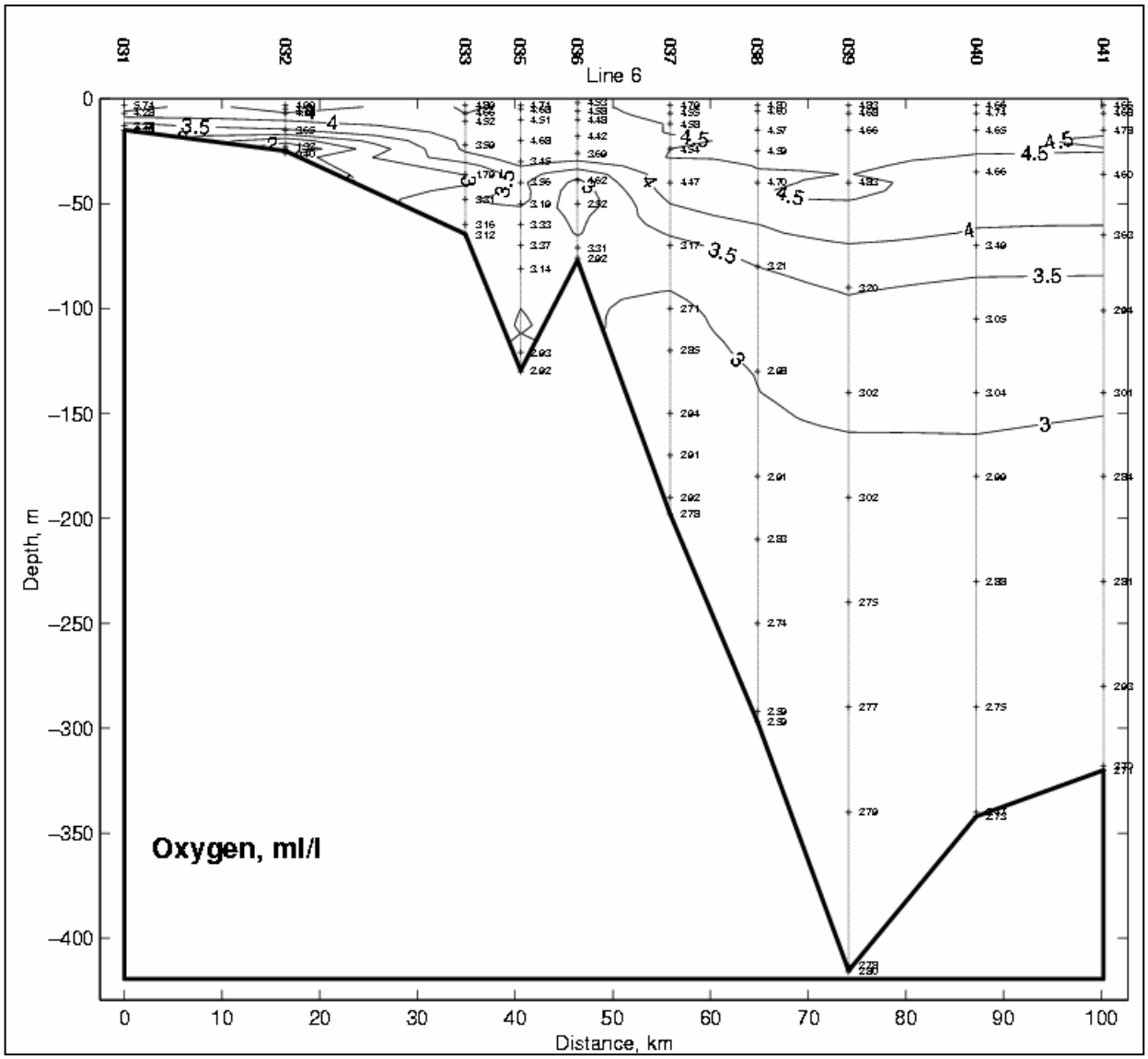

Figure B.41 Vertical profile of dissolved oxygen for Transect 6. The contour interval is 0.5 ml l^{-1}. Note the oxygen minimum seen at station 036.

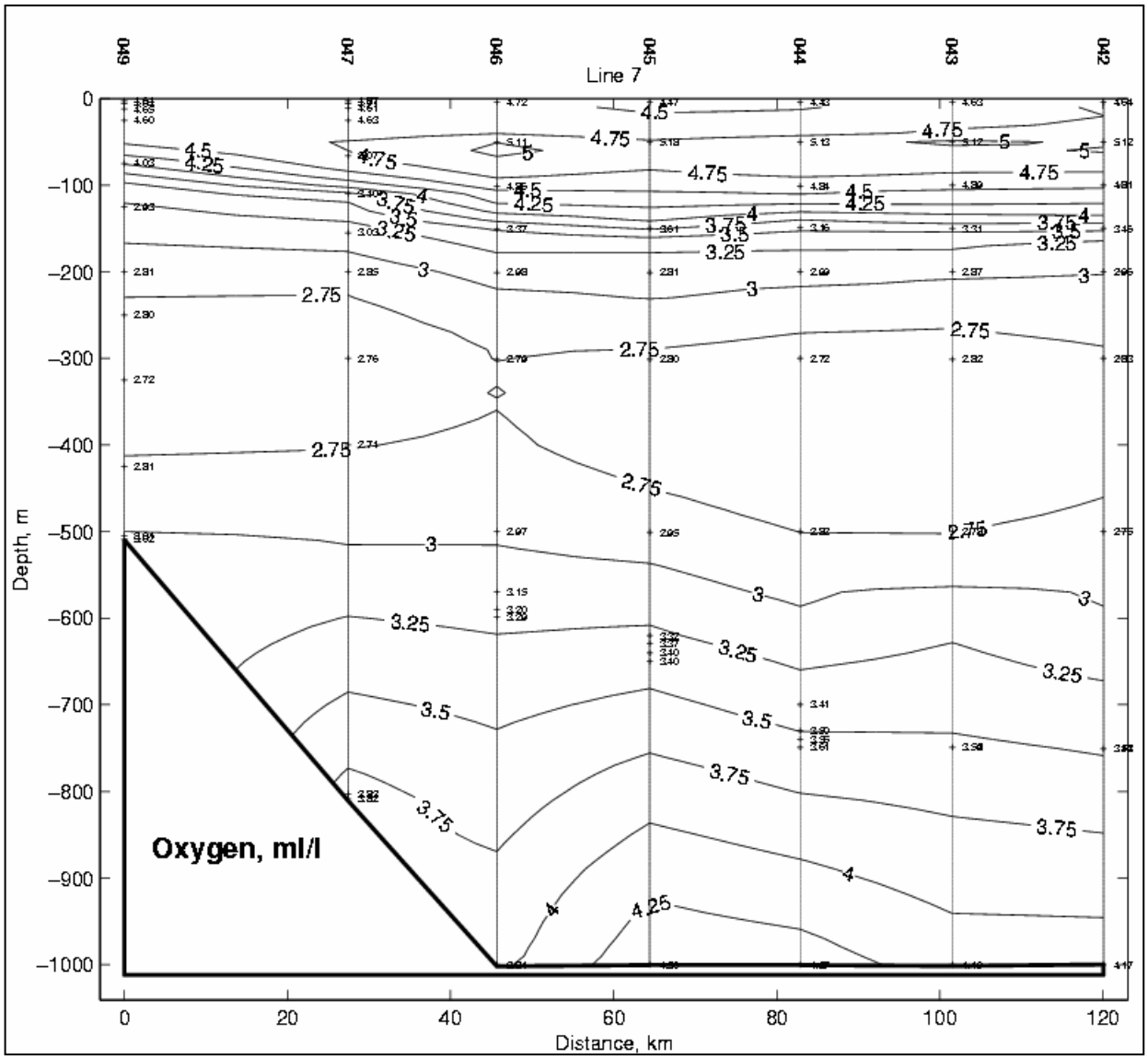

Figure B.42 Vertical profile of dissolved oxygen for Transect 7A. The contour interval is 0.25 ml l^{-1}. Note the oxygen minimum seen between 300 and 400 m depth that is associated with a maximum in the NO_3 concentration.

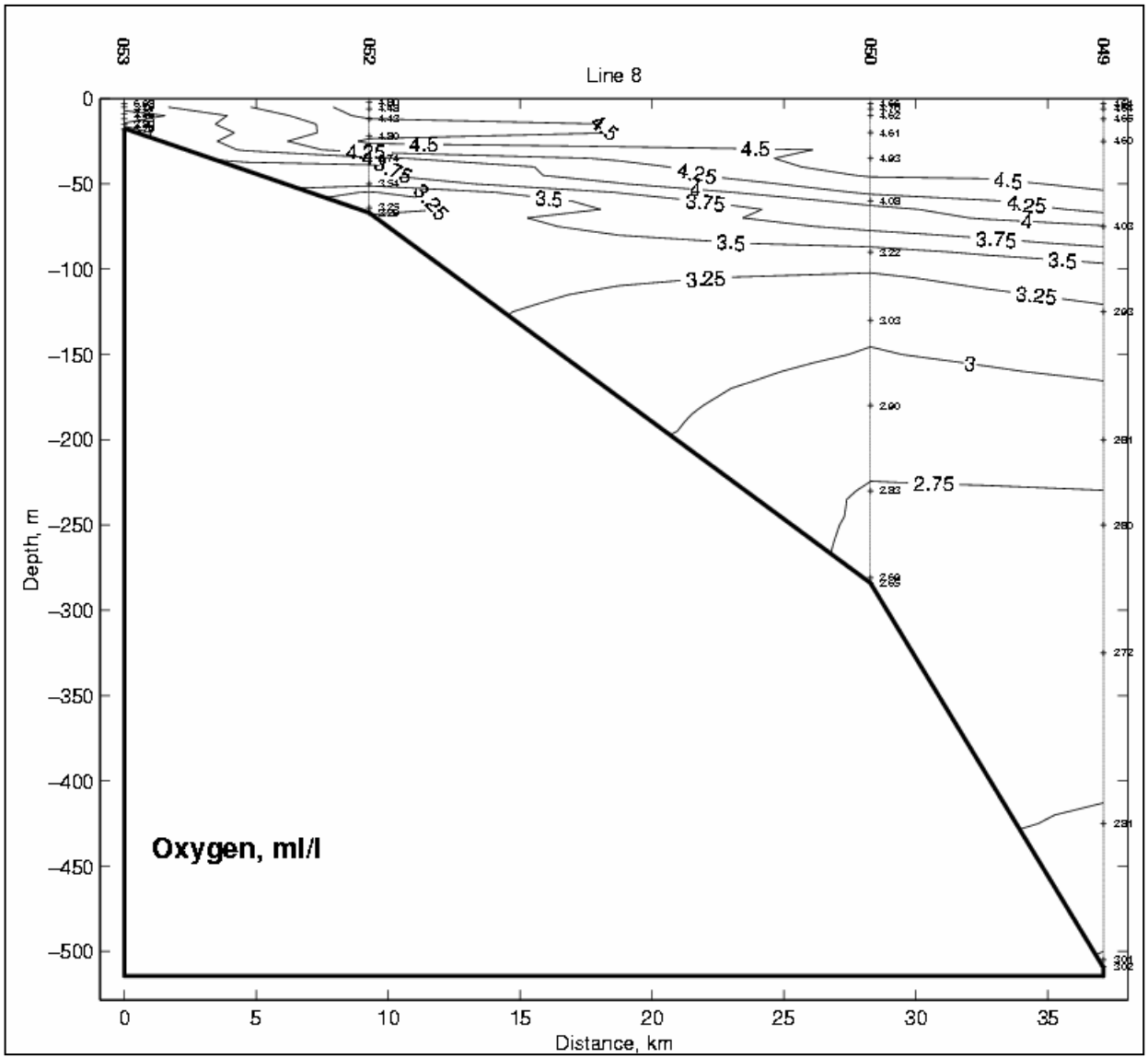

Figure B.43 Vertical profile of dissolved oxygen for Transect 7B. The contour interval is 0.25 ml l^{-1}.

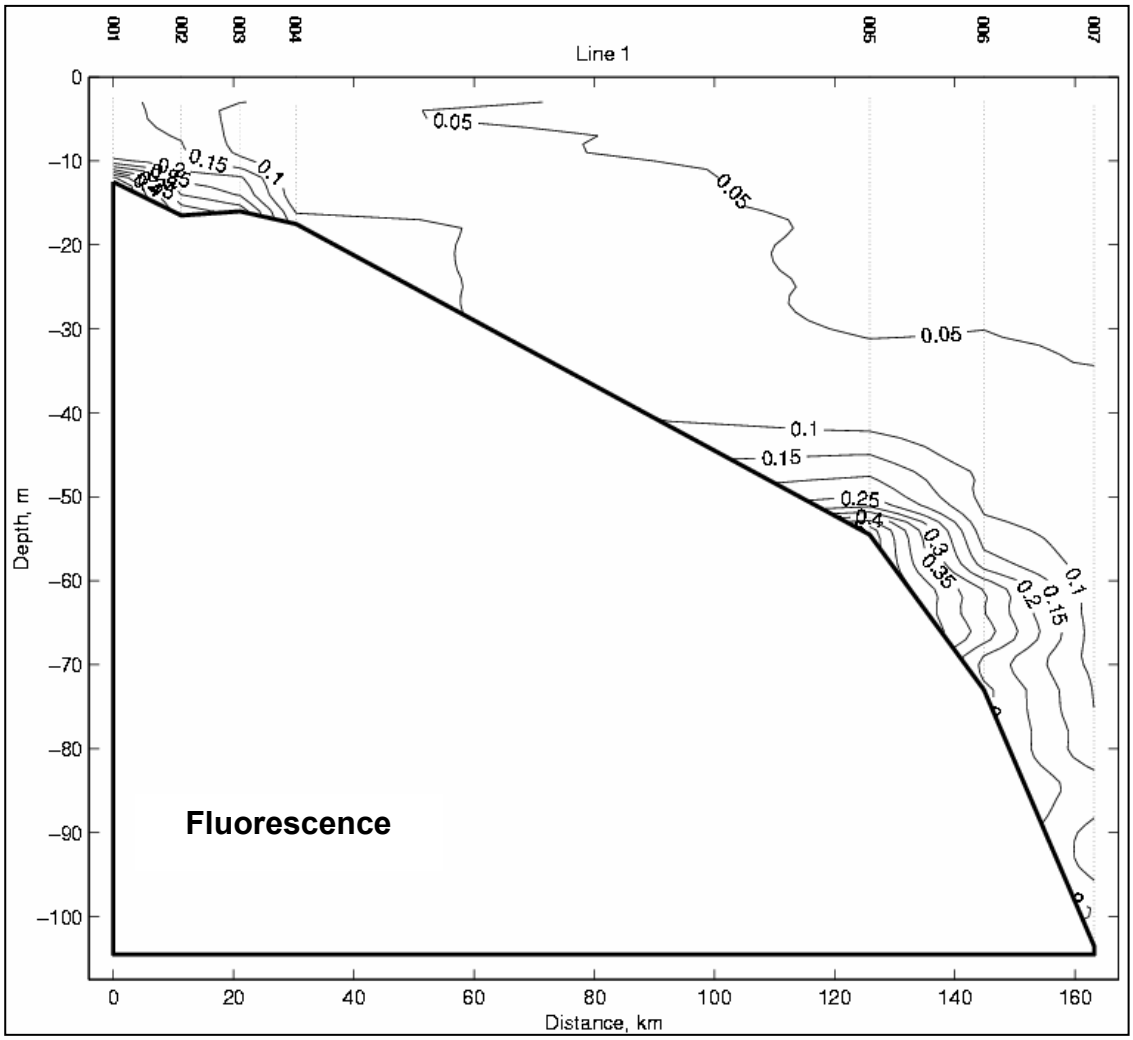

Figure B.44 Vertical profile of fluorescence for Transect 1. The contour interval is 0.05.

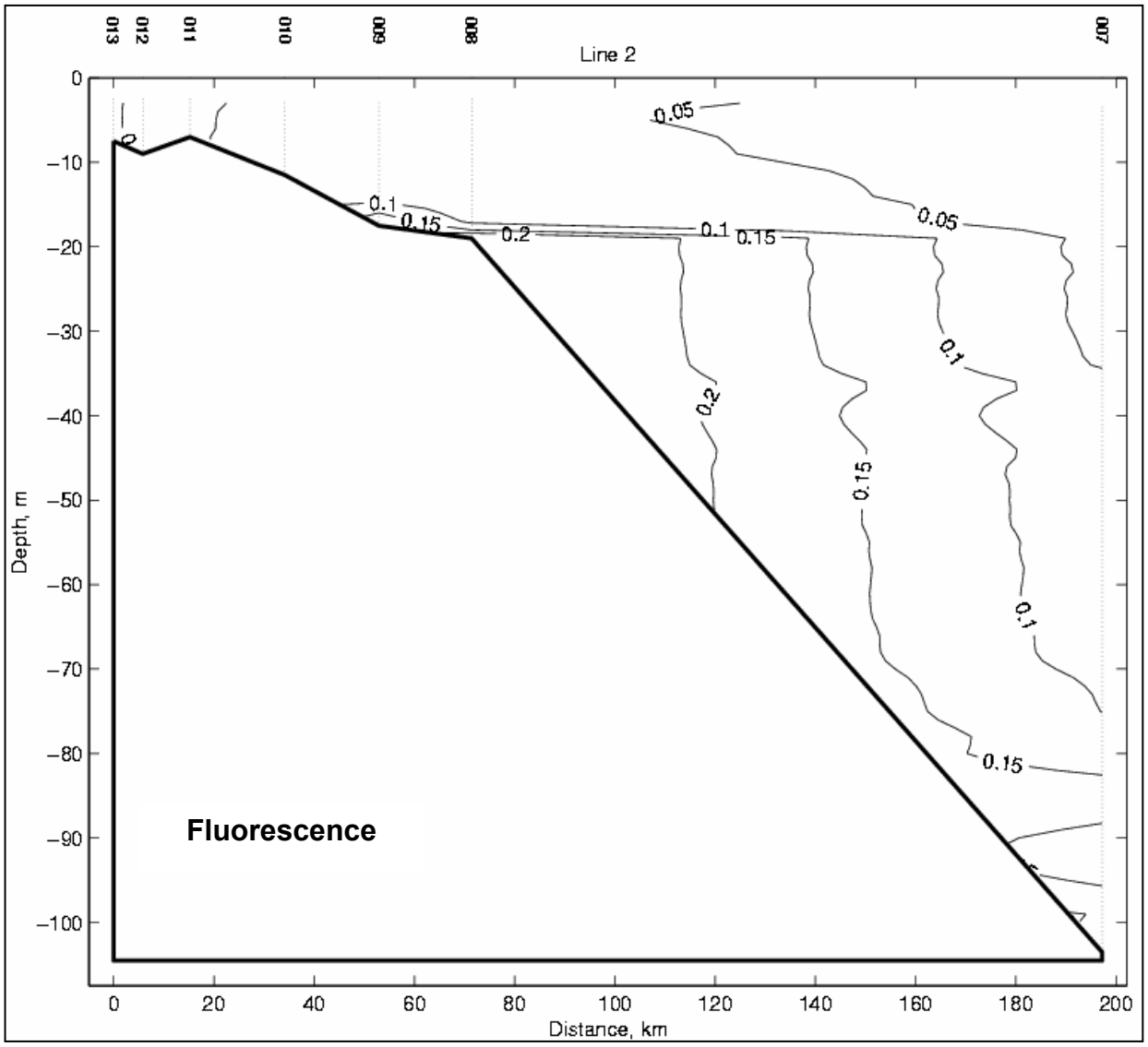

Figure B.45 Vertical profile of fluorescence for Transect 2. The contour interval is 0.20.

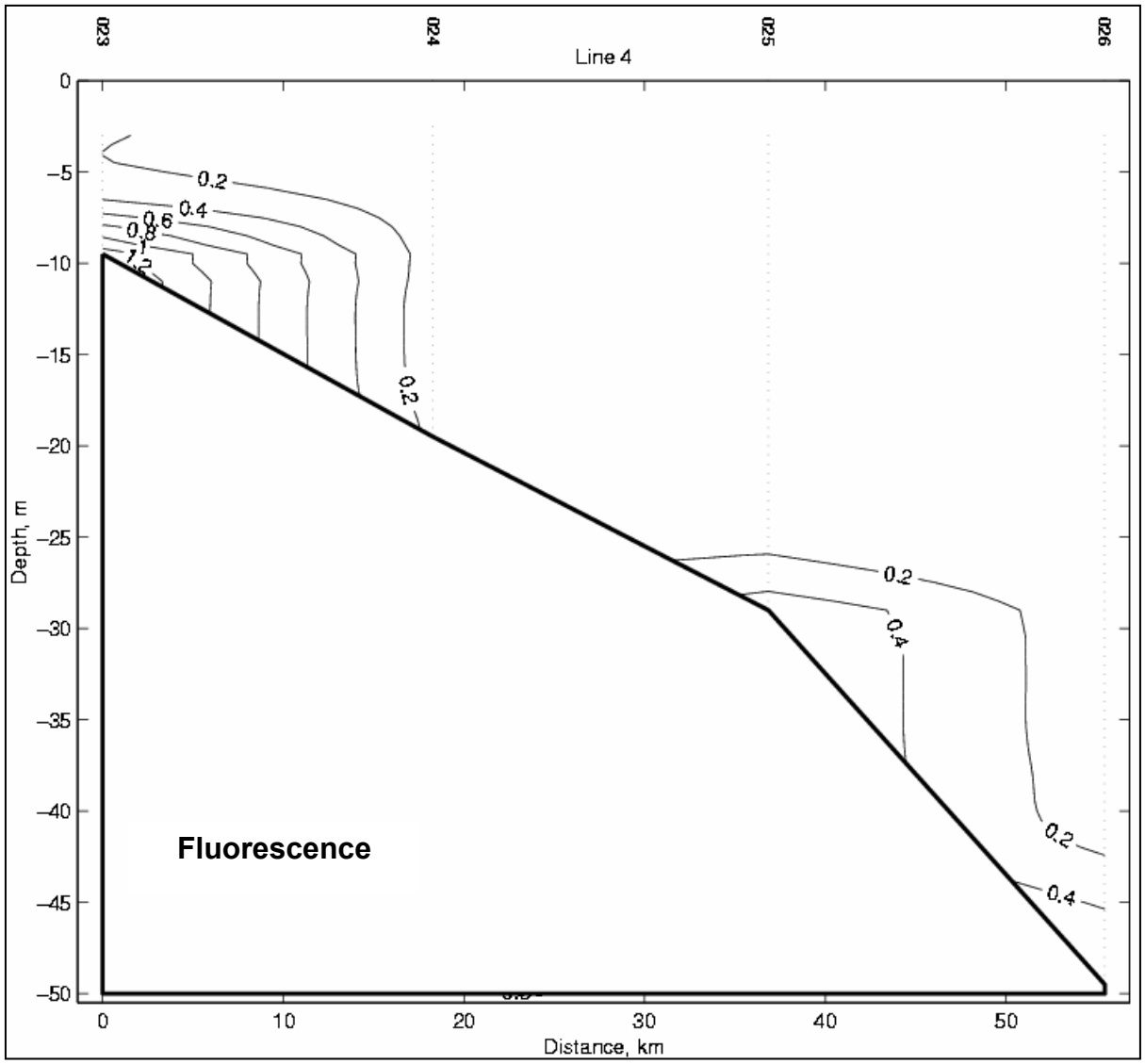

Figure B.46 Vertical profile of fluorescence for Transect 4. The contour interval is 0.10.

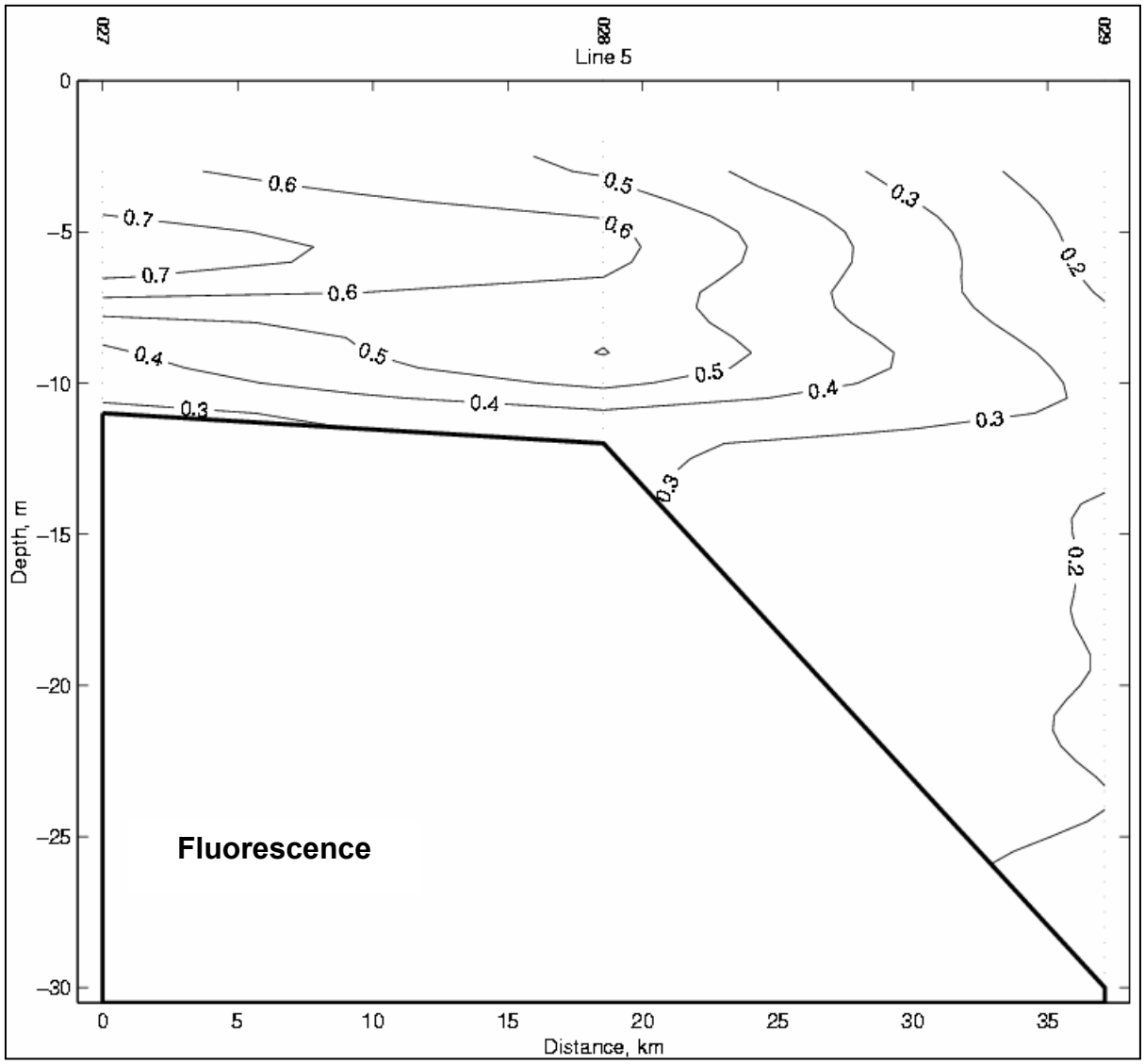

Figure B.47 Vertical profile of fluorescence for Transect 5. The contour interval is 0.1.

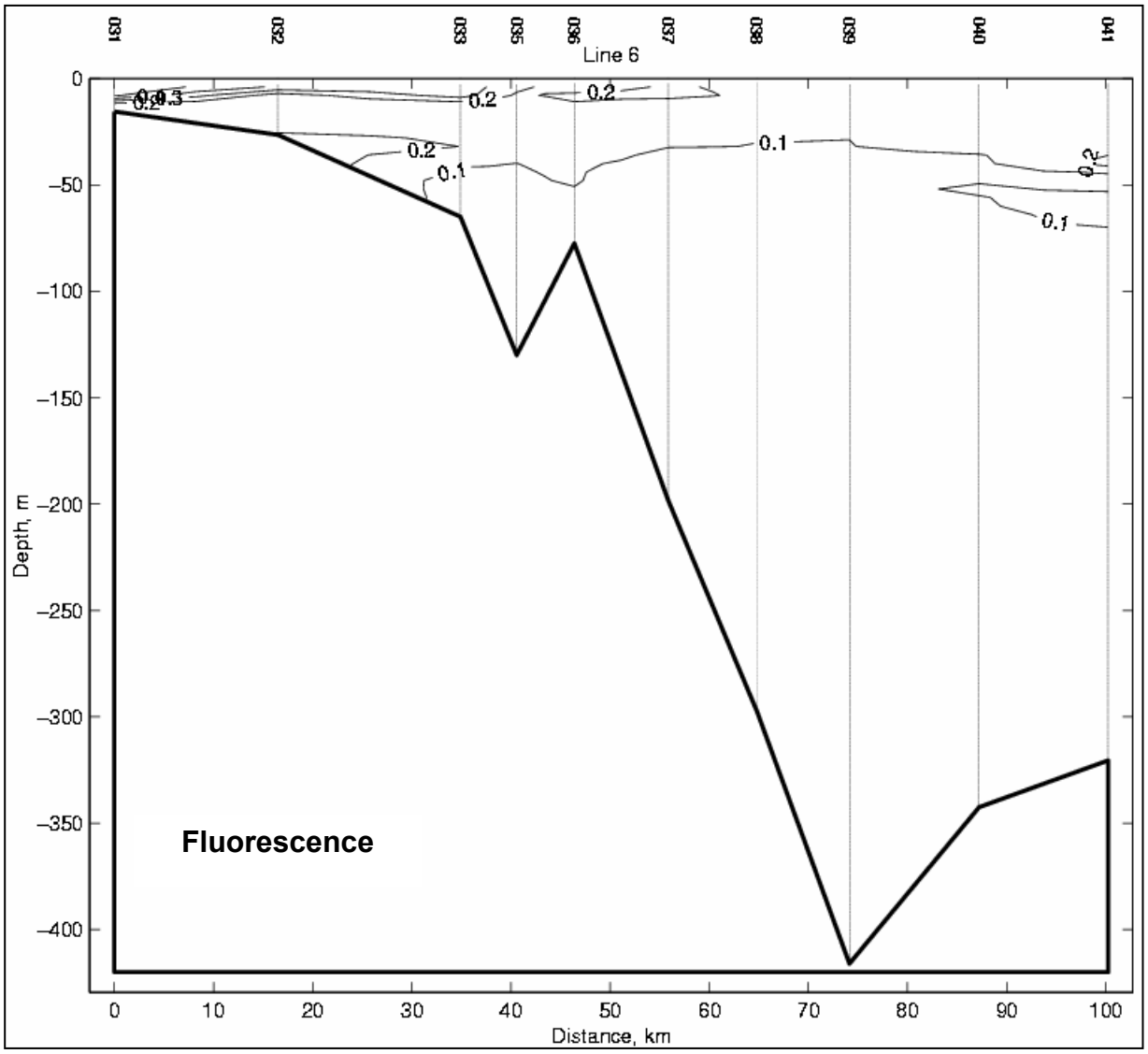

Figure B.48 Vertical profile of fluorescence for Transect 6. The contour interval is 0.10.

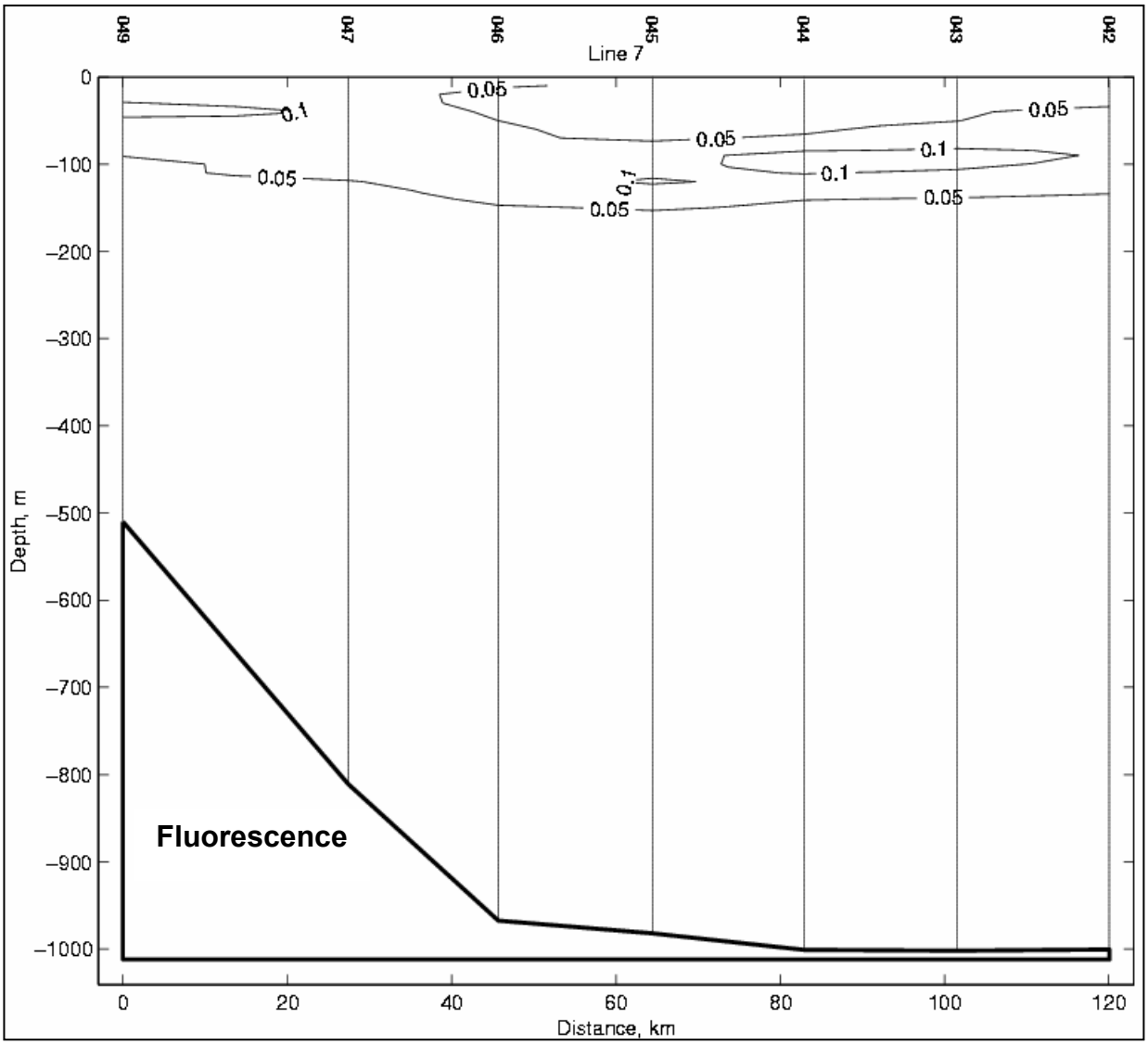

Figure B.49 Vertical profile of fluorescence for Transect 7A. The contour interval is 0.05.

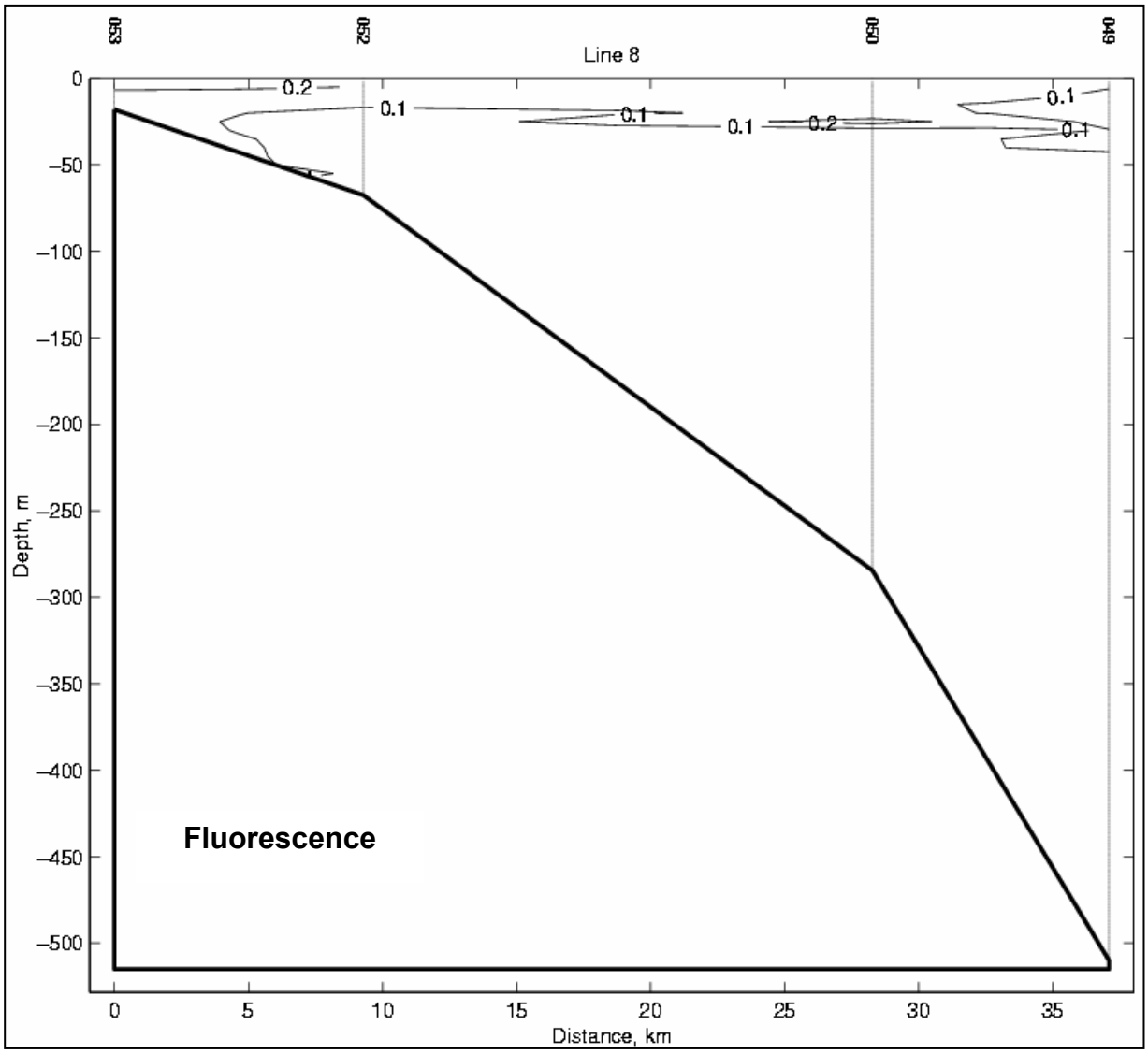

Figure B.50 Vertical profile of fluorescence for Transect 7B. The contour interval is 1.0.

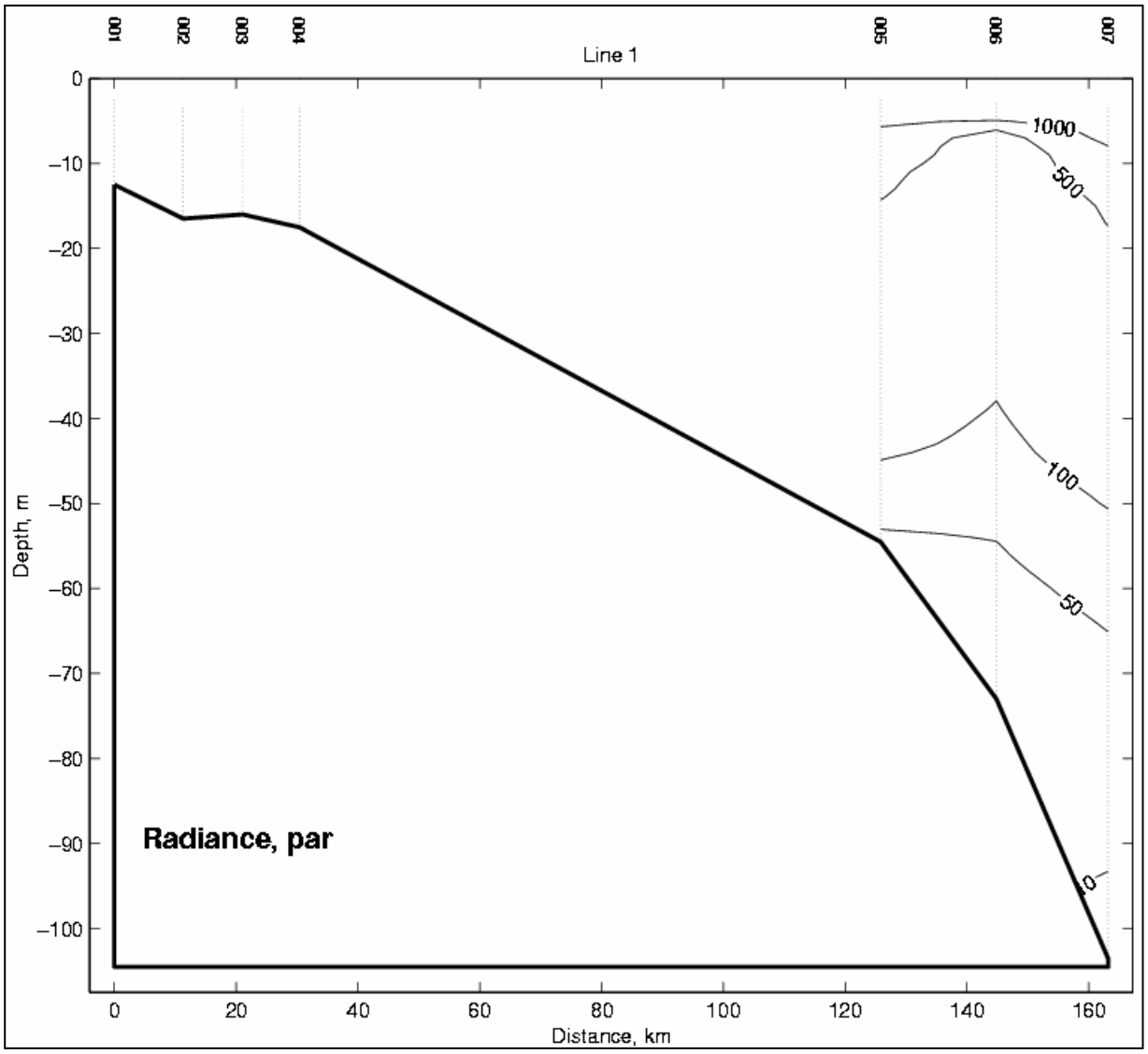

Figure B.51 Vertical profile of radiance for Transect 1. The contour interval is defined in the text. There is no data for stations 001, 002, 003 and 004.

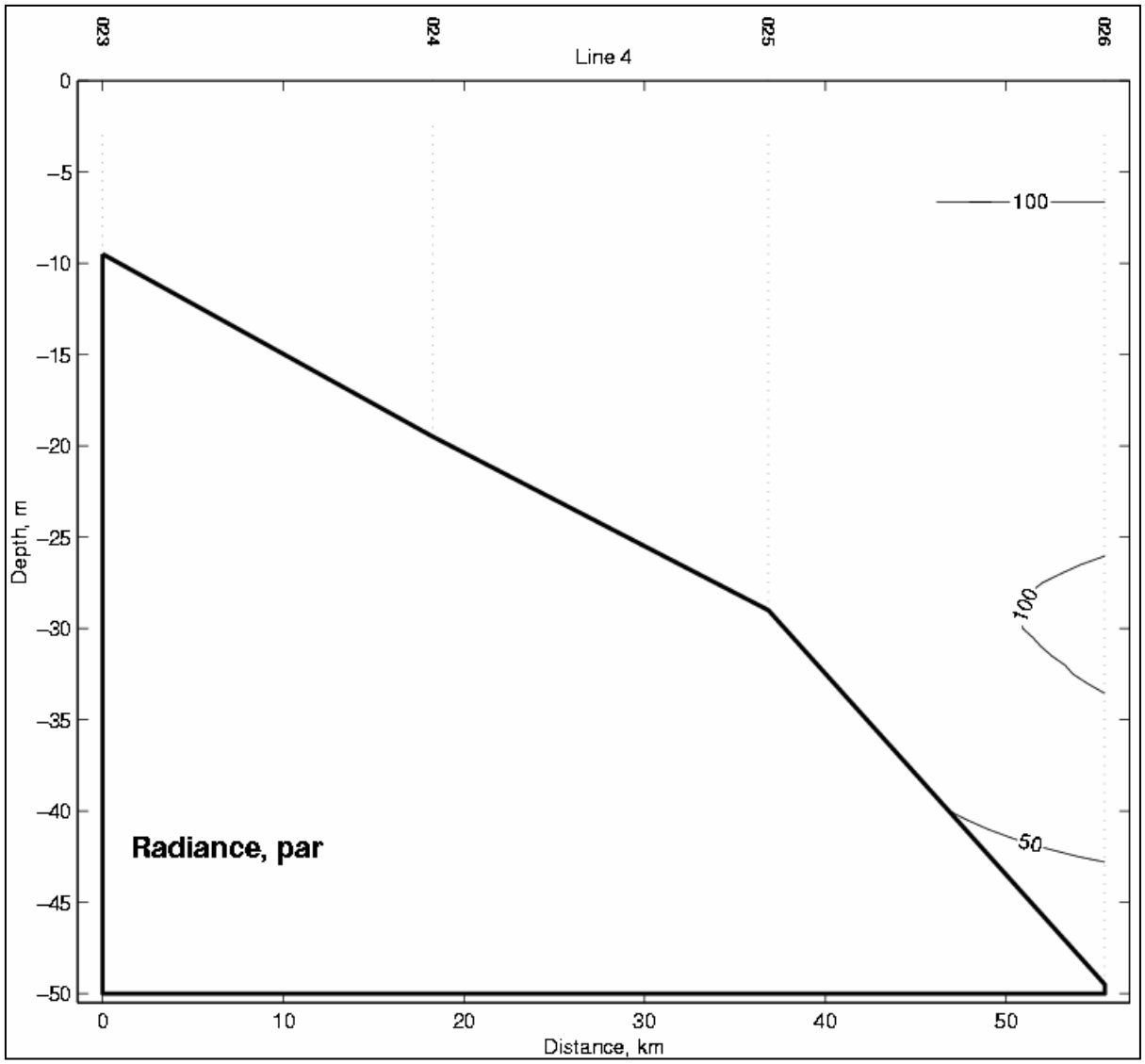

Figure B.52 Vertical profile of radiance for Transect 4. The contour interval is defined in the text. There is no data for stations 023, 024, and 025.

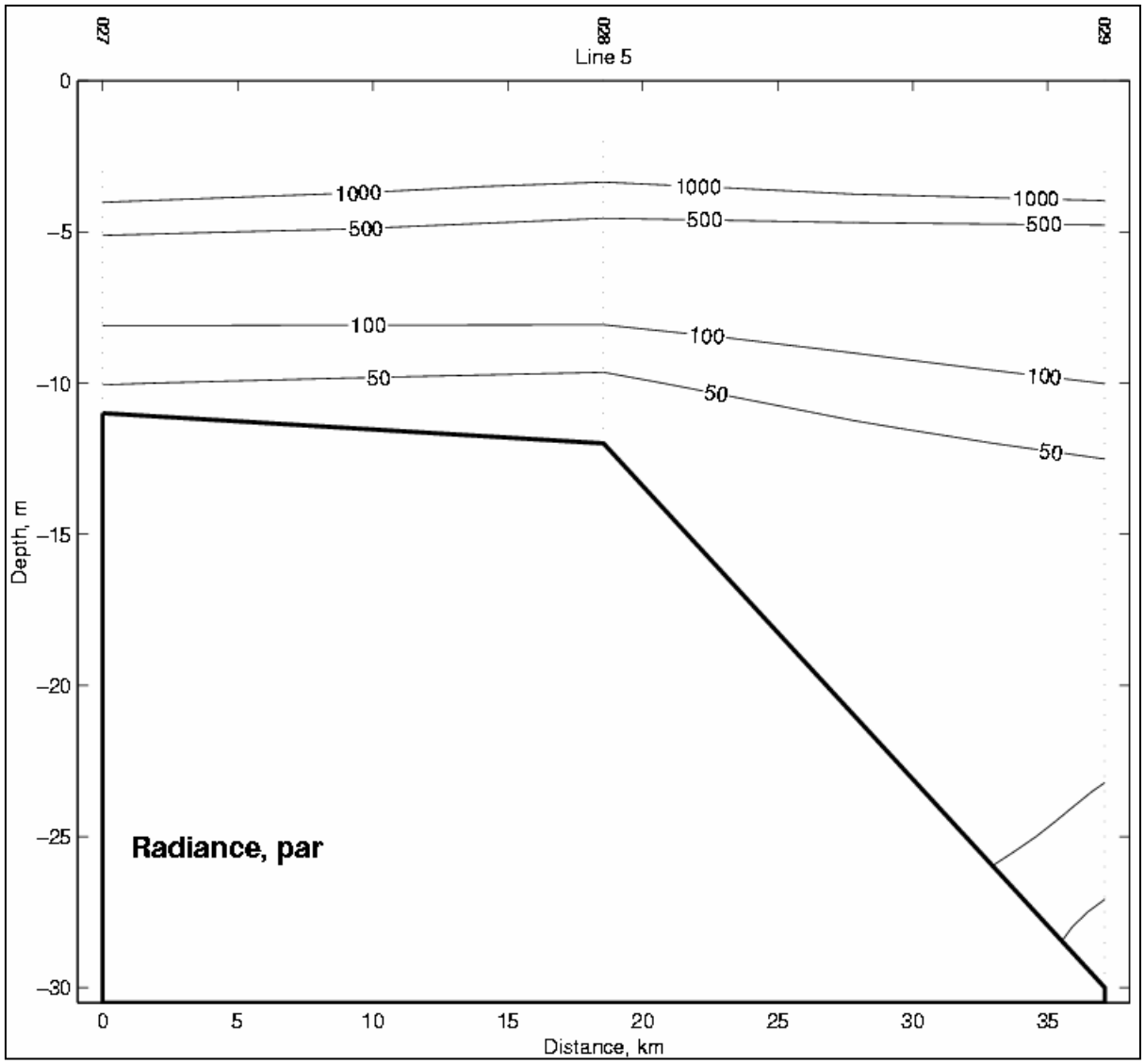

Figure B.53 Vertical profile of radiance for Transect 5. The contour interval is defined in the text. There is no data for stations 020, 021, and 022.

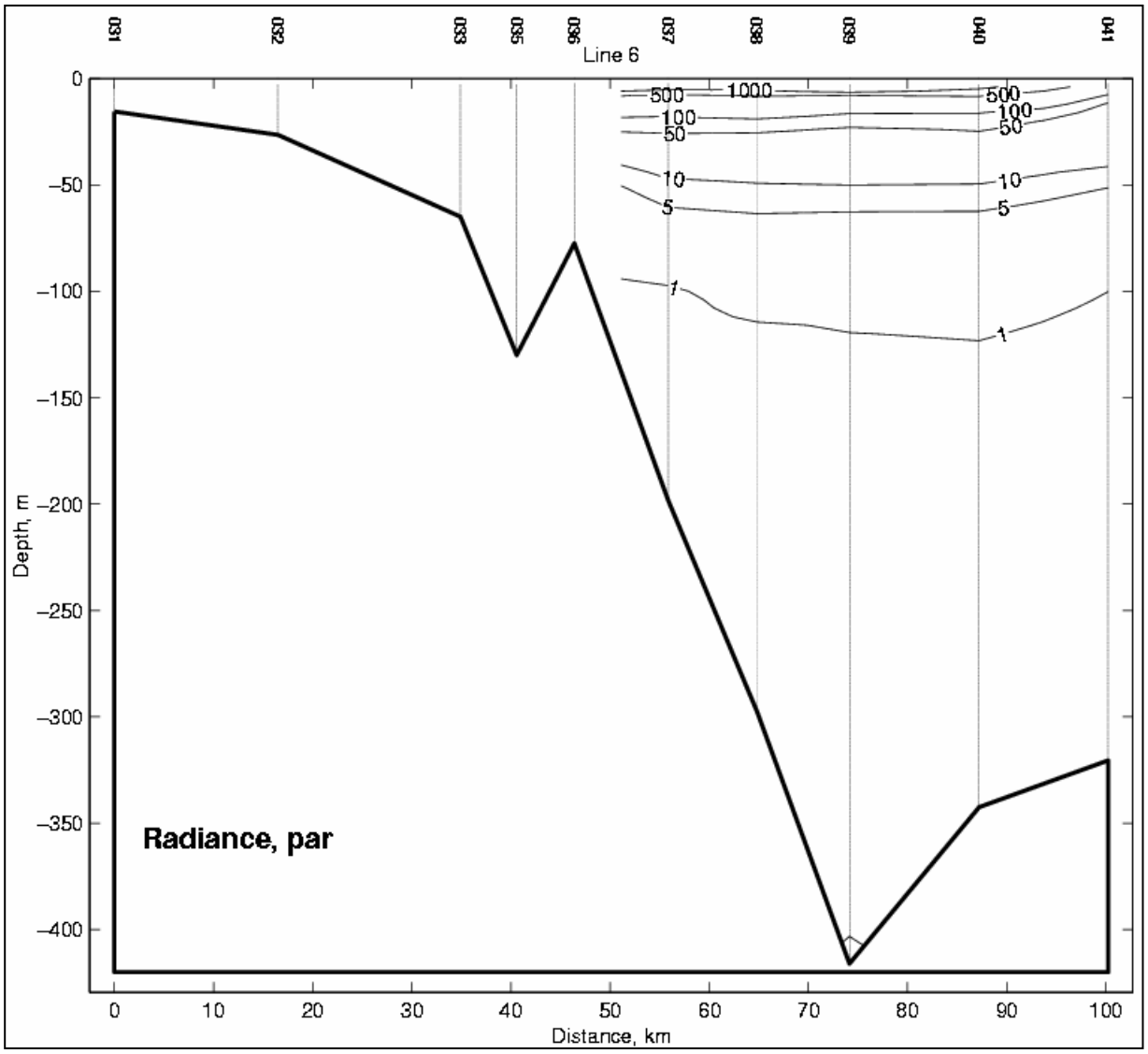

Figure B.54 Vertical profile of radiance for Transect 6. The contour interval is defined in the text. There is no data for stations 031, 032, 033, 035, and 036.

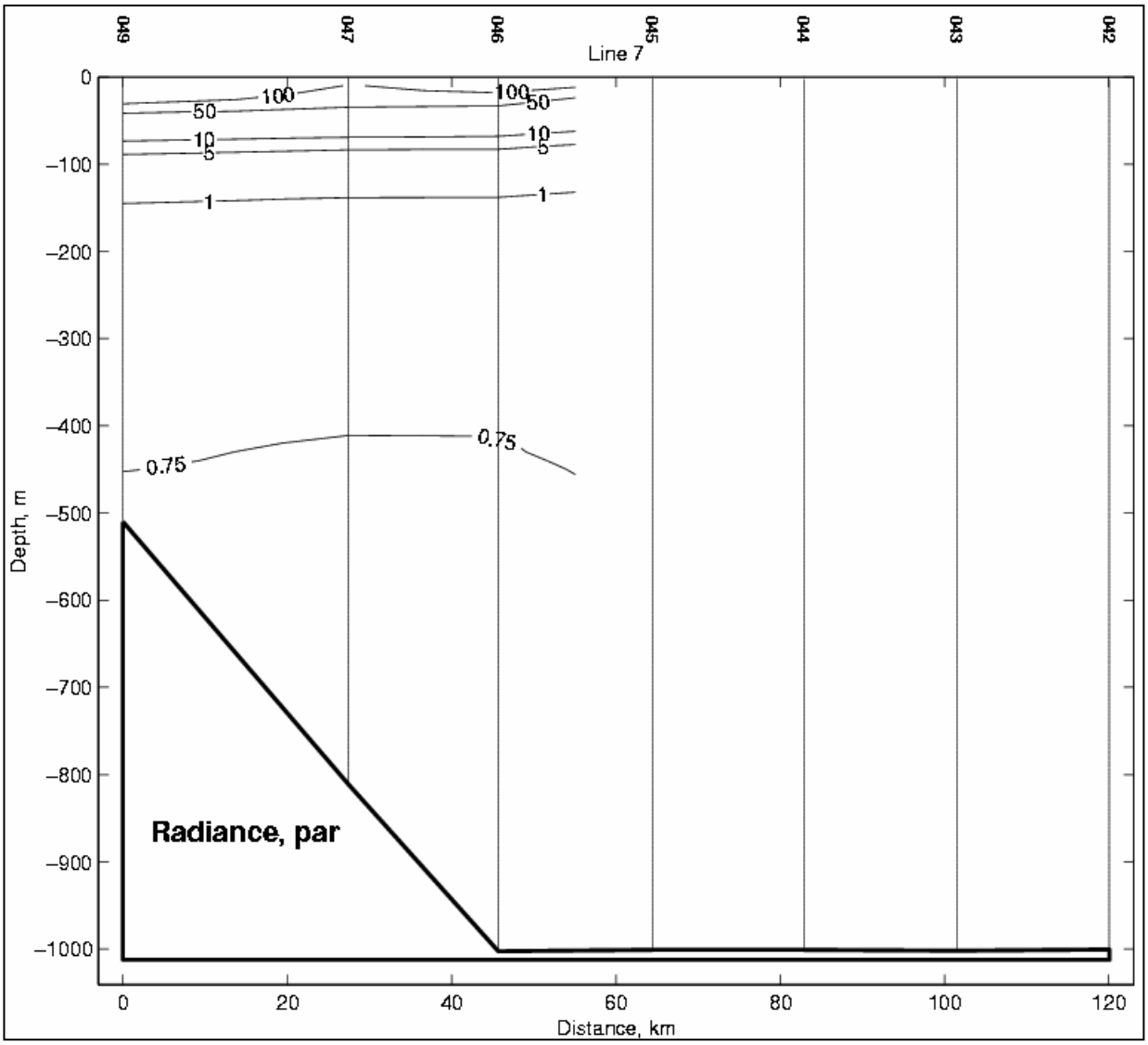

Figure B.55 Vertical profile of radiance for Transect 7A. The contour interval is defined in the text. There is no data for stations 042, 043, 044, and 045.

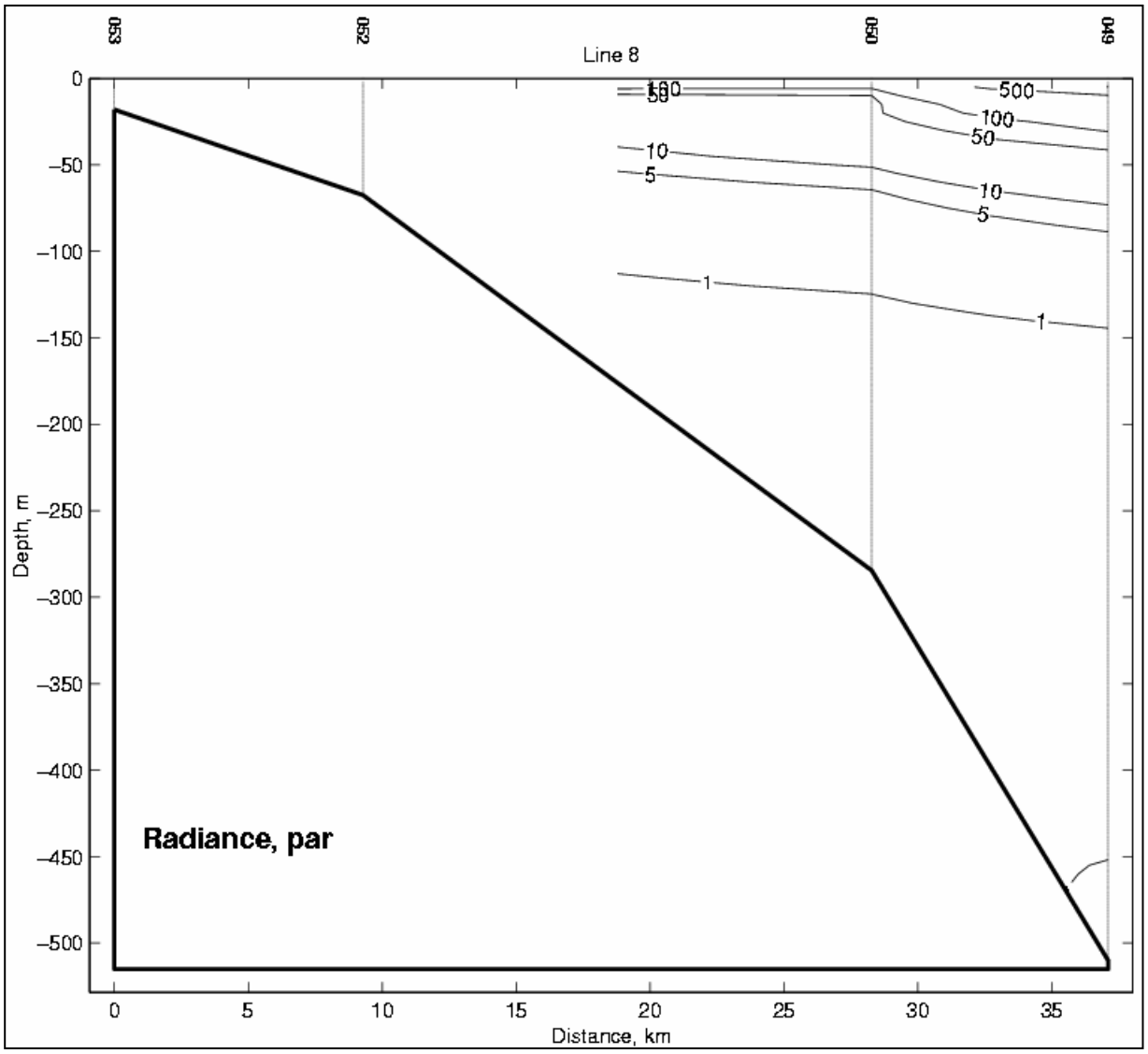

Figure B.56 Vertical profile of radiance for Transect 7B. The contour interval is defined in the text. There is no data for stations 052 and 053.

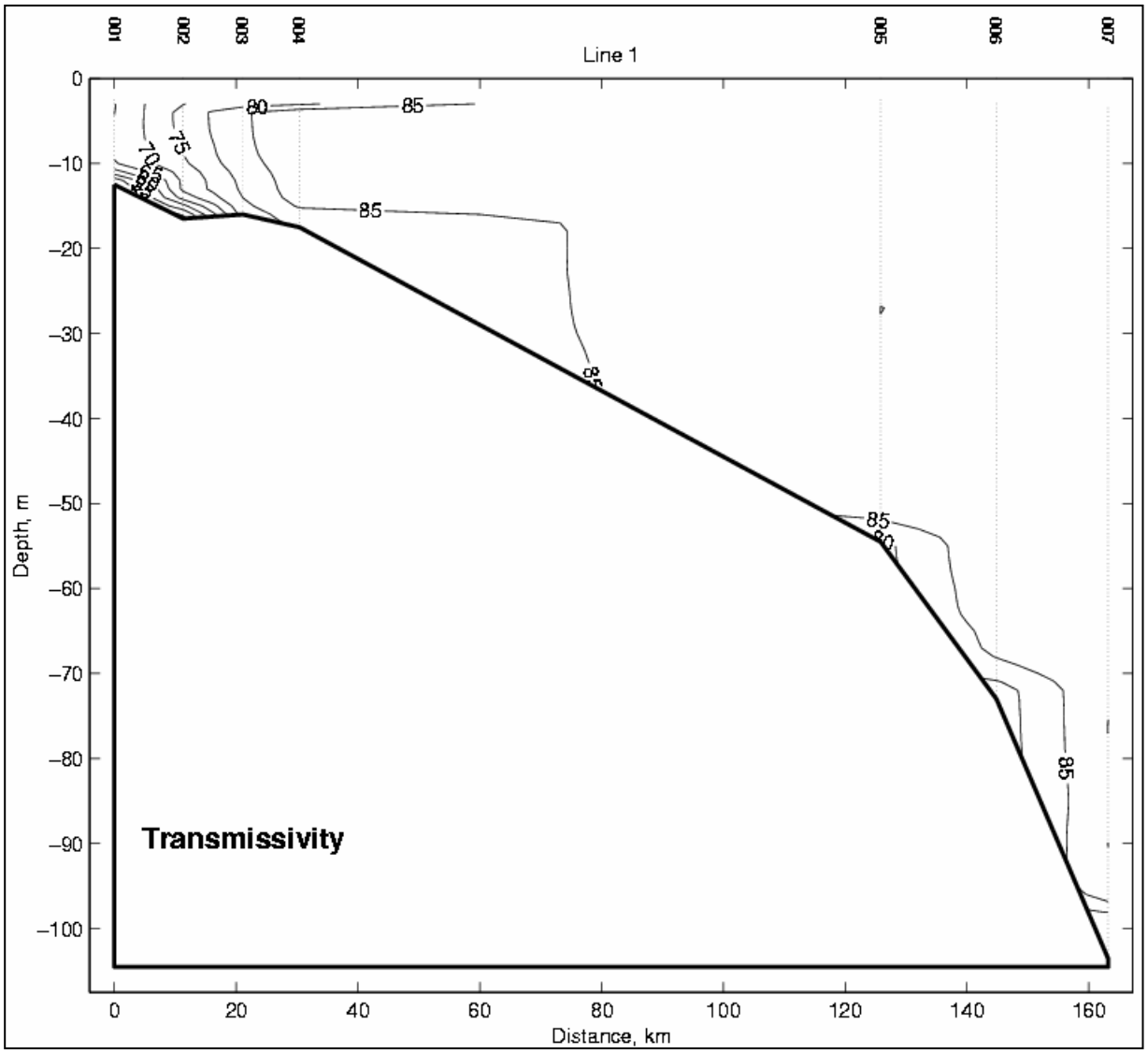

Figure B.57 Vertical profile of transmissivity for Transect 1. The contour interval is 5%.

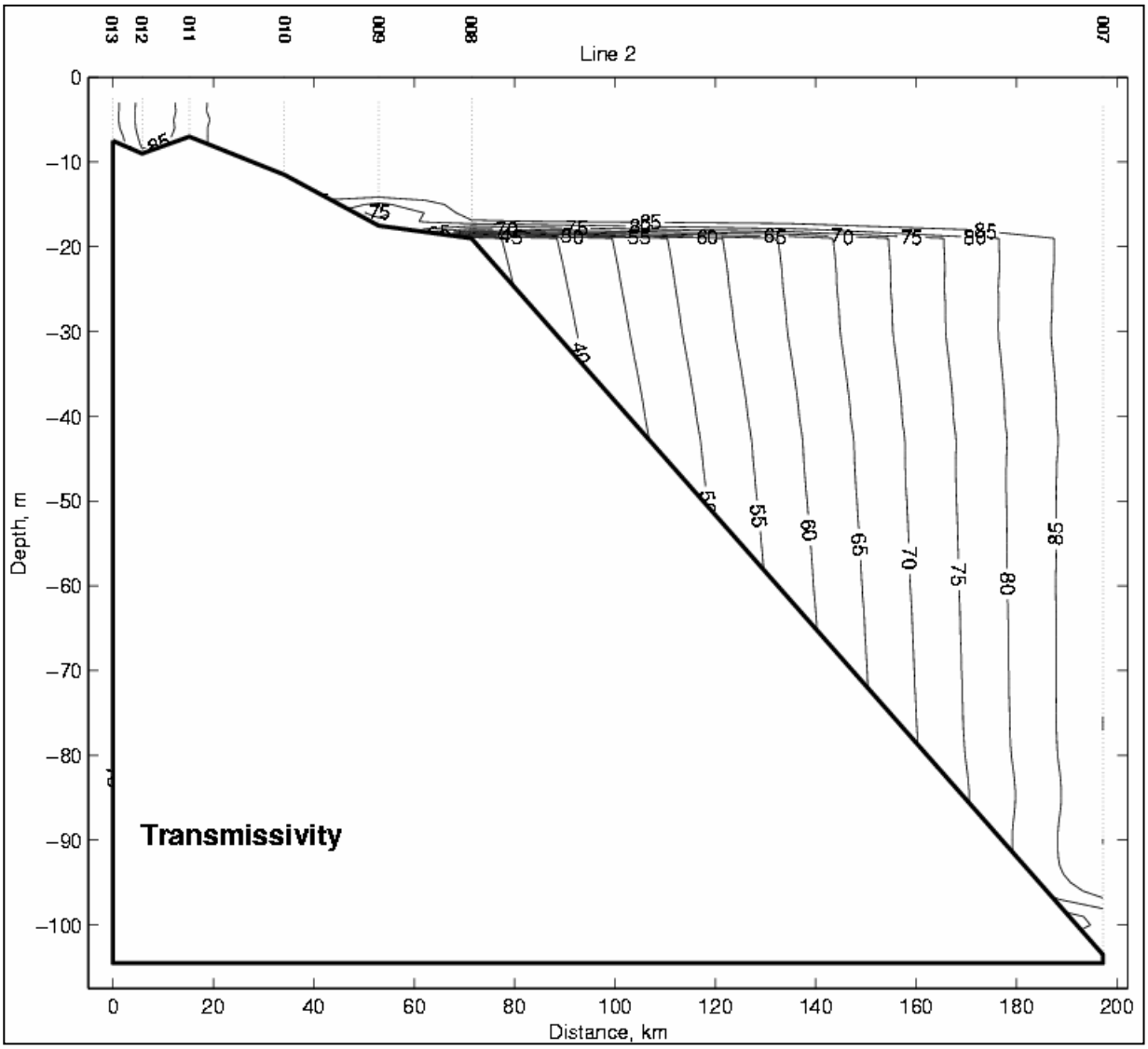

Figure B.58 Vertical profile of transmissivity for Transect 2. The contour interval is 5%.

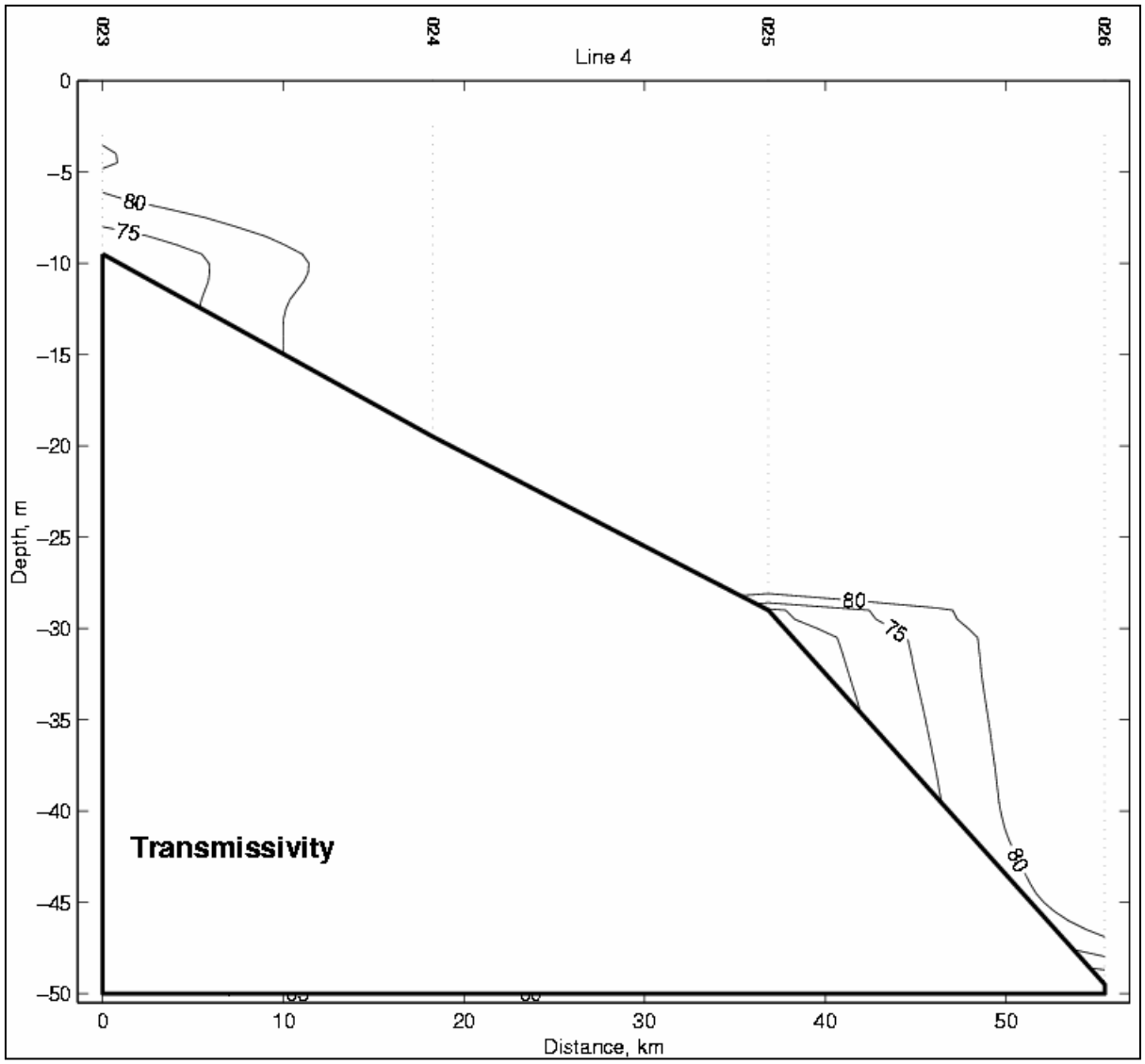

Figure B.59 Vertical profile of transmissivity for Transect 4. The contour interval is 5%.

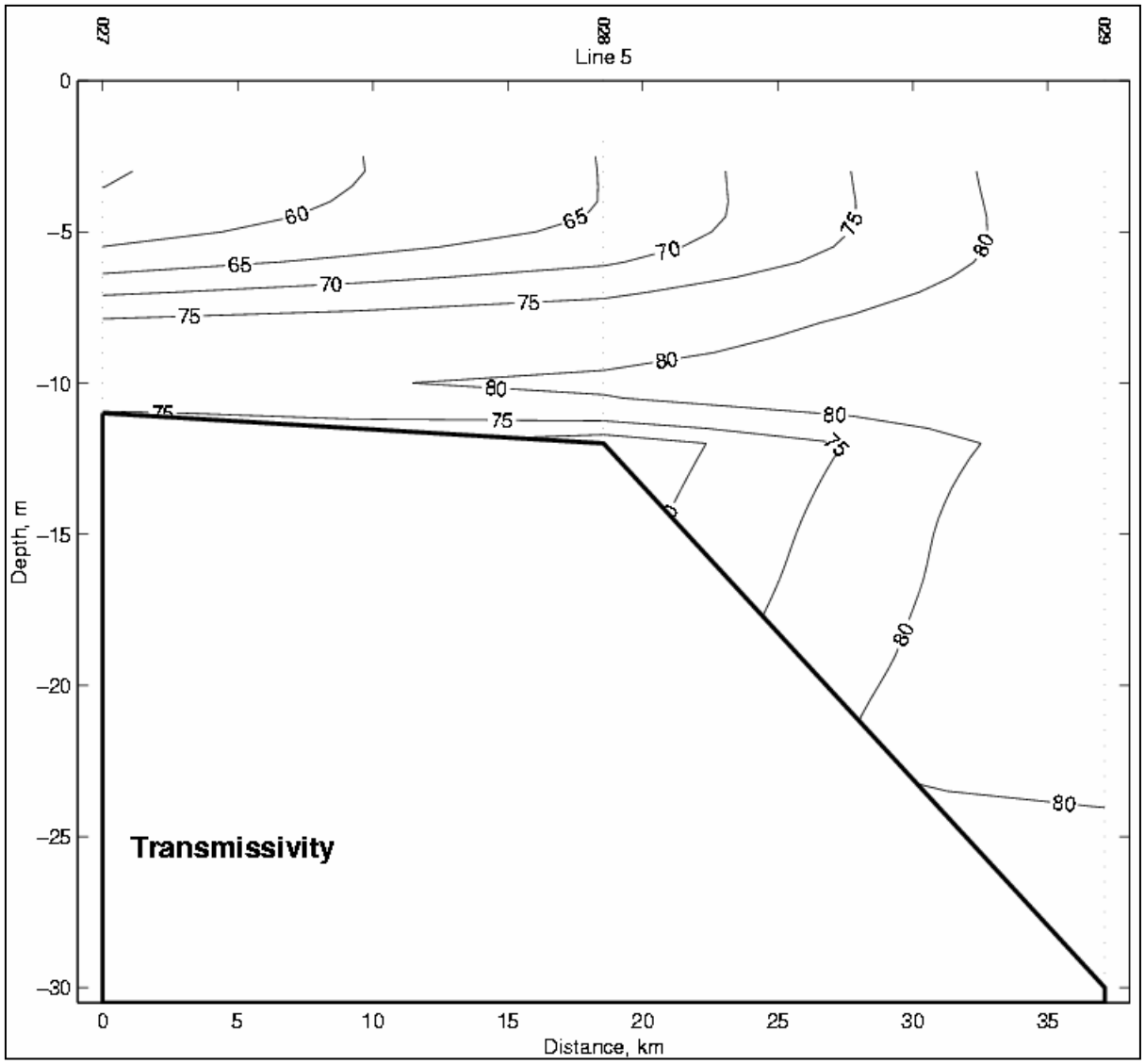

Figure B.60 Vertical profile of transmissivity for Transect 5. The contour interval is 5%.

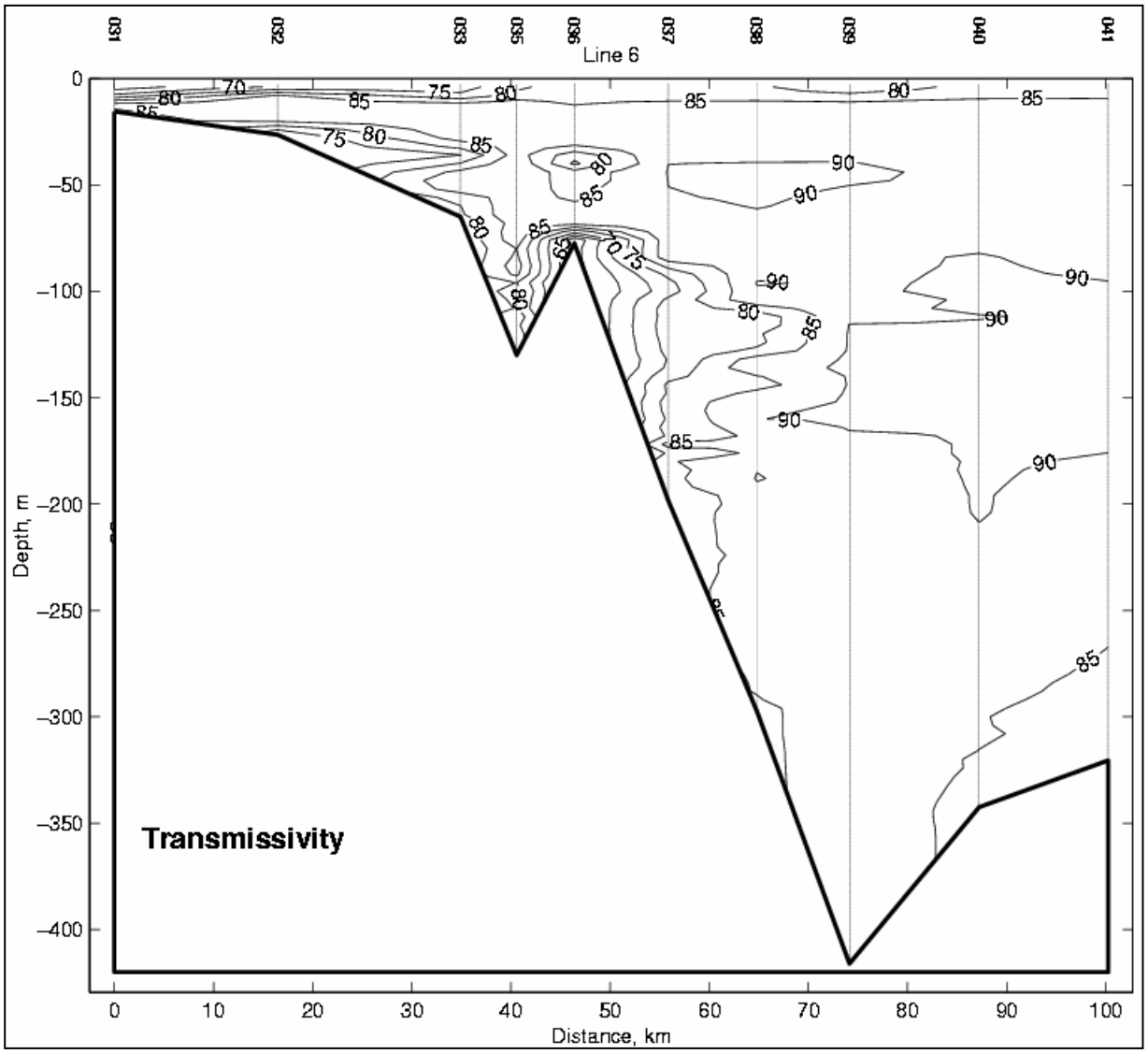

Figure B.61 Vertical profile of transmissivity for Transect 6. The contour interval is 5%.

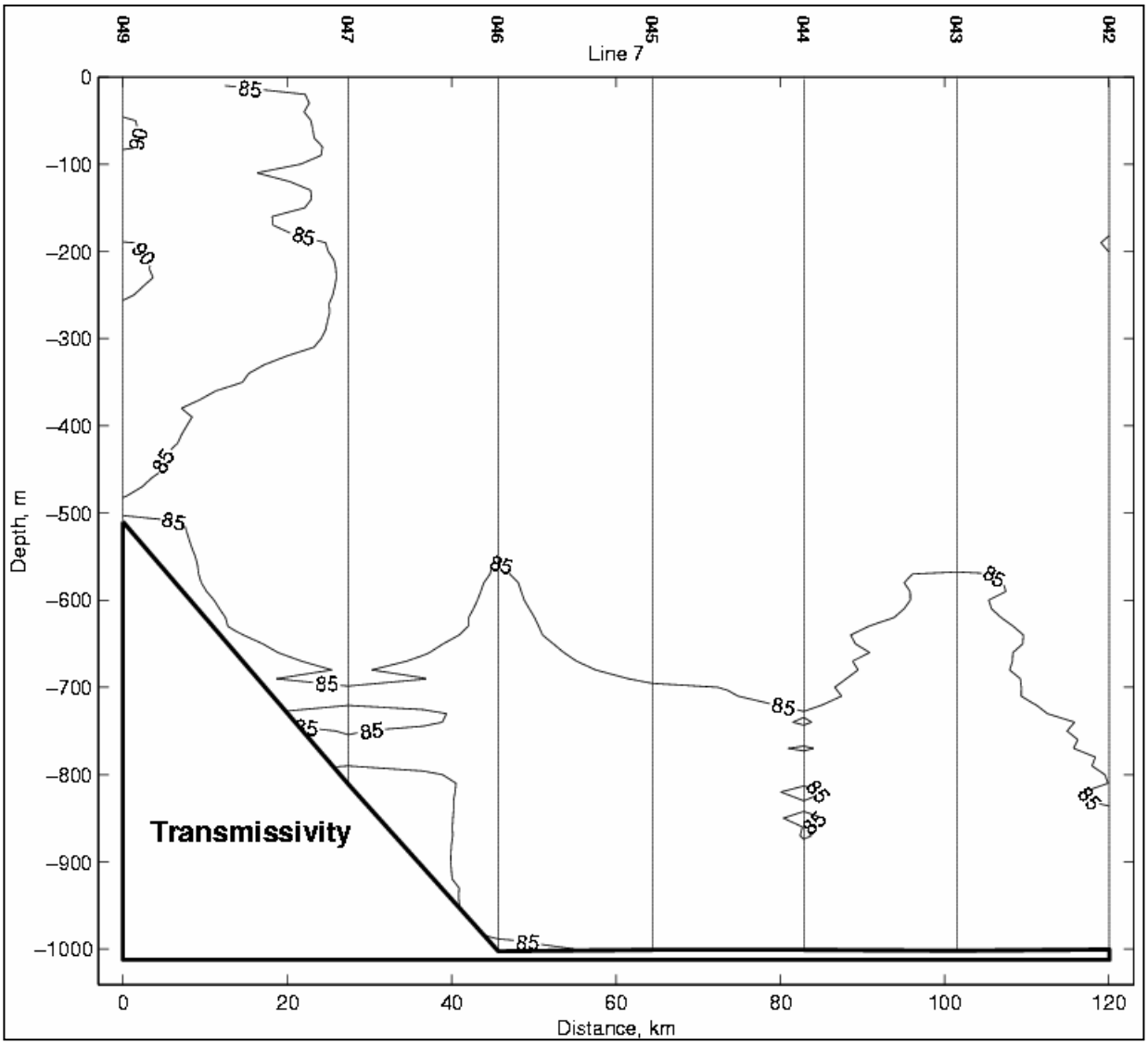

Figure B.62 Vertical profile of transmissivity for Transect 7A. The contour interval is 5%.

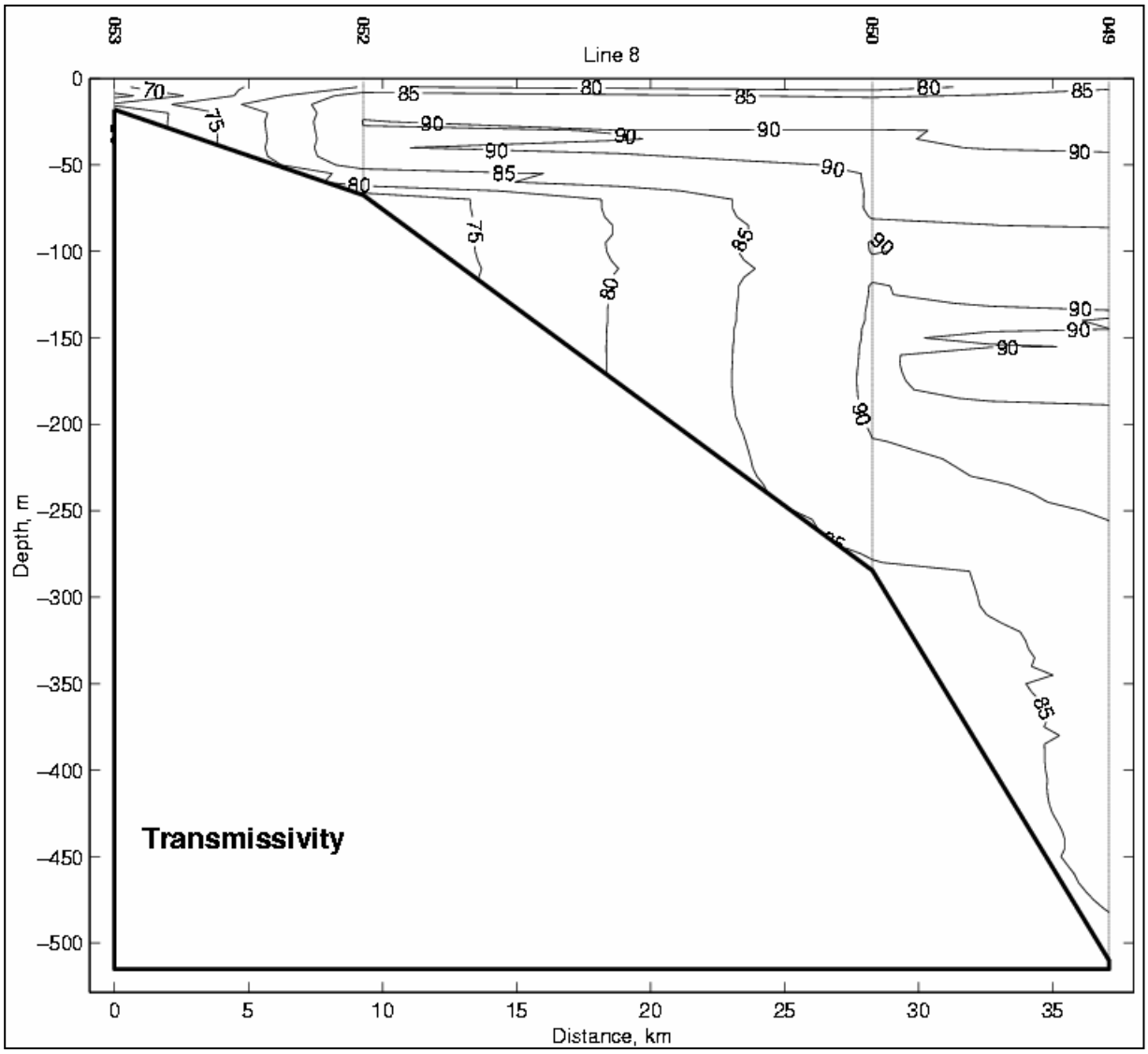

Figure B.63 Vertical profile of transmissivity for Transect 7B. The contour interval is 5%

Appendix C

Maps and Vertical Sections of ADCP Data Collected During *R/V Gyre* Cruise 98-G-9

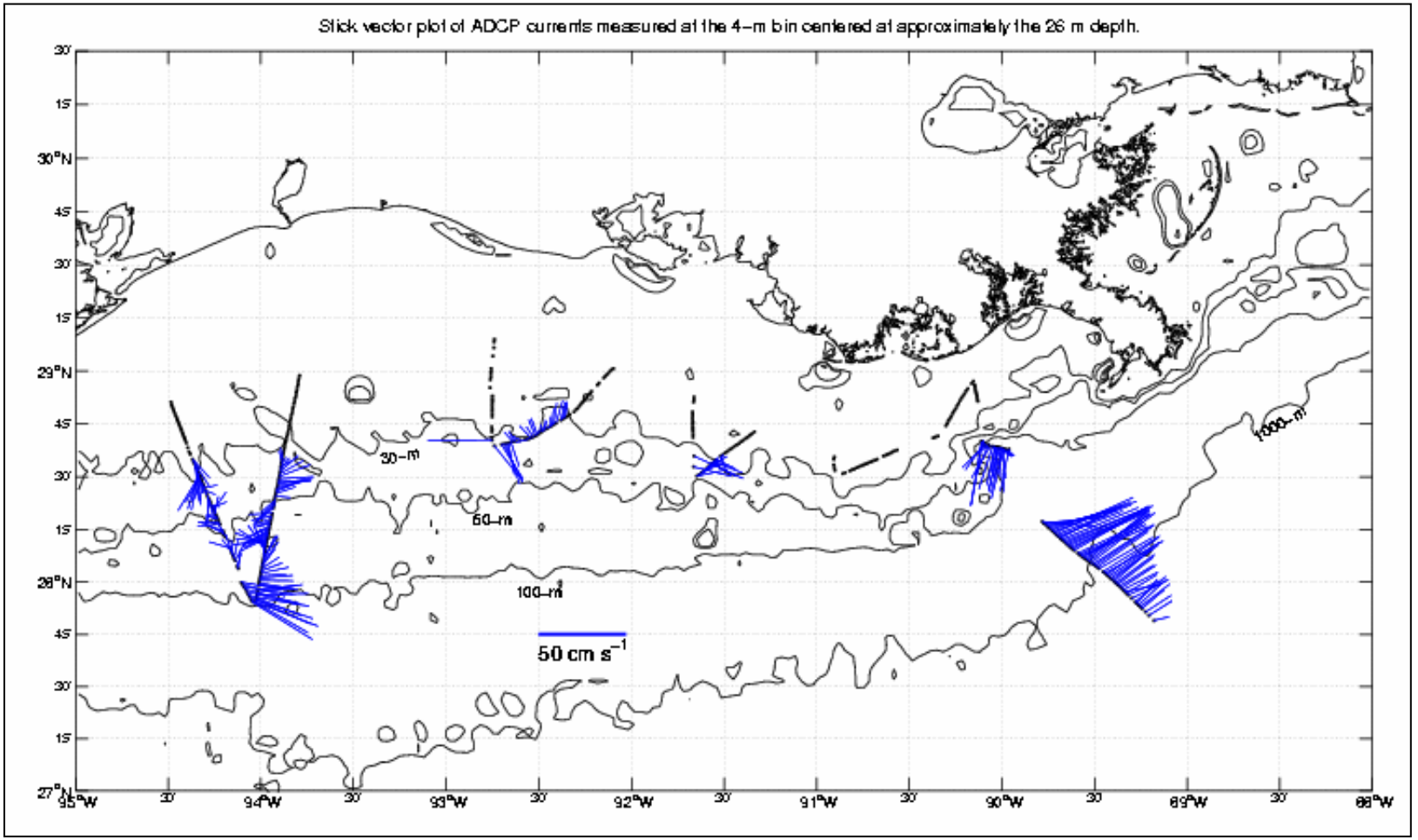

Figure C.1 Stick vector plot of ADCP currents measured at the 4-m bin centered at approximately the 26-m depth. Bathymetric contours are shown for 30-, 50-, 100-, and 1,000-m depths.

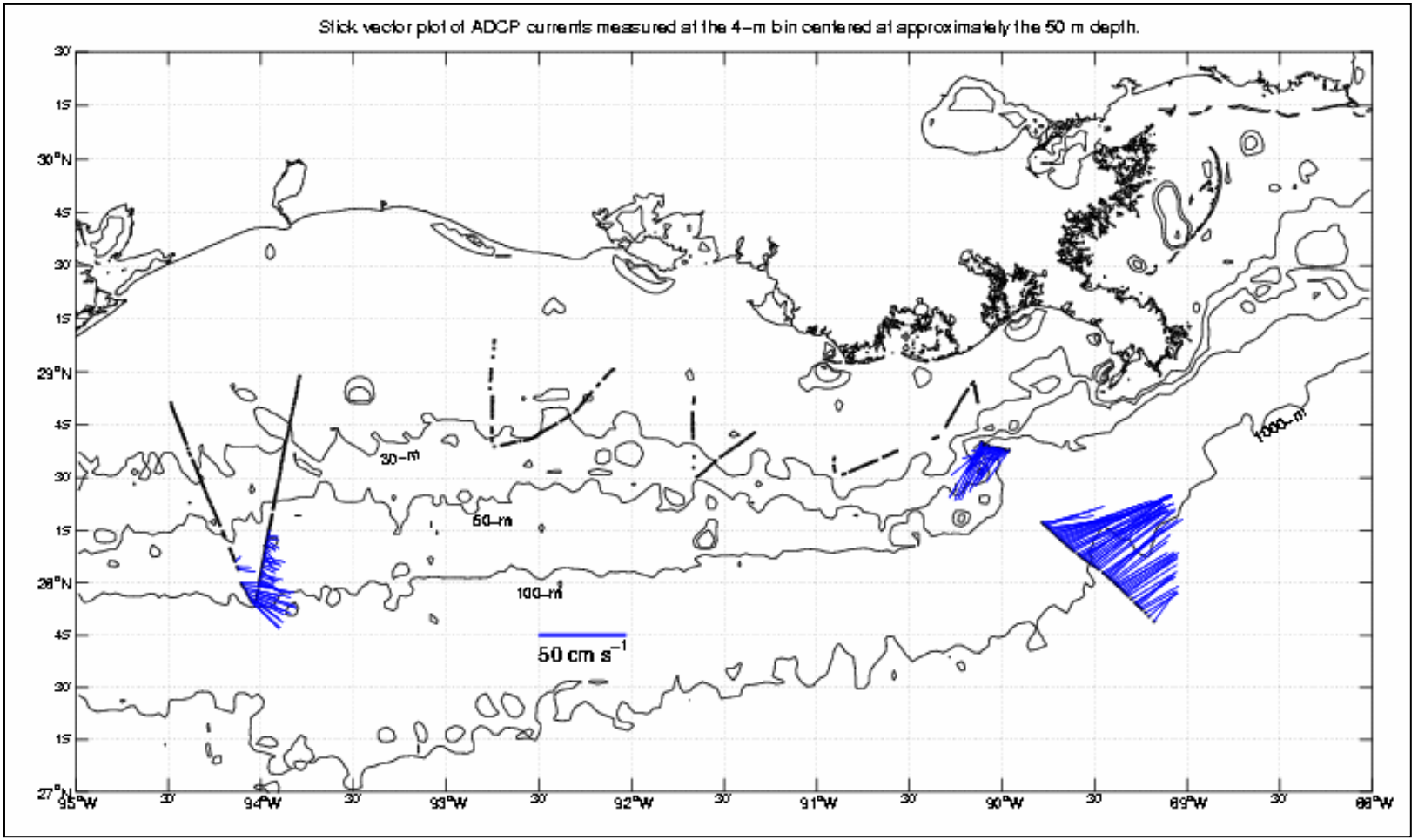

Figure C.2 Stick vector plot of ADCP currents measured at the 4-m bin centered at approximately the 50-m depth. Bathymetric contours are shown for 30-, 50-, 100-, and 1,000-m depths.

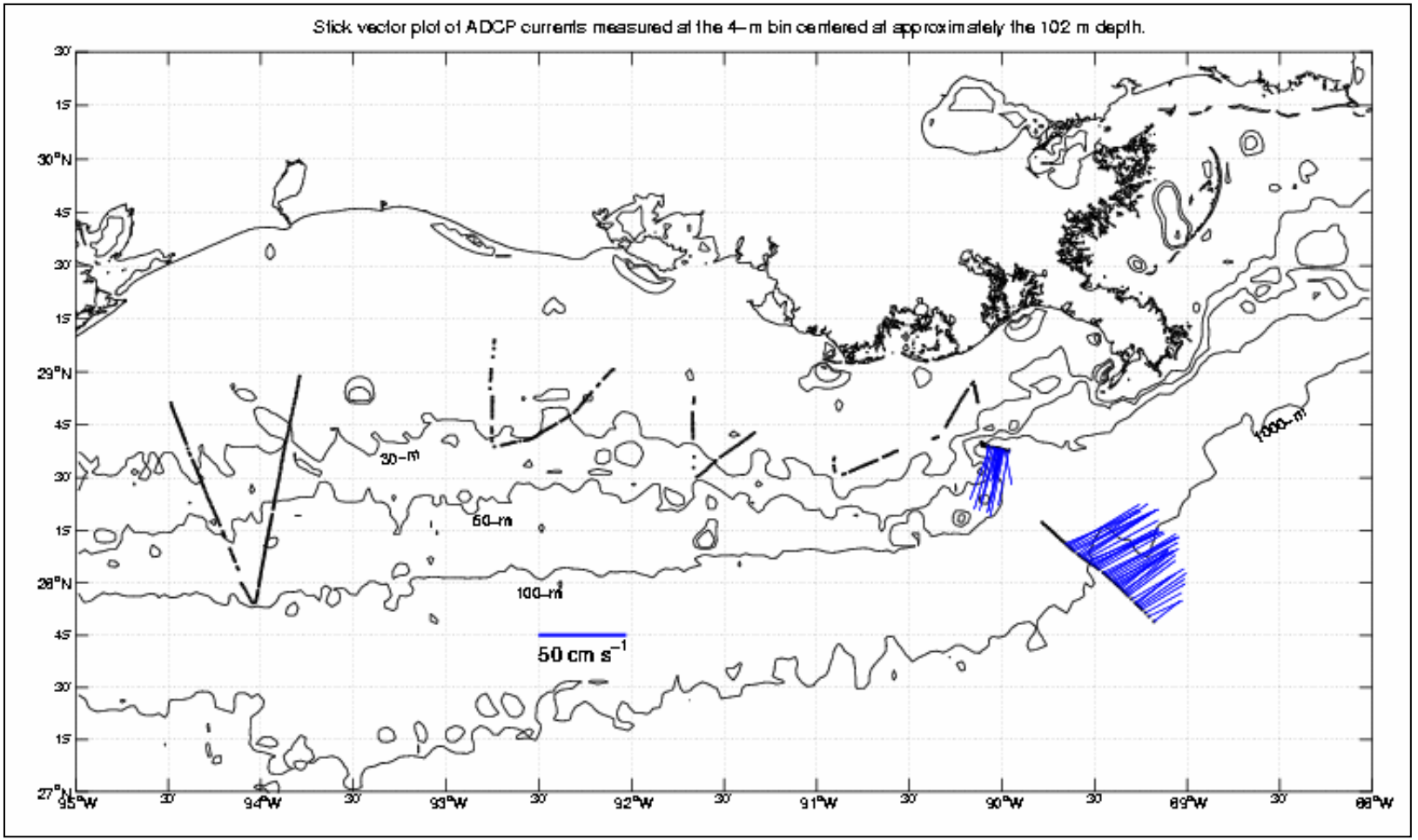

Figure C.3 Stick vector plot of ADCP currents measured at the 4-m bin centered at approximately the 102-m depth. Bathymetric contours are shown for 30-, 50-, 100-, and 1,000-m depths.

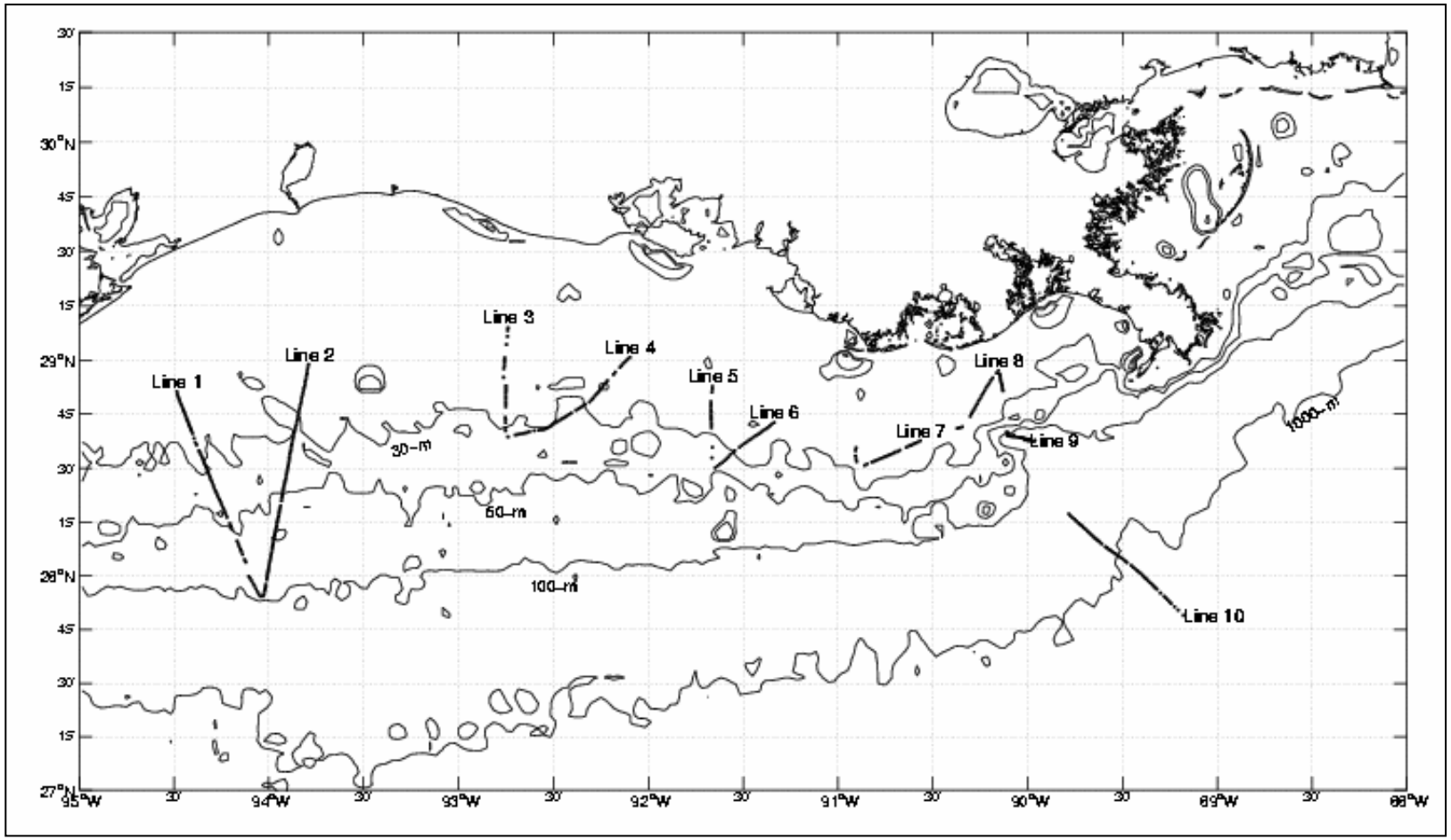

Figure C.4 ADCP lines used to show vertical profiles. Bathymetric contours are shown for 30-, 50-, 100-, and 1,000-m

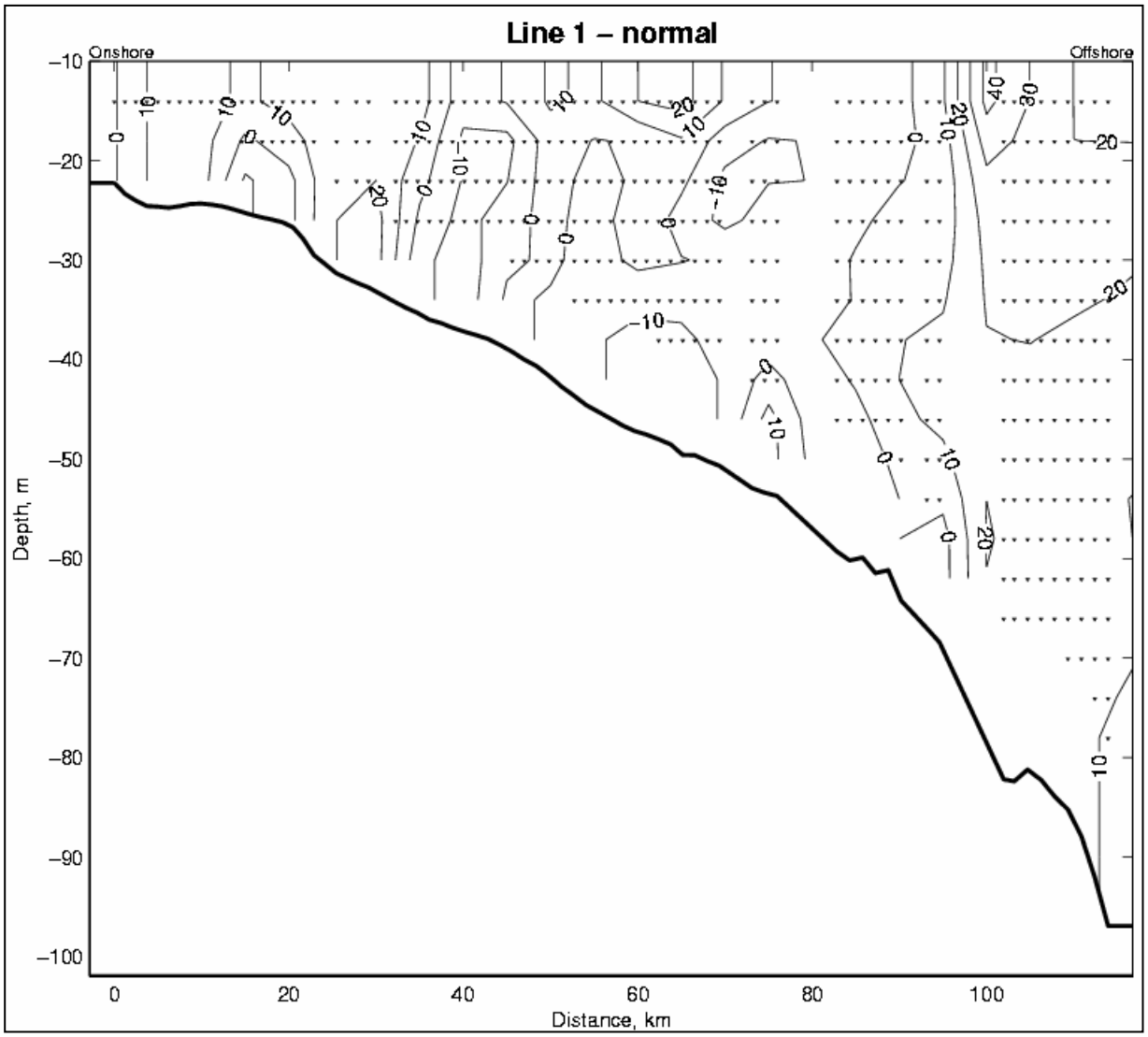

Figure C.5 Vertical section of ADCP velocities (cm s^{-1}) normal to Line 1 for cruise 98-G-9. Upcoast velocities are positive. Ensemble locations are marked with a small triangle.

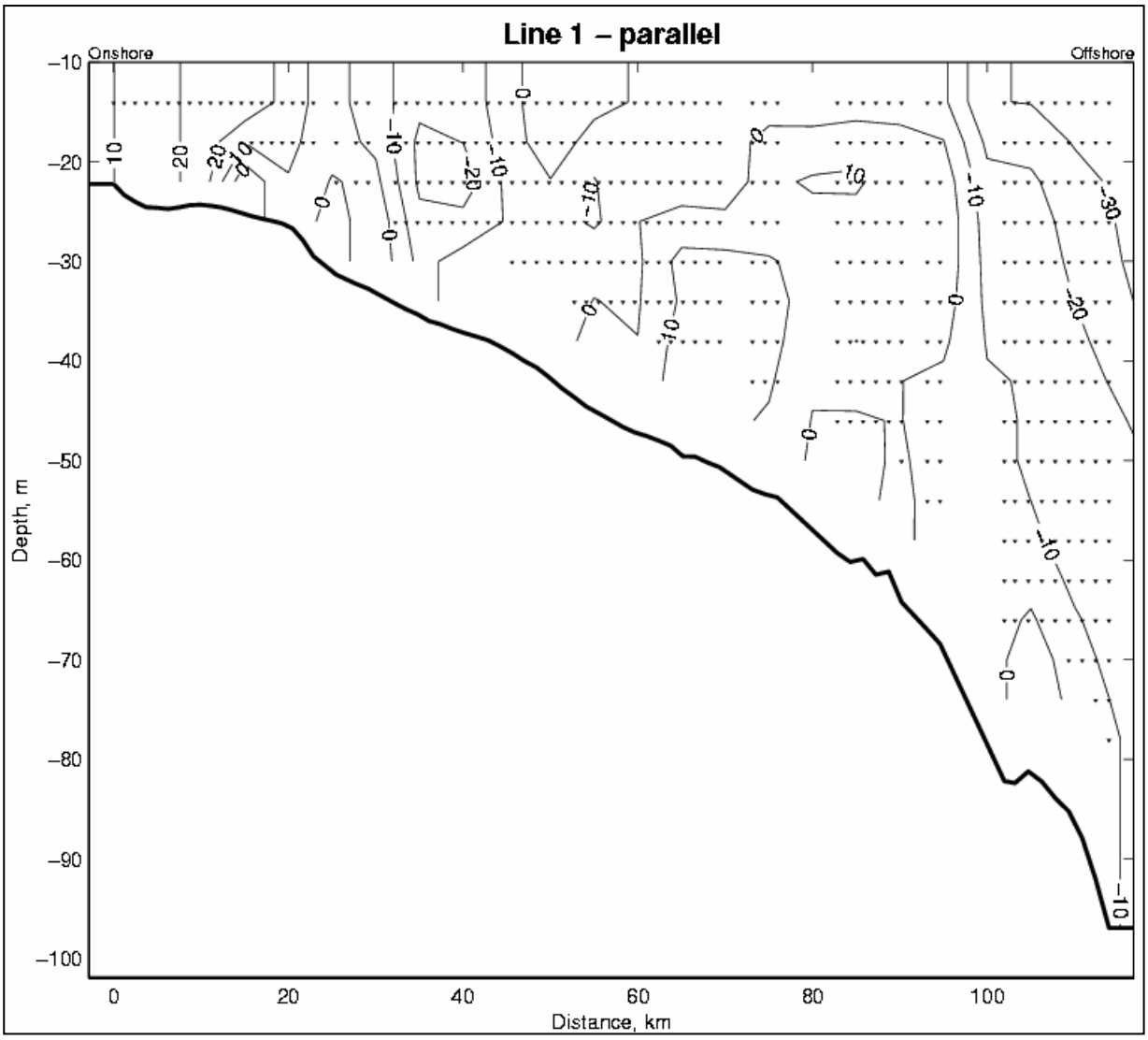

Figure C.6 Vertical section of ADCP velocities (cm s^{-1}) parallel to Line 1 for cruise 98-G-9. Onshore velocities are positive. Ensemble locations are marked with a small triangle.

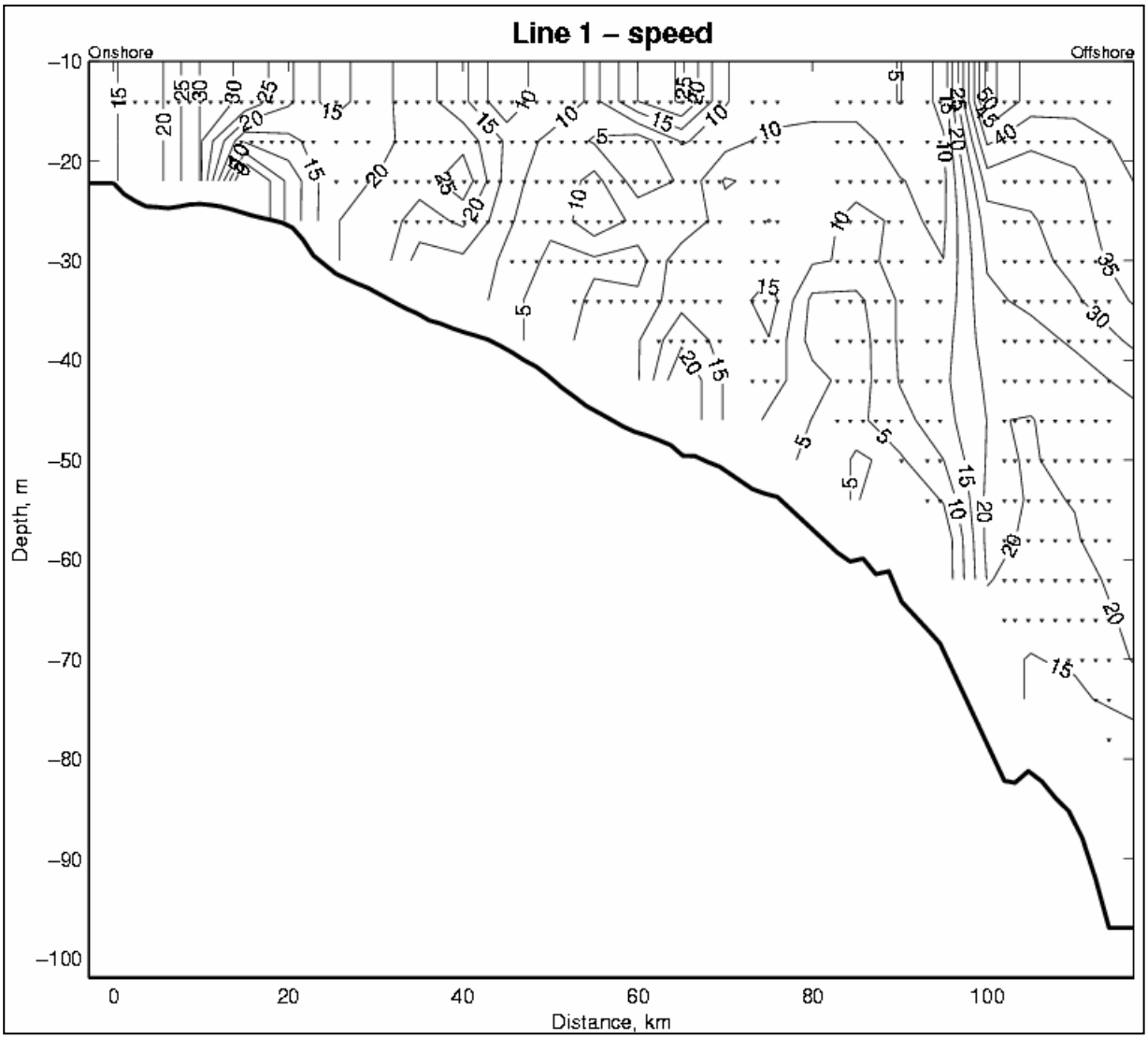

Figure C.7 Vertical section of ADCP speeds (cm s^{-1}) for Line 1 for cruise 98-G-9. Ensemble locations are marked with a small triangle.

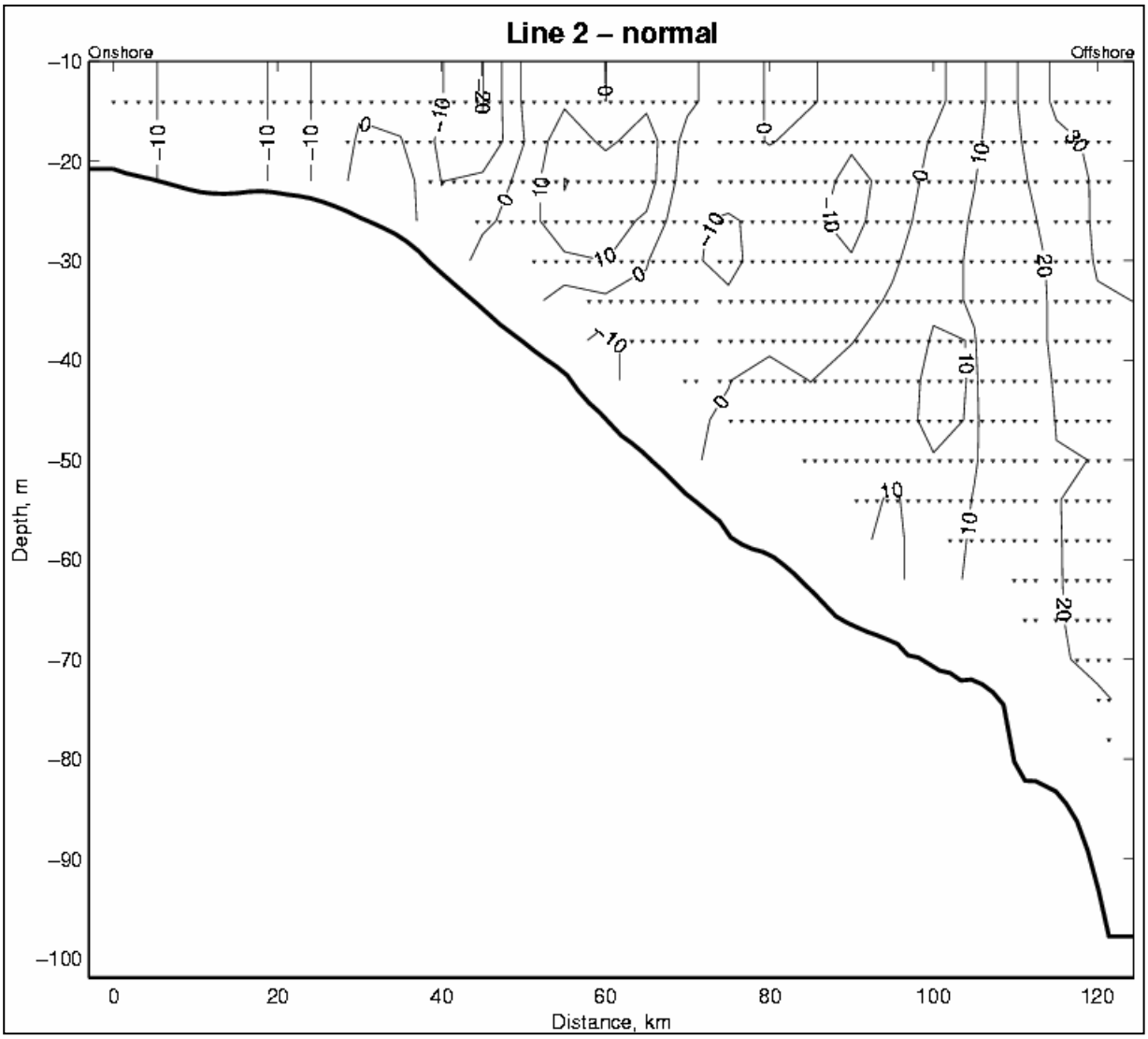

Figure C.8 Vertical section of ADCP velocities (cm s^{-1}) normal to Line 2 for cruise 98-G-9. Upcoast velocities are positive. Ensemble locations are marked with a small triangle.

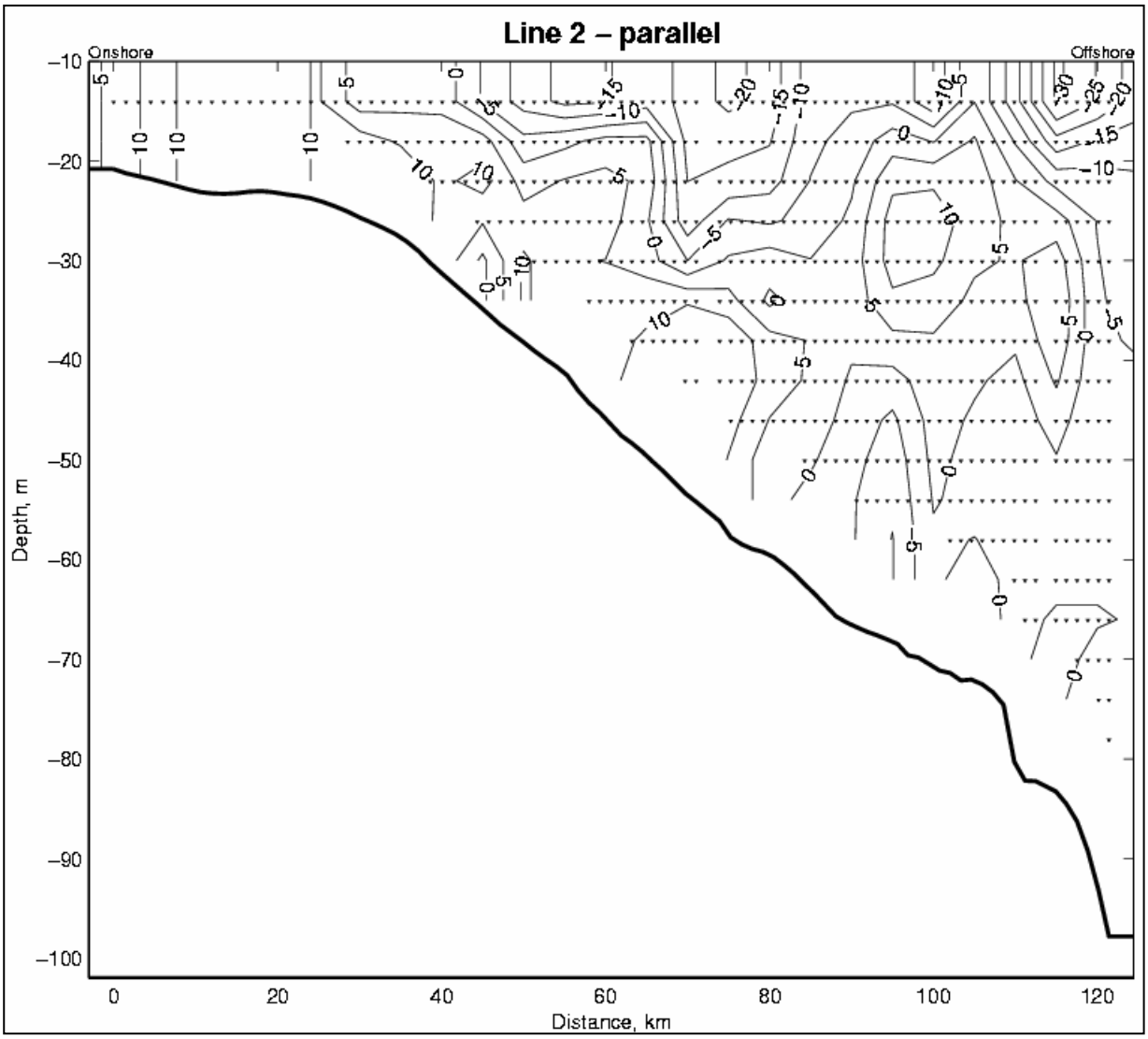

Figure C.9 Vertical section of ADCP velocities (cm s^{-1}) parallel to Line 2 for cruise 98-G-9. Onshore velocities are positive. Ensemble locations are marked with a small triangle.

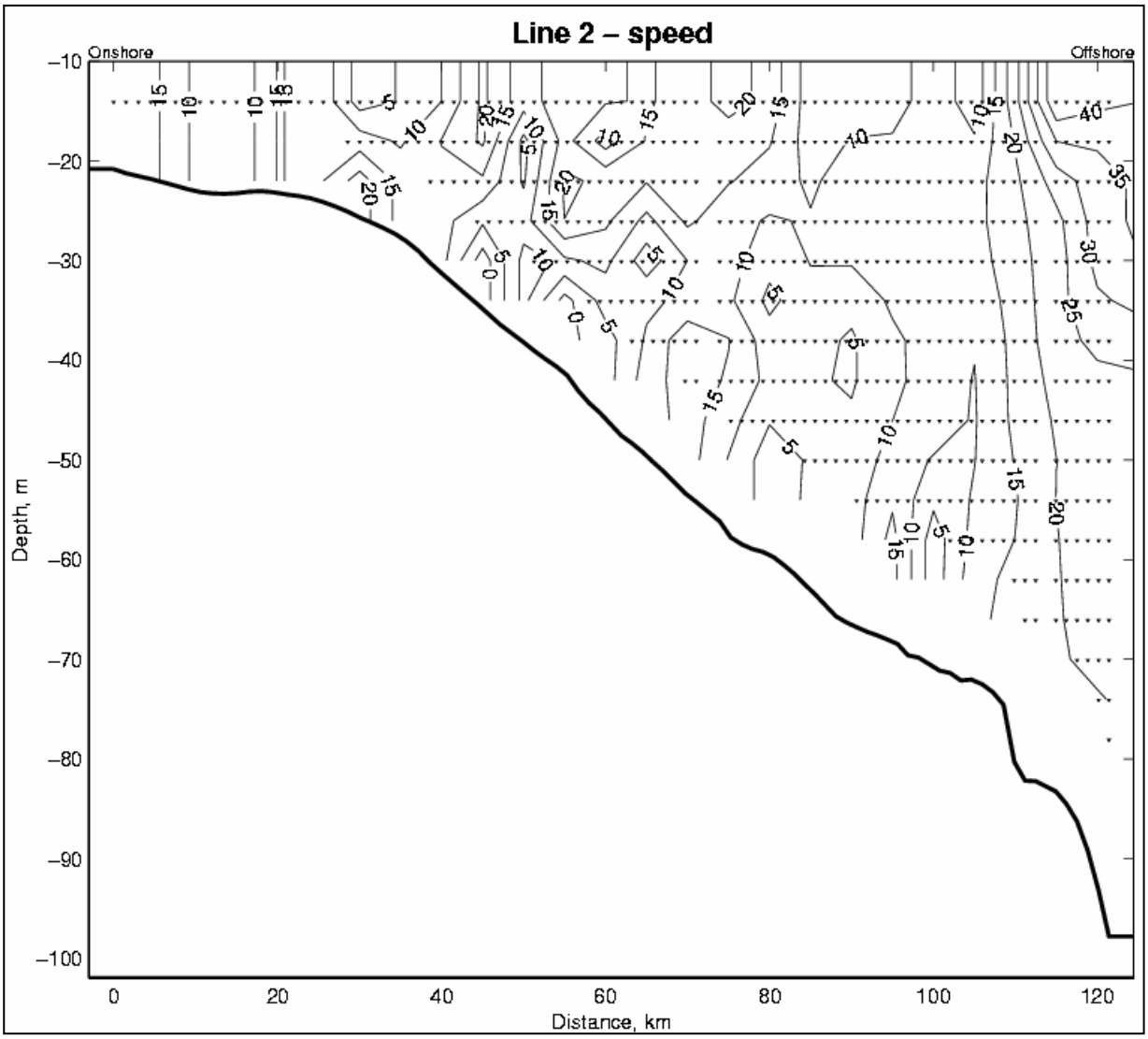

Figure C.10 Vertical section of ADCP speeds (cm s^{-1}) for Line 2 for cruise 98-G-9. Ensemble locations are marked with a small triangle.

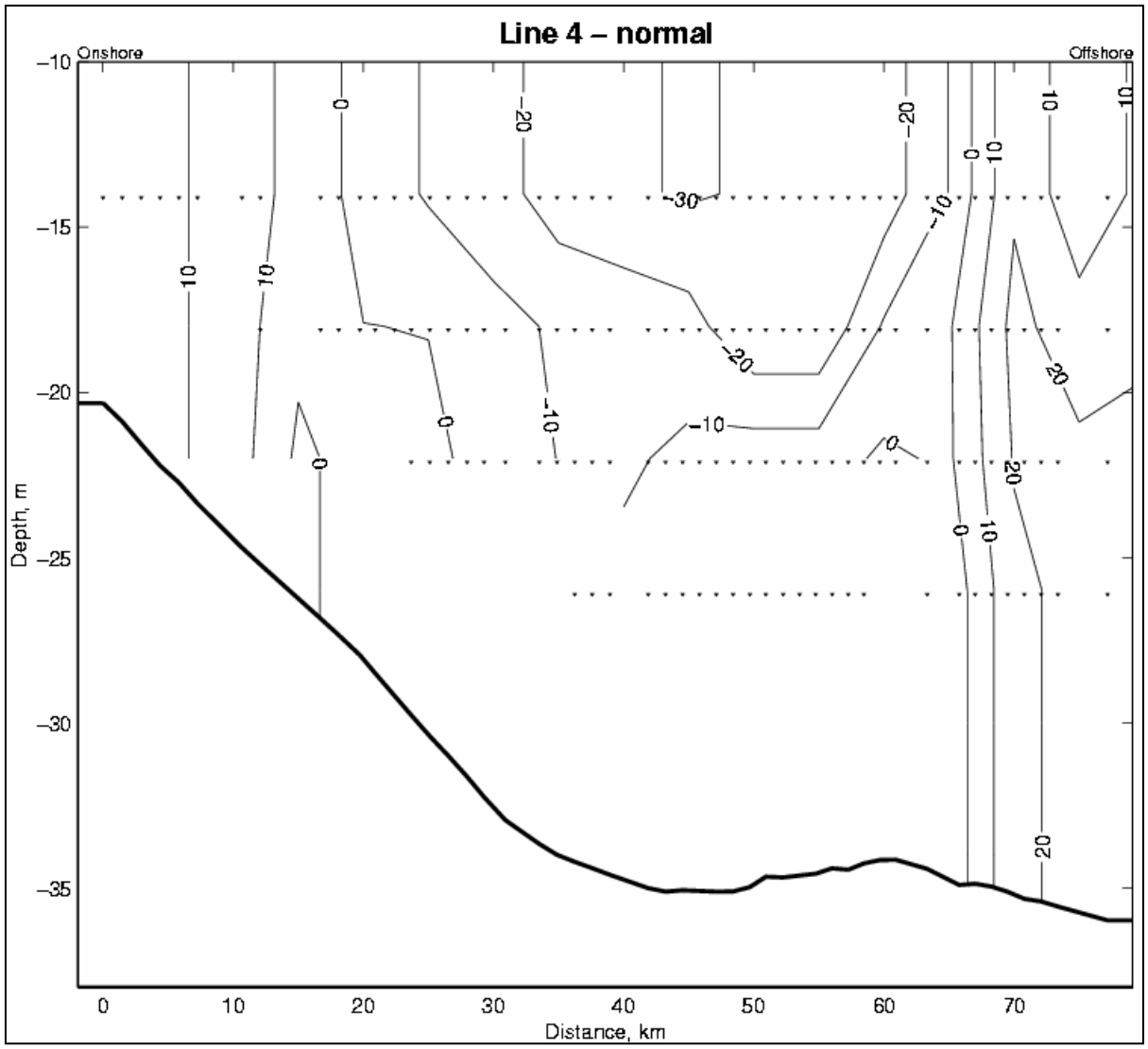

Figure C.11 Vertical section of ADCP velocities (cm s^{-1}) normal to Line 4 for cruise 98-G-9. Upcoast velocities are positive. Ensemble locations are marked with a small triangle.

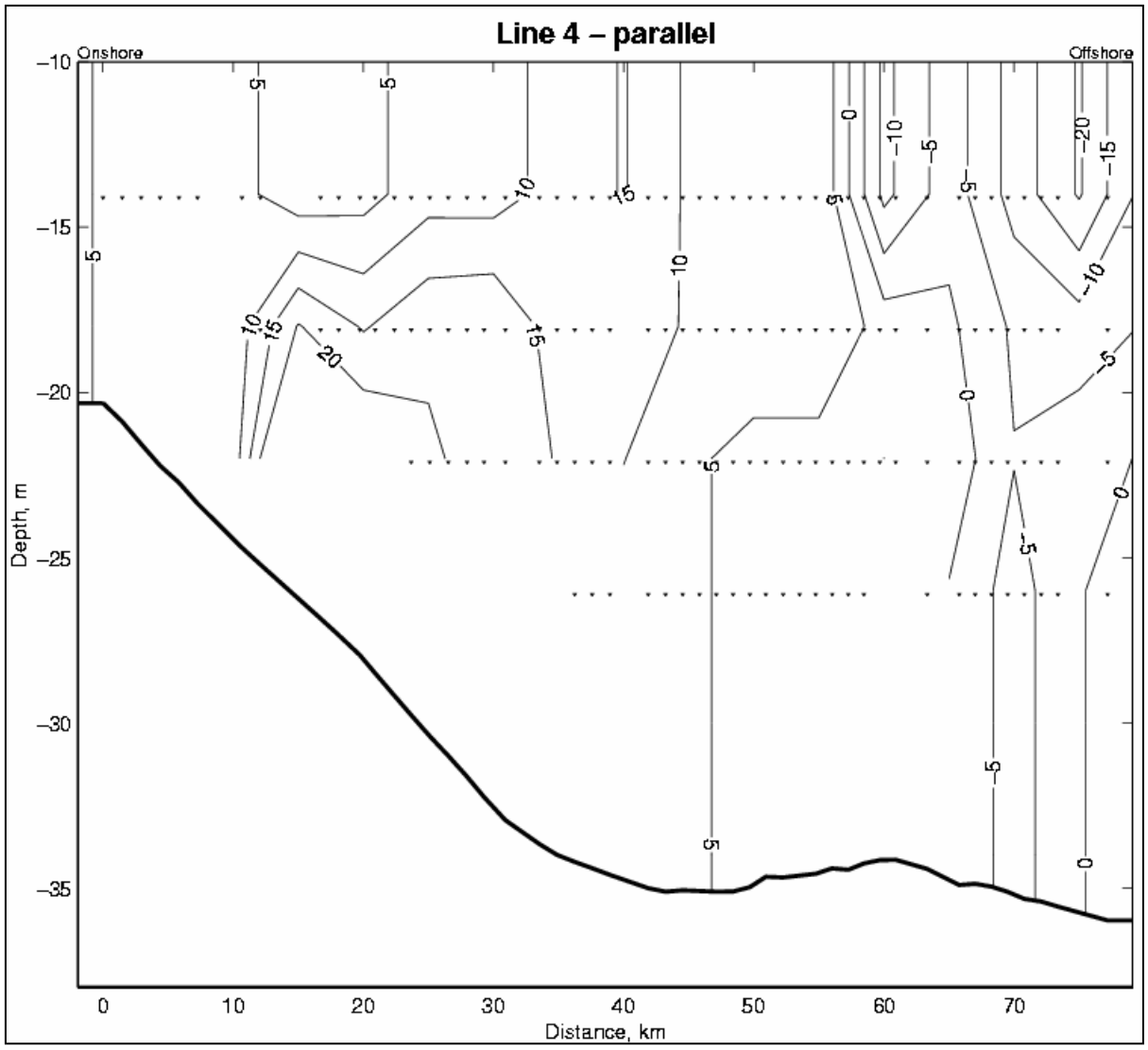

Figure C.12 Vertical section of ADCP velocities (cm s^{-1}) parallel to Line 4 for cruise 98-G-9. Onshore velocities are positive. Ensemble locations are marked with a small triangle.

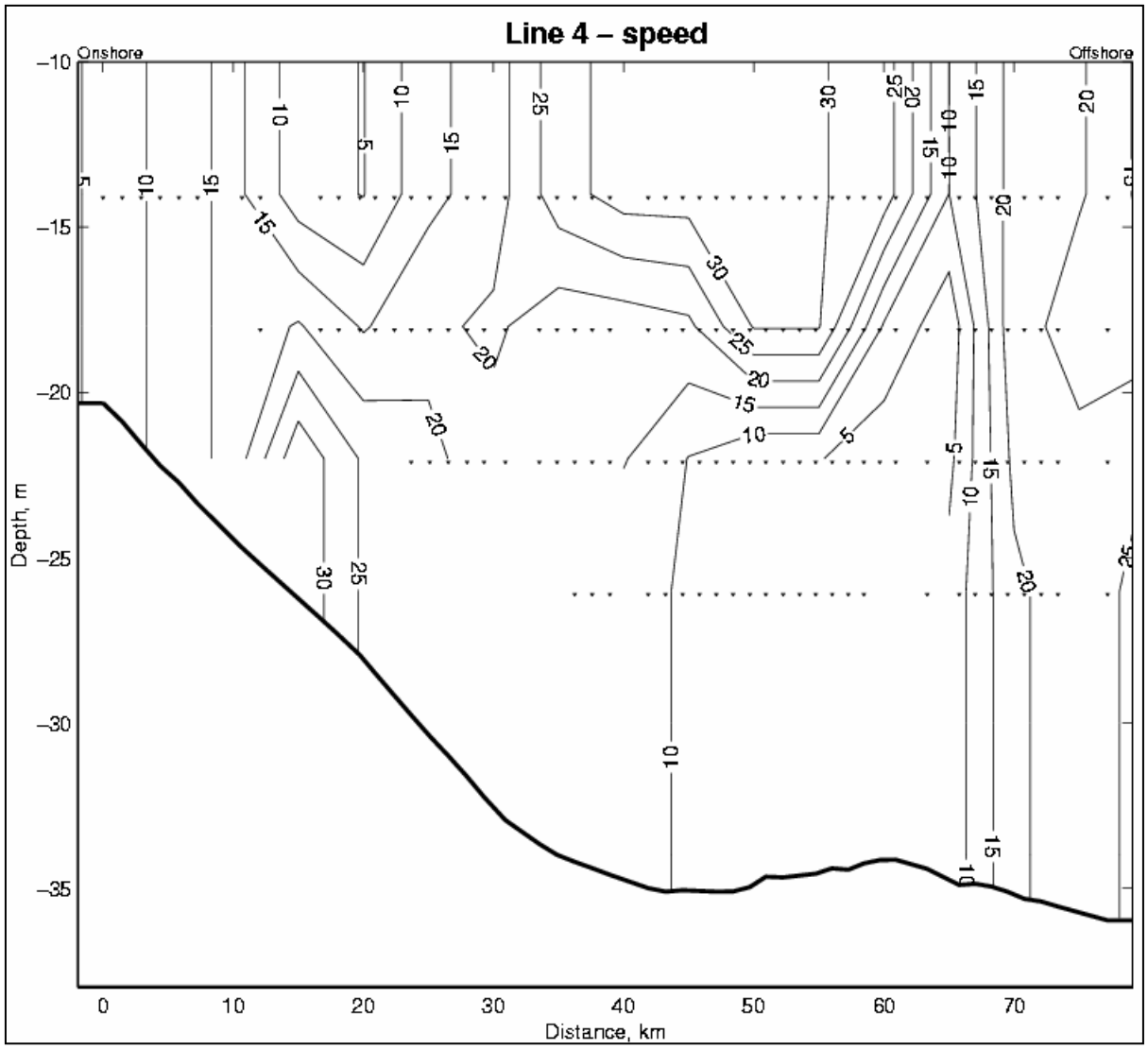

Figure C.13 Vertical section of ADCP speeds (cm s^{-1}) for Line 4 for cruise 98-G-9. Ensemble locations are marked with a small triangle.

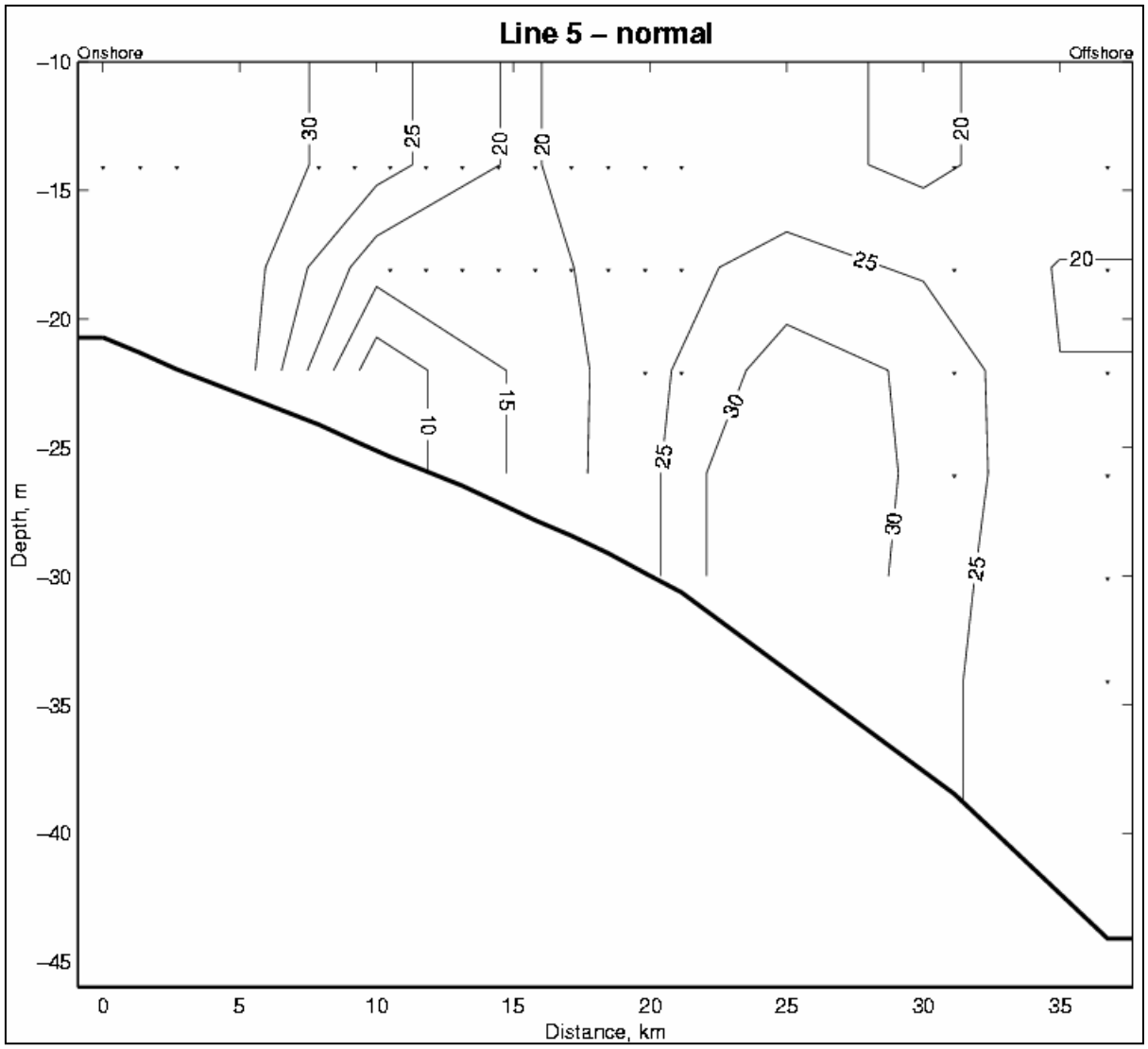

Figure C.14 Vertical section of ADCP velocities (cm s^{-1}) normal to Line 5 for cruise 98-G-9. Upcoast velocities are positive. Ensemble locations are marked with a small triangle.

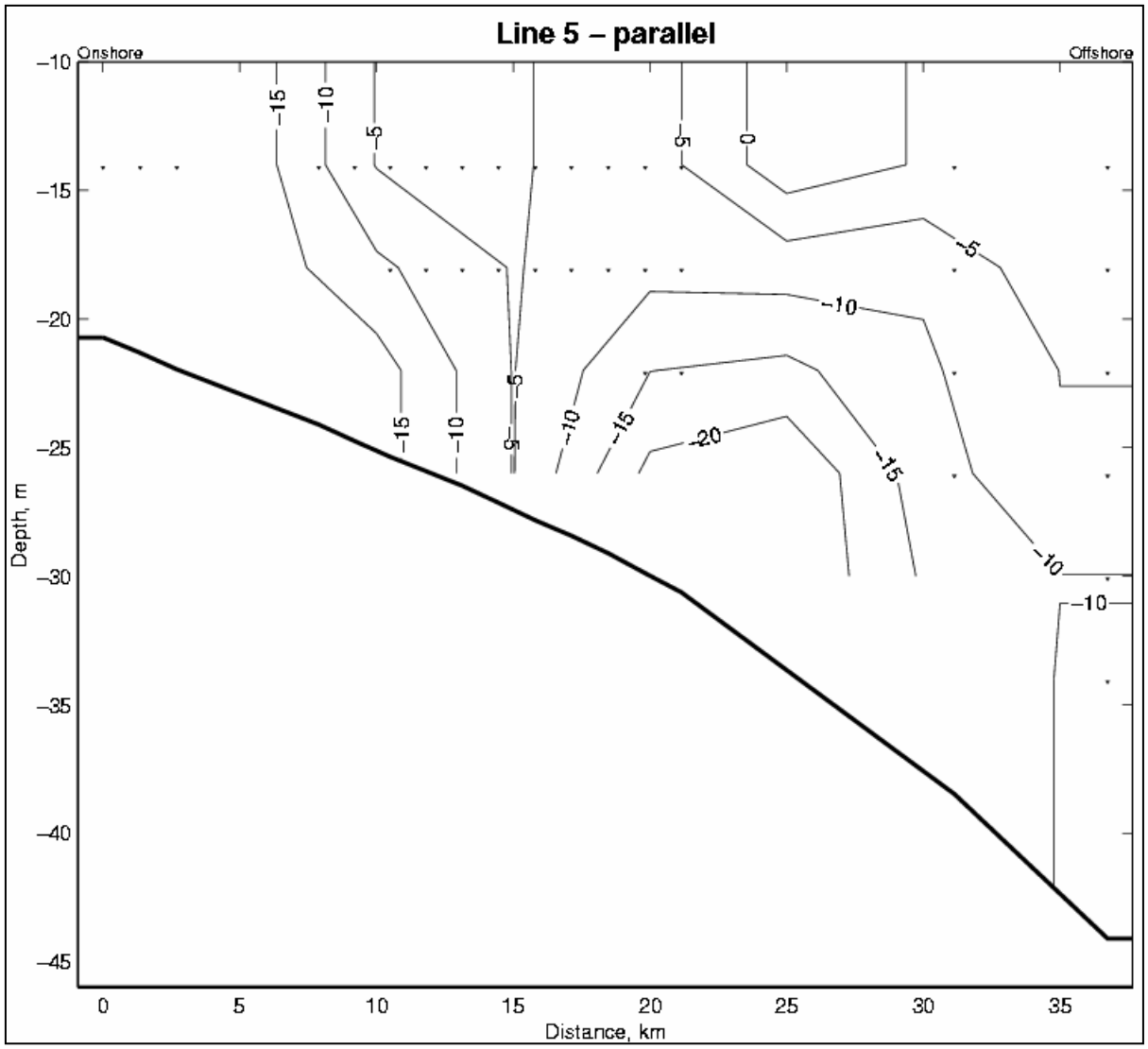

Figure C.15 Vertical section of ADCP velocities (cm s^{-1}) parallel to Line 5 for cruise 98-G-9. Onshore velocities are positive. Ensemble locations are marked with a small triangle.

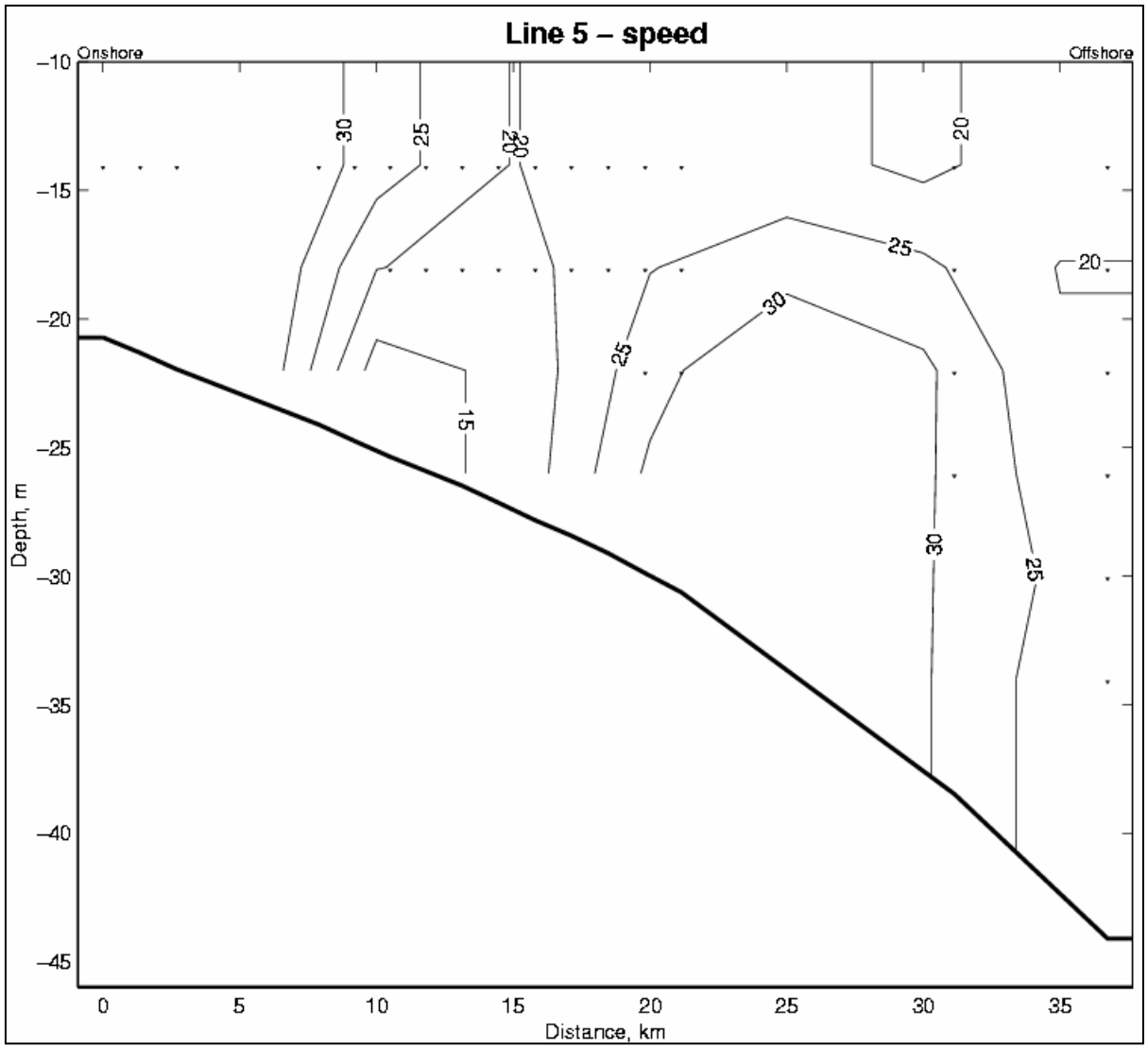

Figure C.16 Vertical section of ADCP speeds (cm s^{-1}) for Line 5 for cruise 98-G-9. Ensemble locations are marked with a small triangle.

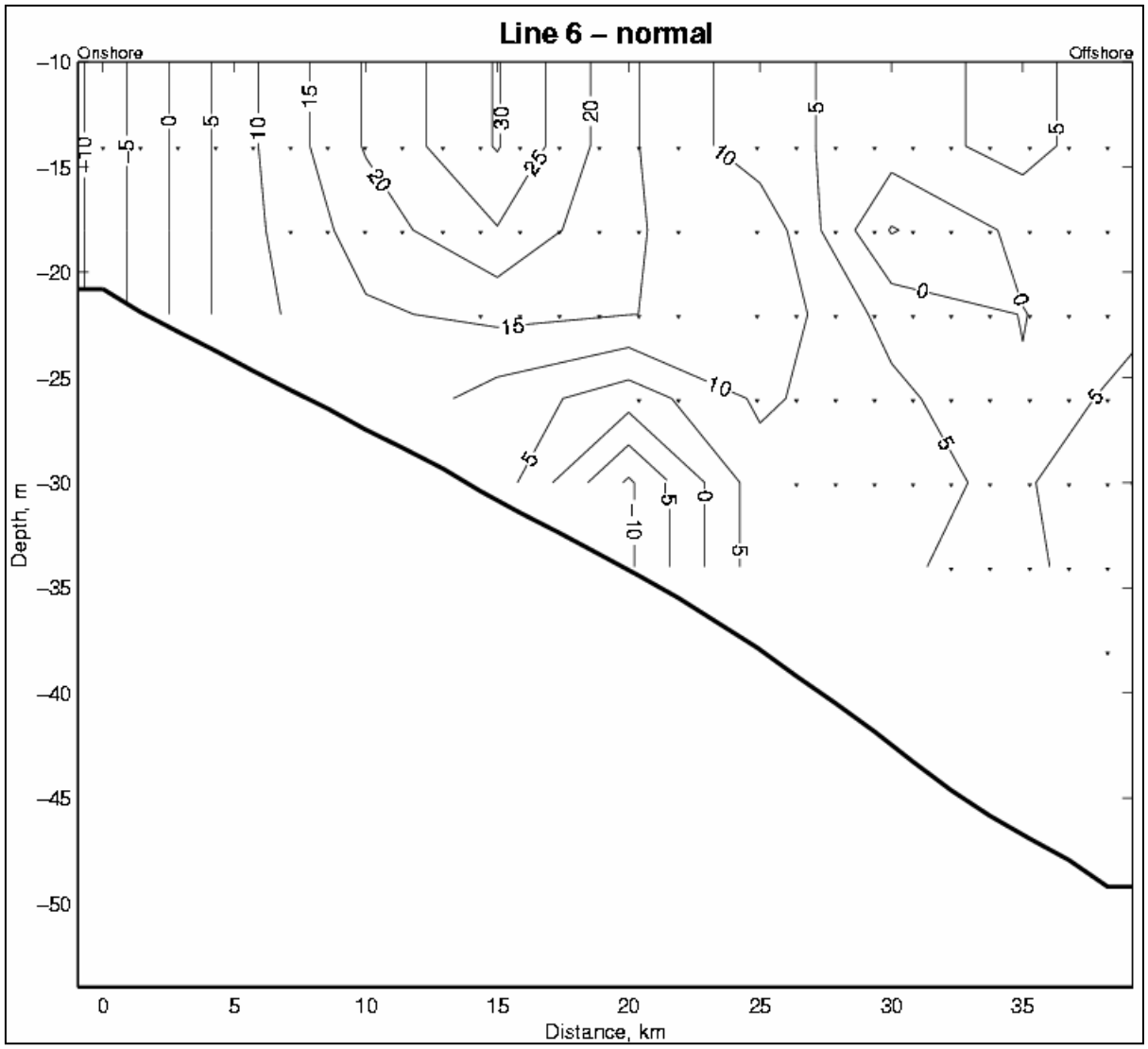

Figure C.17 Vertical section of ADCP velocities (cm s^{-1}) normal to Line 6 for cruise 98-G-9. Upcoast velocities are positive. Ensemble locations are marked with a small triangle.

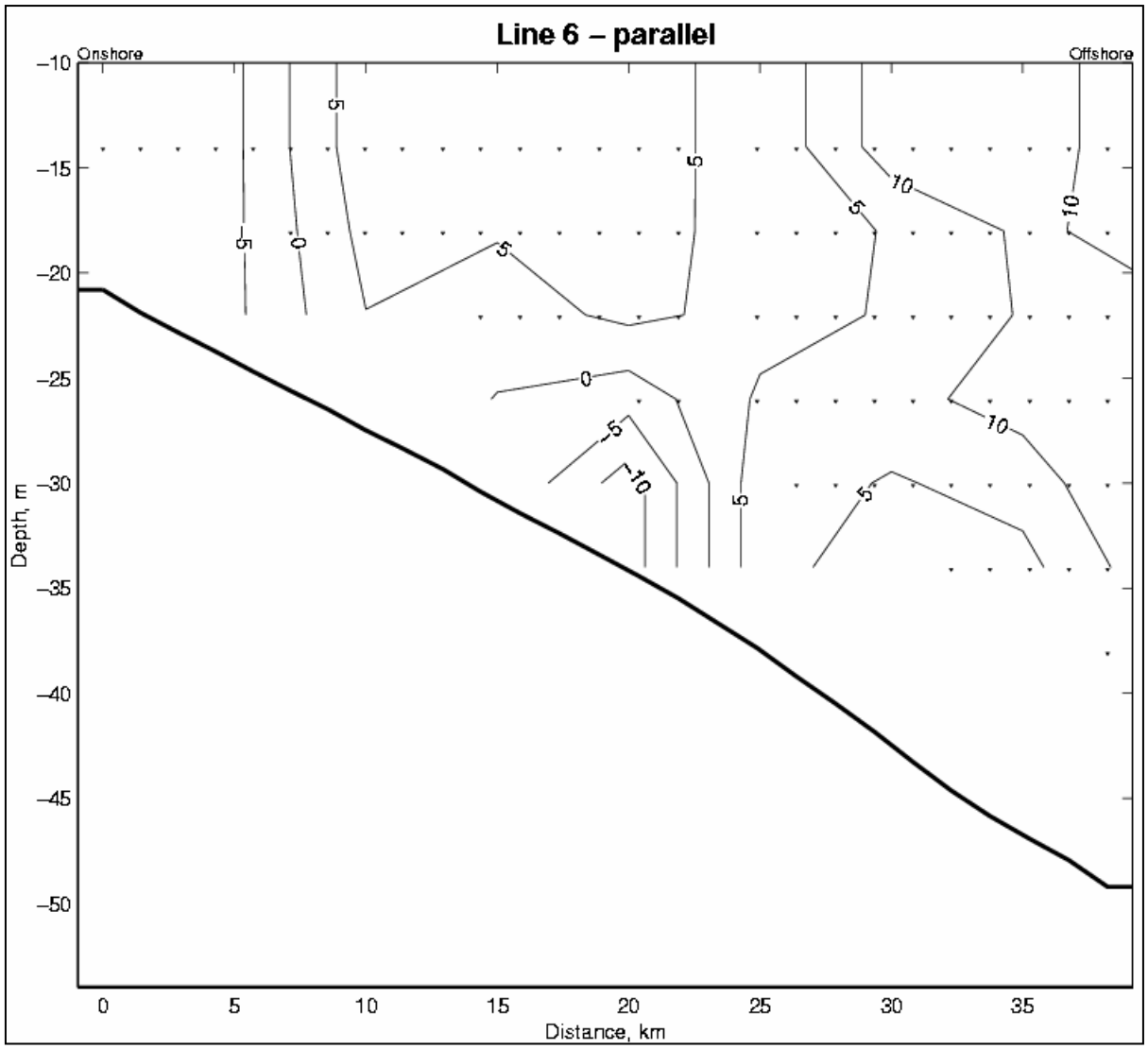

Figure C.18 Vertical section of ADCP velocities (cm s^{-1}) parallel to Line 6 for cruise 98-G-9. Onshore velocities are positive. Ensemble locations are marked with a small triangle.

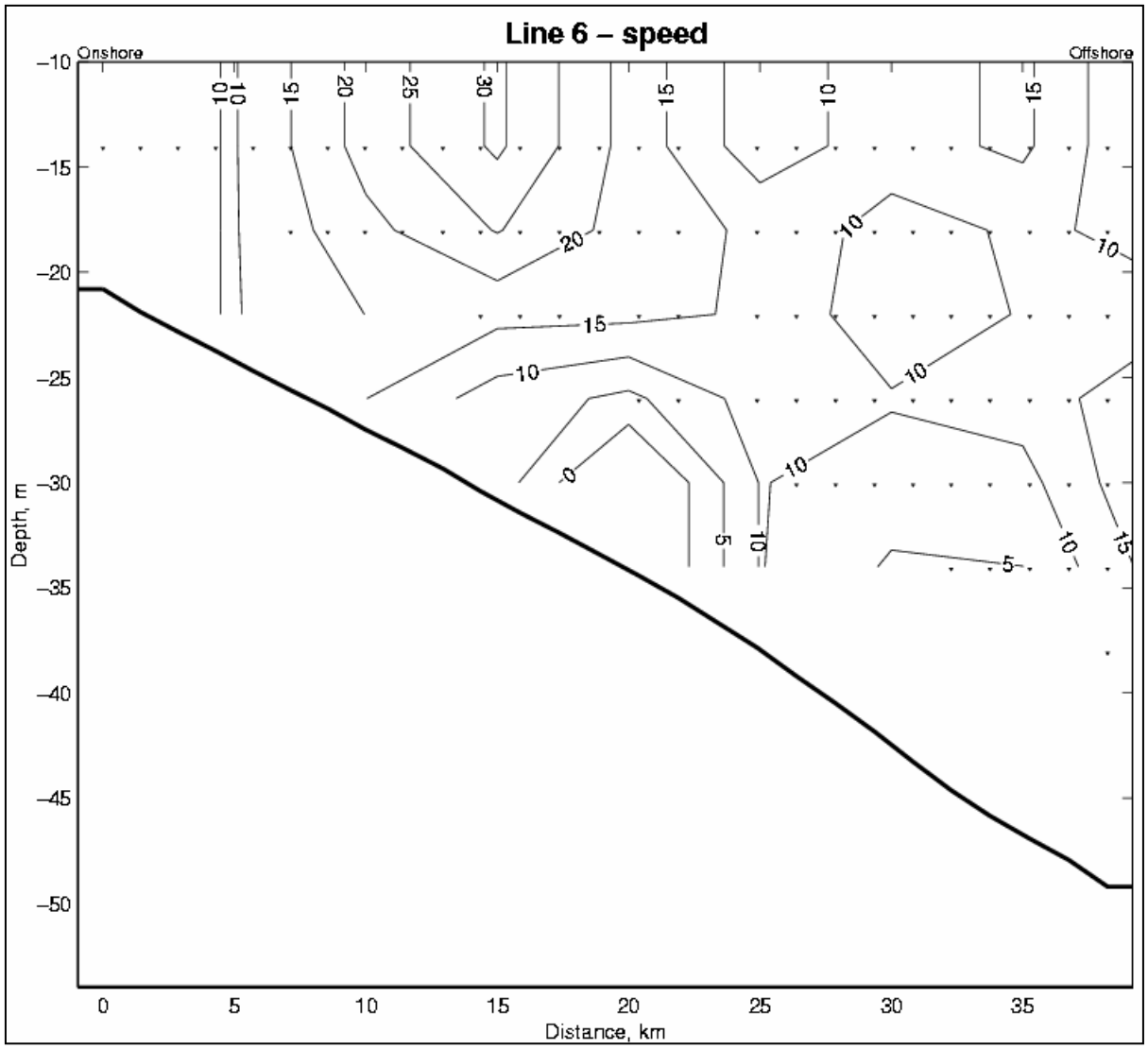

Figure C.19 Vertical section of ADCP speeds (cm s^{-1}) for Line 6 for cruise 98-G-9. Ensemble locations are marked with a small triangle.

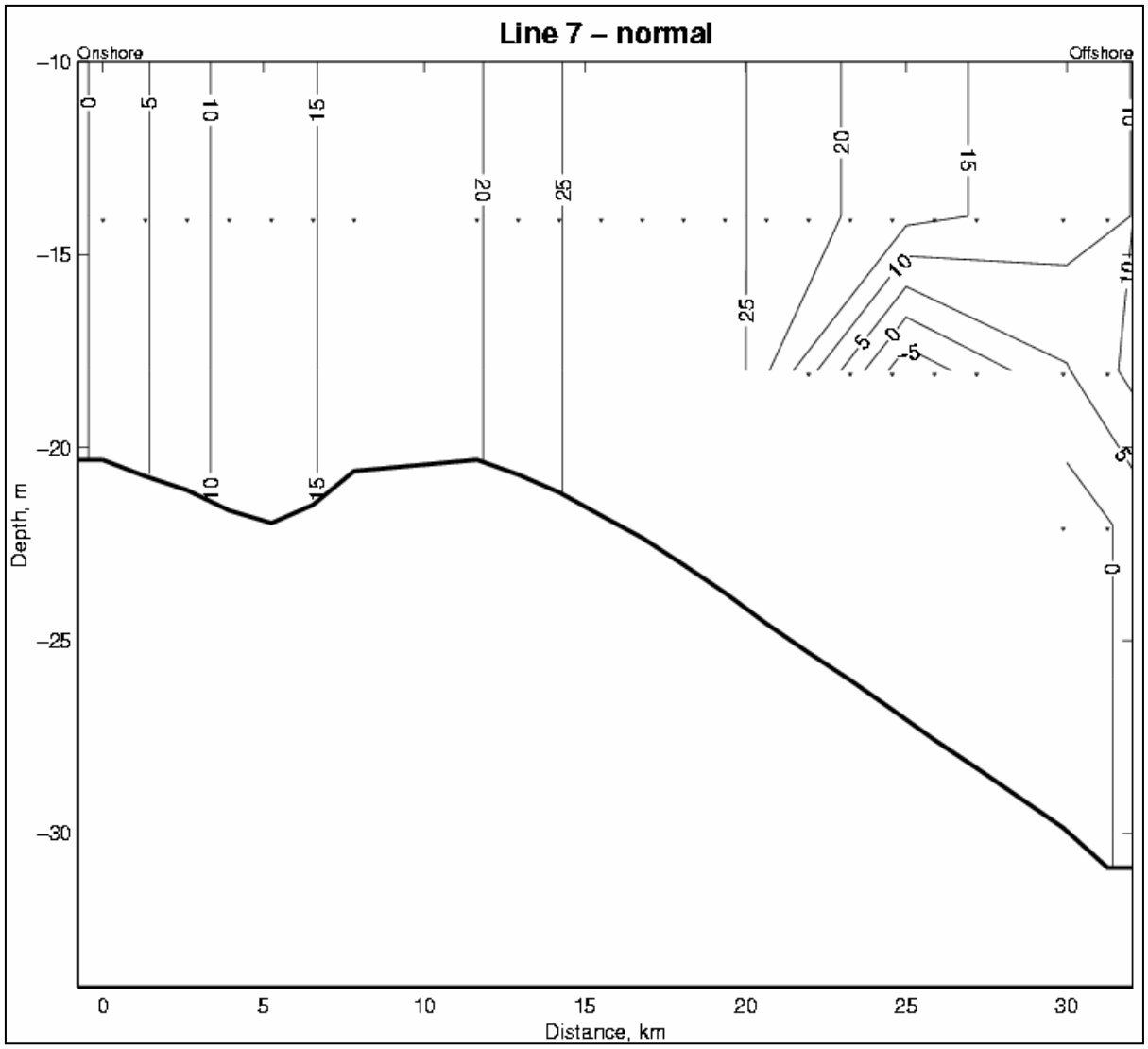

Figure C.20 Vertical section of ADCP velocities (cm s^{-1}) normal to Line 7 for cruise 98-G-9. Upcoast velocities are positive. Ensemble locations are marked with a small triangle.

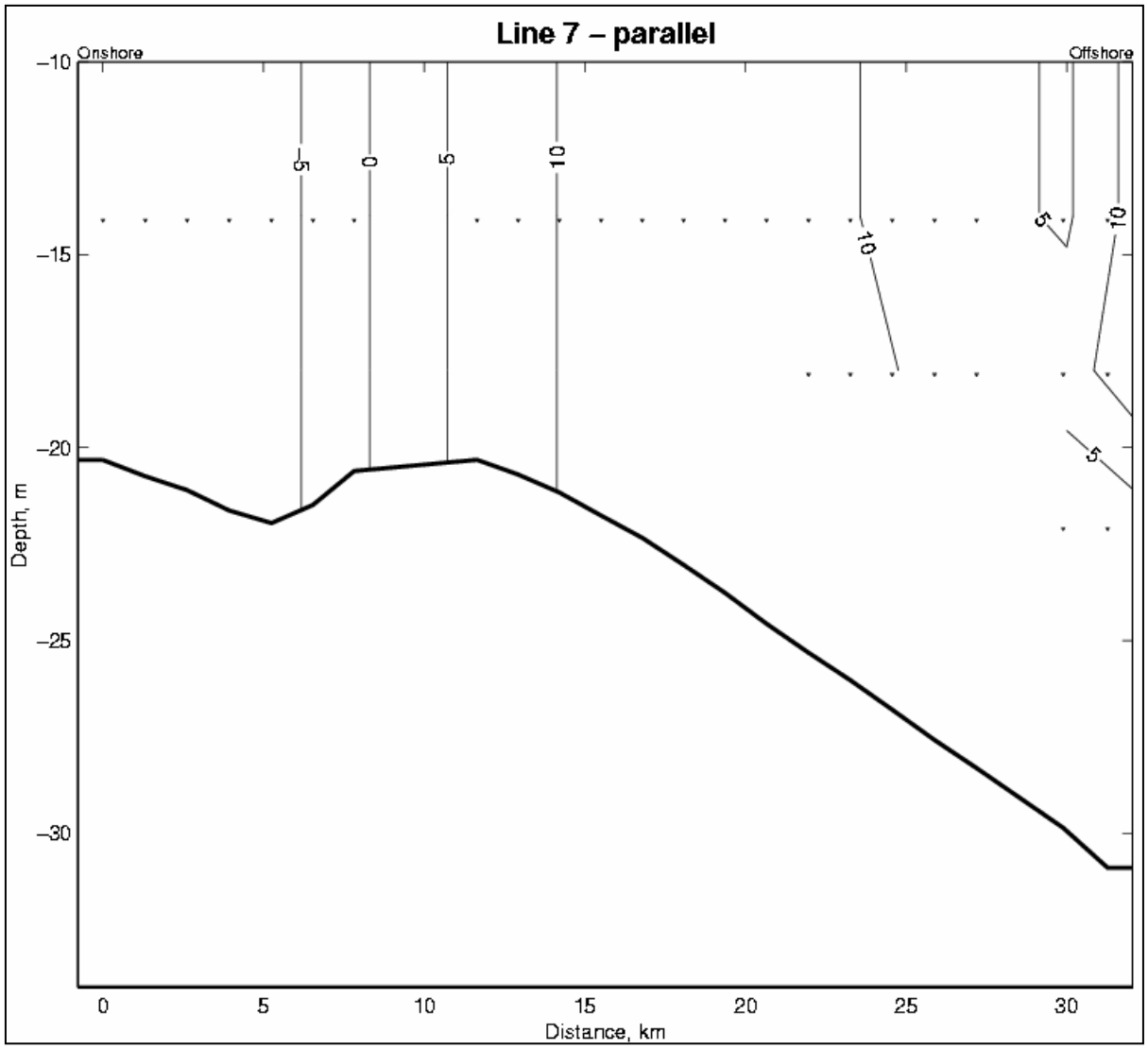

Figure C.21 Vertical section of ADCP velocities (cm s^{-1}) parallel to Line 7 for cruise 98-G-9. Onshore velocities are positive. Ensemble locations are marked with a small triangle.

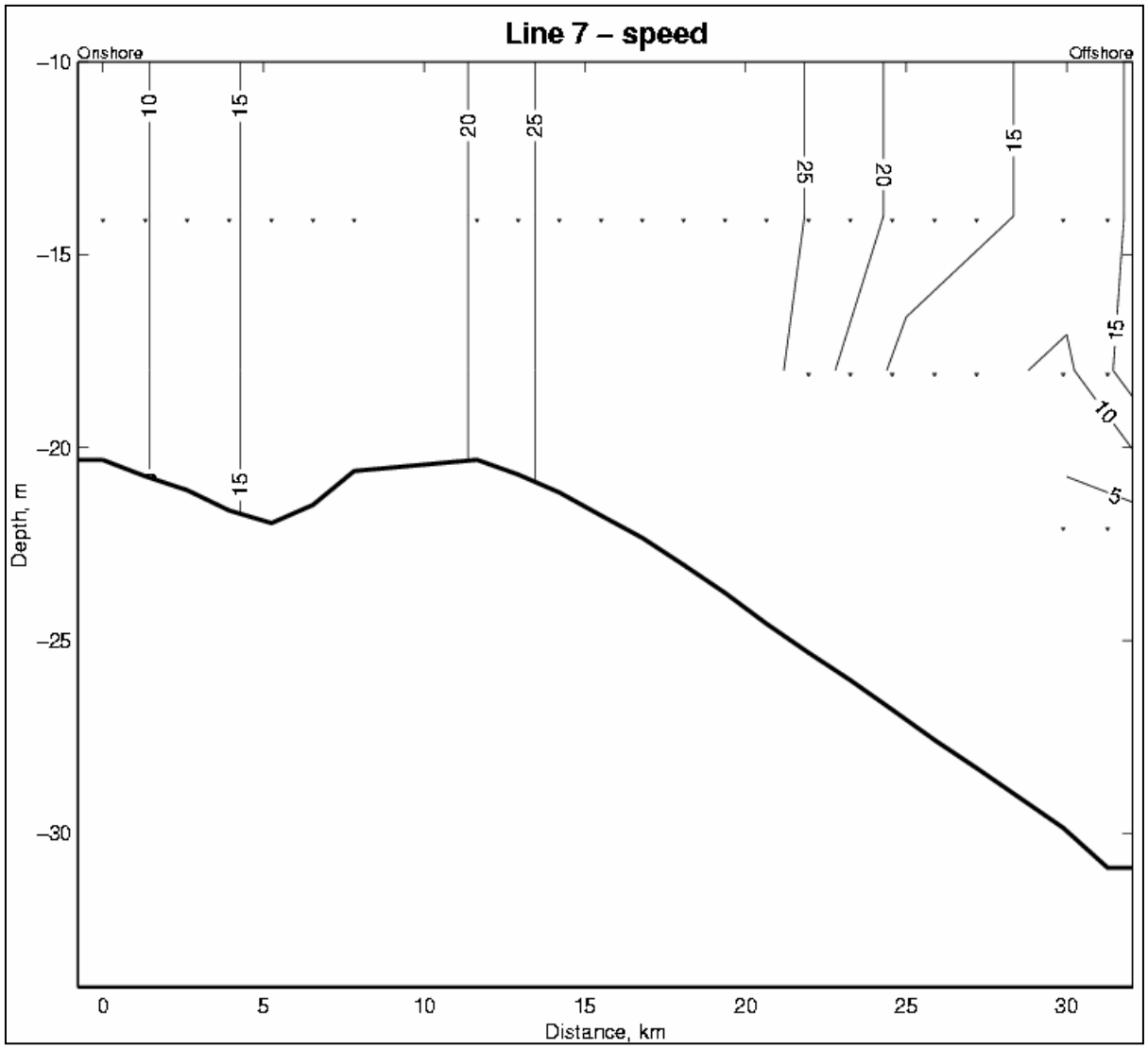

Figure C.22 Vertical section of ADCP speeds (cm s^{-1}) for Line 7 for cruise 98-G-9. Ensemble locations are marked with a small triangle.

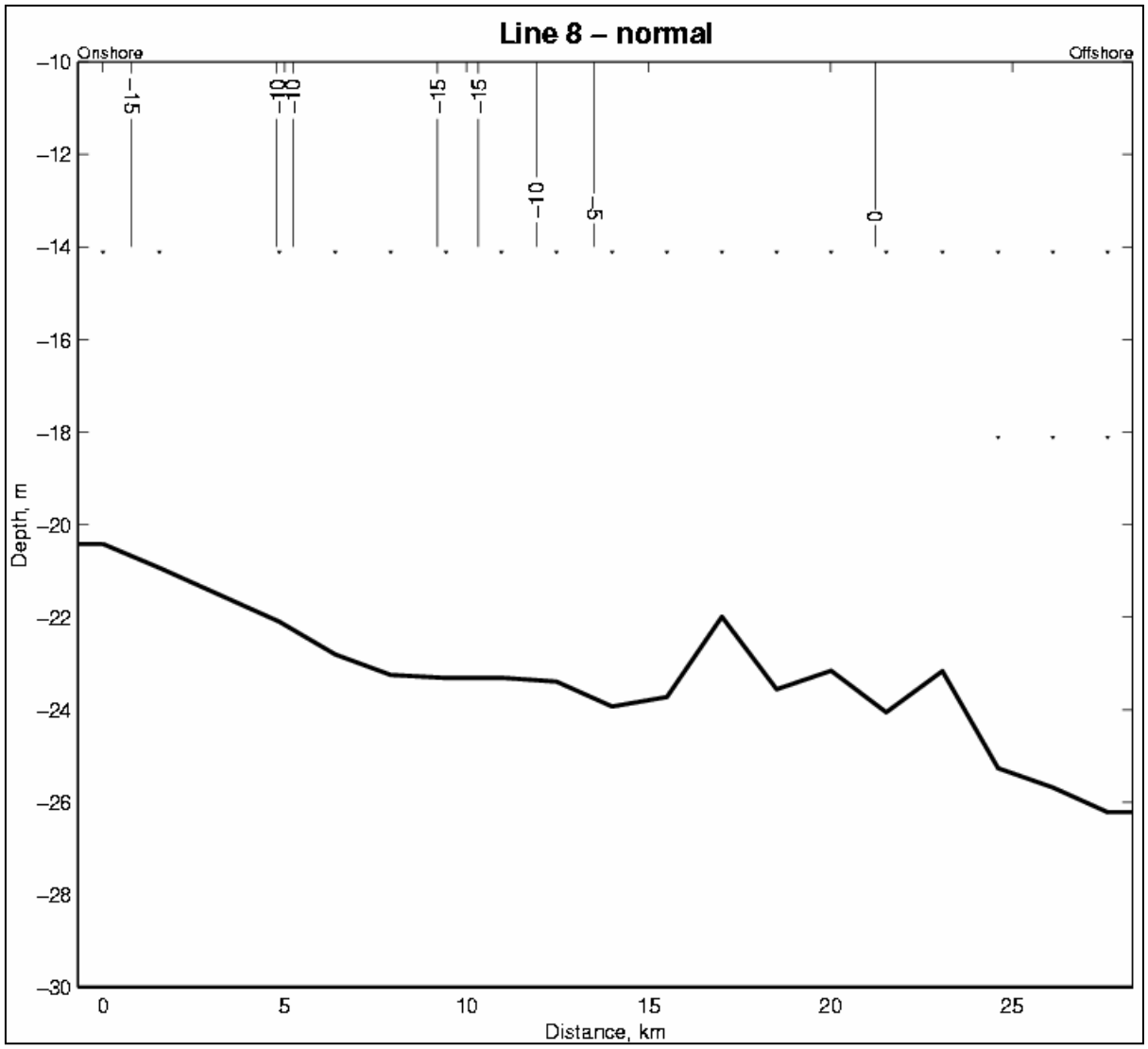

Figure C.23 Vertical section of ADCP velocities (cm s^{-1}) normal to Line 8 for cruise 98-G-9. Upcoast velocities are positive. Ensemble locations are marked with a small triangle.

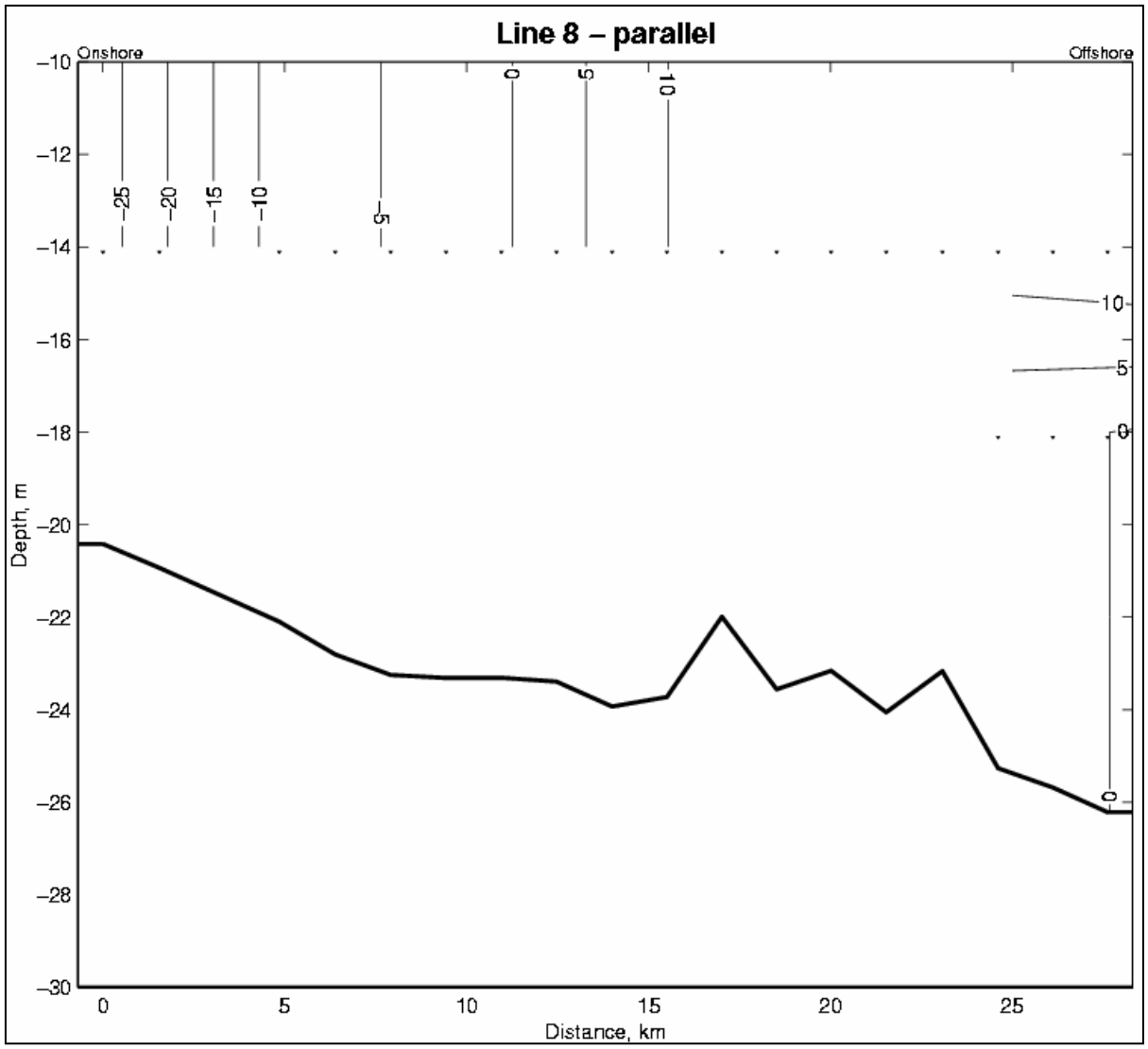

Figure C.24 Vertical section of ADCP velocities (cm s^{-1}) parallel to Line 8 for cruise 98-G-9. Onshore velocities are positive. Ensemble locations are marked with a small triangle.

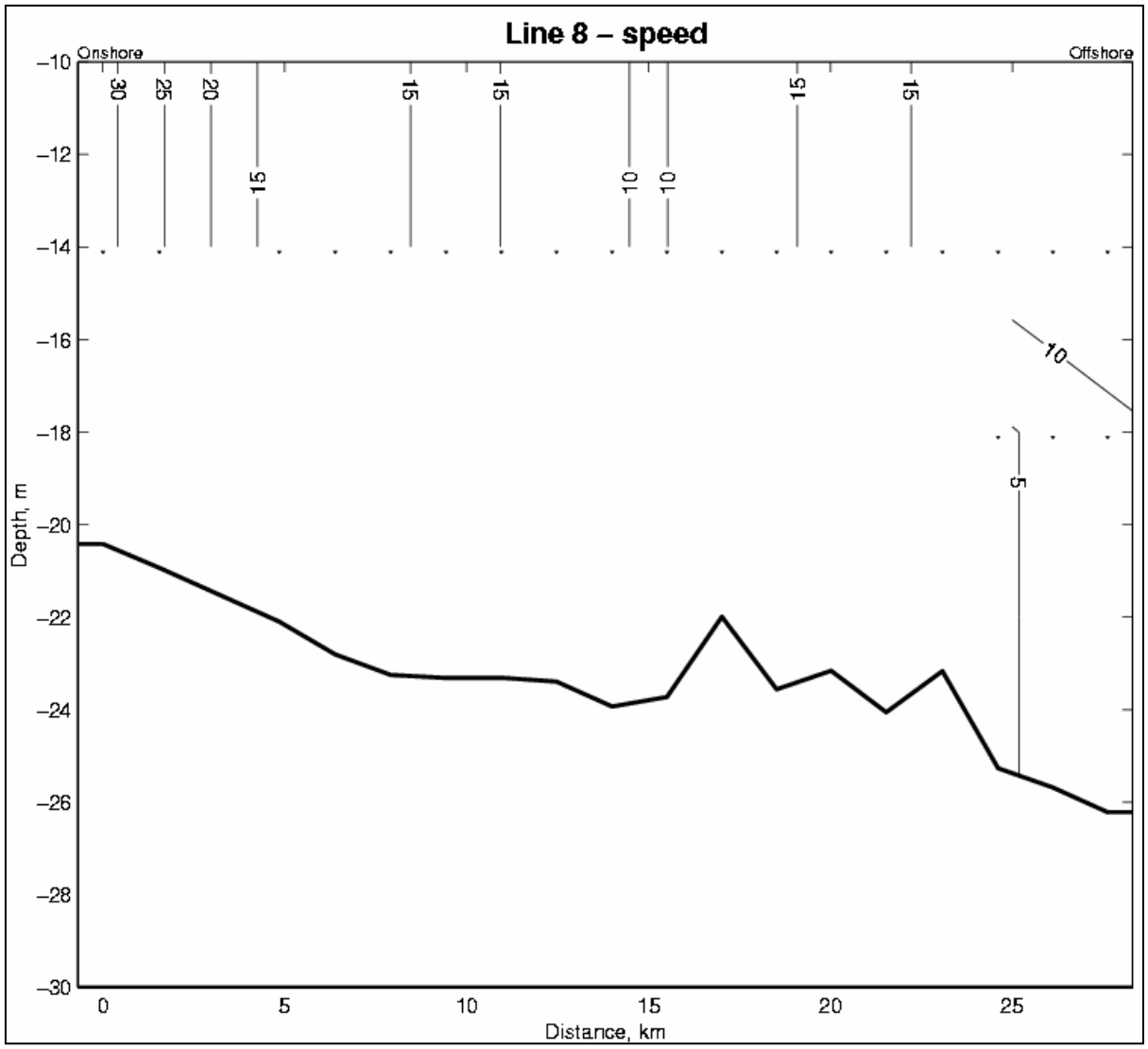

Figure C.25 Vertical section of ADCP speeds (cm s^{-1}) for Line 8 for cruise 98-G-9. Ensemble locations are marked with a small triangle.

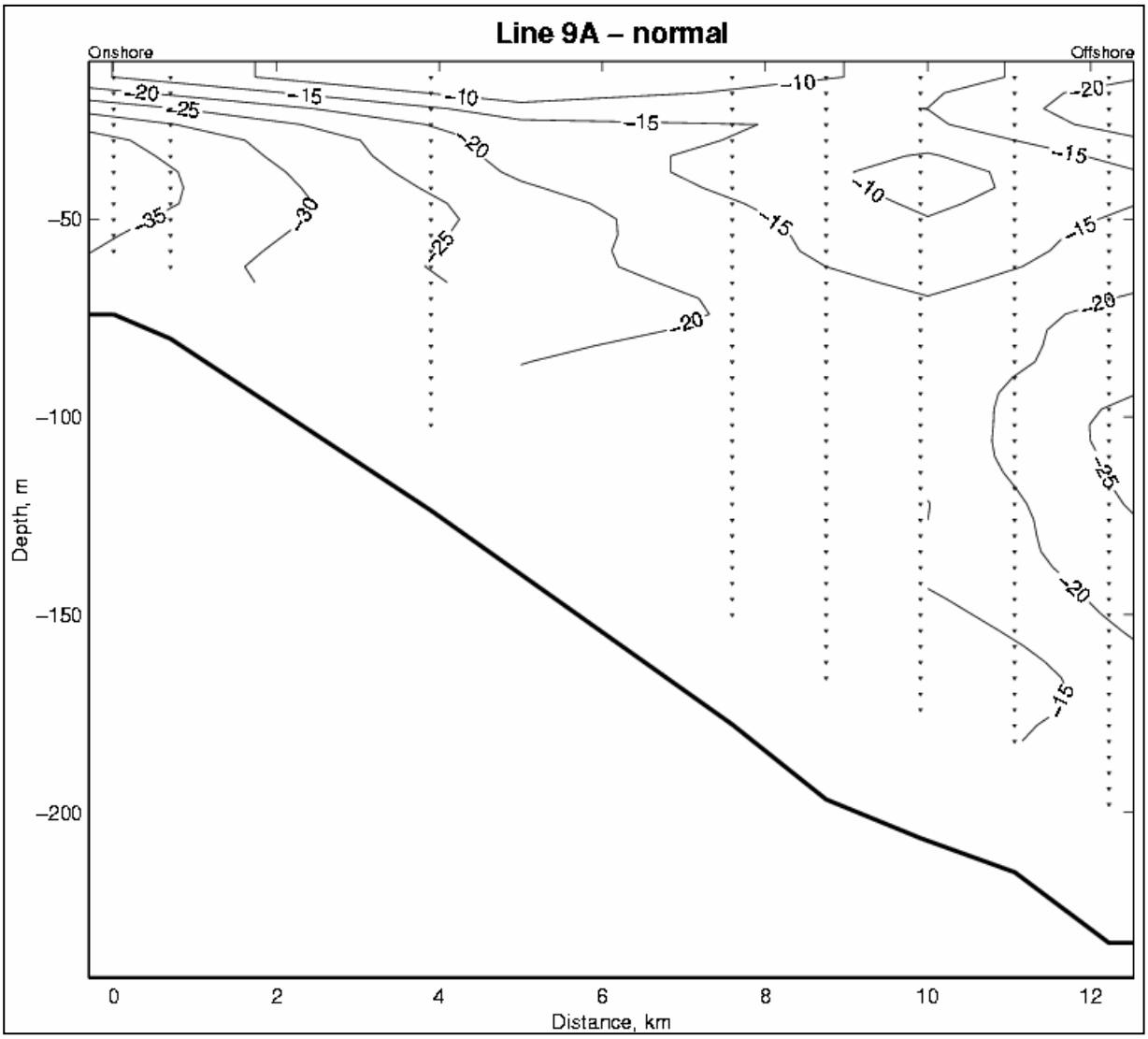

Figure C.26 Vertical section of ADCP velocities (cm s^{-1}) normal to Line 9A for cruise 98-G-9. Upcoast velocities are positive. Ensemble locations are marked with a small triangle.

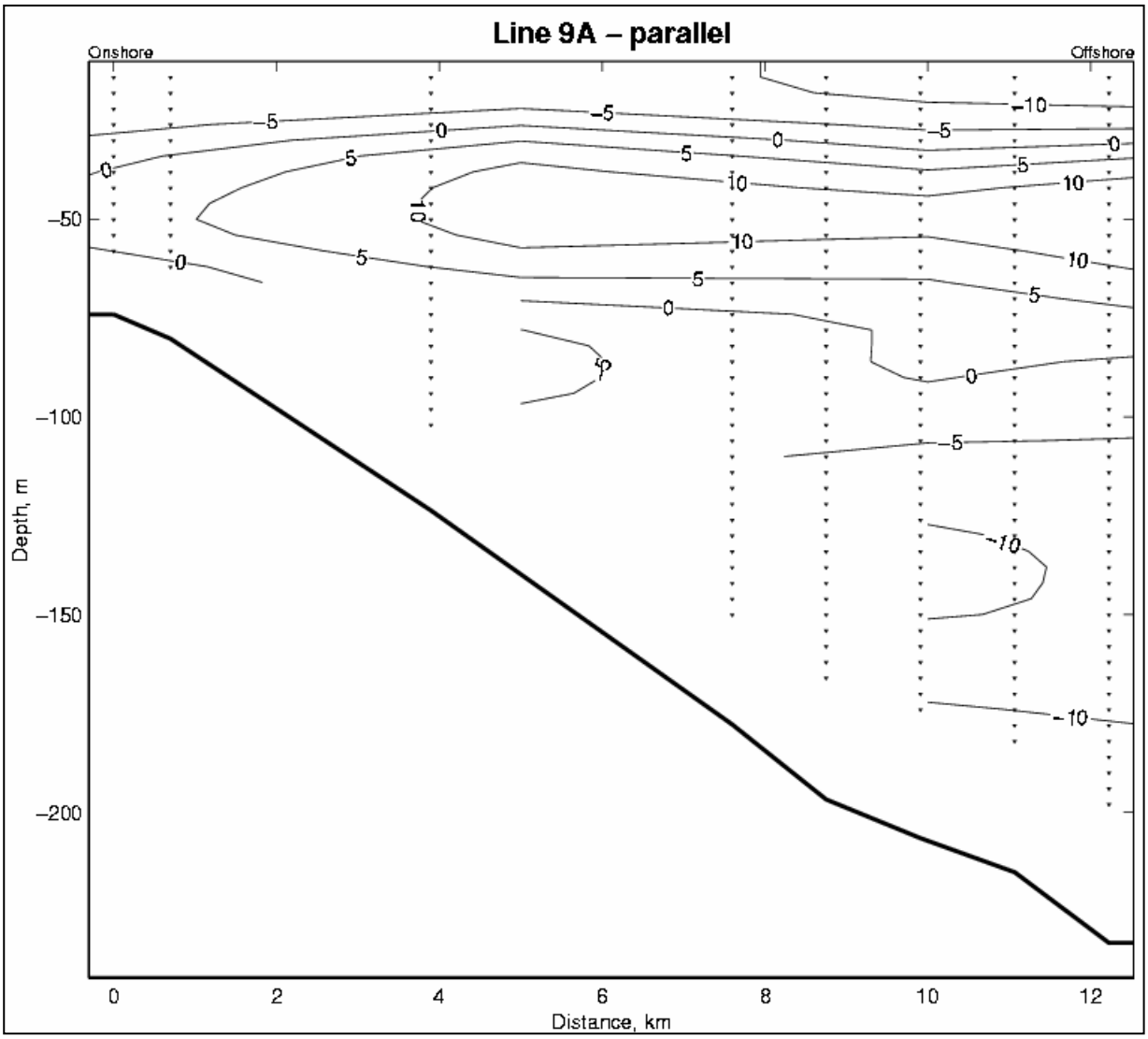

Figure C.27 Vertical section of ADCP velocities (cm s^{-1}) parallel to Line 9A for cruise 98-G-9. Onshore velocities are positive. Ensemble locations are marked with a small triangle.

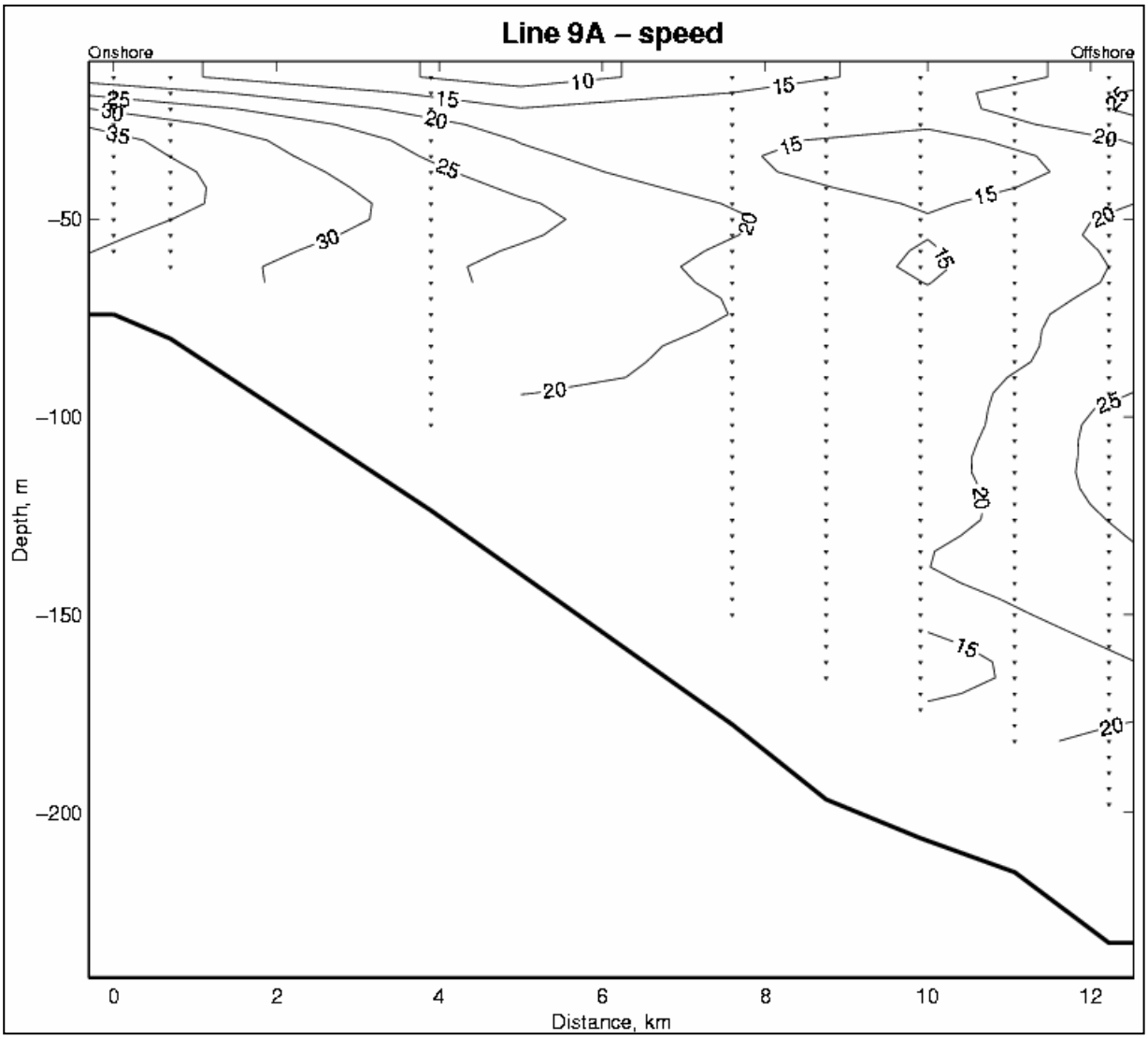

Figure C.28 Vertical section of ADCP speeds (cm s^{-1}) for Line 9A for cruise 98-G-9. Ensemble locations are marked with a small triangle.

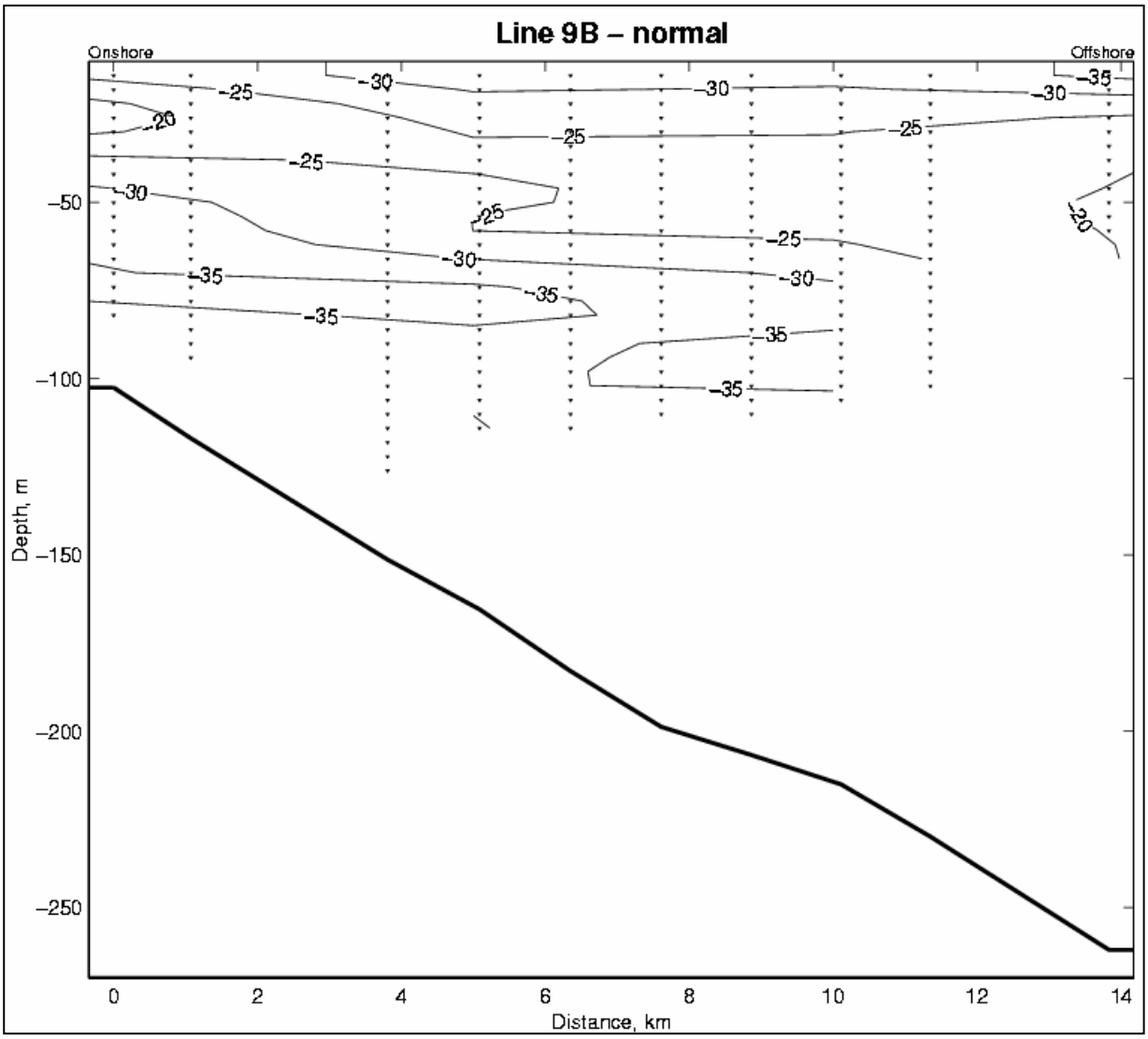

Figure C.29 Vertical section of ADCP velocities (cm s^{-1}) normal to Line 9B for cruise 98-G-9. Upcoast velocities are positive. Ensemble locations are marked with a small triangle.

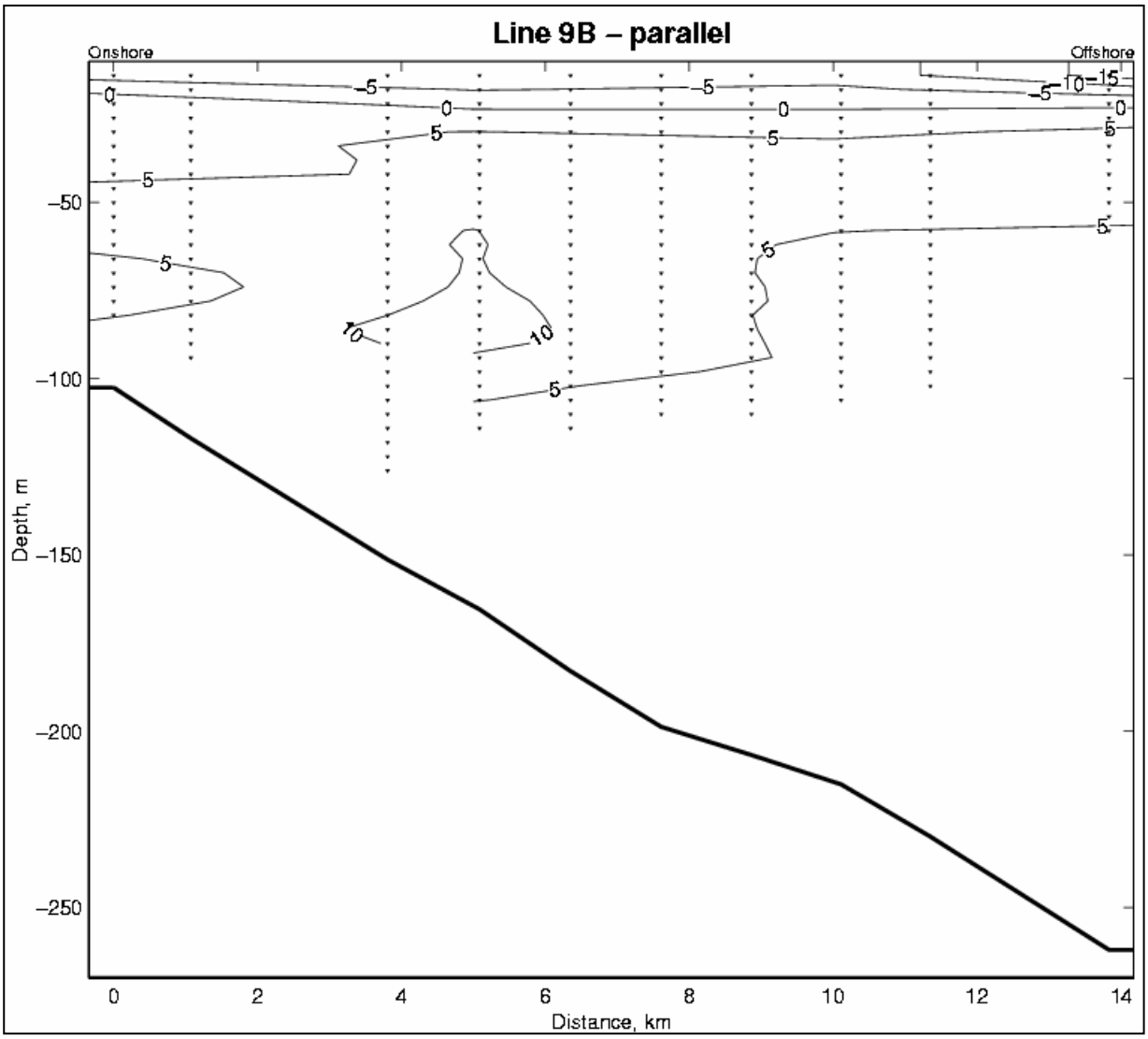

Figure C.30 Vertical section of ADCP velocities (cm s^{-1}) parallel to Line 9B for cruise 98-G-9. Onshore velocities are positive. Ensemble locations are marked with a small triangle.

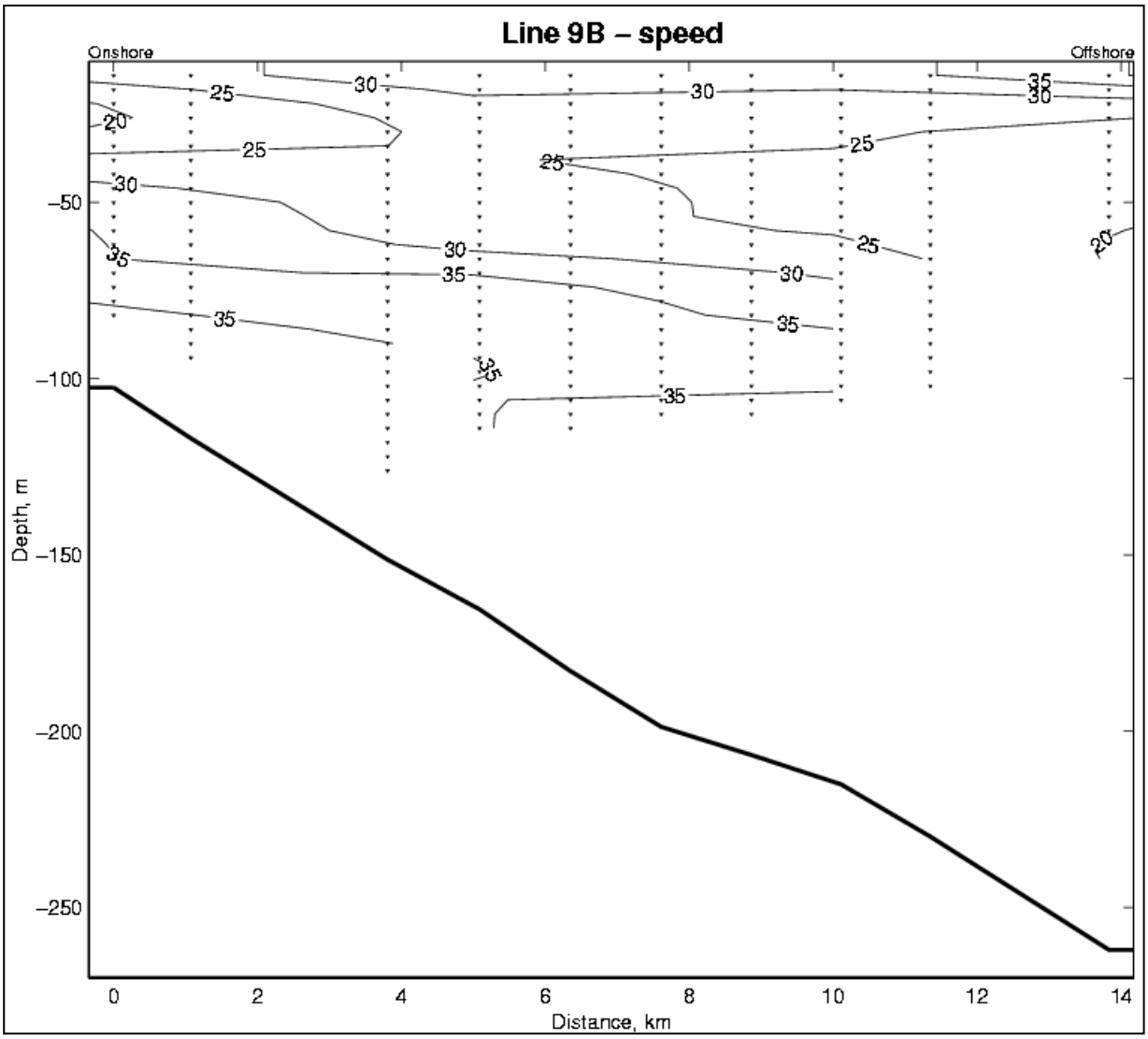

Figure C.31 Vertical section of ADCP speeds (cm s^{-1}) for Line 9B for cruise 98-G-9. Ensemble locations are marked with a small triangle.

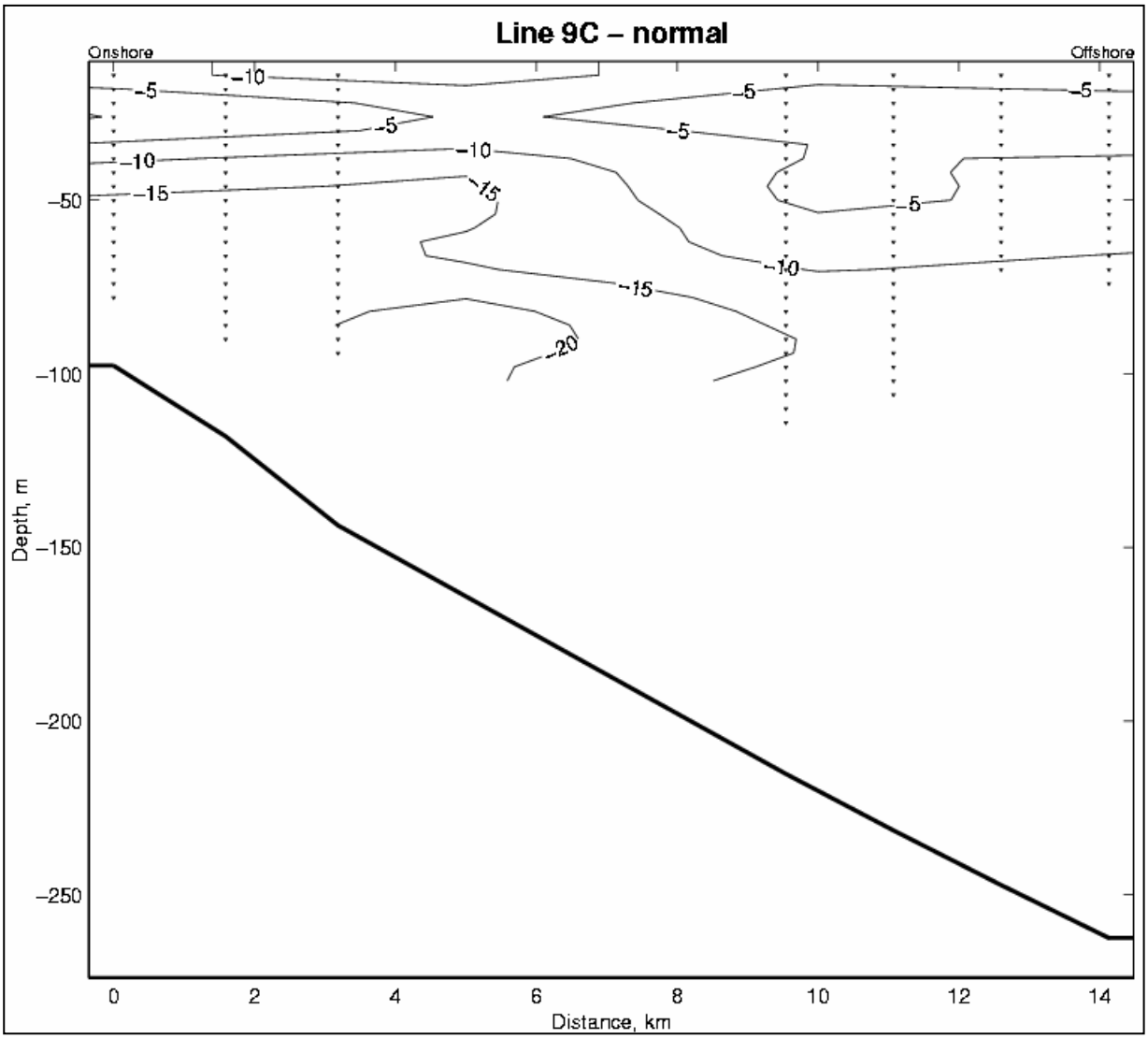

Figure C.32 Vertical section of ADCP velocities (cm s^{-1}) normal to Line 9C for cruise 98-G-9. Upcoast velocities are positive. Ensemble locations are marked with a small triangle.

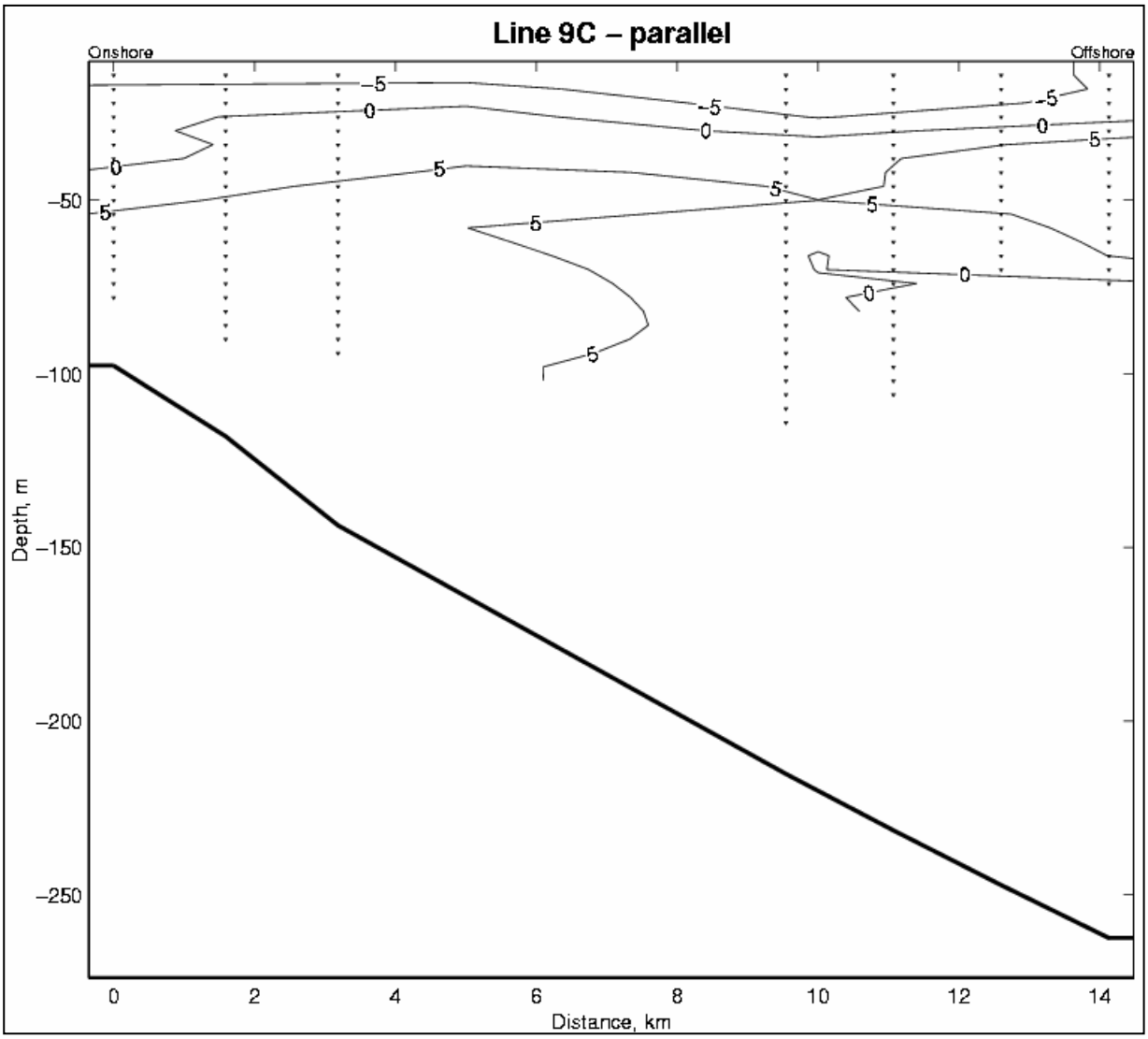

Figure C.33 Vertical section of ADCP velocities (cm s^{-1}) parallel to Line 9C for cruise 98-G-9. Onshore velocities are positive. Ensemble locations are marked with a small triangle.

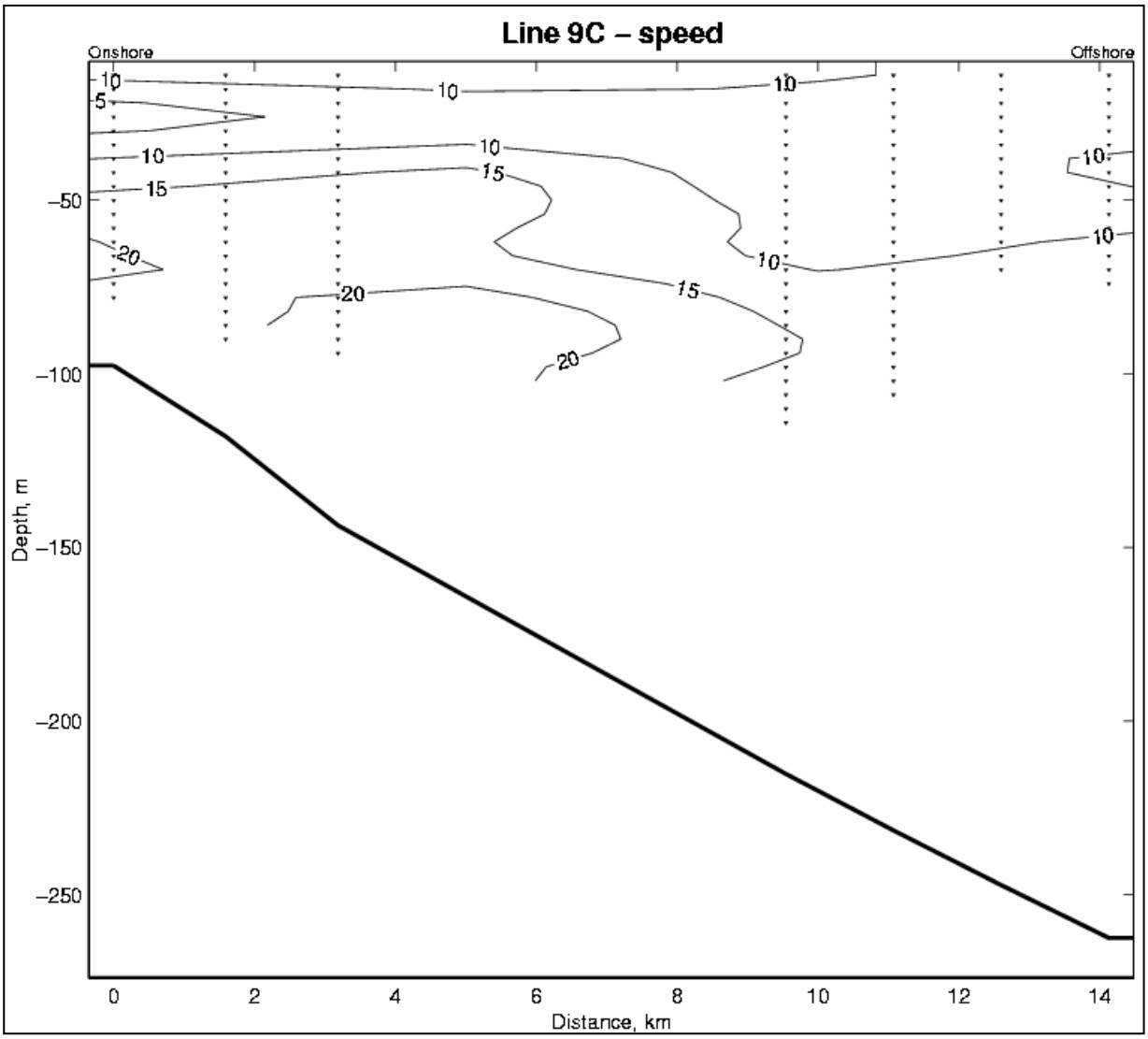

Figure C.34 Vertical section of ADCP speeds (cm s^{-1}) for Line 9C for cruise 98-G-9. Ensemble locations are marked with a small triangle.

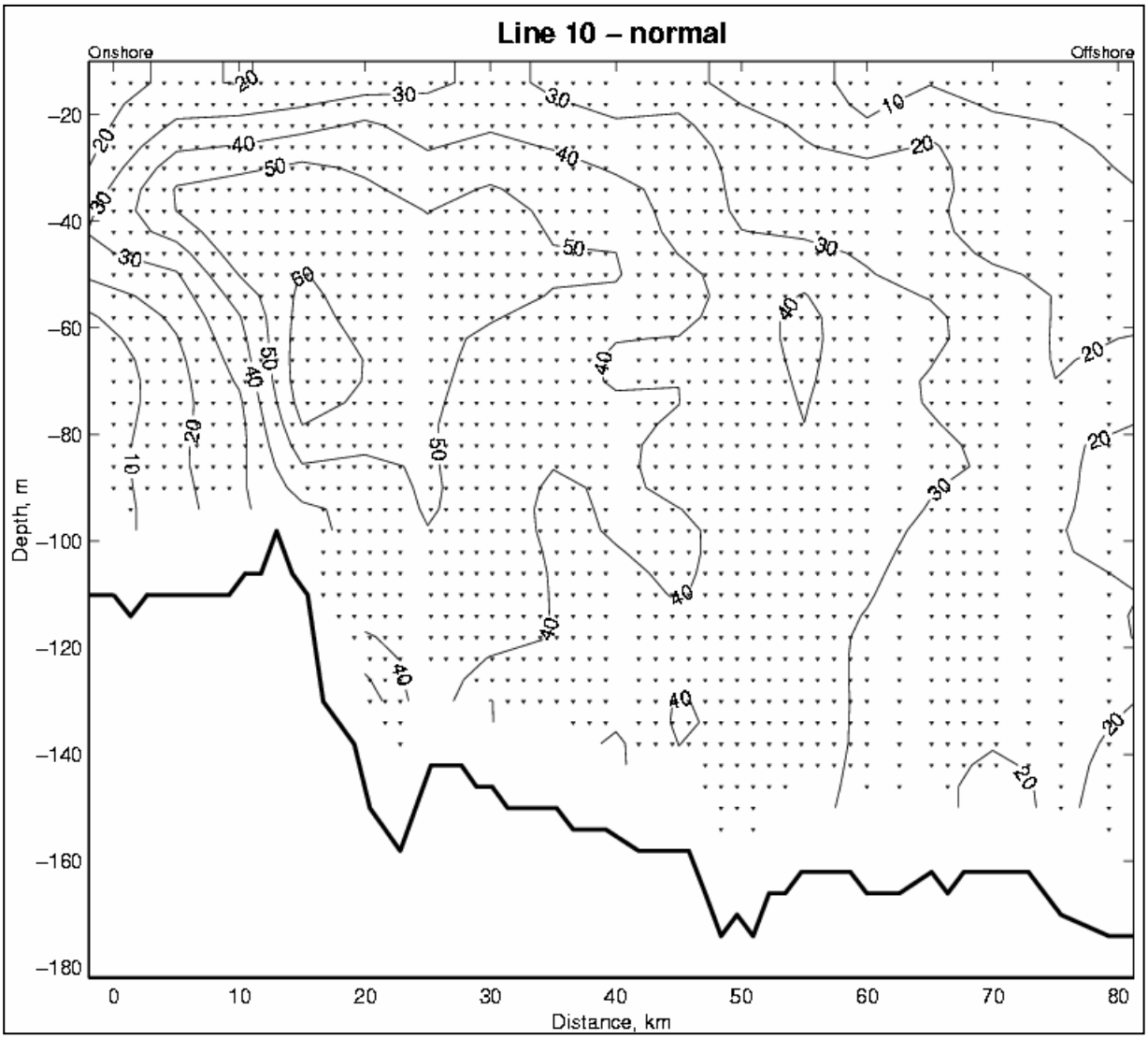

Figure C.35 Vertical section of ADCP velocities (cm s^{-1}) normal to Line 10 for cruise 98-G-9. Upcoast velocities are positive. Ensemble locations are marked with a small triangle.

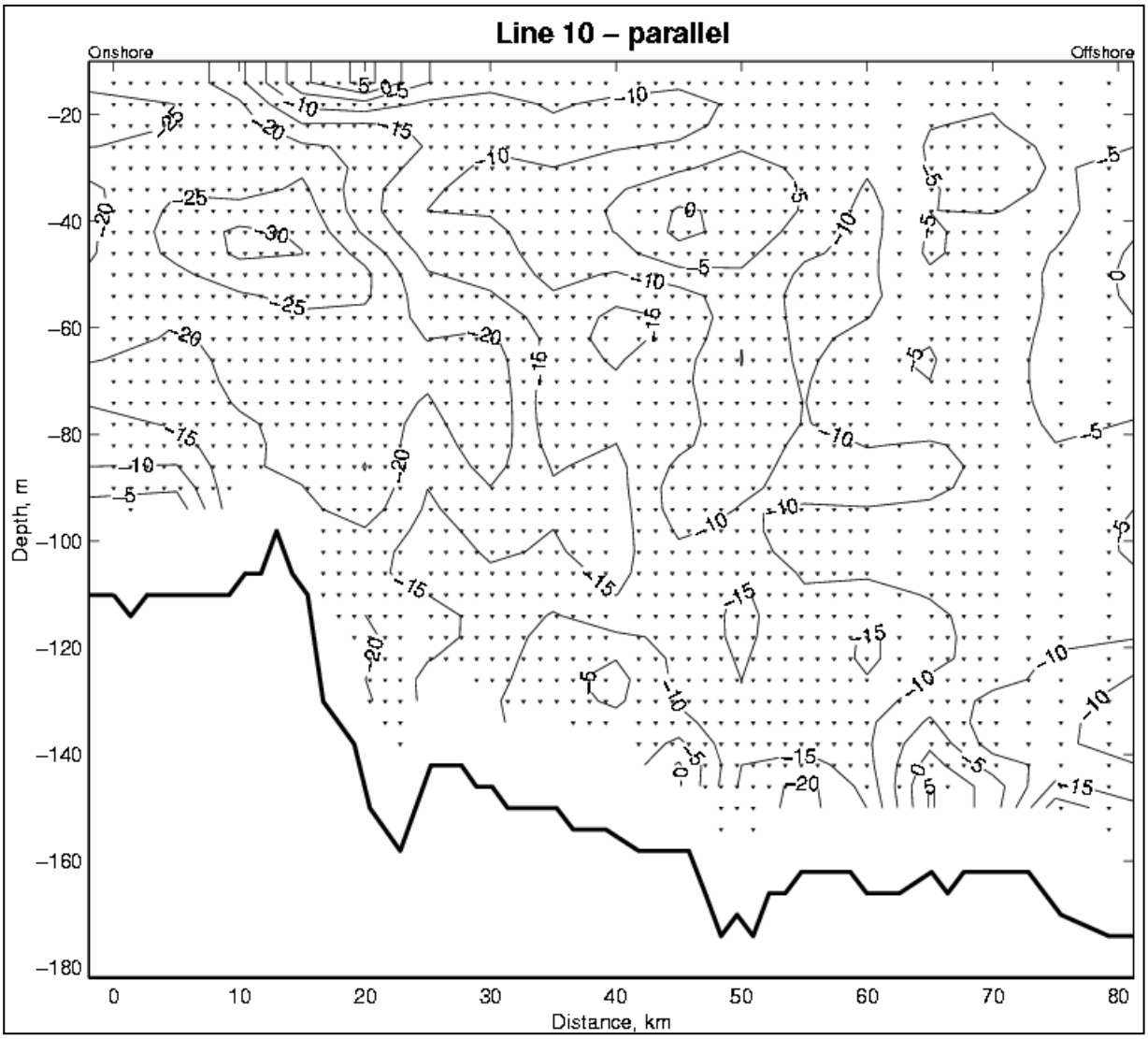

Figure C.36 Vertical section of ADCP velocities (cm s^{-1}) parallel to Line 10 for cruise 98-G-9. Onshore velocities are positive. Ensemble locations are marked with a small triangle.

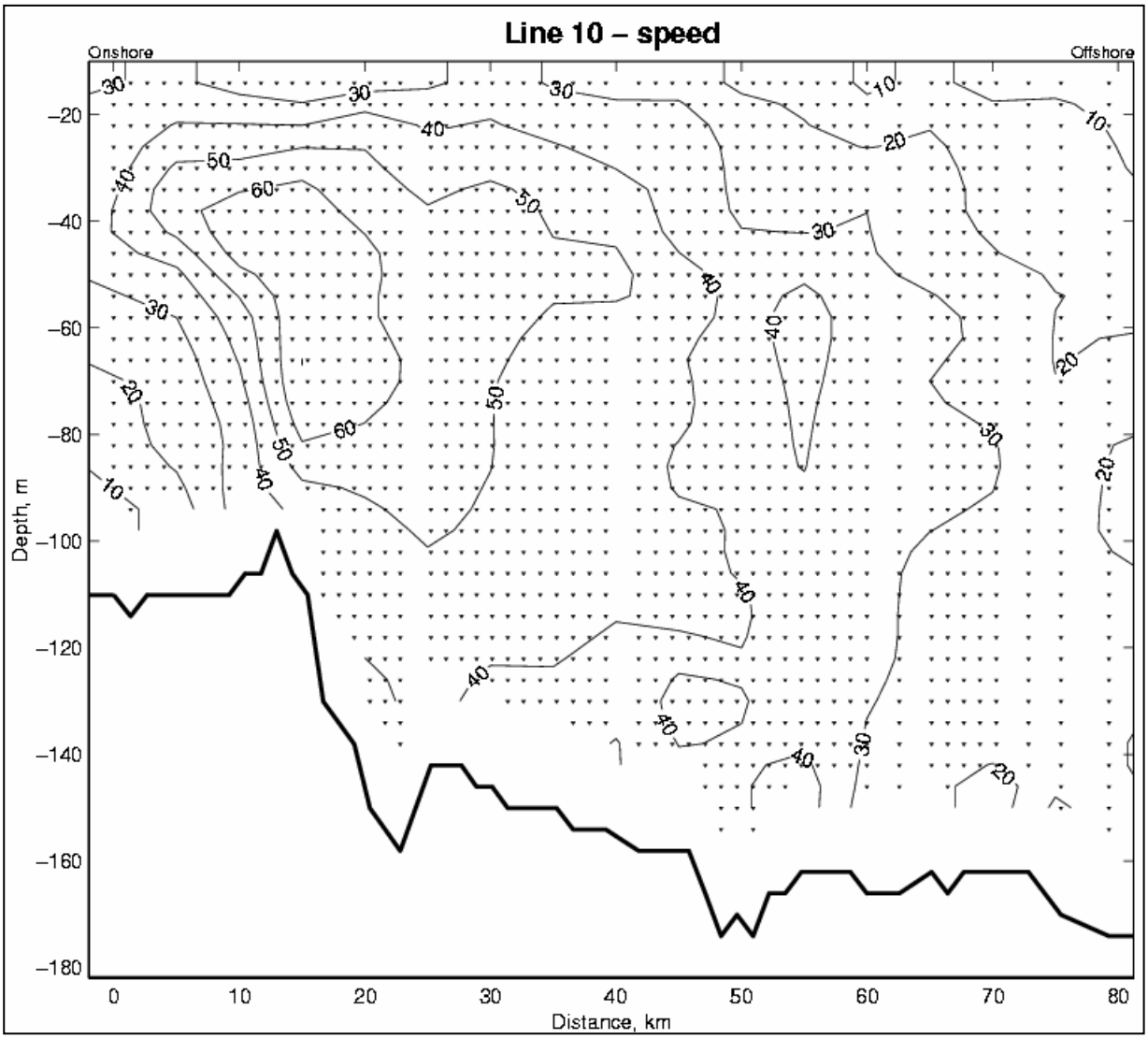

Figure C.37 Vertical section of ADCP speeds (cm s^{-1}) for Line 10 for cruise 98-G-9. Ensemble locations are marked with a small triangle.

The Department of the Interior Mission

As the Nation's principal conservation agency, the Department of the Interior has responsibility for most of our nationally owned public lands and natural resources. This includes fostering sound use of our land and water resources; protecting our fish, wildlife, and biological diversity; preserving the environmental and cultural values of our national parks and historical places; and providing for the enjoyment of life through outdoor recreation. The Department assesses our energy and mineral resources and works to ensure that their development is in the best interests of all our people by encouraging stewardship and citizen participation in their care. The Department also has a major responsibility for American Indian reservation communities and for people who live in island territories under U.S. administration.

The Minerals Management Service Mission

As a bureau of the Department of the Interior, the Minerals Management Service's (MMS) primary responsibilities are to manage the mineral resources located on the Nation's Outer Continental Shelf (OCS), collect revenue from the Federal OCS and onshore Federal and Indian lands, and distribute those revenues.

Moreover, in working to meet its responsibilities, the **Offshore Minerals Management Program** administers the OCS competitive leasing program and oversees the safe and environmentally sound exploration and production of our Nation's offshore natural gas, oil and other mineral resources. The MMS **Minerals Revenue Management** meets its responsibilities by ensuring the efficient, timely and accurate collection and disbursement of revenue from mineral leasing and production due to Indian tribes and allottees, States and the U.S. Treasury.

The MMS strives to fulfill its responsibilities through the general guiding principles of: (1) being responsive to the public's concerns and interests by maintaining a dialogue with all potentially affected parties and (2) carrying out its programs with an emphasis on working to enhance the quality of life for all Americans by lending MMS assistance and expertise to economic development and environmental protection.

MMS Securing Ocean Energy & Economic Value for America